AN ABSTRACT OF THE THESIS OF

Sharon Elaine Roth Franks for the degree of Doctor of Philosophy in Oceanography presented on December 4, 1992.

Title: Temporal and Spatial Variability in the Endeavour Ridge Neutrally Buoyant Hydrothermal Plume: Patterns, Forcing Mechanisms and Biogeochemical Implications

Redacted for privacy

Abstract approved: Jack Dymond

Time series records of horizontal current velocity, temperature, light attenuation and settling particle flux obtained using moored instruments above Endeavour Ridge in the northeast Pacific Ocean elucidate the dynamics of a deep-sea, neutrally buoyant, hydrothermal plume. Data collected in four mooring deployments over three years within 20 km of an active hydrothermal vent field quantify heretofore suspected temporal and spatial variability in the plume, and provide evidence of causality. Over time scales of hours to days, local fluctuations in temperature and suspended particle concentration primarily reflect horizontal transport of hydrothermal effluent by currents. However, it is dramatic variability in lateral transport of hydrothermal material over longer time scales (months to years) which profoundly influences the spatial distribution of settling particle flux. Steering of the hydrothermal plume by horizontal currents, in concert with seasonal effects linked to production of biogenic particulate material in the upper ocean, together explain the predominant temporal patterns in settling hydrothermal particle flux measured within and beneath the plume. Spatial variability in plume-guiding currents is also pronounced; horizontal flow is non-uniform over distances of ≈ 10 km horizontally and hundreds of meters vertically.

Despite the potential complexity of both the physical oceanographic regime and the effects of multiple particle-transformation processes, the changes in settling flux of hydrothermal elements as a function of along-plume distance can be described by a simple model that includes first-order loss of particle flux and along-plume horizontal advection. An innovative technique employing probability density functions of horizontal flow direction is used to scale measured sediment-trap fluxes to reflect true beneath-plume fluxes of hydrothermal elements. These scaled settling particle fluxes are used to define the functionality of settling hydrothermal particle flux with distance from the vent-field, predict the settling flux of specific elements directly above the vent field, and calculate the integrated settling particle flux of hydrothermal elements within $\approx$ 15 km from the vent field. Results emphasize the relevance of temporal variability in physical plume forcing to data interpretation, experimental design and model formulation.

Temporal and Spatial Variability in the Endeavour Ridge Neutrally Buoyant Hydrothermal Plume: Patterns, Forcing Mechanisms and Biogeochemical Implications

by

Sharon Elaine Roth Franks

A THESIS
submitted to
Oregon State University

in partial fulfillment of
the requirements for the
degree of

Doctor of Philosophy

Completed December 4, 1992
Commencement June 1993

APPROVED:

Redacted for privacy

Professor of Oceanography in charge of major

Redacted for privacy

Dean of College of Oceanography

Redacted for privacy

Dean of Graduate School

Date thesis is presented December 4, 1992

Typed by Sharon Elaine Roth Franks

Acknowledgments

Thanksgiving Day seems a particularly appropriate time to express my gratitude to the many wonderful people who have assisted, encouraged, supported, and taught me important lessons during the time I have been a student at Oregon State University.

Jack Dymond, my major professor, has been a great scientific mentor, academic advisor, and friend over the years. My respect for his intellect, his innate curiosity about nature and his commitment to the health of out planet is immense. I am fortunate to have had the opportunity to interact with him. Jack has offered inspiration, understanding, constructive criticism, humor, and faith in my abilities, even during times when I had lost that faith.

Peter J. S. Franks, my beloved husband, has been an extraordinary source of love, joy, encouragement, support, and scientific insight over the past two-plus years. Peter introduced me to computer and modeling techniques that allowed me to interpret the enormous quantity of data with which I had been struggling. We have spent many productive hours discussing my work, its value and its limitations. I have enormous admiration for his multidisciplinary scientific ability. Aside from the much appreciated scientific counsel, Peter Potamus has given me his love, unending encouragement, and superbly excellent schneeblage that has sustained me during stressful times. Our deep love for each other has put all other aspects of life into perspective.

Rick Thomson has been so very generous with his time, energy and resources. I consider Rick to be a great role model. Not only is he an excellent scientist - thorough, thoughtful and prolific - he also exudes a rare combination of energy, cooperative spirit, and perpetual good cheer. It has been a great pleasure to work with him and all of the other fine people at the Institute of Ocean Sciences. Special thanks go to Reg Bingham, John Love and Paul Frost. The competence, efficiency and pleasantness of the Canadian team are truly impressive. I will always carry with me fond memories of our many trips to sea. I suspect my favourable impression of Canadians in general was a factor in my decision to marry one.

This work could not have been carried out without the help of many people here at OSU. I am grateful to Chris Moser, Kathryn Brooksforce, Bobbi Conard and Pat Collier, who showed me the ropes figuratively and literally, at sea and in the lab. Many thanks to my committee members: Bob Collier, John Lupton, Leonard Walstad and Jeff Barnes. Special thanks to Bill Winkler, whose fire drills and full circuits helped me keep fit over the years, and to Mike Hare who helped me save my own life.

For a strong, beautiful, and wise woman, my mother, Sylvia E. Roth, I am deeply grateful, not only because she gave me life, but also because she has offered boundless love, support and encouragement as I have grown and pursued my formal education. I am also appreciative of the support of my father, Alex Roth. Without his financial help I might not have been able to complete my studies.

Financial support for my work was provided by the U.S. National Science Foundation grants OCE-8515876 and OCE-8817300, the Institute of Ocean Sciences in Sidney, B.C., Canada, the Houston Underwater Club and the Association of Women Geoscientists.

Table of Contents

List of Figures

List of Figures - continued

List of Figures - continued

List of Figures - continued

List of Figures - continued

List of Figures - continued

List of Figures - continued

List of Figures - continued

List of Figures - continued

List of Tables

Temporal and Spatial Variability in the Endeavour Ridge Neutrally Buoyant Hydrothermal Plume: Patterns, Forcing Mechanisms and Biogeochemical Implications

I: General Introduction

Since the discovery of hydrothermal vents along the Earth's submarine spreading ridges, considerable effort has been directed towards quantifying the temporal variability of deep-sea hydrothermal activity. Much of the focus has been on changes in thermal and chemical output from the vents over time scales extending from minutes or days (Johnson and Tunnicliffe, 1985; Little et al., 1988; Baker et al., 1989; McDuff, 1990; Tivey et al., 1990; Schultz et al., 1992) to years (Chadwick et al., 1991; Stakes and Moore, 1991; Baker, in press, and references therein) to millions of years (Lyle et al., 1987, Metz et al., 1988). Indeed, characterizing the temporal and spatial variability of deep-sea plumes is a fundamental step in understanding the role hydrothermal emissions play in marine biogeochemical processes. But factors other than fluctuation in the intensity of venting contribute significantly to the variability of water-column dispersal and subsequent removal of hydrothermal material. Rather than focussing on the impact of time-variable hydrothermal output on the overlying water column, the focus of this thesis is toward elucidating the effects of variability in the water column on the oceanic distribution of hydrothermal material.

Physical transport of hydrothermal plumes by abyssal currents, and rates of biogeochemical particle transformation, among other factors, regulate the oceanic fate of hydrothermal effluent. Efforts to quantify variability in plume-guiding currents have been few (Cannon et al, 1991) and often limited to relatively short term experiments (Little et al., 1988; Baker and Massoth, 1987; Thomson et al., 1992). Moreover results of experiments conducted at one site may not be indicative of conditions in general. The chemistry of suspended hydrothermal particles has been extensively studied (Trefry et al., 1985; Feely et al., 1987, 1990 a, b, 1991, 1992; Trocine and Trefry, 1988;) and rates of chemical reactions thought to occur in hydrothermal plumes have been constrained by innovative techniques (Rosenberg et

al., 1988; Cowen et al, 1990; Kadko et al., 1990; Metz and Trefry, submitted), yet little is known about the temporal and spatial variability of these reactions *in situ*. Based on estimates of lateral and settling particle flux (Baker et al., 1985; Dymond and Roth, 1988) , and modeling of hydrothermal Mn deposition (Lavelle et al, 1992) it is thought that the bulk of hydrothermal material does not settle near the vent field, rather that it is carried laterally by currents many kilometers prior to incorporation in seafloor sediments. In order to truly understand the role of advection in regulating the distribution and oceanic residence time of hydrothermal components, characterization of variability in the physical oceanographic regime into which hydrothermal emissions flow must encompass temporal and spatial scales over which particle transformations occur.

In this thesis, I present and interpret data collected over three years using moored instruments to monitor the neutrally buoyant hydrothermal plume above Endeavour Ridge in the northeast Pacific Ocean. Time series records of horizontal flow, temperature, fine particle concentration, and settling particle flux obtained within 15 km of an active vent field show that: 1) Horizontal advection of hydrothermal material is variable over time scales of hours to years, over the depth range of the plume and horizontally over distances up to at least 15 km from the vent field; and 2) Removal of hydrothermal material from the plume via particle settling is also temporally and spatially variable, and this variability reflects, in addition to physical transport, rates of particle transformations, some of which are biologically mediated, mixing of fluids from diffuse and high-temperature sources, and, possibly, temporal or compositional changes in vent output.

This thesis is divided into three main chapters. Chapter II is an evaluation of temporal and spatial variability in the Endeavour Ridge plume. It includes: 1) presentation and discussion of all flow, temperature, light attenuation and particle flux time series; 2) introduction of a conceptual plume model that describes the causes of hydrothermal plume variability; 3) quantification of all scales of temporal and spatial variability resolved in the experiment and evaluation of the causes of this variability; and 4) implications of my findings and relationship of this study to other investigations. Chapter III is a simple analytical model of settling hydrothermal particle flux with distance from the vent field based on first order particle removal and along-plume advection. Chapter IV interprets vertical changes in near-vent-field

settling particle flux as possible evidence of simultaneous addition and removal of organic material at plume depths.

II: Dynamics of a deep sea hydrothermal particle plume: Spatial and temporal characteristics based on moored current meter, transmissometer and sediment trap data

Abstract

Results of a three-year, moored-instrument experiment at Endeavour Ridge in the northeast Pacific Ocean show that the neutrally buoyant plume originating at an active seafloor hydrothermal vent field is a highly dynamic deep-sea feature. Variability in temperature and particle flux measured within the area influenced by the neutrally buoyant plume can be explained by one or more of four processes: 1) horizontal advection; 2) mixing of chemically/thermally distinct hydrothermal emissions; 3) biogeochemical particle transformations; and 4) temporal or compositional changes in vent output. For example, all four of these processes influence the temporally and spatially variable relationship between fine-particle concentration and heat content in the plume, whereas near-vent-field, tidal-frequency temperature fluctuations can be explained solely by horizontal advection.

Time series of current velocity, temperature, light attenuation and settling particle flux document temporal variability over time scales of hours to years. Tidal and inertial variability are pronounced in flow, temperature and attenuation coefficient records. These rotary motions, with frequencies of 1-2 cycles per day, and speeds > 15 cm/s, increase the lateral extent of hydrothermal plume influence by 1-2 km. They are also factors in regulating the amount of time a fixed point in the ocean (or on the seafloor, via settling hydrothermal particle flux) experiences the plume. The amplitude of lower-frequency temperature variability (< 1 cpd) is about half that of variability due to tidal and inertial oscillations. For horizontal velocity, amplitudes of the lowest-frequency variations are up to a factor of 20 less than those associated with tides and inertial motion. Low-frequency changes in mean current velocity account for some but not all of the low-frequency temperature variability. Over time scales of at least 1-2 months, within several kilometers of the vent field, the horizontal transport of heat at plume depths is coupled to the settling flux of hydrothermal particles. The flux of hydrothermal copper within the plume core (at approximately 1950 m depth) varies by a factor of 15 between 48-day sampling periods and by a factor of 20 between mooring

deployments with durations of 2-11 months. Both advection, which controls the location of the hydrothermal effluent plume, and seasonal fluxes of particles from the upper water column, which apparently regulate removal of some hydrothermal elements from the plume, are important determinants of the timing and local magnitude of settling hydrothermal particle flux. Interannual variation in horizontal advection is significant; at plume-core depths, mean annual current speed varied by 50% (about 0.6 km/day) and flow direction varied by 100°. Evidence of episodicity observed in the attenuation and temperature records is limited to small amplitude (≤ 0.05 m-1; 0.04°C), short duration (< 3 day) events which can be explained by horizontal advection.

Spatial variability in the water column over the Endeavour Ridge vent field extends vertically from well above the neutrally buoyant plume (hundreds of meters above bottom) to tens of meters above the seafloor, and horizontally to at least 15 km from the vent field. Mean velocity vectors that rotate anticlockwise up to 180° over depths from 1700 to 2100 m constitute a pattern of vertical shear of horizontal currents that persists for at least two years at near-vent-field moorings. This vertical shear may restrict the radial distance settling particles travel away from the vent field during their descent. Horizontally, plume-depth flow is well-correlated among three moorings within 3 km of the vent field, but coherence of current velocity measured 15 km from the vent field and that simultaneously recorded only 0.5 km from the vents is low. This result constrains correlation length scales in this region to between 3 and 15 km. Spatial patterns in the magnitude of settling particle fluxes include increasing flux of hydrothermal elements beneath the neutrally buoyant plume and decreasing hydrothermal flux with distance from the vent field. Compositional changes in hydrothermal particle flux which include decreases in Fe-to-Cu, Zn, Mn, and S ratios between the plume-core and beneath-plume sediment traps; this reflects rapid precipitation of large-particle Cu and Zn sulfides near the seafloor and injection of Mn-rich, Fe-depleted, low-temperature, diffuse hydrothermal fluids. Reduced fluxes of biogenic and inorganic detrital particles at plume depths may both reflect water-column biological activity and exert ecological control on deep-sea faunal distributions.

Introduction

Along submarine volcanic ridges where oceanic crust is produced, a remarkable link between the solid earth and the oceans is observed. Seawater travels through fissures in the young, hot rock and is altered thermally and chemically by reactions with basalt. Both heat and mass are transferred from the lithosphere to the sea water in hydrothermally driven circulation systems. Where hydrothermal flow is most vigorous, particle-enriched, thermal plumes rise buoyantly hundreds of meters from seafloor vents, then spread laterally, dispersing heat as well as dissolved and particulate material (Figure II.1). It is on the dispersing oceanic limb of the hydrothermal circulation cell that this thesis is focused. More specifically, the goal of this chapter is to use current meter, sediment trap and transmissometer data collected over three years near an active vent field in the northeast Pacific Ocean to evaluate the spatial and temporal characteristics of a neutrally buoyant hydrothermal plume. In bringing together physical oceanographic and geochemical data, the intent of this work is to provide a foundation for understanding how seafloor hydrothermal emissions interact with the oceanic environment. A fundamental step in this endeavour is to characterize the physical, water column dispersal of the hydrothermal plume. Quantitative observations regarding horizontal advection are later used in a simple analytical model of settling hydrothermal particle flux (Chapter III).

Seafloor hydrothermal activity along the Earth's spreading ridges was first detected less than two decades ago, and only very recently have experiments been undertaken to quantify the fluxes of heat and mass through these fissures. While it is known that hydrothermal plumes can be traced for hundreds of kilometers from their ridge crest origins (Baker et al., 1985; Klinkhammer and Hudson, 1986), our understanding of what happens to the hydrothermal emissions once they exit the seafloor vents is still rudimentary. A simple conceptual model of a relatively steady-state, buoyantly rising, then laterally spreading plume has served as a basis for the majority of oceanographic hydrothermal plume investigations, including our moored instrument study at Endeavour Ridge which began in 1984. Efforts to quantify temporal variability in hydrothermal venting have taken precedence over quantification

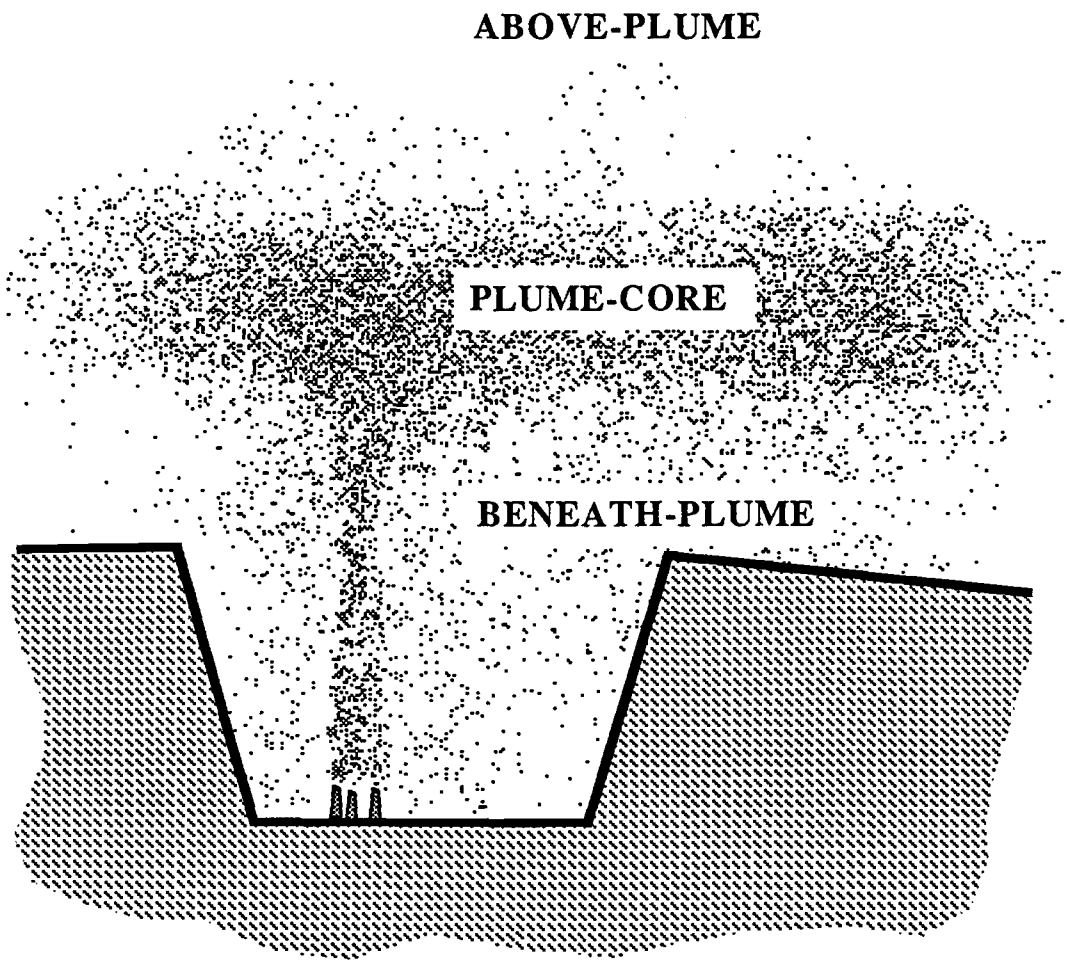

Figure II.1. Schematic cross section of a seafloor spreading ridge crest showing vents along the axial valley floor and emanating plumes which coalesce to form a neutrally buoyant plume. Above-plume, plume-core and beneath-plume regions referred to in text are shown.

of the physical variability in the water column that influences the distribution and subsequent removal of hydrothermal material.

The discussion that follows focusses on quantifying temporal and spatial variability in the Endeavour Ridge hydrothermal plume and identifying the multiple causes of this variability. The general hypothesis I explore is:

The Endeavour Ridge hydrothermal plume is a dynamic deep-sea feature.

Information on the local physical oceanographic setting, suspended particle concentration and the composition of the settling particle flux is brought to bear on testing the following specific hypotheses:

1. Both periodic and episodic physical events regulate the transport of hydrothermal particles and heat in the neutrally buoyant plume.
2. Temporal variations in horizontal flow that regulate the distribution of hydrothermal effluent span a minimum range from tidal to interannual cycles; spatial variations extend vertically from the top of the neutrally buoyant plume to the seafloor, and horizontally at least to a distance of approximately 15 km from the vent field, which is the maximum distance of our measurements.
3. Physical oceanographic forcing alone cannot account for all observed patterns of hydrothermal particle flux. Variations in the quantity/chemistry/temperature of hydrothermal vent output, water column chemical transformations (e.g. precipitation, scavenging, dissolution), particle removal by settling, patterns of and deep-sea response to upper water column productivity, and deep-sea biological activity are also important factors in determining the dispersal, residence time, and ultimate removal of hydrothermal material from the ocean.

Background and Clarification of Terms

Endeavour Ridge is a 90-km-long northern segment of the six-segment, 525-km-long Juan de Fuca Ridge in the northeast Pacific Ocean, about 300 km west of the southern tip of Vancouver Island (Figure II.2). The Juan de Fuca Ridge is a medium rate spreading center; the full-spreading rate is about 6 cm per year (Riddihough, 1984). Active hydrothermal venting occurs along all but one segment of the ridge system. Shaped like a shallow, inverse "S", the geologically complicated Endeavour segment is oriented along an axis that strikes N20°E (hereafter expressed as 20°T) (Baker and Hammond, 1992). Its well-defined axial valley is less than one km wide and bounded by steep walls 50-100 m high along the topographically high, central portion of the segment where venting occurs. Along the central valley floor, at a water depth of about 2200 m, an active hydrothermal vent field was identified at 47° 57'N, 129° 06.5' (Hammond et al., 1984; MERGE Group, 1984) and its associated plume later mapped and sampled (Baker and Massoth, 1987; Rosenberg et al., 1988). Detailed mapping of this 200 m by 400 m vent field, located along the western axial valley wall, shows that it contains at least 15 large (30 m diameter, 20 m high), vigorously venting sulfide structures and tens of smaller, commonly inactive structures (Delaney et al., 1992). Venting temperatures as high as 405°C have been reported (Tivey et al., 1990), as well as more diffuse, lower-temperature emissions. Temperature anomalies in the neutrally buoyant plume, which is centered approximately on the 27.665 potential density surface, are typically greater at this site than at any of the other along the Juan de Fuca Ridge (Baker and Hammond, 1992).

Additional areas of water column temperature and light attenuation anomalies were later found along Endeavour Ridge. One, dubbed Fairycastle Site (Stakes and Moore, 1991), about two km north of the first vent field is characterized by extensive tube worm fields but generates a plume of lower temperature and light attenuation anomalies (Baker and Massoth, 1987). A second area is about 25 km south of the primary vent field (Baker and Hammond, 1992). Recent water-column surveys indicate other possible new vent sites along Endeavour Ridge 4 and 8 km northeast and 6 km south of the primary vent field (Thomson et al., 1992b). At the time we began our moored-instrument investigation in 1984, only the primary vent field had been

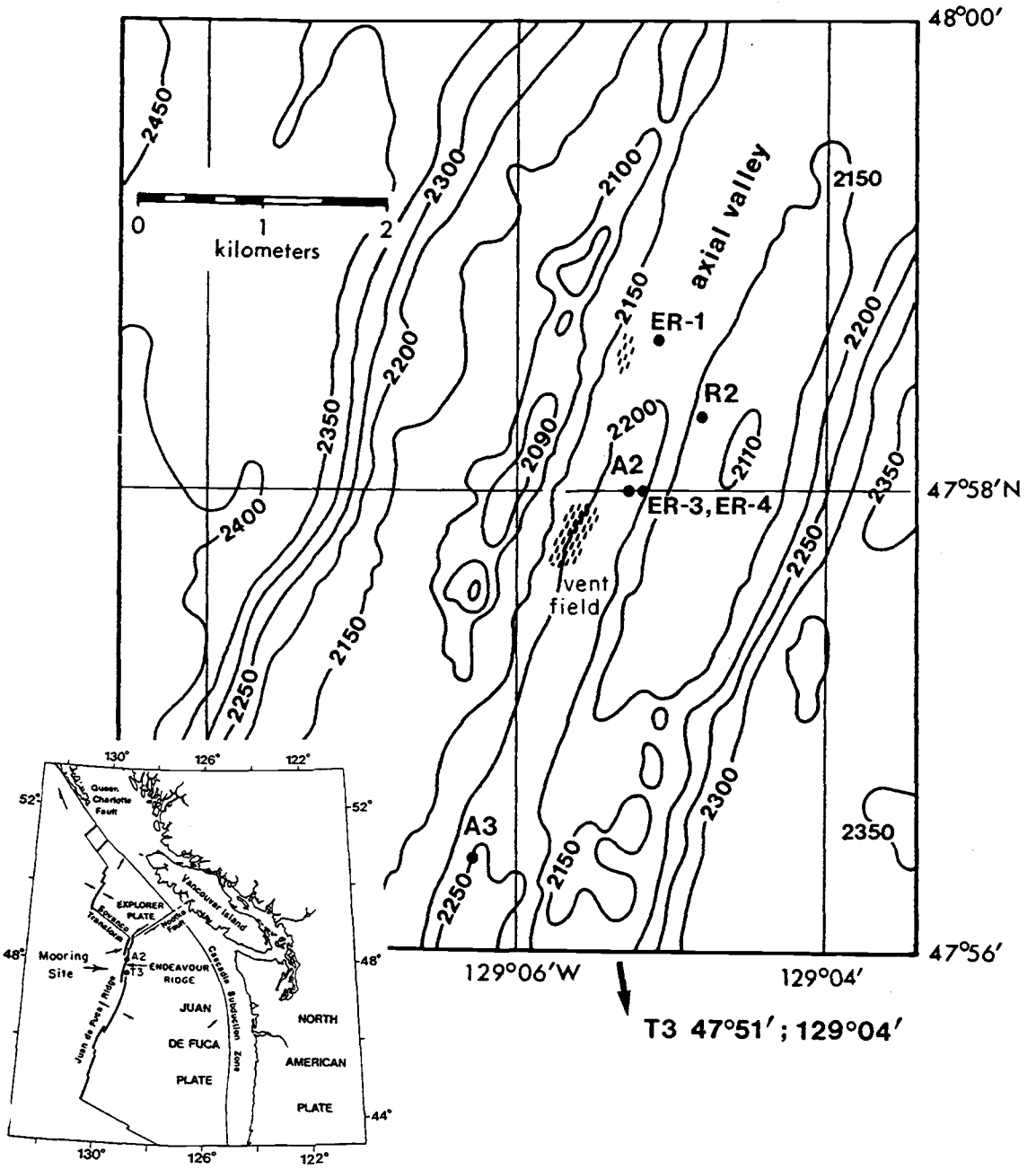

Figure II.2. Location of moorings A2, R2, A3 and T3 which together comprise the ER-2 deployment at Endeavour Ridge, relative to bathymetry and known vent fields. Note that T3 is off the scale of the map. Also shown are positions of the previous (ER-1) and subsequent (ER-3 and ER-4) single mooring deployments. ER-3 and ER-4 occupied the same site. Inset: Location of Endeavour Ridge, a segment of the Juan de Fuca Ridge in the northeast Pacific Ocean.

discovered. Because of the 25 km separation, it is unlikely that venting to the south contributed significantly to our experimental results. It is possible, however, that the effects of hydrothermal material emanating from closer sites influenced the results of our experiment which was intended to observe the primary vent field. This possibility cannot be rejected even though submersible observations of the Fairycastle Site suggest that it is older, heavily sedimented, and produces clear fluid, in contrast to the voluminous quantities of black smoke that gush from the primary vent field (Stakes and Moore, 1991).

Upon recognition that numerous physical, chemical and biological processes in the advecting, neutrally buoyant plume ultimately determine the fate of hydrothermal emissions in the ocean, studies were undertaken to map and sample these water column features. The Endeavour Ridge plume has been the subject of some groundbreaking research. Baker and Massoth (1987) compared the regional structure and chemistry of the Endeavour Ridge plume and the plume above another vent field along the southern portion of the Juan de Fuca Ridge. Lupton (1990) provided a discussion of the ^{3}He and Mn signatures of plumes from different vent fields along the Juan de Fuca Ridge. Salinity and temperature anomalies in the neutrally buoyant plume and pure vent fluids were used to calculate that the neutrally buoyant Endeavour Ridge plume is composed of about 70% entrained bottom water and 0.01% vent fluid (Lupton et al., 1985). Measurements of ^{222}Rn in the neutrally buoyant plume were used to estimate heat and chemical fluxes from the Endeavour Ridge vent field (Rosenberg et al., 1988). Kadko et al. (1990) used $^{222}Rn/^{3}He$ ratios to constrain chemical reaction rates in the Endeavour Ridge plume. They determined that H_2 is removed within hours of input, in contrast to Mn which has a residence time in the plume of more than two weeks. Particles, ^{222}Rn and CH_4 had residence times between these extremes. Plume anomalies of Si and ^{226}Ra were attributed to bottom water entrainment rather than to a predominantly hydrothermal origin.

Characteristics of the Endeavour Ridge neutrally buoyant plume include positive temperature, salinity and light attenuation anomalies of 0.05°C, 0.005 psu, and 0.03 m^{-1}, respectively below 1900 m depth. Maximum temperature, salinity and light attenuation anomalies in the plume core (2000-2050 m depth) relative to background waters were +0.17°C, +0.016 psu and +0.20 m^{-1}, respectively (Thomson et al., 1992b). The temperature anomaly suggests that vent effluent has been diluted by a

factor of about 7000 by the time it reaches the neutrally buoyant plume; the salinity anomaly reflects massive entrainment of high-salinity bottom water (Lupton, et al., 1985). The neutrally buoyant plume often forms a tier-like structure, with bands of particle laden water separated by 10 to 50-m-thick layers of relatively clear water (Thomson et al., 1990). The top of the plume is characterized by a strong positive acoustic backscatter anomaly, however backscatter intensity within the plume layer below is anomalously low, a pattern thought to reflect the vertical distribution of zooplankton (Thomson et al., 1991).

The composition of the particulate matter in neutrally buoyant hydrothermal plumes has been the focus of some important investigations. A fundamental observation is that the composition of the advecting plume changes with distance from the source. Precipitation, oxidation, particle dissolution and scavenging, all of which may be subject to microbial transformations (Cowen et al., 1986 and 1990), are some of the processes that modify the chemistry of the plume water and the associated suspended and settling particles. Hydrothermal plume particles are enriched in Si, P, V, Mn, Fe, Cu, Zn and As relative to background deep-ocean suspended matter. Feely et al. (1992) used Cu enrichment in Endeavour Ridge plume particles along with other physical and chemical tracers of the plume to track it more than 85 km from the vent field source. They found the P/Fe ratio in the suspended plume material to be a sensitive off-axis plume tracer. Grain sizes of the plume-carried Fe oxyhydroxides, sulfides and sulfates range from <2 μm (Cu and Zn sulfides) to more than 500 μm (Feely et al., 1987; Dymond and Roth, 1988). Aggregates composed of fine sulfide grains, coccoliths and other biogenic debris collected in sediment traps within 2 km of the Endeavour Ridge vent field had diameters as large as 1.0 mm (Dymond and Roth, 1988). While a sharp decrease in settling particle flux with distance from the vent field was observed, only a small fraction of the total particulate load of the hydrothermal plume is removed within the first few kilometers of the vent field. Dymond and Roth (1988) estimate that more than 90% of the particulate effluent is widely dispersed via the advecting plume. There is also a growing body of evidence which suggests that the neutrally buoyant hydrothermal plume is a biologically active zone in the deep sea (Roth and Dymond, 1989; Mullineaux et al., 1991; Thomson et al., 1992a; Burd et al., 1992).

Studies of hydrothermal plumes have been conducted over a range of spatial scales, by scientists of many oceanographic sub-disciplines, and so it is necessary to specify how certain terms are used in this paper. To aid the discussion, reference to three, stacked, horizontally extending plume zones is made, with the recognition that these are not fixed in space, nor are their boundaries necessarily sharp. The terms **above-plume**, **plume-core**, and **beneath-plume** are explained below and depicted schematically in Figure II.1. Use of these terms is based on the characteristic, layered structure of the water overlying the vent field. The dimensions of the regions will vary depending on whether the hydrothermal plume is defined with respect to thermal, particulate or dissolved chemical anomalies. Only temperature and particle concentration/flux data are interpreted here. It has been observed at Endeavour Ridge that the buoyant, particle-laden plume reaches a level of neutral buoyancy approximately 200-300 m above the 2200 m deep seafloor vent field, at which depth it spreads laterally along isopycnal surfaces, predominantly in the direction of the prevailing current. The vertical thickness of the spreading plume (also called the non-buoyant or neutrally buoyant plume) is variable and often has a tier-like structure spanning several hundred meters vertically (Thomson et al., 1991). The upper and lower boundaries of the spreading plume are not constant for they may respond to changes in lateral flow, topography, and changes in the volume and buoyancy of the hydrothermal effluent (Thomson et al., 1990; Little et al., 1987). The upper boundary of the particle plume is generally more distinct than the lower boundary (Thomson et al., 1991) which is blurred by particulate material settling from the plume as well as possible manifestations of turbulent bottom water entrainment and resuspension of sediments. **Plume**, in this paper means the coalesced output from all orifices within the principal Endeavour Ridge vent field. This may be an amalgamation of effluent from black smokers and more diffuse seepage that is entrained upward. Unless otherwise stated, **plume** refers to the neutrally buoyant plume, the portion of the effluent that has risen buoyantly to its maximum height and is spreading laterally along isopycnal surfaces. **Above-plume** means the portion of the water column overlying the neutrally buoyant plume where thermal or chemical evidence of hydrothermal output is minimal or undetectable; typically this zone extends from 1800 m water depth up to the sea surface. **Plume-core** refers to the depth range within the neutrally buoyant plume where hydrothermal indicators such as temperature anomaly, vent-derived chemical signatures and particulate hydrothermal tracer concentrations are at a maximum; the core is typically centered between depths of 1900 and 2050 m.

Beneath-plume is the zone of the water column extending from the main body of the neutrally buoyant plume to the seafloor. Discussion of data in this paper assigns instruments, based on their depth, to the above zones. The purpose of this assignation is to allow examination of the hypothesis that there are depth ranges in the water column that are affected by hydrothermal effluent to varying degrees. For example, the upper water column is virtually unaffected, the plume-core is most influenced, and the lower water column exhibits intermediate effects. Since the focus of this chapter is the region directly influenced by hydrothermal particles, primary attention is given to records from instruments positioned at depths greater than 1900 m, the depth which corresponds approximately to the top of the neutrally buoyant, laterally-advecting, hydrothermal plume.

In addition to the designation of water-column layers, several additional terms require clarification. Reference to specific instruments (current meters and their interfaced transmissometers or corresponding sediment traps) is abbreviated by a two-term expression, for example: A2 2005, where the first term, A2, is the mooring name and the second, 2005, is the nominal depth of the instrument in meters. Flow **velocity** includes both current speed and direction. Processed current meter records were rotated from north-south and east-west components to along-ridge and across-ridge orthogonal vectors, based on the along-axis trend of the Endeavour Segment of the Juan de Fuca spreading ridge which is rotated 20° east of north (20°T). **Along-ridge** means flow parallel to the axial valley; positive along-ridge flow moves to the northeast, 20°T; negative values are to the southwest, 200°T. Analogously, **across-ridge** flow is perpendicular to the ridge crest, with the positive orientation 110°T and a negative sign indicating flow to the northwest, 290°T.

In the discussion of time series, the relative terms high-frequency and low-frequency are used to describe categories of variability. In the section called *General features of the flow and rotary spectra* , three specific frequency ranges are defined and used in regard to spectral analyses. Prior to that point, a looser, operational distinction is made where, unless stated otherwise, **high-frequency** means variability greater than or equal to the diurnal tidal cycle, $\geq$ 1 cycle per day (cpd), and **low-frequency** describes variability less than 1 cpd.

Methods

Experimental rationale

The plume study on which this chapter is based is a collaborative Canadian-American venture. We used moored instruments (described below) within a radius of < 20 km from the primary vent field to obtain information about the temporal and spatial variability of the Endeavour Ridge plume. Both physical oceanographic data and geochemical samples were recovered with the intent of interpreting settling particle flux data in light of synchronously monitored advective flow, water column temperatures and suspended particle concentrations.

Mooring deployments

The data were collected over three years beginning in early September 1984. The time series starts on Julian Day (JD) 250 of 1984 (6 September 1984) and extends in consecutively numbered days to JD 1348, which is 10 September 1987. Over the three years, four mooring deployments were made, only the second of which was a multiple mooring experiment. The mooring deployments are named ER-1 through ER-4 (ER denotes Endeavour Ridge); the timing and duration of each is given in Table II.1. The four moorings which are collectively ER-2 are designated A2, A3, R2, and T3 (A is for Axial valley; R is for Ridge crest; T is for Tertiary); their positions are shown in Figure II.2. The ER-1, ER-3 and ER-4 single moorings were positioned within the axial valley, as was mooring A2 of the ER-2 group. All of the mooring deployments, with the exception of ER-1, were a collaborative effort with Dr. Richard Thomson of the Institute of Ocean Sciences in Sidney, B.C., Canada.

Instruments

The sediment trap component of our study utilized primarily the Oregon State University (OSU) trap design described in detail by Fischer (1984). On the single ER-1 mooring, a Soutar trap (Soutar et al., 1977) at 2100 m was also used. Listed in Table II.1 are the nominal depths of the sediment traps on each mooring that will be discussed in this paper along with the corresponding current meter/transmissometer positions. Dates corresponding to the sediment trap cup sampling intervals are listed in Table II.2. Current meter/transmissometer pairs were always positioned on the moorings beneath their corresponding sediment trap to avoid contamination of the trap samples. The

depths used in the trap names correspond to the intended depth of the instrument based on the mooring configuration and the water depth at the intended mooring position as given on bathymetric maps. Due to the difficulty of anchoring a mooring with absolute accuracy in 2200 m of water, and to possible map inaccuracy, the actual depth of the instruments sometimes differed slightly from the intended depth. The depths given in Table II.1 for the current meters were derived from pressure sensors on these instruments. The reliability of these sensors is not absolute, yet these depths are correct to within 30 meters. At the level of the neutrally buoyant plume, the effects of horizontal currents on instrument depth as a result of mooring "blow-down" are minimal (R. Thomson, personal communication). Data from instruments at other depths are reported elsewhere, along with a complete description of the mooring array (Thomson et al., 1990; Roth and Dymond, 1989; Dymond and Roth, 1988).

Aanderaa current meters, which also served as data loggers for the transmissometers, recorded current speed and direction as well as water temperature. Thomson et al. (1990) base their discussion of the water column physics and interaction of abyssal currents with seafloor topography at Endeavour Ridge on these data. Here I offer a more general description of plume-guiding flow relevant to interpretation of synchronous temperature data, optical records of suspended particle concentration, and settling particle flux data. There are inherent limitations in using moored current meter data in highly variable environment. While point measurements of flow are not adequate to discern spatial details of plume structure, they are useful in resolving the time scales of variability in hydrothermal tracer fields (temperature and suspended particles). Collection of settling particles in the sediment traps is influenced by the time-integrated effect of advection.

Sea Tech 25-cm-pathlength light-beam transmissometers interfaced with the current meters provided hourly measurements of suspended particle concentration as a function of light attenuation.

Temperature data from Aanderaa current meters have a resolution of $\pm 0.3°$ C on the standard sensor range and $\pm 0.01°$C on the expanded range. Current speeds are accurate to ± 1 cm/s or 2% of the actual speed, whichever is greater. The stall speed of the current meter rotor is approximately 2 cm/s. Directions are accurate to $\pm 5°$ for speeds in the range of 5 to 100 cm/s. The current meters recorded average speeds and

instantaneous directions at 20, 30 or 60 minute intervals which are converted to hourly data using a smoothing filter that averages records collected at periods shorter than one hour. Resolution of the attenuation coefficient by the Sea Tech transmissometer is 0.002 m^{-1}.

Table II.1. Endeavour Ridge mooring deployments

Mooring	Sed. trap depth (m)	Location relative to major vent field	Current meter depth*	JD start-JD end of deployment	Duration
ER-1	1700 1950 2100	2 km northeast, in axial valley	2127*	250-587	6 Sept.,1984- 10 Aug. 85
ER-2 A2	1700 1950 2050 2150	0.5 km northeast, in axial valley	1656* 1905 2005*	636-895	28 Sept.,'85- 14 June '86
ER-2 A3	1950 2050 2150	2.5 km southwest, in axial valley	1955 2055* 2156*	636-895	28 Sept.,'85- 14 June '86
ER-2 R2	1950 2050	1.5 km northeast, on eastern ridge crest	1986*	636-895	28 Sept.,'85- 14 June '86
ER-2 T3	1950 2050	15 km southeast, east of the ridge	1955 2055	636-895	28 Sept.,'85- 14 June '86
ER-3	1680 1930 2130	0.5 km northeast, in axial valley	1686* 1936* 2036 2136*	990-1278	17 Sept.,'86- 2 July, '87
ER-4	1930 2130	0.5 km northeast, in axial valley	1706* 1956*^ 2056*^	1281-1348	5 July,'87 10 Sept.'87

* also transmissometer
^ no temperature data

Table II.2. Sediment trap cup collection periods

Mooring	Sediment Trap Cup		Julian Days	Dates
ER-1	2		252-342	8 Sep.- 7 Dec. 1984
	3		343-433	8 Dec.'84 - 8 Mar.'85
	4		434-524	9 Mar.-7 Jun. 1985
	5		525-587	8 Jun.- 10 Aug. 1985
ER-2	2		644-691	6 Oct. - 22 Nov. 1985
(A2,R2,	3		692-739	23 Nov.'85-9 Jan. '86
A3,T3)	4		740-787	10 Jan.- 26 Feb. 1986
	5		788-835	27 Feb. - 15 Apr. 1986
	1		836-895	16 Apr. - 14 Jun. 1986
		(also:	636-644	28 Sep. - 5 Oct. 1985)
ER-3	2		998-1059	25 Sep.- 25 Nov. 1986
	3		1060-1121	26 Nov.'86-26 Jan.'87
	4		1122-1183	27 Jan.- 29 Mar. 1987
	5		1184-1245	30 Mar.-30 May 1987
	1		1246-1278	31 May - 2Jul. 1987
		(also:	990-997	17 Sep.-24 Sep. 1986)
ER-4	2		1287-1299	11 Jul. - 23 Jul. 1987
	3		1300-1312	24 Jul. - 5 Aug. 1987
	4		1313-1325	6 Aug. - 18 Aug. 1987
	5		1326-1338	19 Aug.- 31 Aug. 1987
	1		1339-1348	1 Sep.- 10 Sep. 1987
		(also:	1281-1286	5 Jul. - 10 Jul. 1986)

Data processing

Analyses of the sediment trap data are described in Dymond and Roth (1988). Briefly, samples were analyzed for 1) organic and carbonate carbon using a modified LECO procedure; 2) Al, S, V, Mn, and Ba by instrumental neutron activation analysis; and 3) Si, Mg, Ca, Ti, Sr, Fe, Cu and Zn by atomic absorption spectrophotometry.

For some analyses of the physical oceanographic data, high-frequency variations in the current meter and transmissometer time series have been removed by applying an 8th order Butterworth filter with a half-power point of 1/40 hours (Thomson et al., 1990; Thomson and Chow, 1980). This means variance associated with periods of 1.67 days is passed through the filter at 50 percent of its original power, variance at higher frequencies is excluded, and lower frequency variance is

unchanged. The purpose of this low-pass filtering is to remove effects of tidal and inertial oscillations which dominate the raw records. The rationale is to reveal other periodic and episodic variations in hydrothermal flux that may be obscured by the easily identified high-frequency energy.

Since the primary focus of this paper is longer-term variability and the broader oceanic and sedimentological aspects of hydrothermal particle flux, the removal of high-frequency tidal energy is appropriate. Removal of the high-frequency variability does not imply that it is unimportant, rather that the effects of the tidal and inertial motions on the hydrothermal plume are generally predictable and ubiquitous. Horizontal excursions produced by this rotational flow is small scale (approximately 1-2 km) and can be seen in progressive vector diagrams (PVD) generated from unfiltered current records (Figure II.3). Unrectified tidal motion, in theory, has no net effect on particle transport. These lateral motions advect the water about an ellipse, thereby increasing the residence time of the hydrothermal effluent in the region above the vent area (a potentially important consideration), but they do not necessarily enhance plume dispersion. There may be some net transport due to interactions of tidal motions with topography, and through nonlinear interactions among tidal components, but this will appear as lower-frequency energy or high-frequency harmonics. It is the regional flow which advects hydrothermal material away from the source. Later I will quantify and discuss further the implications of temporal variability due to tidal and inertial flow. Low-pass filtering reduces signal amplitudes of the resultant time series by removing the high-frequency variability. Flow speeds associated with tides are characteristically higher (>15 cm/s) than those of lower-frequency regional flow, so removal of tidal energy results in time series with attenuated extrema. The reduction in amplitudes of the temperature and attenuation coefficient time series is also an expected result of the filtering process since much of the energy in these signals is at high frequencies. The cause of the high-frequency variability in the raw temperature and attenuation records will be discussed later. For many of our analyses removal of high-frequency, tidal/inertial energy is not problematic, since I am concerned with processes that occur on spatial scales larger than tidal rotations and over periods longer than one day. However, in the sections employing spectral analyses I use unfiltered data to compare flow and temperature records over time and in space.

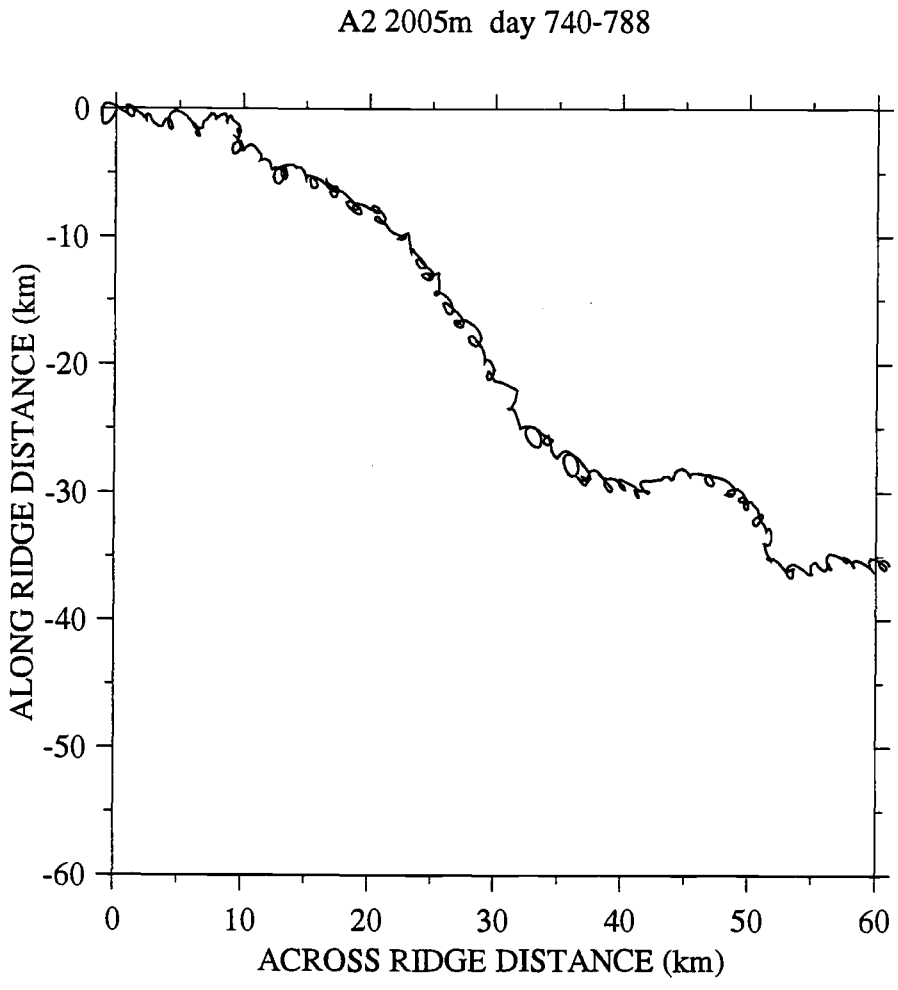

Figure II.3. Progressive vector diagram based on a 48-day portion of the unfiltered, hourly current meter record from A2 2005 showing high-frequency, clockwise, rotary motion. The vector begins at the origin. Negative along-ridge direction is 200°T.

Transmissometer use

Use of the transmissometer as a tool for *in situ* quantification of suspended particle concentration has been verified in previous work (e.g., Spinrad and Zaneveld, 1982; Spinrad et al., 1983; McCave, 1983), and I summarize here the basic principles of this method (Bartz et al., 1978). The intensity of a highly-colimated beam of light decreases with distance from the source due to scattering and absorption by water, particles, and dissolved organic substances. The sum of scattering (which is significant only for particulate matter) and absorption is referred to as the beam attenuation coefficient, c, in units of m^{-1}. Attenuance due to dissolved organic substances is minimized by choosing a wavelength of 660 nm. Attenuance due to pure sea water has been satisfactorily constrained and the instrument calibrated accordingly (Spinrad et al., 1983). Bishop (1986) determined that the beam attenuation coefficient of particle-free sea water is $0.358 \pm 0.003\ m^{-1}$. Thus the attenuance due to particles can be determined. The relationship between c and the fraction of light transmitted, T, is: $T = e^{-cr}$, where r is the beam pathlength, 0.25 m, for our instruments.

The relationship between suspended particle volume concentration, P, and c is linear when the characteristics of the particles (size, index of refraction and shape distributions) are constant over time and uniform in space. Empirical relationships between P and c have been obtained for certain oceanic regions by using resistive pulse counters to independently determine P (e.g. Spinrad, 1982 and McCave, 1983). Another method of calibrating the transmissometer is filtration of water samples to calculate particle concentration; the reliability of this method, however, is limited by the difficulty of sampling the same parcel of water being observed by the moored instrument.

I did not determine the relationship between P and c for transmissometers on our moorings, however, one can refer to calibrations obtained by others who have used optical methods in surveys of hydrothermal plume areas to estimate particle concentrations (Baker and Massoth, 1987). I will use the records primarily to characterize relative changes in particle concentration at a given site.

Attenuation coefficient trend removal

Characteristic of the records for the longer (roughly year-long) deployments is a trend of decreasing light transmission and abrupt instrument failure. I attribute this pattern to a gradual clouding of the transmissometer lens. Fouling of the optical windows has been noted in the upper water column where a buildup of organic material coats the instrument (Spinrad, 1987) and in near-bottom deployments on the Nova Scotia Rise (Pak, 1983). In our experiment, optical obstruction could be caused by accumulation of hydrothermal material, bacterial growth or biological secretions. It was noted, on recovery of our instruments, that a dark-colored slime coated other mooring components. Juniper et al. (1986) found that mucus produced by a vent alvinellid polycheate worm thriving at a Juan de Fuca Ridge vent field accumulated hydrothermal minerals, perhaps as a detoxification strategy. Greyish-black wrappings of mineral-laden mucus are periodically shed from these animals. This sticky material may be upwardly entrained in the buoyant plume and adhere upon contact to moored instruments.

Since I consider the trend to be caused by interference with normal transmissometer functioning, I have chosen to remove the trend, thereby isolating the higher frequency variability which dominates the record. In addition to the preliminary, low-pass Butterworth filter, I applied a second filter to the time series that removes frequencies higher than 1/720 hours (periods longer than 30 days) using a Parzen window filter. Zero-padding minimizes loss of data at the ends of the time series. The resultant low-frequency attenuation coefficient (the linear trend plus low-frequency variability) was subtracted from the trended time series to yield the detrended record (Figures II.4 - II.12).

The choice of low-pass filter characteristics is somewhat subjective and I experimented with a range of cutoff frequencies. The 30-day filter satisfactorily removed the trend, yet sufficiently preserved longer-period features of interest. Consistent treatment of data from all deployments to facilitate comparison, combined with the pursuit of temporal resolution comparable to that of the settling particle flux data (which are resolved in the range of one week to two months) were factors in choosing the 30-day filter. Application of detrending filters that smooth over intervals less than 30 days remove too much low frequency information (Figure II.13). As shown, the 10-day filter fits the trended data too tightly; some of the fluctuations of

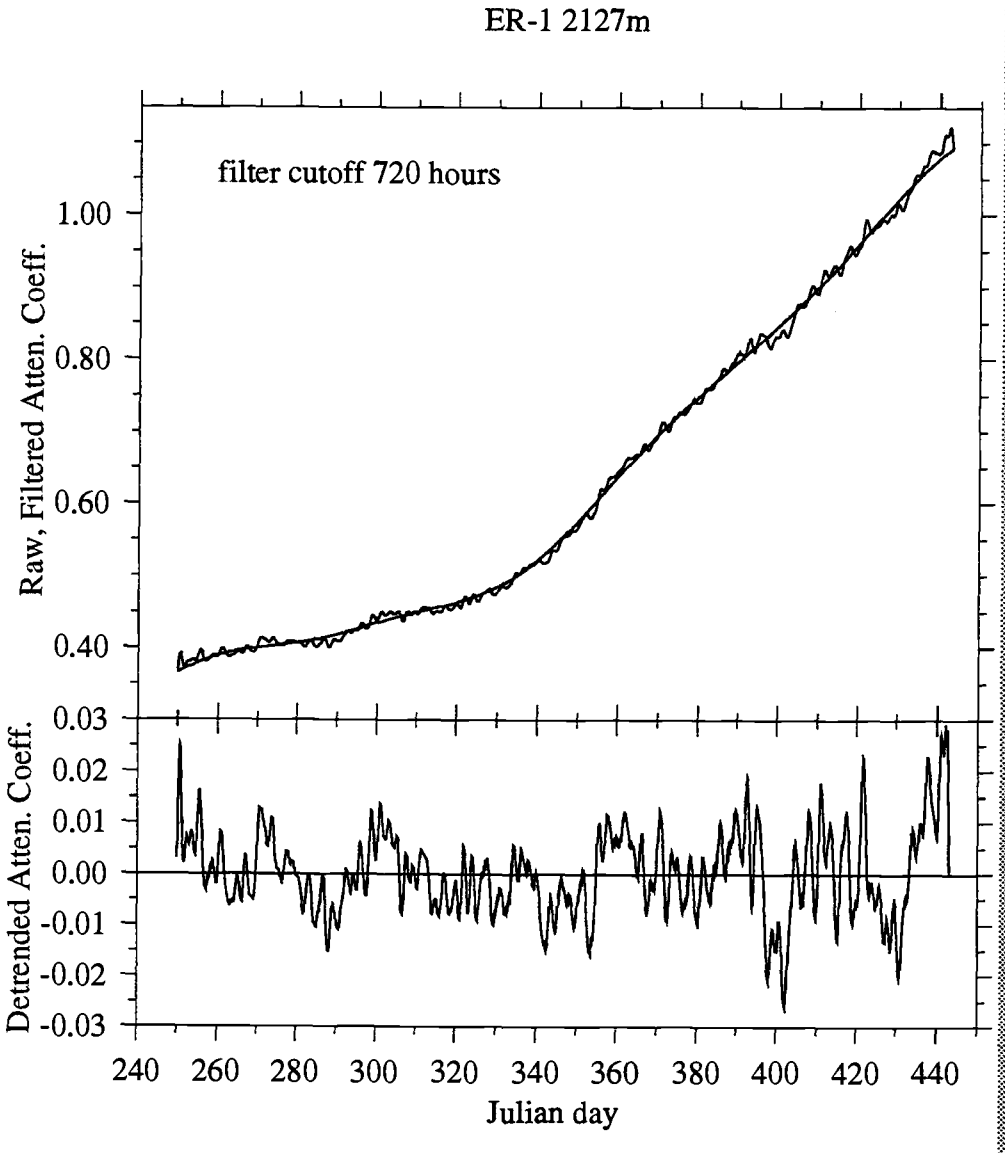

Figure II.4. Detrended transmissometer record for ER-1 2127 m. In the upper panel low-pass filtered (de-tided) attenuation coefficient (m^{-1}) is overlain by the trend produced with a filter cutoff of 720 hours (30 days). The lower panel shows the detrended time series. Note that the y-axes in Figures II.4 - II.12 are commonly scaled, however the x-axes vary in length since only the usable portion of each record (prior to instrument failure) is plotted. The small ticks on the x-axis represent 10-day increments. Julian day 250 is 6 September 1984.

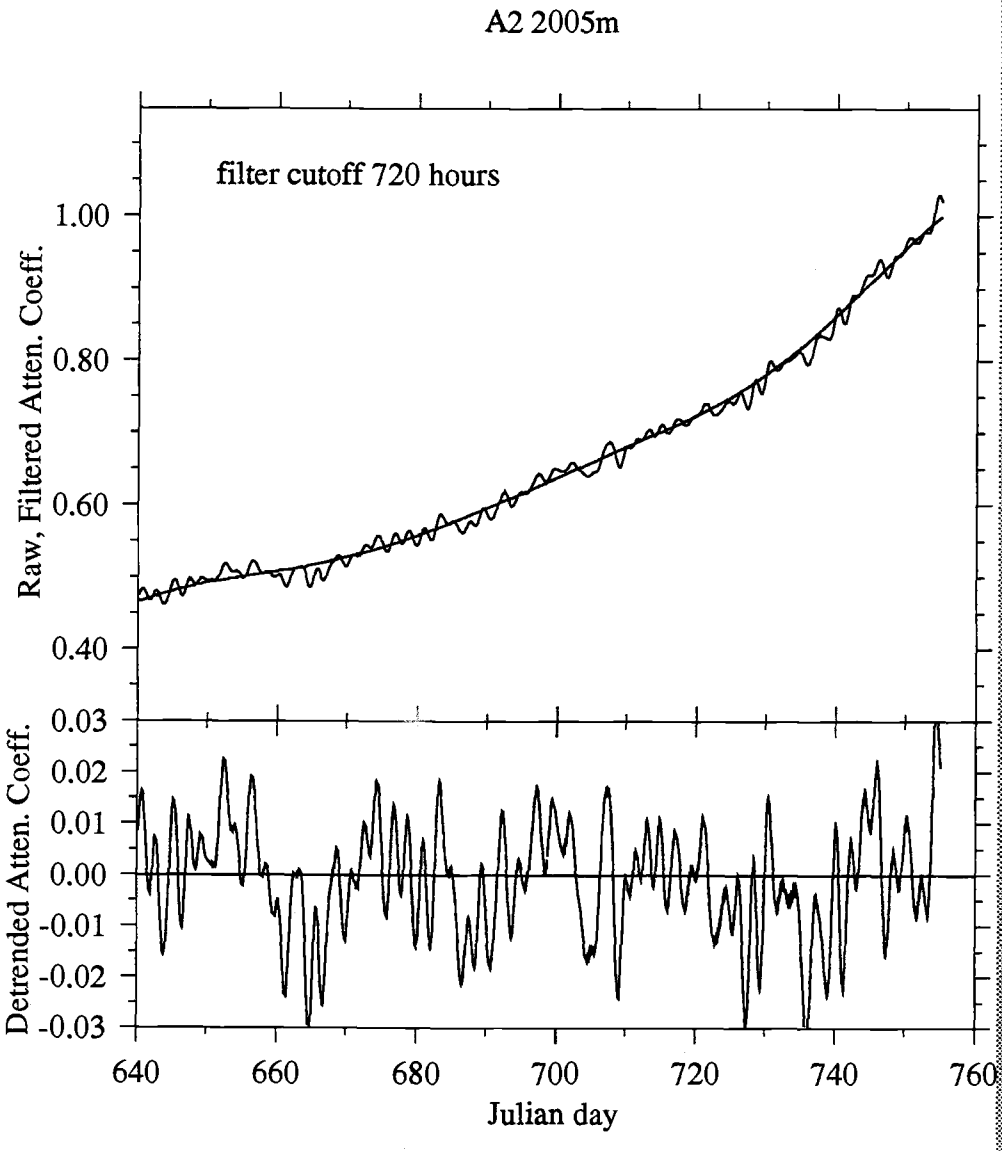

Figure II.5. Detrended transmissometer record for A2 2005 m. In the upper panel low-pass filtered (de-tided) attenuation coefficient (m^{-1}) is overlain by the trend produced with a filter cutoff of 720 hours (30 days). The lower panel shows the detrended time series. Note that the y-axes in Figures II.4 - II.12 are commonly scaled, however the x-axes vary in length since only the usable portion of each record (prior to instrument failure) is plotted. The small ticks on the x-axis represent 10-day increments. Julian day 640 is 2 October 1985.

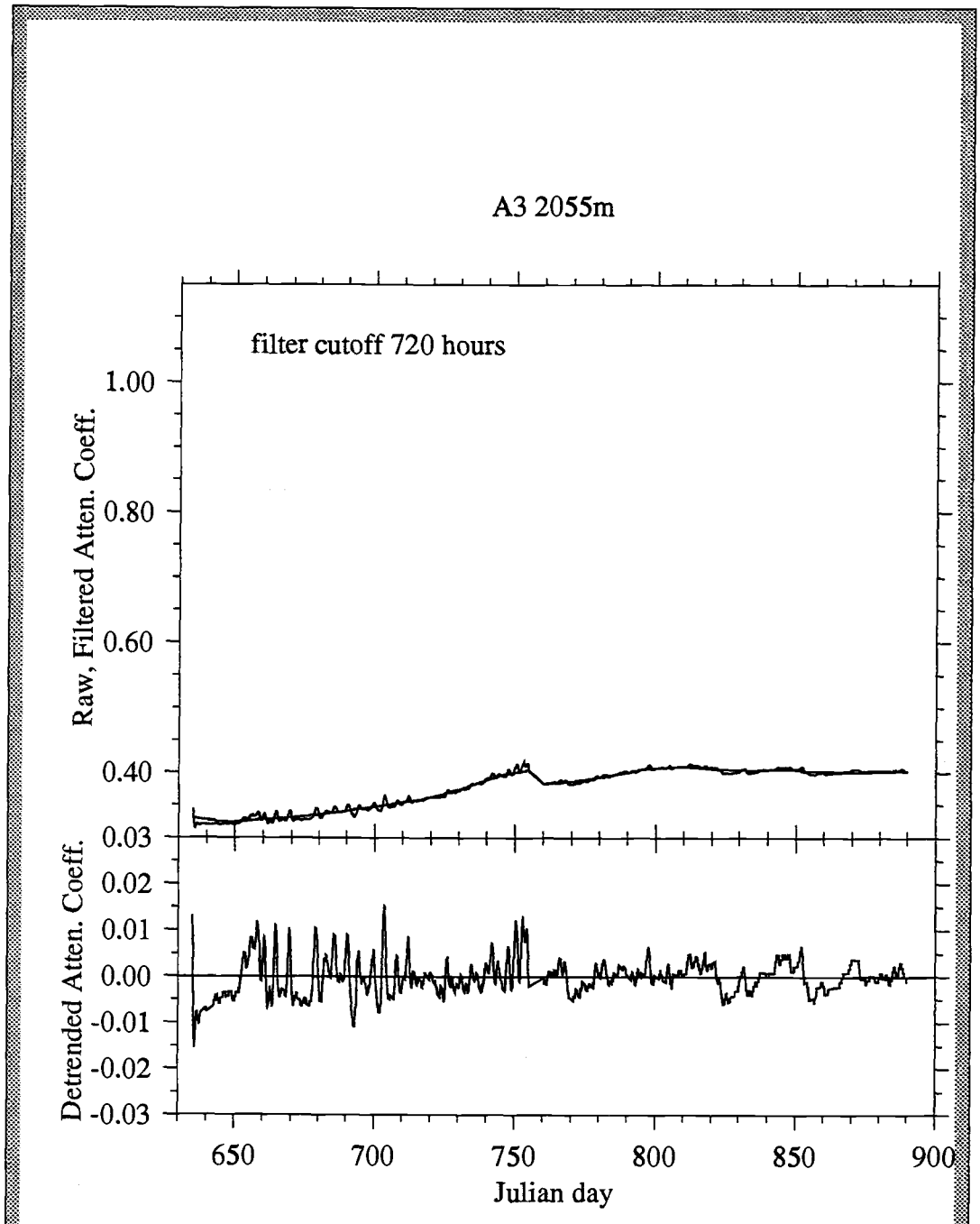

Figure II.6. Detrended transmissometer record for A3 2055 m. In the upper panel low-pass filtered (de-tided) attenuation coefficient (m^{-1}) is overlain by the trend produced with a filter cutoff of 720 hours (30 days). The lower panel shows the detrended time series. Note that the y-axes in Figures II.4 - II.12 are commonly scaled, however the x-axes vary in length since only the usable portion of each record (prior to instrument failure) is plotted. The small ticks on the x-axis represent 10-day increments. Julian day 640 is 2 October 1985.

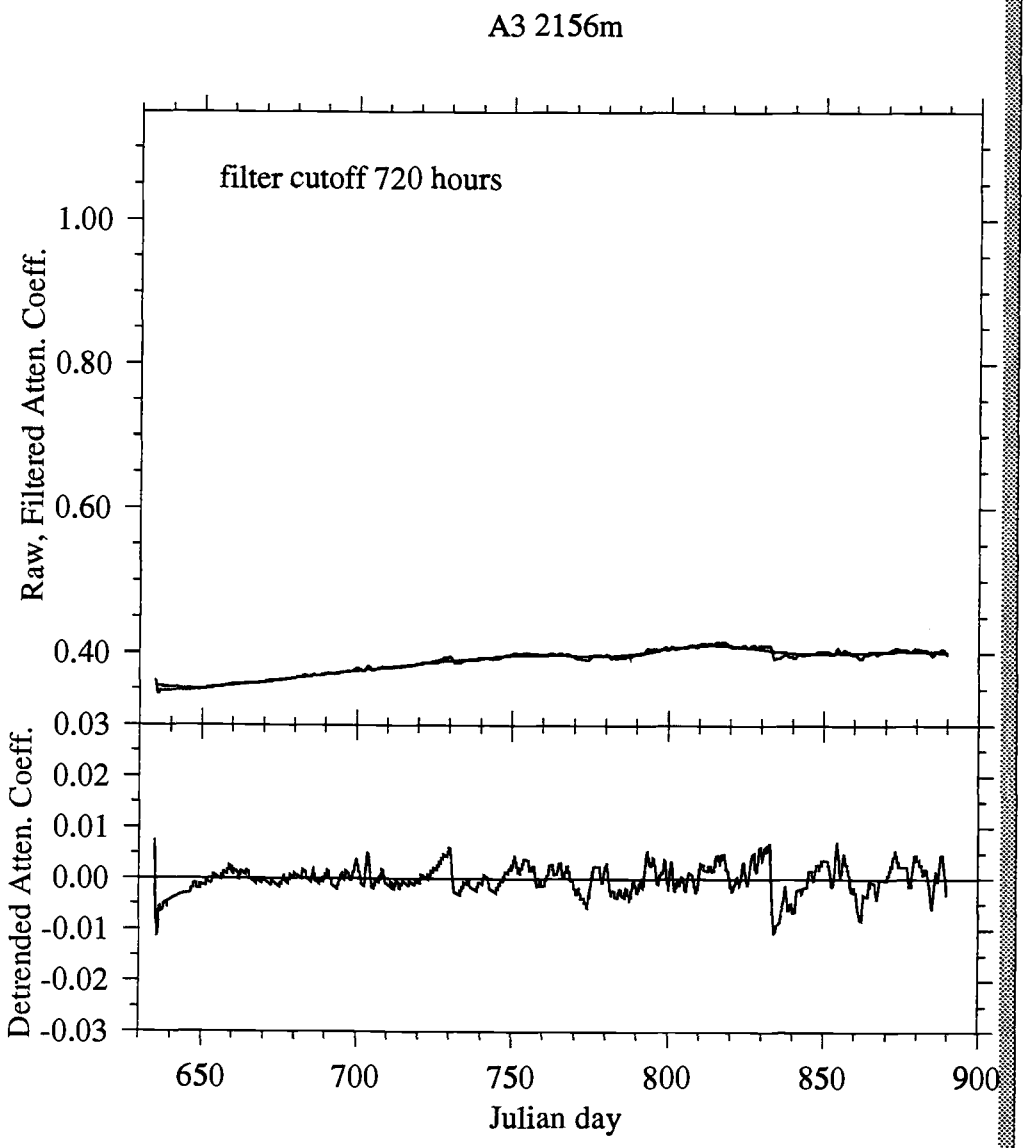

Figure II.7. Detrended transmissometer record for A3 2156 m. In the upper panel low-pass filtered (de-tided) attenuation coefficient (m^{-1}) is overlain by the trend produced with a filter cutoff of 720 hours (30 days). The lower panel shows the detrended time series. Note that the y-axes in Figures II.4 - II.12 are commonly scaled, however the x-axes vary in length since only the usable portion of each record (prior to instrument failure) is plotted. The small ticks on the x-axis represent 10-day increments. Julian day 640 is 2 October 1985.

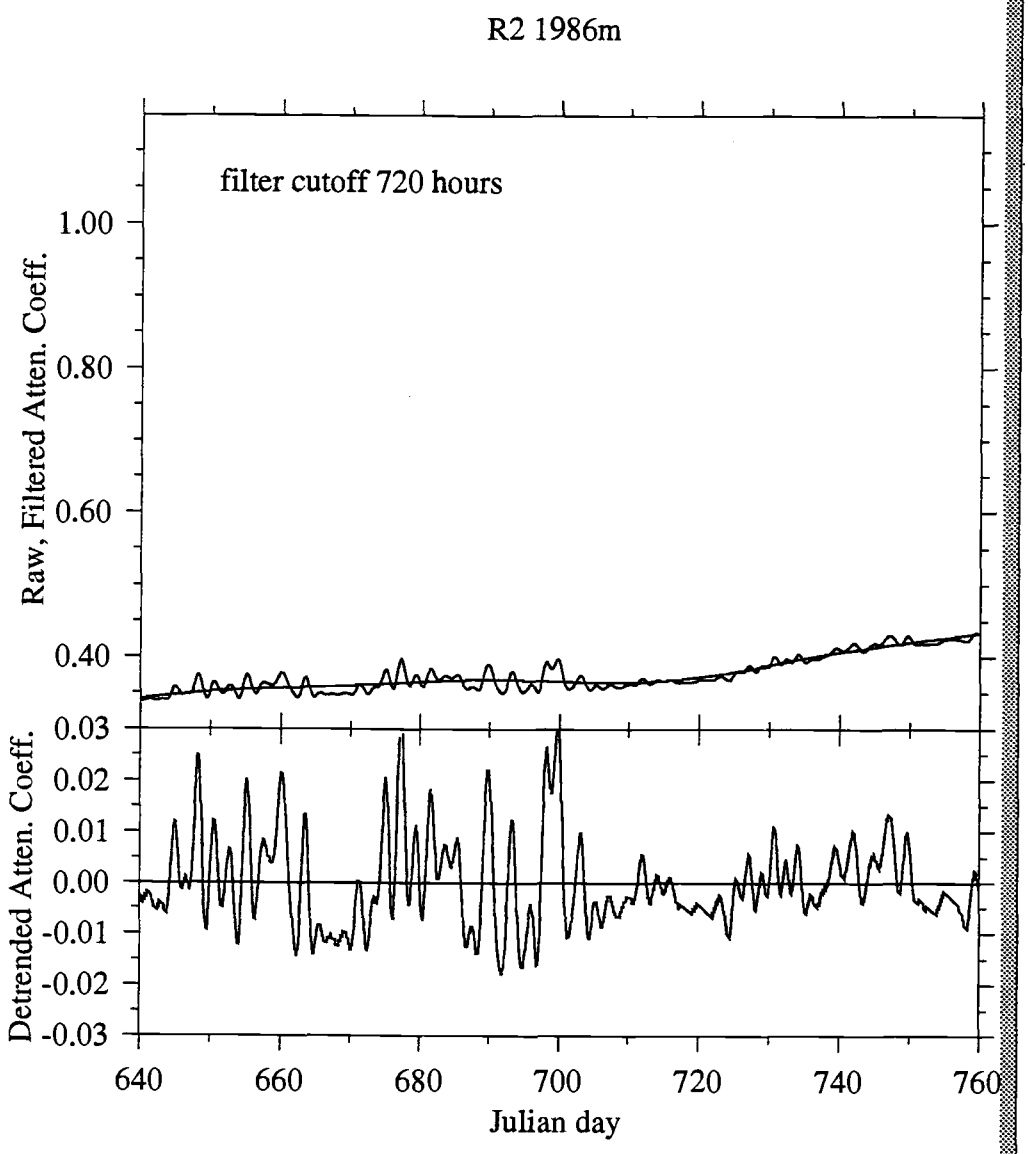

Figure II.8. Detrended transmissometer record for R2 1986 m. In the upper panel low-pass filtered (de-tided) attenuation coefficient (m^{-1}) is overlain by the trend produced with a filter cutoff of 720 hours (30 days). The lower panel shows the detrended time series. Note that the y-axes in Figures II.4 - II.12 are commonly scaled, however the x-axes vary in length since only the usable portion of each record (prior to instrument failure) is plotted. The small ticks on the x-axis represent 10-day increments. Julian day 640 is 2 October 1985.

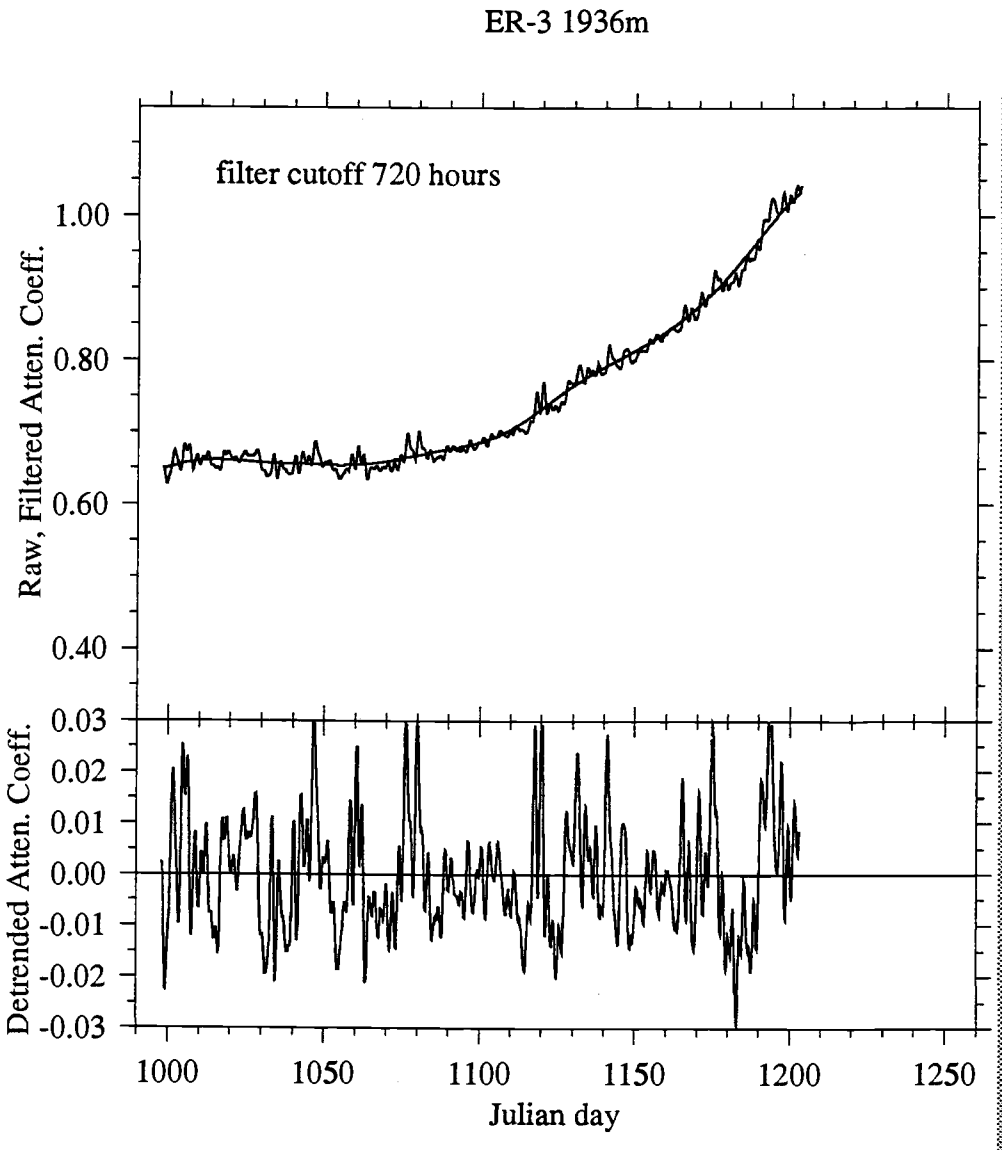

Figure II.9. Detrended transmissometer record for ER-3 1936 m. In the upper panel low-pass filtered (de-tided) attenuation coefficient (m^{-1}) is overlain by the trend produced with a filter cutoff of 720 hours (30 days). The lower panel shows the detrended time series. Note that the y-axes in Figures II.4 - II.12 are commonly scaled, however the x-axes vary in length since only the usable portion of each record (prior to instrument failure) is plotted. The small ticks on the x-axis represent 10-day increments. Julian day 1000 is 27 September 1986.

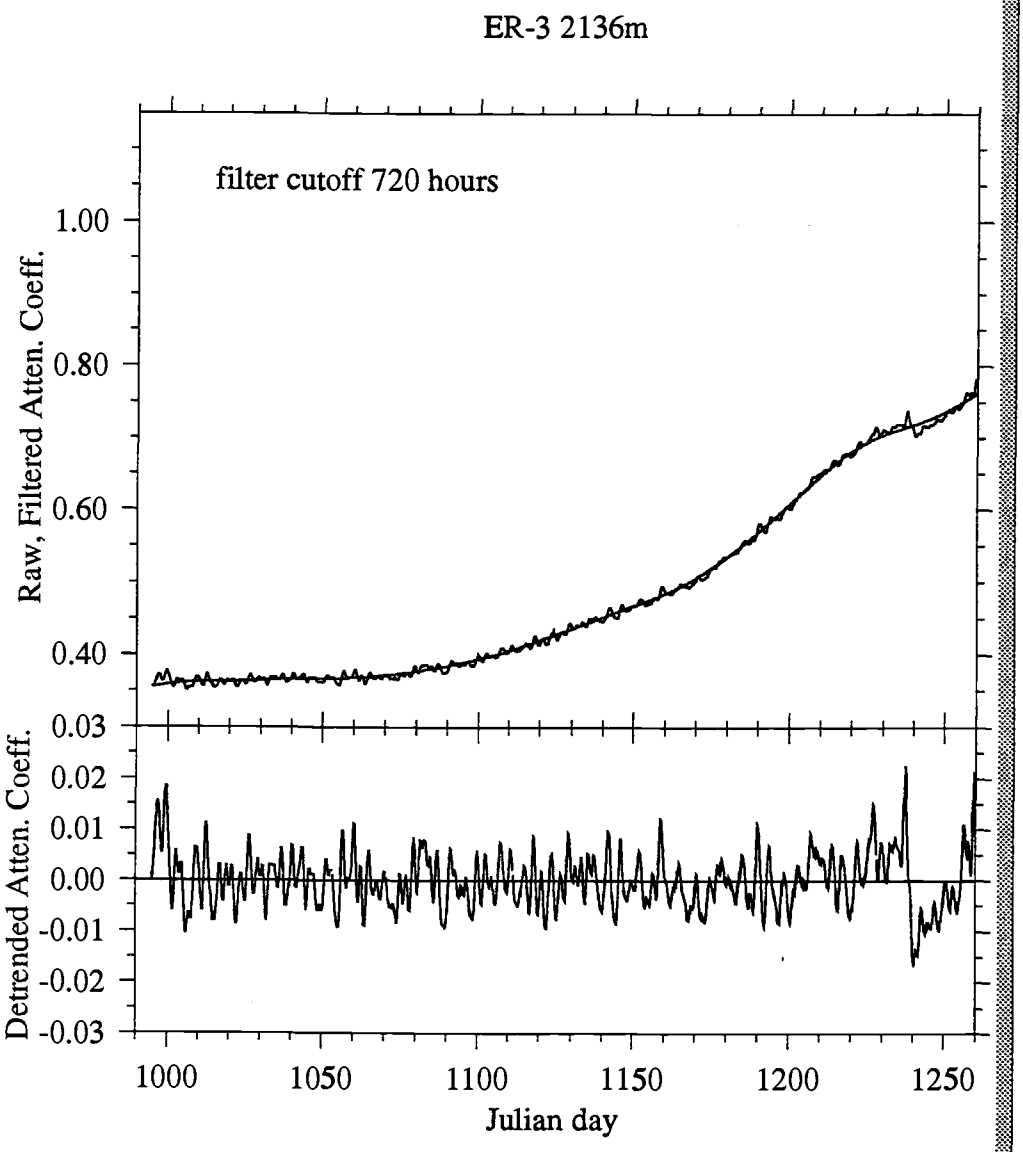

Figure II.10. Detrended transmissometer record for ER-3 2136 m. In the upper panel low-pass filtered (de-tided) attenuation coefficient (m^{-1}) is overlain by the trend produced with a filter cutoff of 720 hours (30 days). The lower panel shows the detrended time series. Note that the y-axes in Figures II.4 - II.12 are commonly scaled, however the x-axes vary in length since only the usable portion of each record (prior to instrument failure) is plotted. The small ticks on the x-axis represent 10-day increments. Julian day 1000 is 27 September 1986.

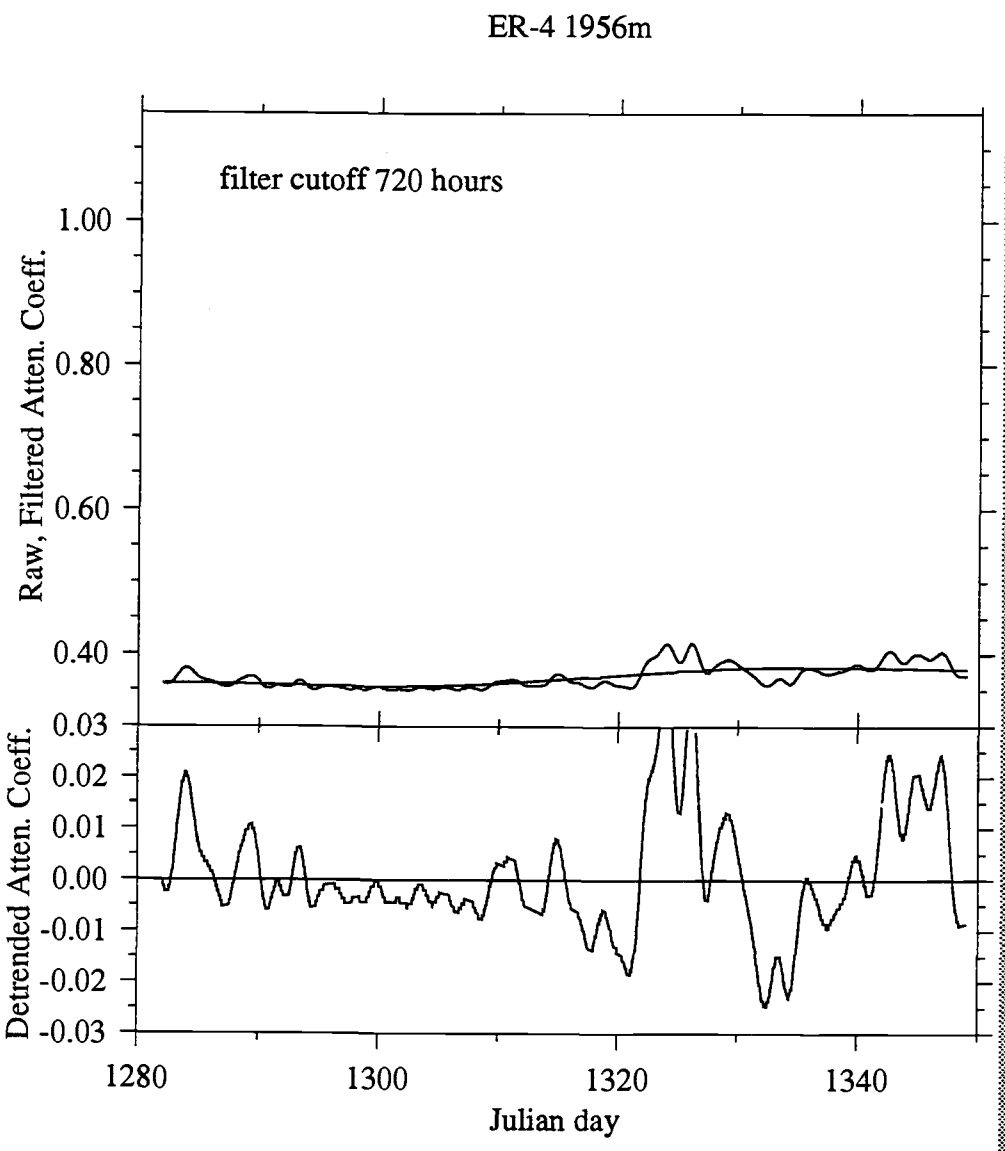

Figure II.11. Detrended transmissometer record for ER-4 1956 m. In the upper panel low-pass filtered (de-tided) attenuation coefficient (m^{-1}) is overlain by the trend produced with a filter cutoff of 720 hours (30 days). The lower panel shows the detrended time series. Note that the y-axes in Figures II.4 - II.12 are commonly scaled, however the x-axes vary in length since only the usable portion of each record (prior to instrument failure) is plotted. The small ticks on the x-axis represent 10-day increments. Julian day 1280 is 4 July 1987.

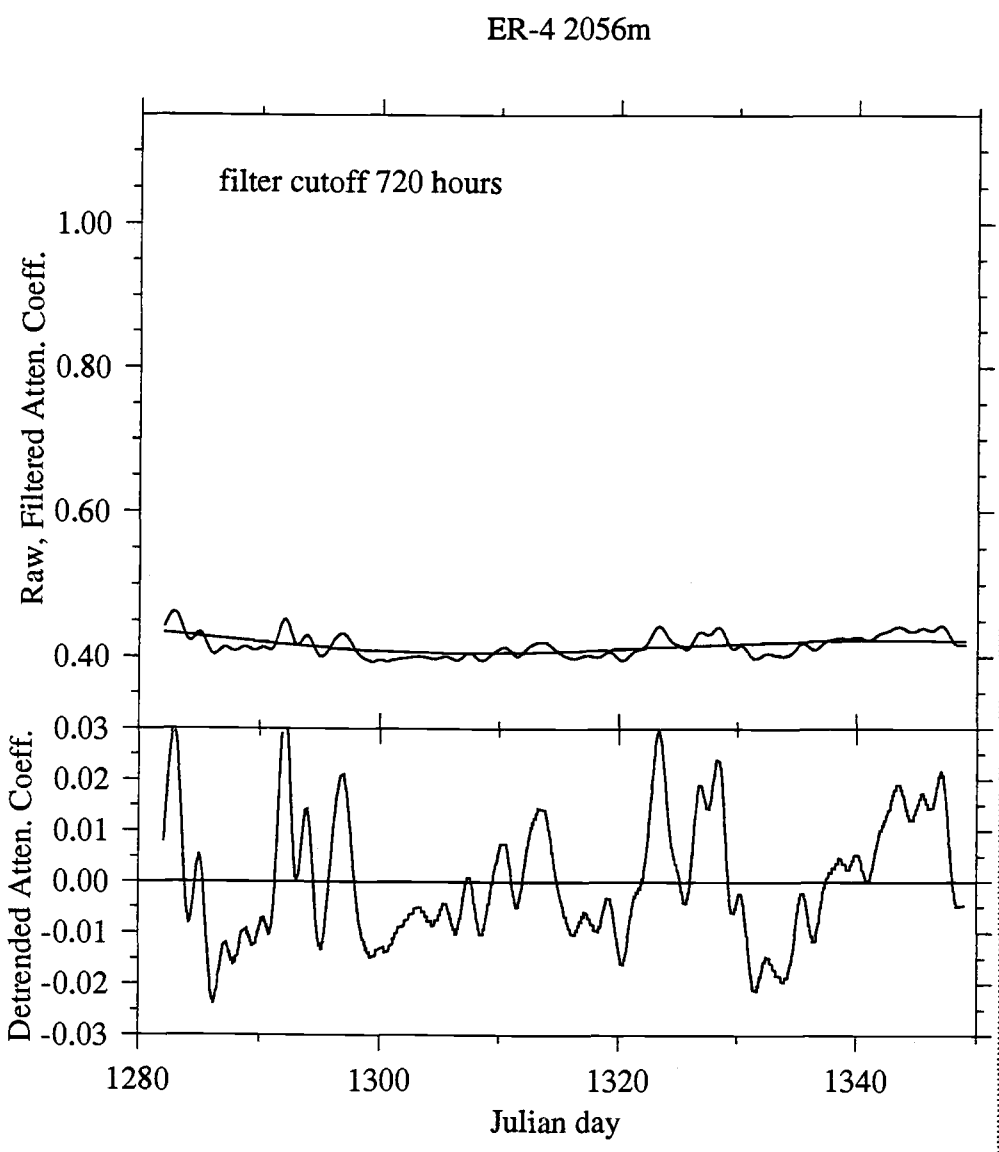

Figure II.12. Detrended transmissometer record for ER-4 2056 m. In the upper panel low-pass filtered (de-tided) attenuation coefficient (m^{-1}) is overlain by the trend produced with a filter cutoff of 720 hours (30 days). The lower panel shows the detrended time series. Note that the y-axes in Figures II.4 - II.12 are commonly scaled, however the x-axes vary in length since only the usable portion of each record (prior to instrument failure) is plotted. The small ticks on the x-axis represent 10-day increments. Julian day 1280 is 4 July 1987.

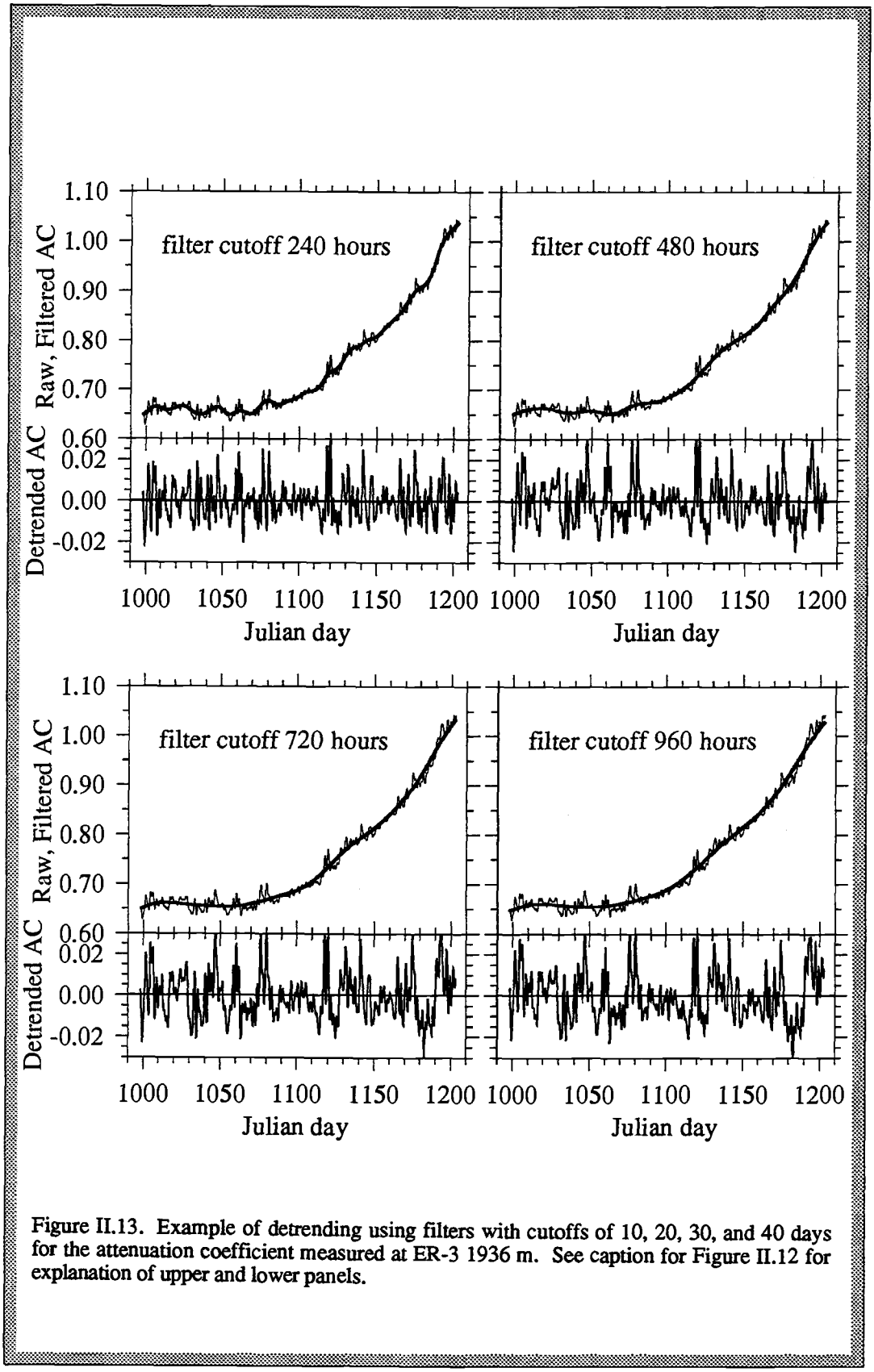

Figure II.13. Example of detrending using filters with cutoffs of 10, 20, 30, and 40 days for the attenuation coefficient measured at ER-3 1936 m. See caption for Figure II.12 for explanation of upper and lower panels.

roughly 20 days on the de-tided record are probably not part of the trend, and should therefore be retained. At the other extreme, the filter with a cutoff of ≥ 40 days tends to undesirably accentuate abrupt changes which appear in some of the attenuation coefficient time series (e.g. A3 2055), and might reflect sudden removal of built-up material on the lens, rather than actual changes in the suspended particle concentration. Trial of these different filters with the records in Figures II.4 - II.12 led to a decision to use the 30-day cutoff. For certain analyses, such as establishing the relationship between temperature and attenuation coefficient, I detrend the data using filters that remove even more low-frequency variability. In summary, the two filtering operations performed on the attenuation coefficient time series amount to a band pass filter which removes the highest (tidal; > 0.6 cpd) and lowest (trend; < 0.03 cpd) frequencies which are not of primary interest in the analyses presented here.

The filtered, detrended attenuation coefficient time series have a mean of approximately zero as a result of removal of the linear trend and the artificial low-frequency signal. This has both advantageous and deleterious effects. Comparison of optical records from various deployments is facilitated because inter-instrumental baseline offset is eliminated. (Possible implications of such offsets are discussed later.) However, information is lost regarding the absolute values of attenuation coefficient. In theory, attenuation coefficient values can be converted to suspended particle concentrations, which in turn can be used to calculate lateral particle transport. The zero-mean values might be corrected to reflect realistic values of attenuation coefficient by adding to them a positive value representing the average initial value of the original record (i.e. a baseline attenuation coefficient). Unfortunately, choosing this value is not straightforward as it is not known if the differences in initial values of the records, prior to detrending, reflect true differences in water column particle concentration or instrumental calibration. Even if this problem is overcome, determination of true attenuation coefficients is precluded because the instrument calibration changes with time in an unknown way.

Results and Discussion

In this section, I present and interpret features of the current meter, transmissometer, temperature and sediment trap records that define variability in the water column above a hydrothermal vent field. Processes that generate specific temporal and spatial patterns are identified, and where possible the relative magnitudes of these influences is assessed. The analysis is based on four types of data: flow velocity, attenuation coefficient, temperature, and settling particle flux. Observed patterns are explained by processes that I incorporate into a conceptual model of neutrally buoyant plume behaviour and hydrothermal particle flux. First, I establish the validity of using light attenuation and temperature records as hydrothermal indicators through three lines of evidence. Second, I introduce a conceptual model of the plume that includes four types of variance-generating effects. Third, spectral analysis is used to evaluate the relationship between currents and the distribution of hydrothermal effluent. Fourth, I describe and quantify temporal variations in plume behavior in order of high to low frequency. Fifth, spatial patterns in hydrothermal particle flux with respect to depth and distance from the hydrothermal vent source are documented. Finally, important findings are summarized, implications are discussed, and conclusions are drawn.

For reference throughout this paper, time series plots of the low-pass filtered (tide-free) flow, temperature, and attenuation coefficient data are provided for each current meter (and transmissometer, where applicable) in Figures II.14 - II.34. Refer to Figures II.4 - II.12 for the band-pass filtered (detrended) attenuation coefficient time series for the nine, plume-influenced transmissometers; note that the above-plume (≈1700 m) transmissometer records did not require detrending. A lack of one or more parameters for a given instrument indicates either that the parameter was not measured at the location in question or that the sensor failed; truncated records also indicate instrument failure. Figures II.35 - II.39 show PVDs which illustrate the horizontal flow at the position of each current meter over the deployment period. As an example, the raw, unfiltered time series (including tidal and inertial fluctuation) is given for A2 2005 in Figure II.40.

Figure II.14. Low-pass filtered time series of across and along-ridge current components recorded at ER-1 2127 m. Positive across-ridge flow is directed 110°T; positive along-ridge flow is directed 20°T. Temperature and attenuation coefficient data, if collected, are also shown. Julian day 250 is 6 September 1984.
The y-axes for across and along-ridge currents are equivalent in Figures II.14 - II.34. For temperature the y-axes are at the same scale but cover different ranges; y-axes for attenuation coefficient change scale and range for each record. The x-axes lengths, with the exception of ER-1 2127 which spans a longer, 350-day period, are drawn proportionally with respect to each other. Note the trend of increasing attenuation coefficient terminated by abrupt instrument failure.

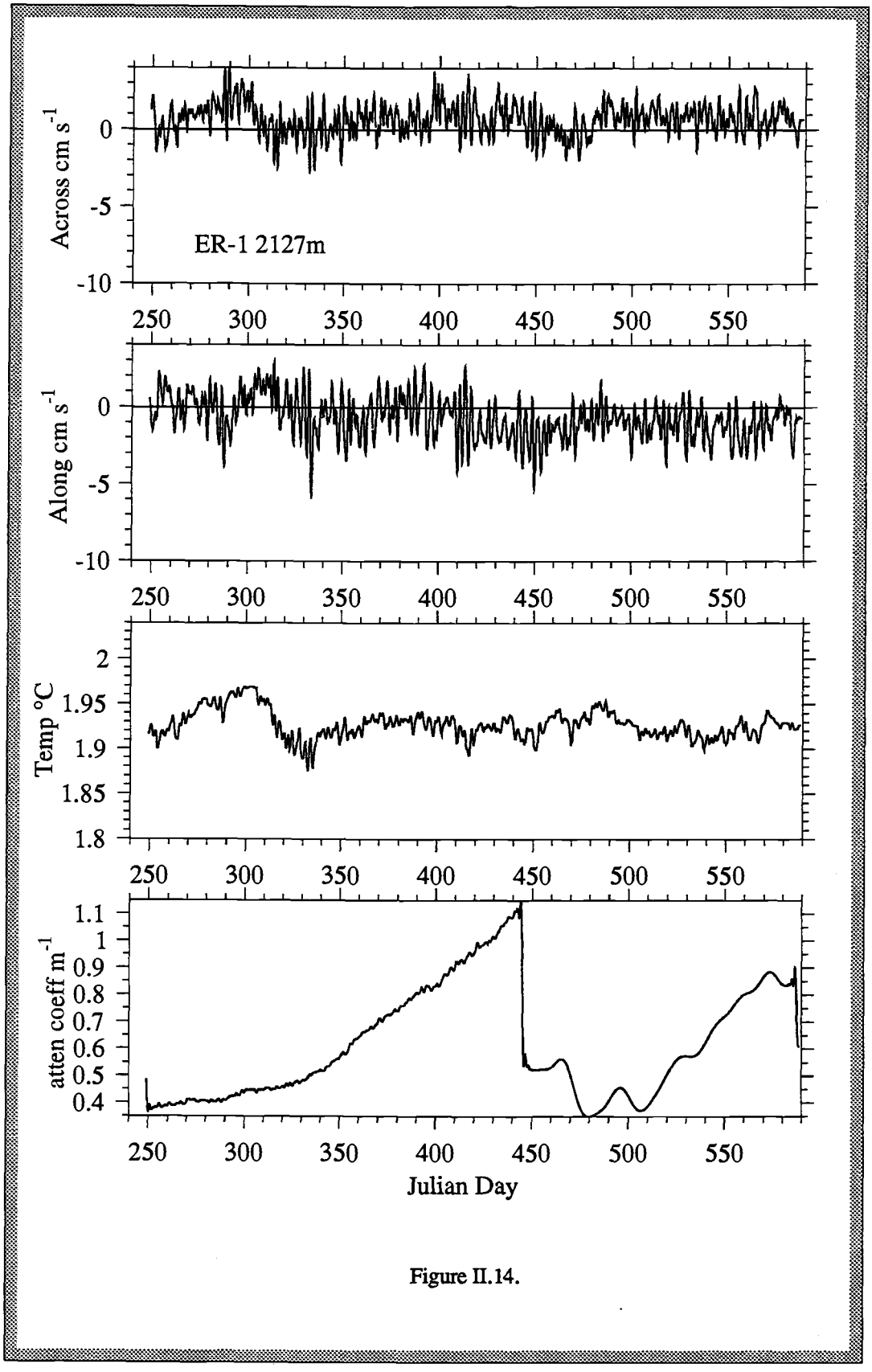
Across cm s-1
0
-5
-10
ER-1 2127m
250
300
350
400
450
500
550
Along cm s-1
0
-5
-10
Temp °C
2
1.95
1.9
1.85
1.8
atten coeff m-1
1.1
1
0.9
0.8
0.7
0.6
0.5
0.4
Julian Day

Figure II.14.

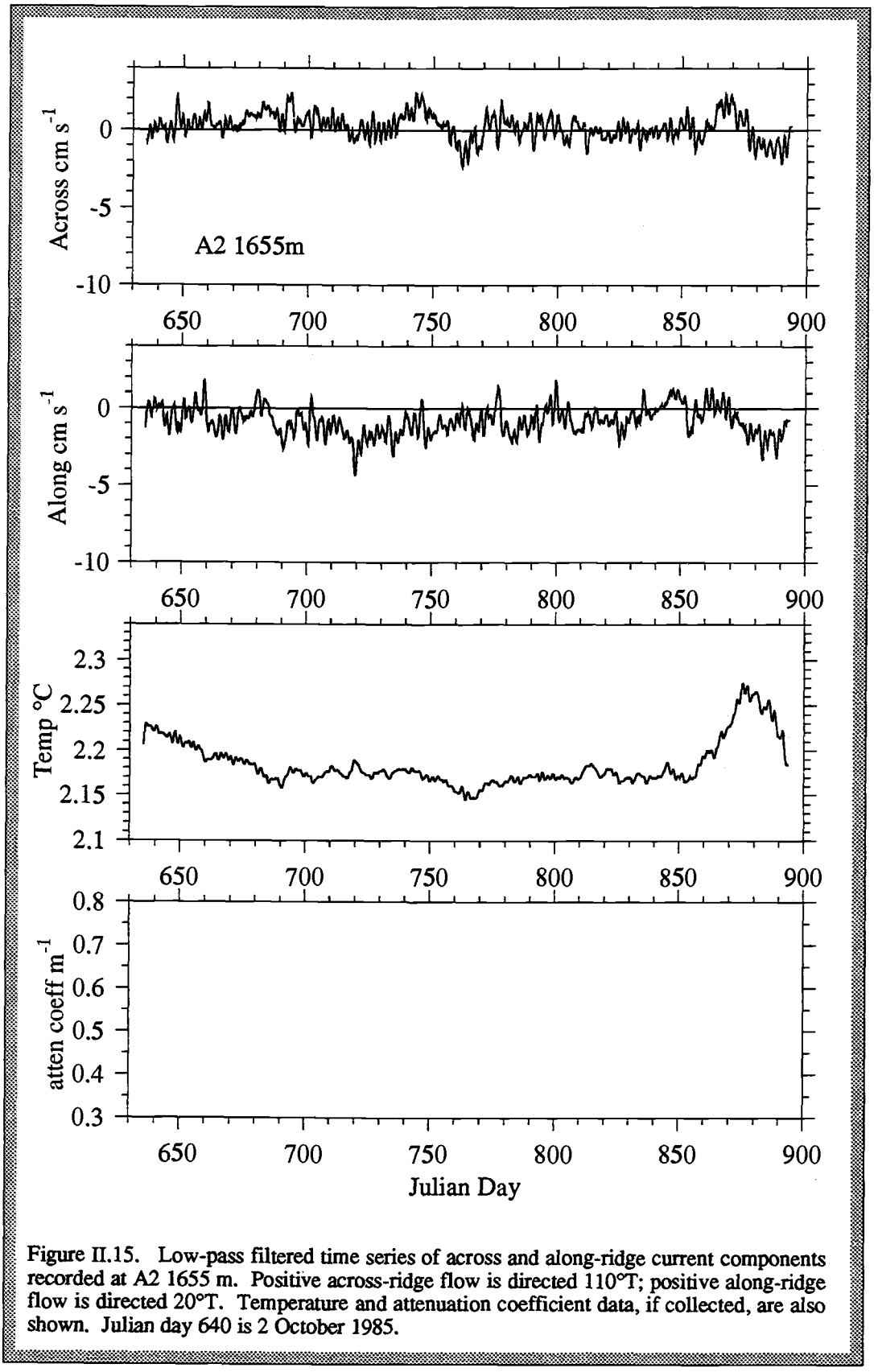

Figure II.15. Low-pass filtered time series of across and along-ridge current components recorded at A2 1655 m. Positive across-ridge flow is directed 110°T; positive along-ridge flow is directed 20°T. Temperature and attenuation coefficient data, if collected, are also shown. Julian day 640 is 2 October 1985.

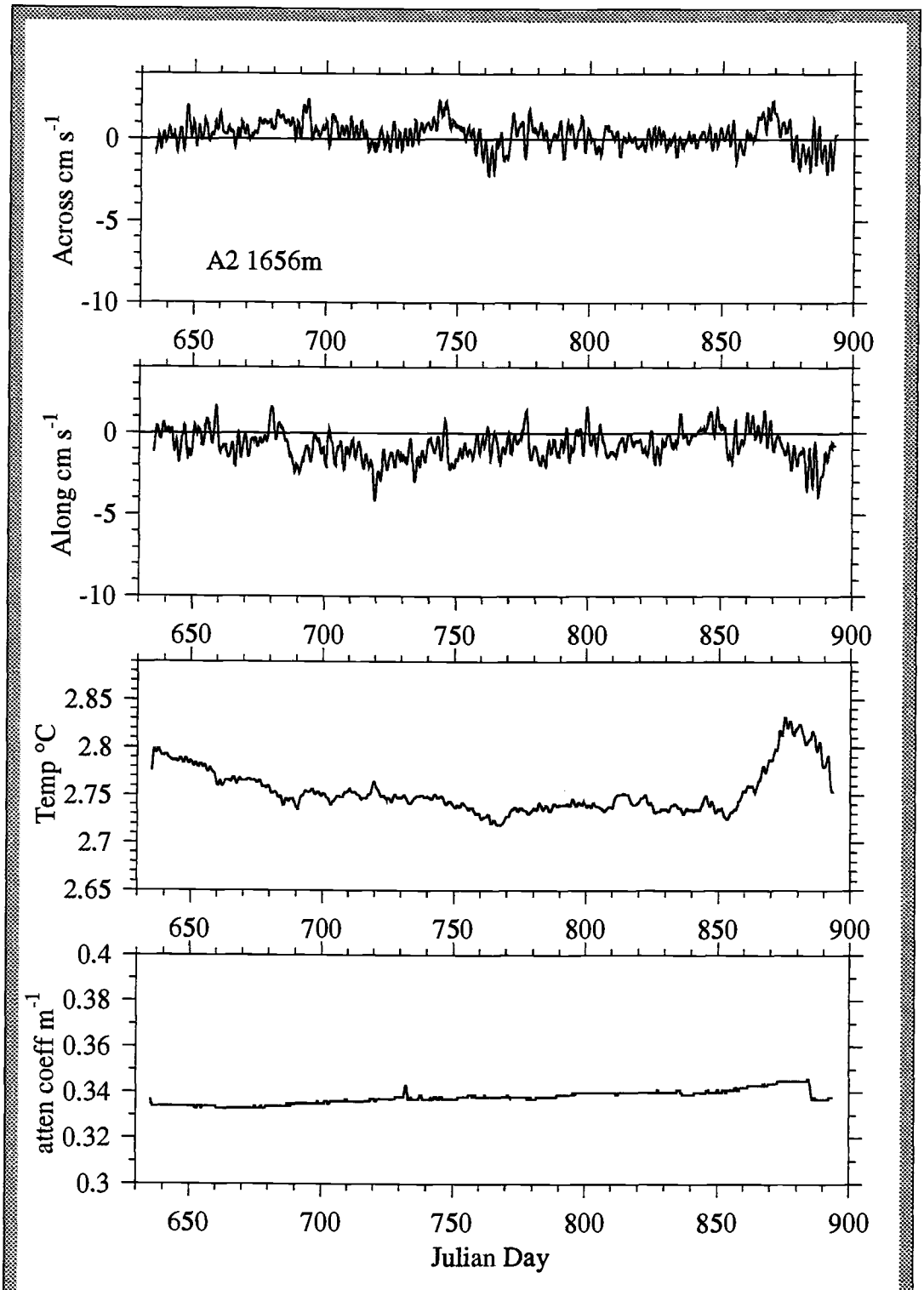

Figure II.16. Low-pass filtered time series of across and along-ridge current components recorded at A2 1656 m. Positive across-ridge flow is directed 110°T; positive along-ridge flow is directed 20°T. Temperature and attenuation coefficient data, if collected, are also shown. Julian day 640 is 2 October 1985.

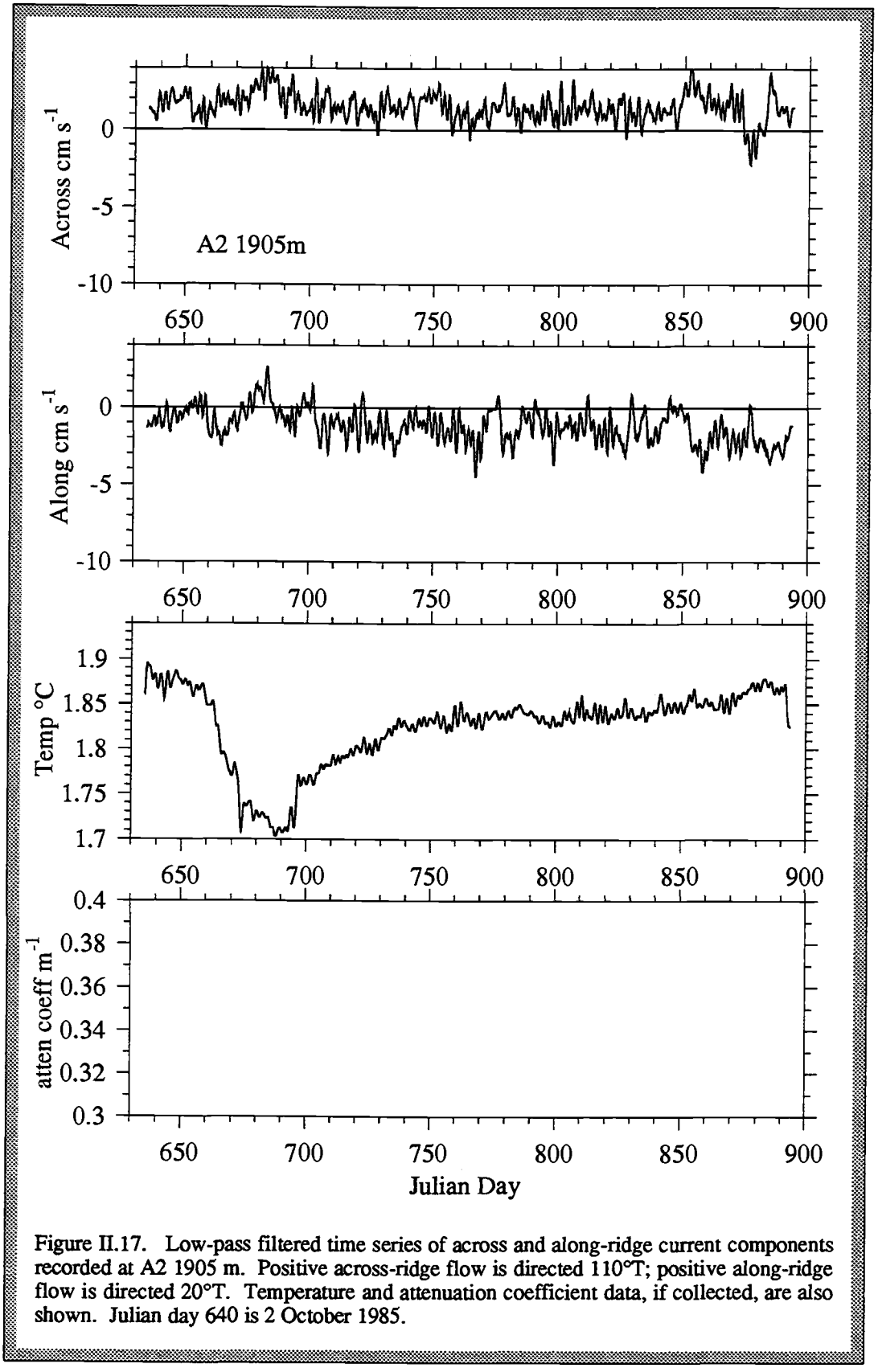

Figure II.17. Low-pass filtered time series of across and along-ridge current components recorded at A2 1905 m. Positive across-ridge flow is directed 110°T; positive along-ridge flow is directed 20°T. Temperature and attenuation coefficient data, if collected, are also shown. Julian day 640 is 2 October 1985.

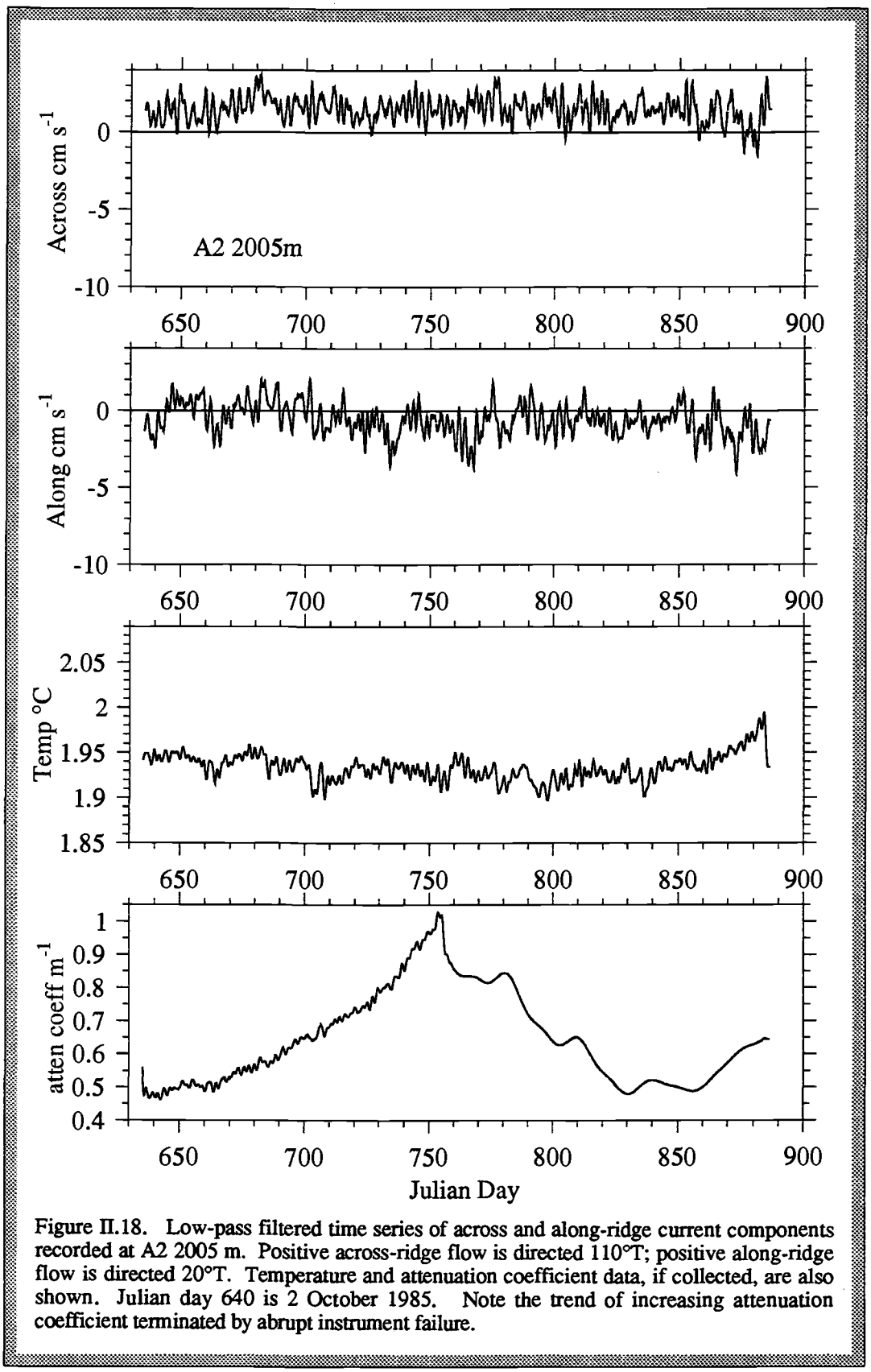

Figure II.18. Low-pass filtered time series of across and along-ridge current components recorded at A2 2005 m. Positive across-ridge flow is directed 110°T; positive along-ridge flow is directed 20°T. Temperature and attenuation coefficient data, if collected, are also shown. Julian day 640 is 2 October 1985. Note the trend of increasing attenuation coefficient terminated by abrupt instrument failure.

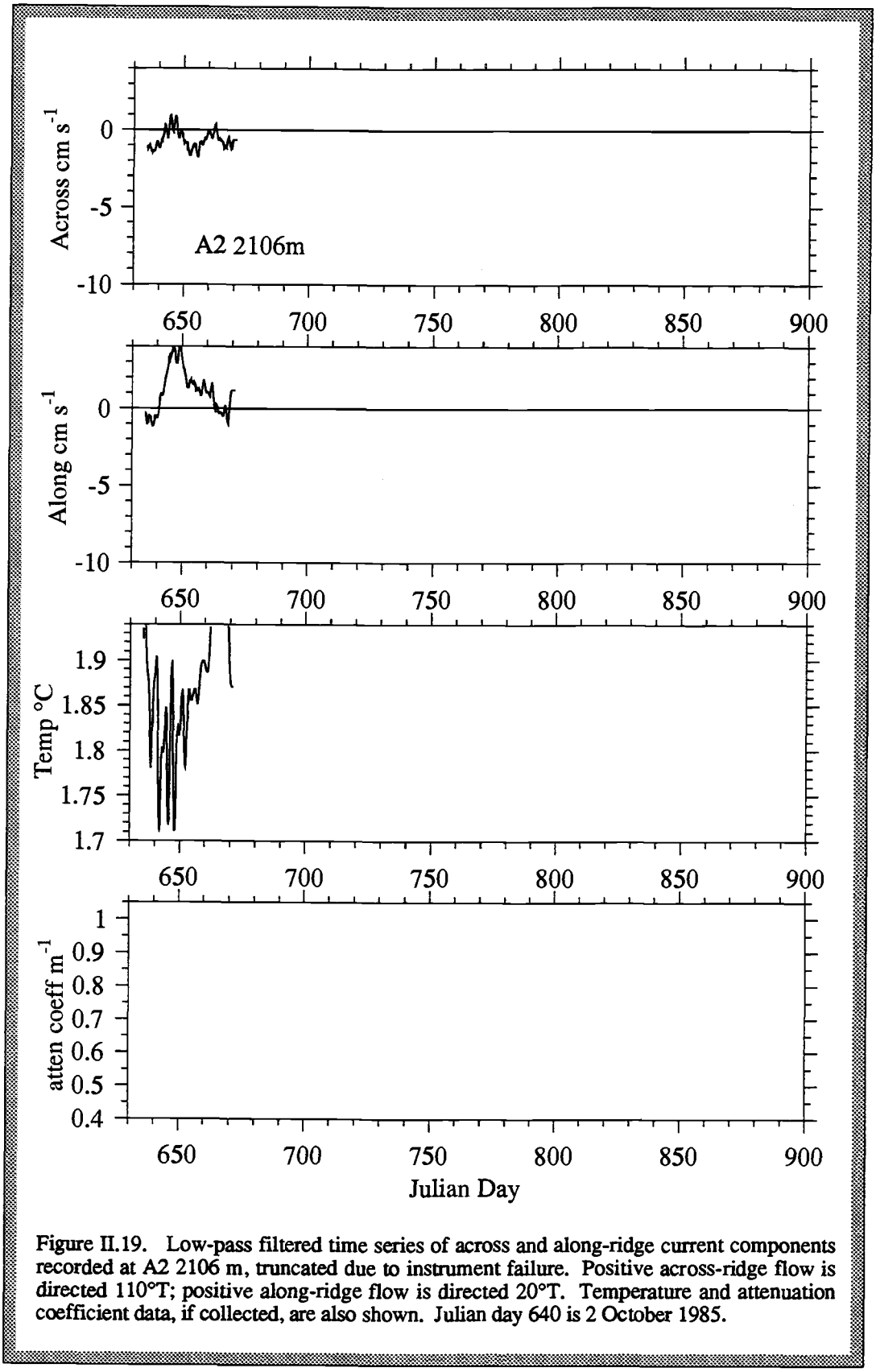

Figure II.19. Low-pass filtered time series of across and along-ridge current components recorded at A2 2106 m, truncated due to instrument failure. Positive across-ridge flow is directed 110°T; positive along-ridge flow is directed 20°T. Temperature and attenuation coefficient data, if collected, are also shown. Julian day 640 is 2 October 1985.

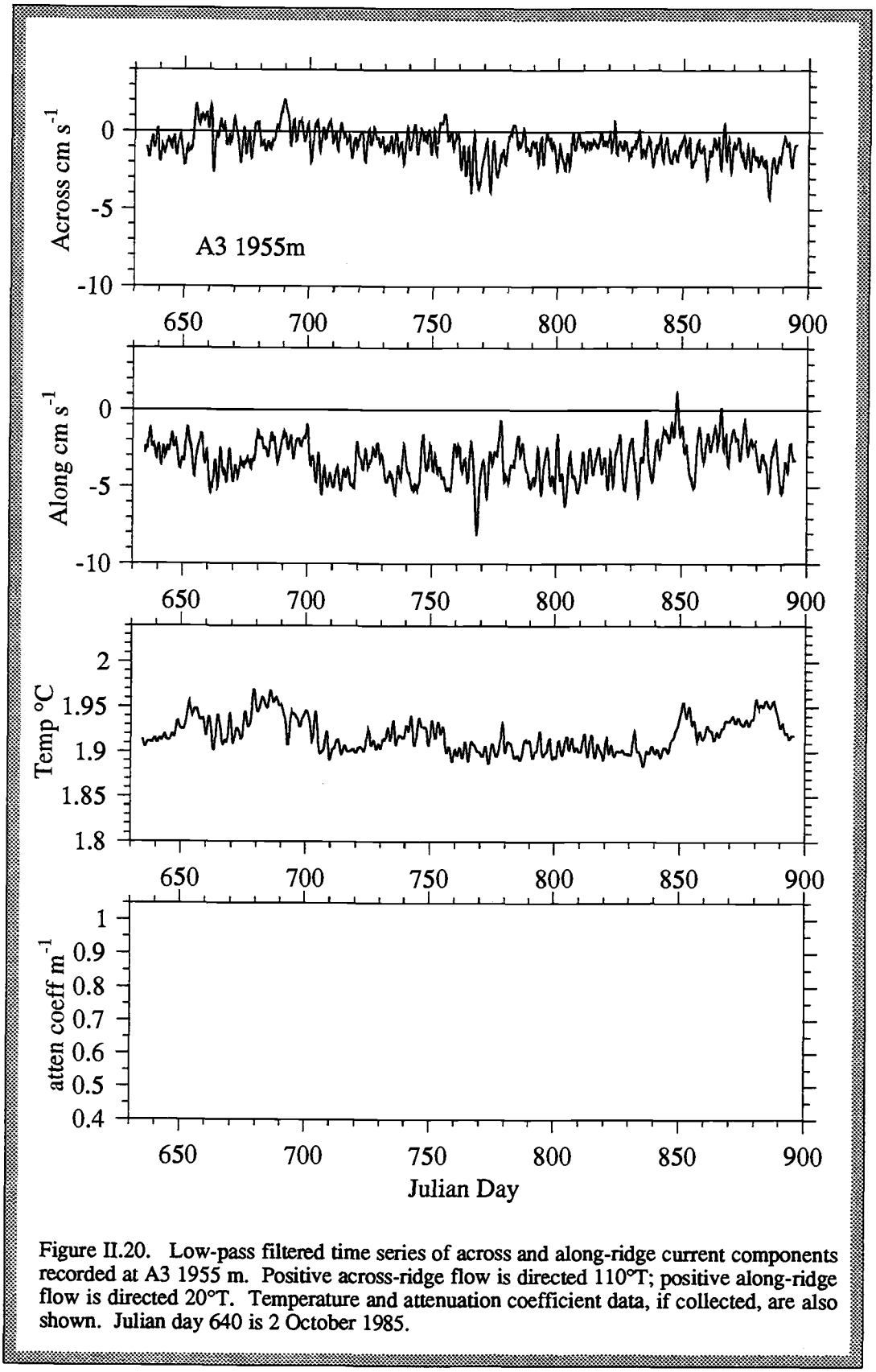

Figure II.20. Low-pass filtered time series of across and along-ridge current components recorded at A3 1955 m. Positive across-ridge flow is directed 110°T; positive along-ridge flow is directed 20°T. Temperature and attenuation coefficient data, if collected, are also shown. Julian day 640 is 2 October 1985.

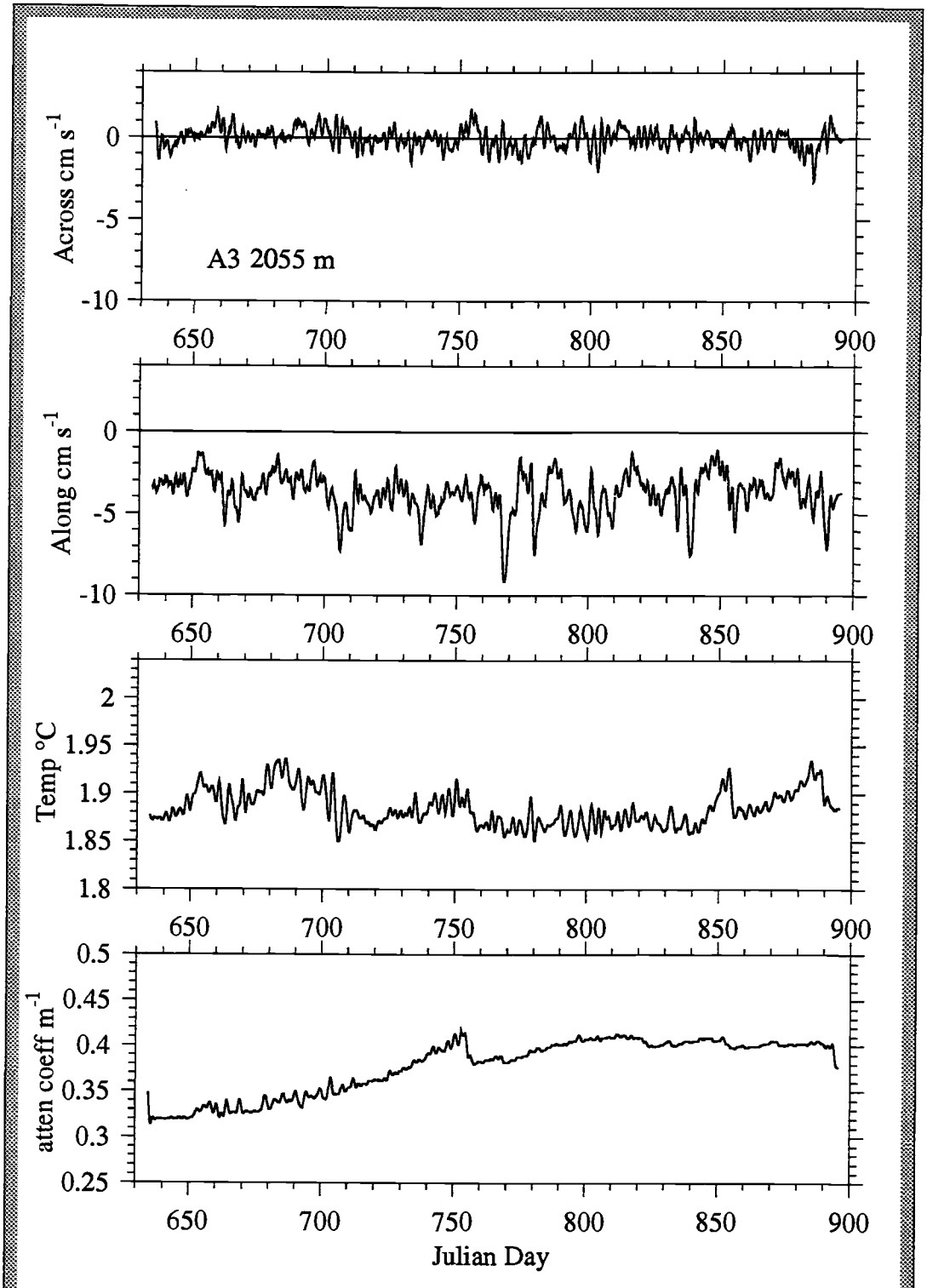

Figure II.21. Low-pass filtered time series of across and along-ridge current components recorded at A3 2055 m. Positive across-ridge flow is directed 110°T; positive along-ridge flow is directed 20°T. Temperature and attenuation coefficient data, if collected, are also shown. Julian day 640 is 2 October 1985. Note the trend of increasing attenuation coefficient over time.

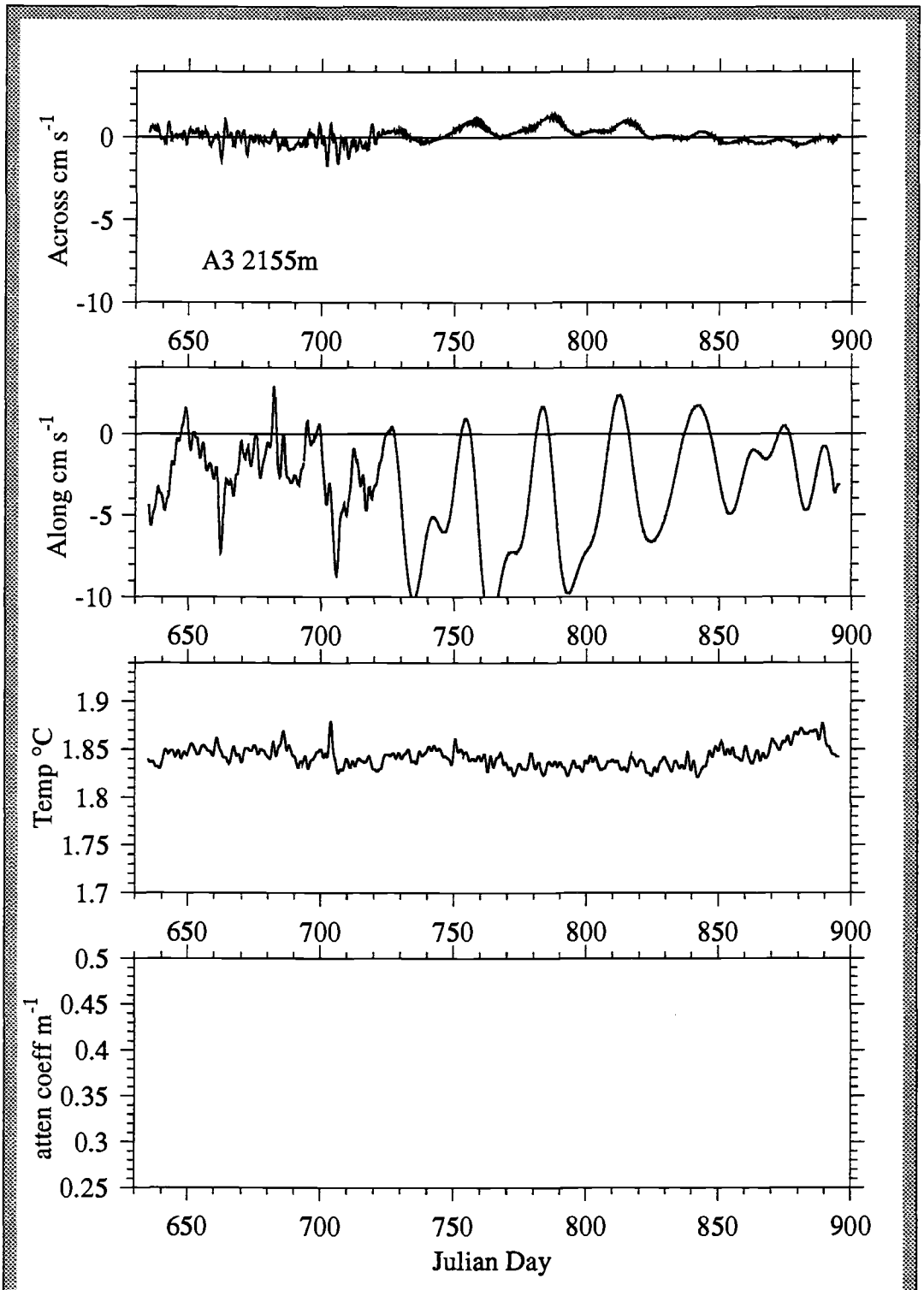

Figure II.22. Low-pass filtered time series of across and along-ridge current components recorded at A3 2155 m. Flow data are meaningful only until JD 720. Positive across-ridge flow is directed 110°T; positive along-ridge flow is directed 20°T. Temperature and attenuation coefficient data, if collected, are also shown. Julian day 640 is 2 October 1985.

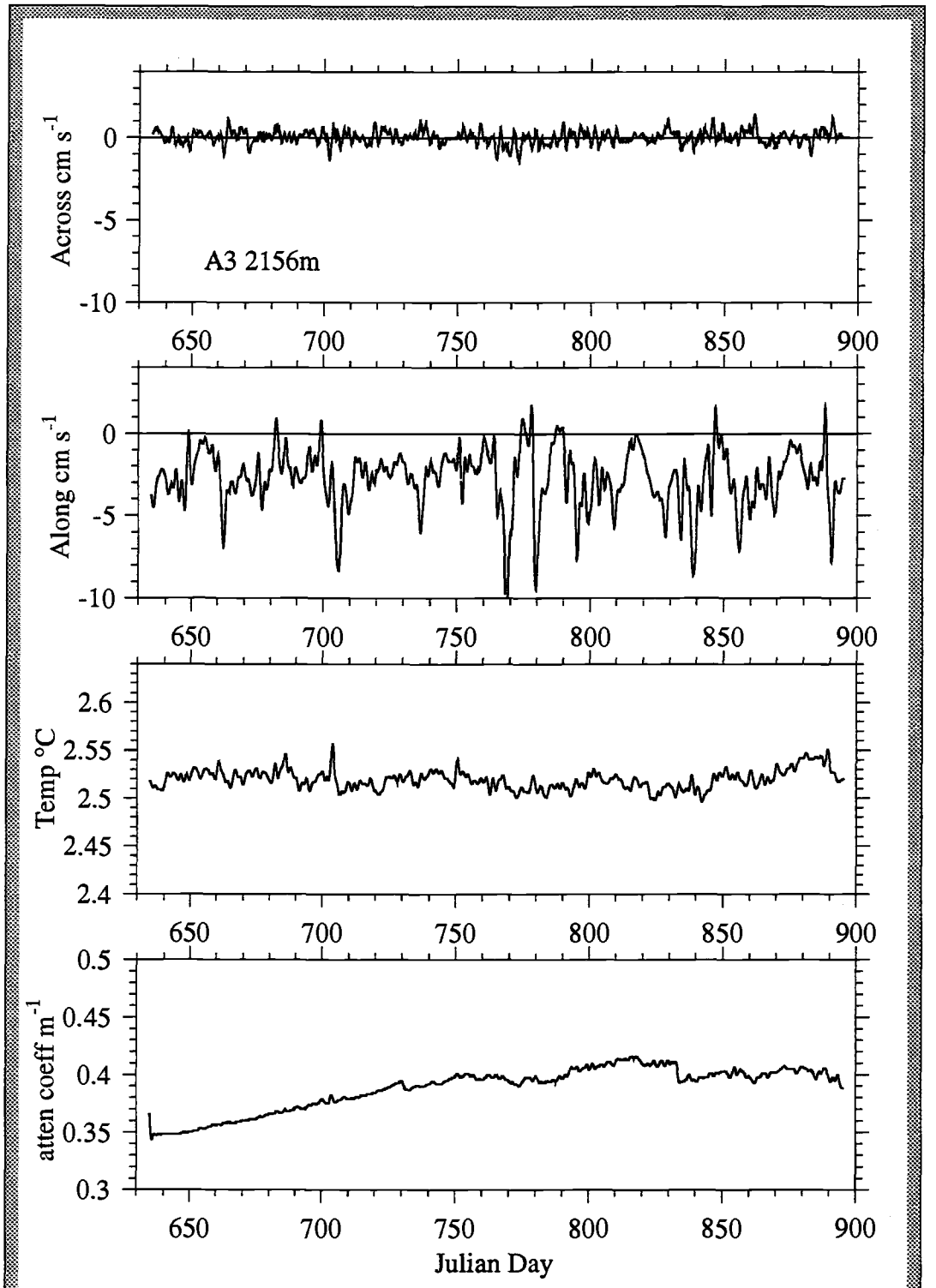

Figure II.23. Low-pass filtered time series of across and along-ridge current components recorded at A3 2156 m. Positive across-ridge flow is directed 110°T; positive along-ridge flow is directed 20°T. Temperature and attenuation coefficient data, if collected, are also shown. Julian day 640 is 2 October 1985. Note the trend of increasing attenuation coefficient over time.

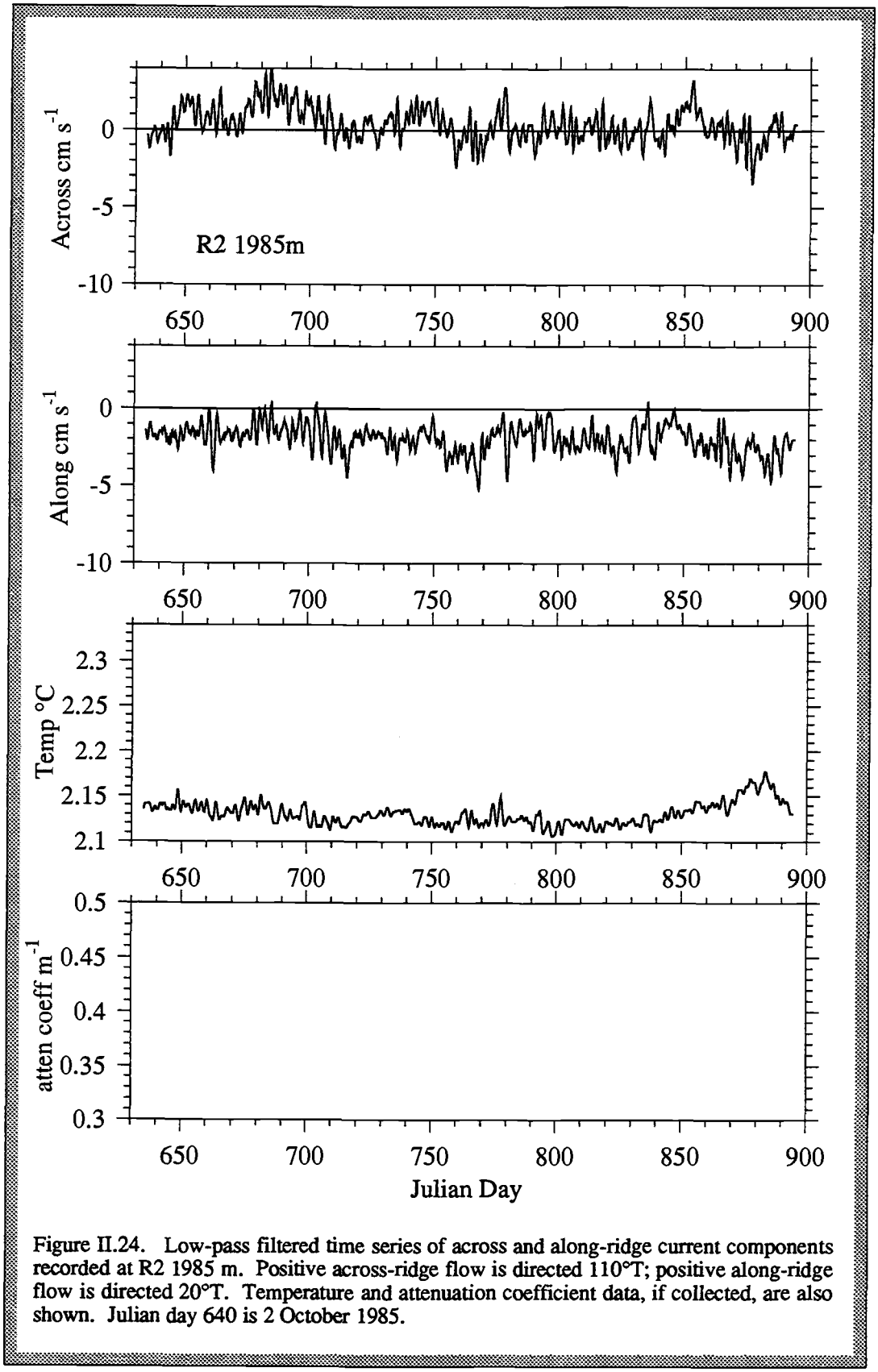

Figure II.24. Low-pass filtered time series of across and along-ridge current components recorded at R2 1985 m. Positive across-ridge flow is directed 110°T; positive along-ridge flow is directed 20°T. Temperature and attenuation coefficient data, if collected, are also shown. Julian day 640 is 2 October 1985.

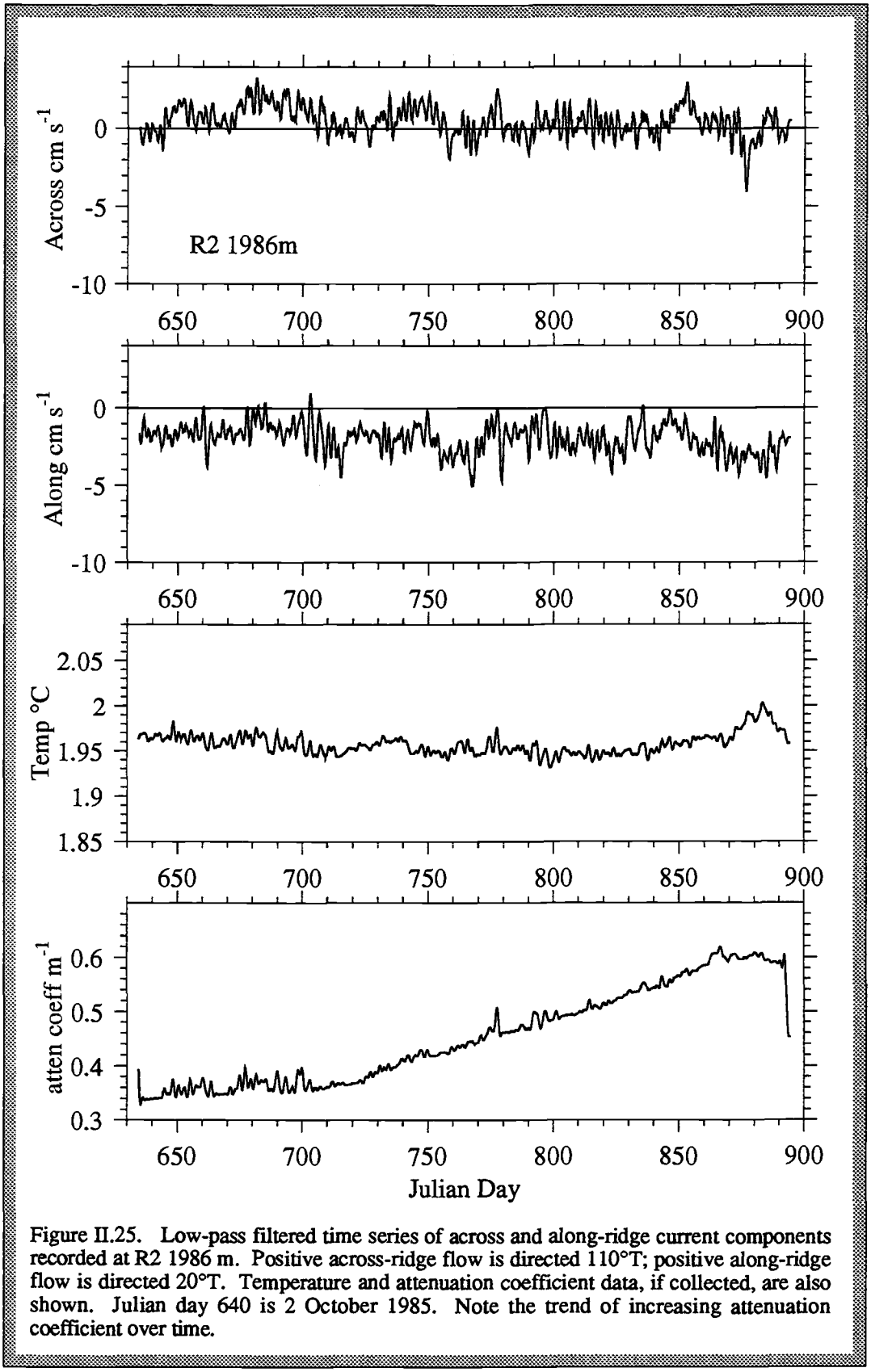

Figure II.25. Low-pass filtered time series of across and along-ridge current components recorded at R2 1986 m. Positive across-ridge flow is directed 110°T; positive along-ridge flow is directed 20°T. Temperature and attenuation coefficient data, if collected, are also shown. Julian day 640 is 2 October 1985. Note the trend of increasing attenuation coefficient over time.

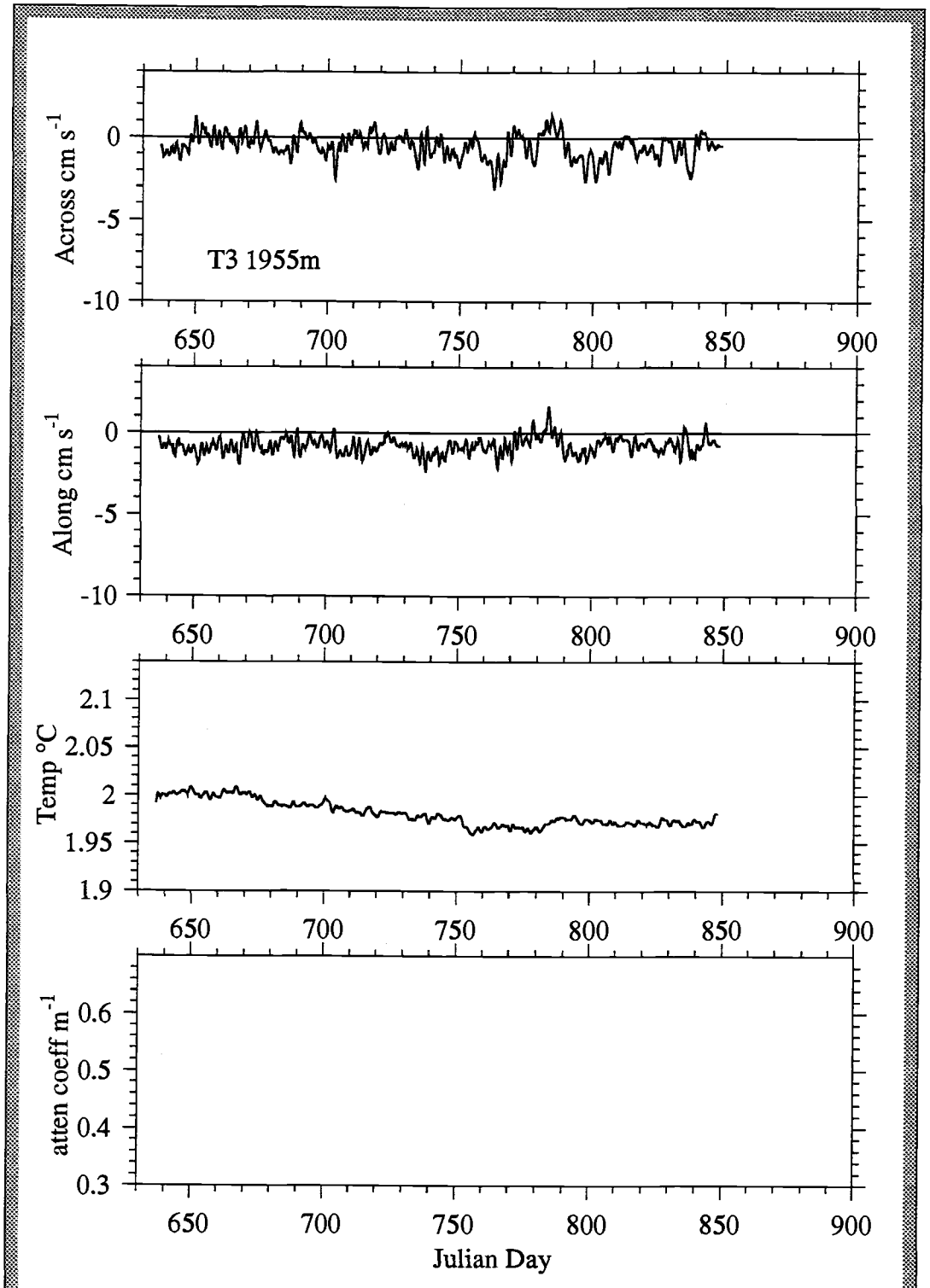

Figure II.26. Low-pass filtered time series of across and along-ridge current components recorded at T3 1955 m. Positive across-ridge flow is directed 110°T; positive along-ridge flow is directed 20°T. Temperature and attenuation coefficient data, if collected, are also shown. Julian day 640 is 2 October 1985.

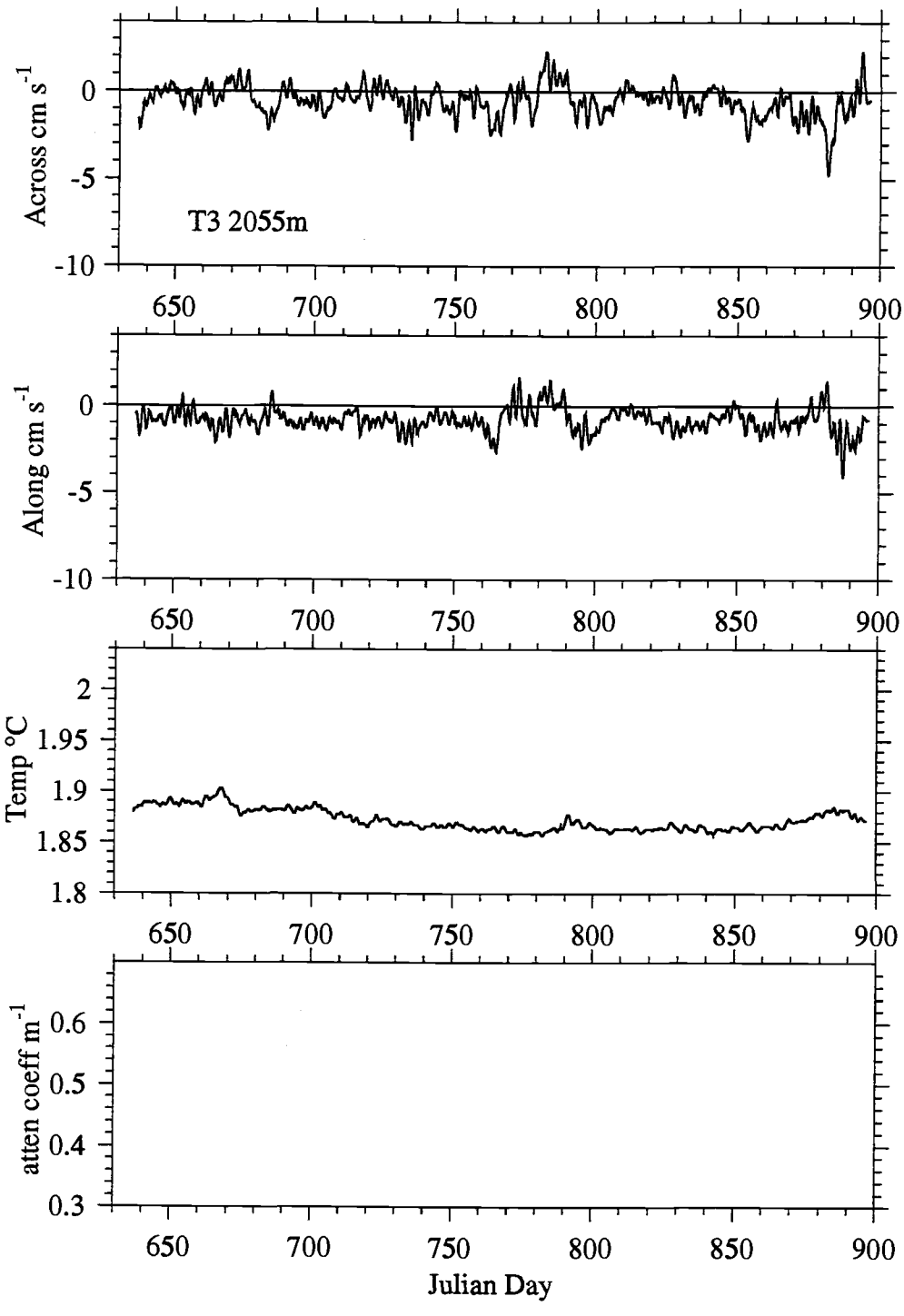

Figure II.27. Low-pass filtered time series of across and along-ridge current components recorded at T3 2055 m. Positive across-ridge flow is directed 110°T; positive along-ridge flow is directed 20°T. Temperature and attenuation coefficient data, if collected, are also shown. Julian day 640 is 2 October 1985.

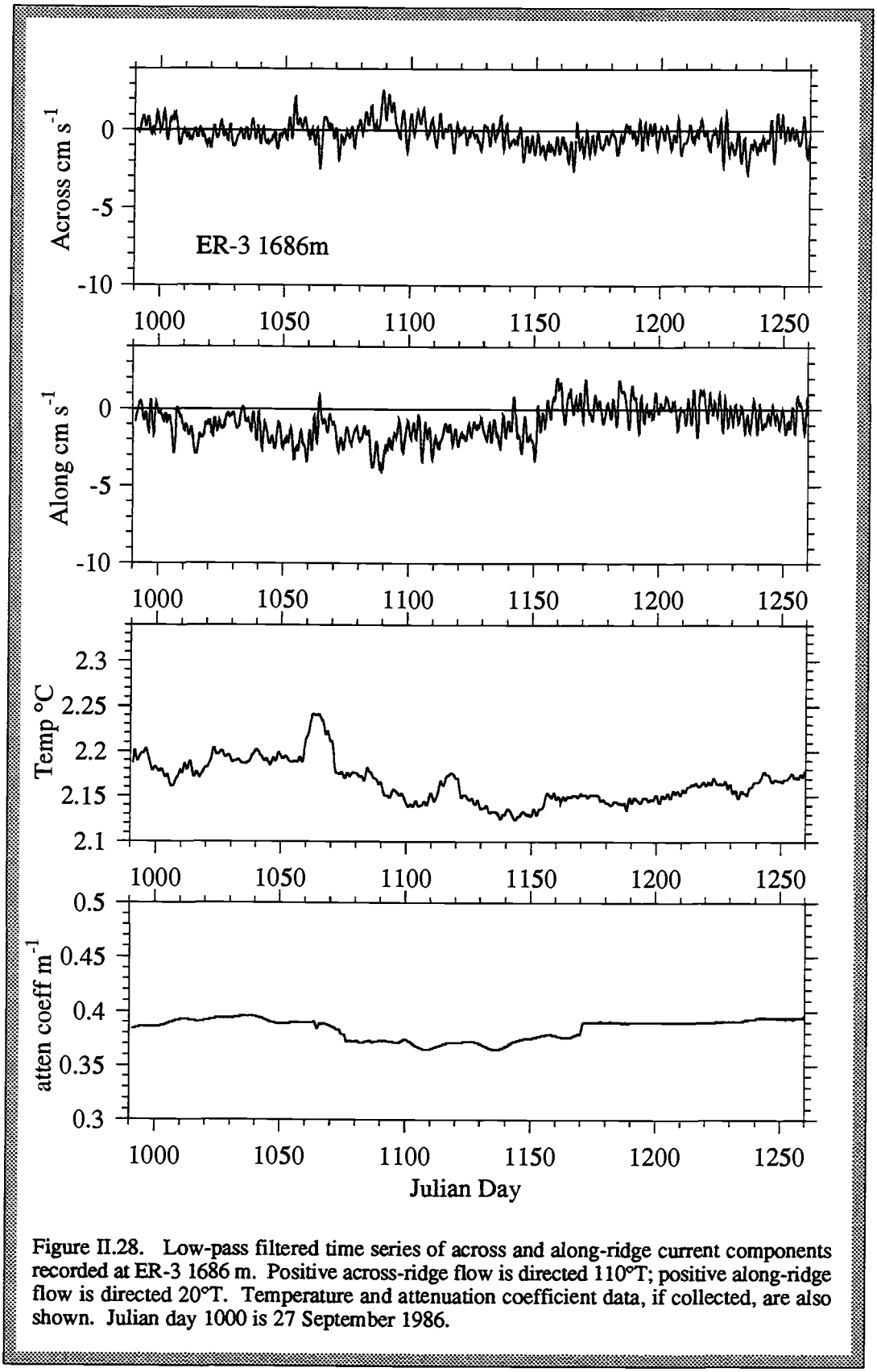

Figure II.28. Low-pass filtered time series of across and along-ridge current components recorded at ER-3 1686 m. Positive across-ridge flow is directed 110°T; positive along-ridge flow is directed 20°T. Temperature and attenuation coefficient data, if collected, are also shown. Julian day 1000 is 27 September 1986.

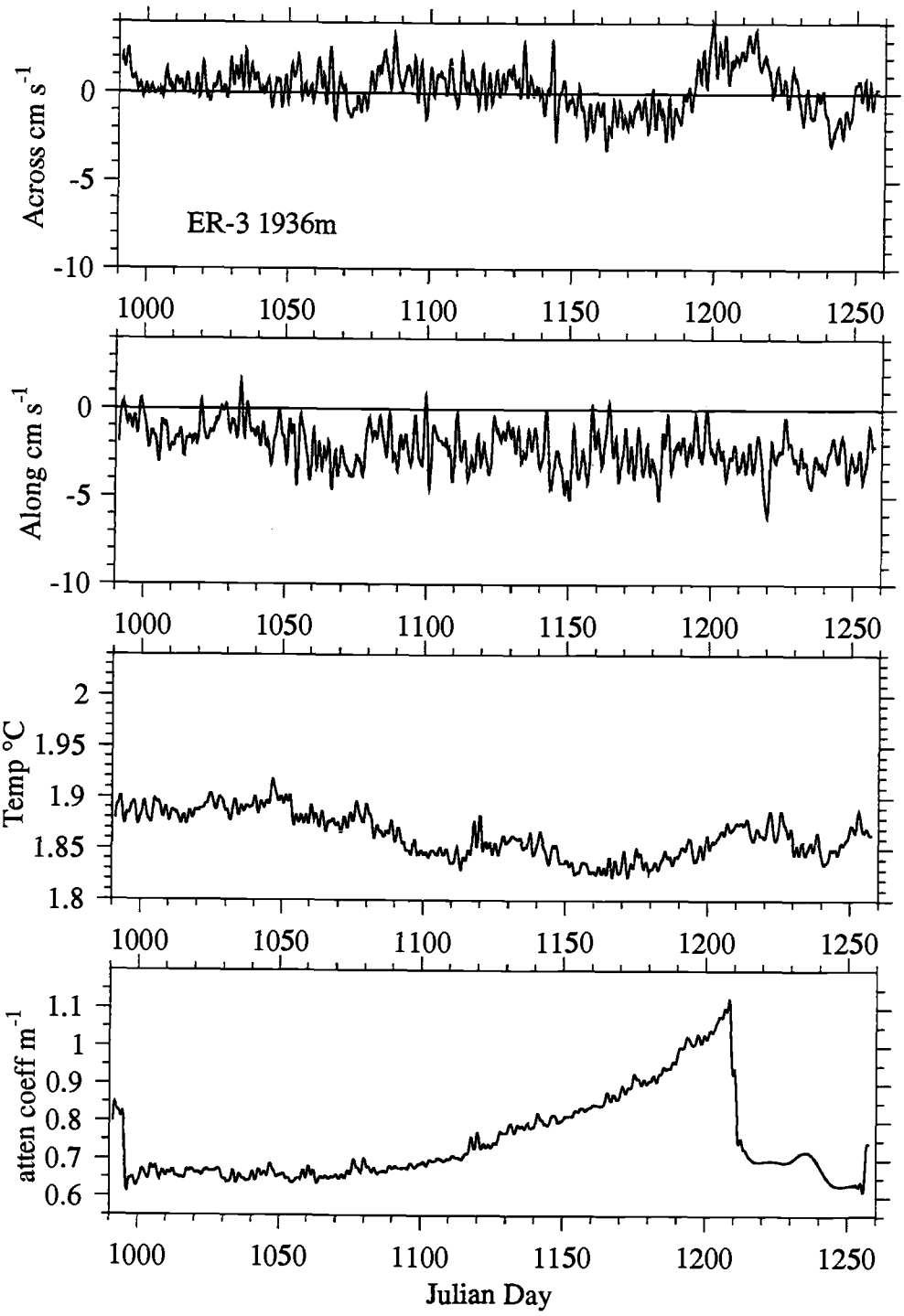

Figure II.29. Low-pass filtered time series of across and along-ridge current components recorded at ER-3 1936 m. Positive across-ridge flow is directed 110°T; positive along-ridge flow is directed 20°T. Temperature and attenuation coefficient data, if collected, are also shown. Julian day 1000 is 27 September 1986. Note the trend of increasing attenuation coefficient terminated by abrupt instrument failure.

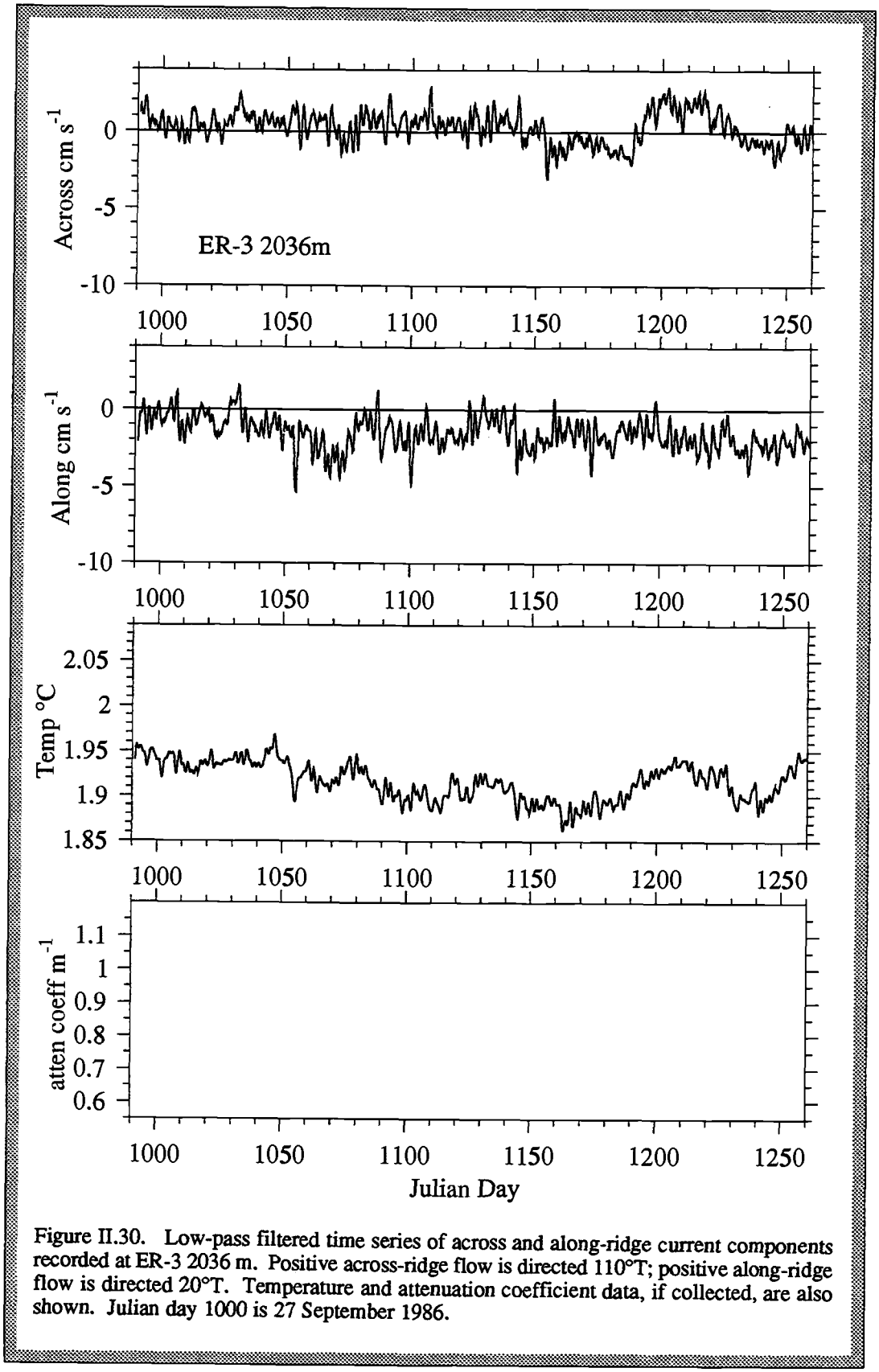

Figure II.30. Low-pass filtered time series of across and along-ridge current components recorded at ER-3 2036 m. Positive across-ridge flow is directed 110°T; positive along-ridge flow is directed 20°T. Temperature and attenuation coefficient data, if collected, are also shown. Julian day 1000 is 27 September 1986.

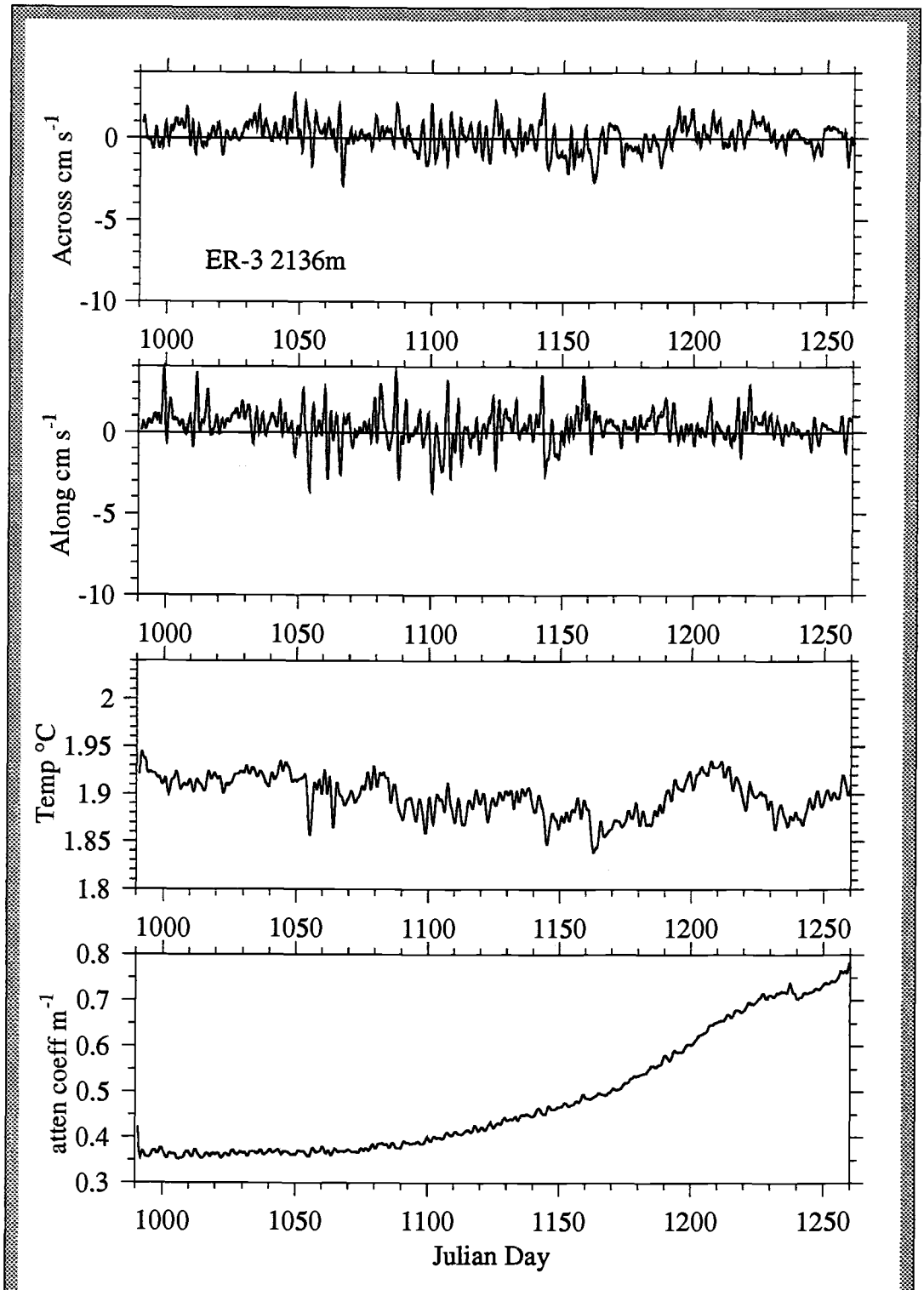

Figure II.31. Low-pass filtered time series of across and along-ridge current components recorded at ER-3 2136 m. Positive across-ridge flow is directed 110°T; positive along-ridge flow is directed 20°T. Temperature and attenuation coefficient data, if collected, are also shown. Julian day 1000 is 27 September 1986. Note the trend of increasing attenuation coefficient over time.

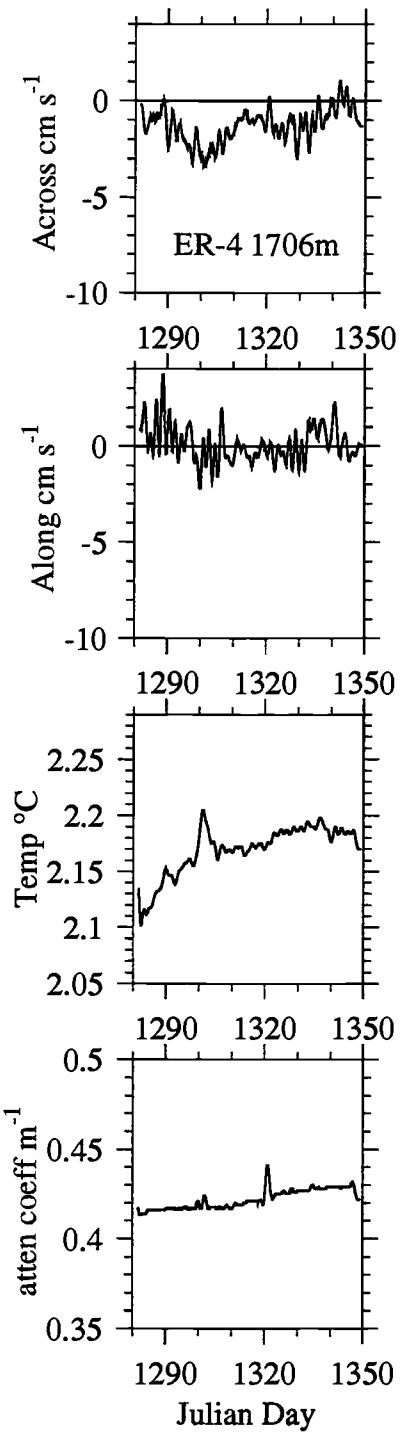

Figure II.32. Low-pass filtered time series of across and along-ridge current components recorded at ER-4 1706 m. Positive across-ridge flow is directed 110°T; positive along-ridge flow is directed 20°T. Temperature and attenuation coefficient data, if collected, are also shown. Julian day 1290 is 14 July 1987.

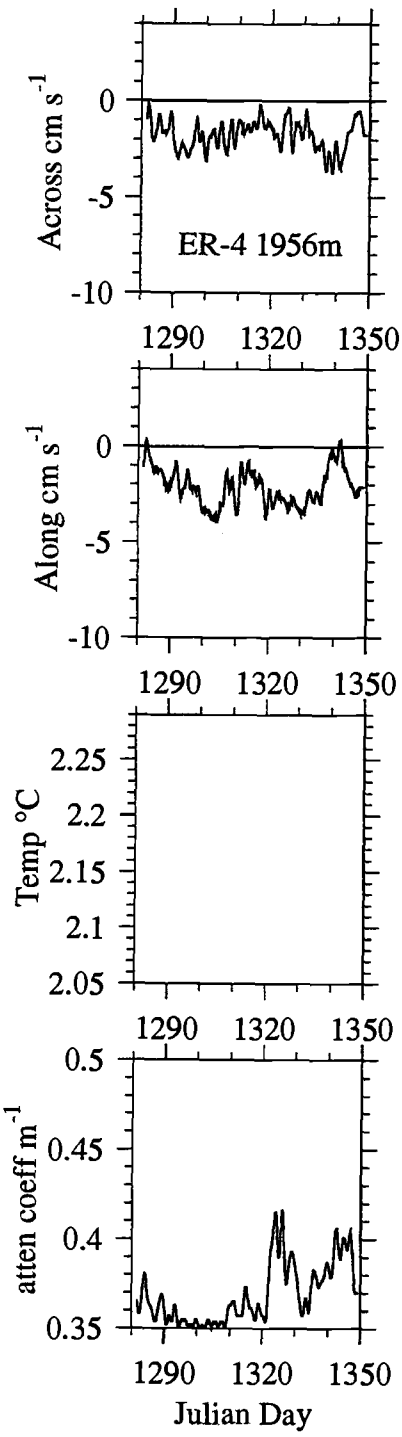

Figure II.33. Low-pass filtered time series of across and along-ridge current components recorded at ER-4 1956 m. Positive across-ridge flow is directed 110°T; positive along-ridge flow is directed 20°T. Temperature and attenuation coefficient data, if collected, are also shown. Julian day 1290 is 14 July 1987.

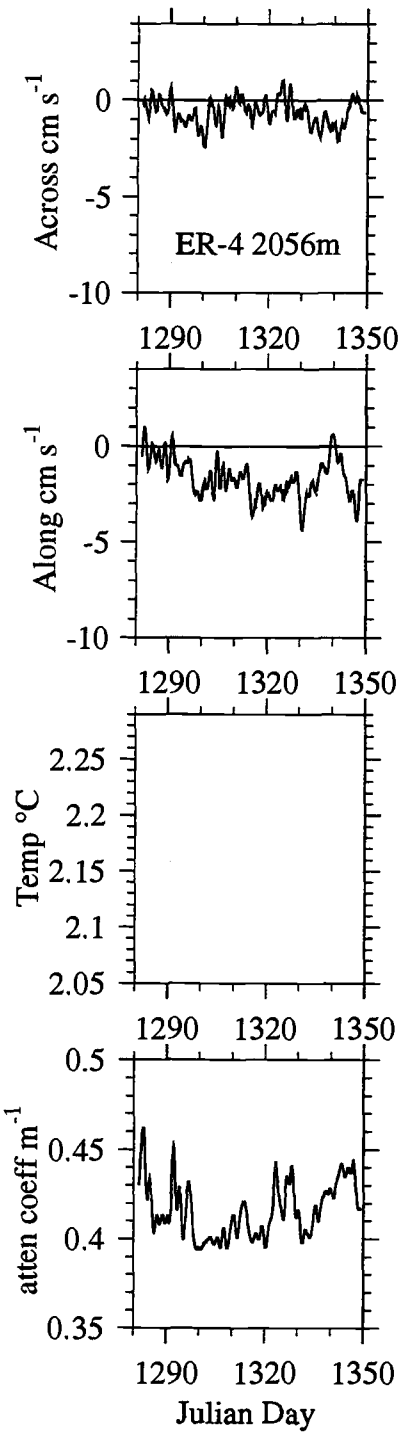

Figure II.34. Low-pass filtered time series of across and along-ridge current components recorded at ER-4 2056 m. Positive across-ridge flow is directed 110°T; positive along-ridge flow is directed 20°T. Temperature and attenuation coefficient data, if collected, are also shown. Julian day 1290 is 14 July 1987.

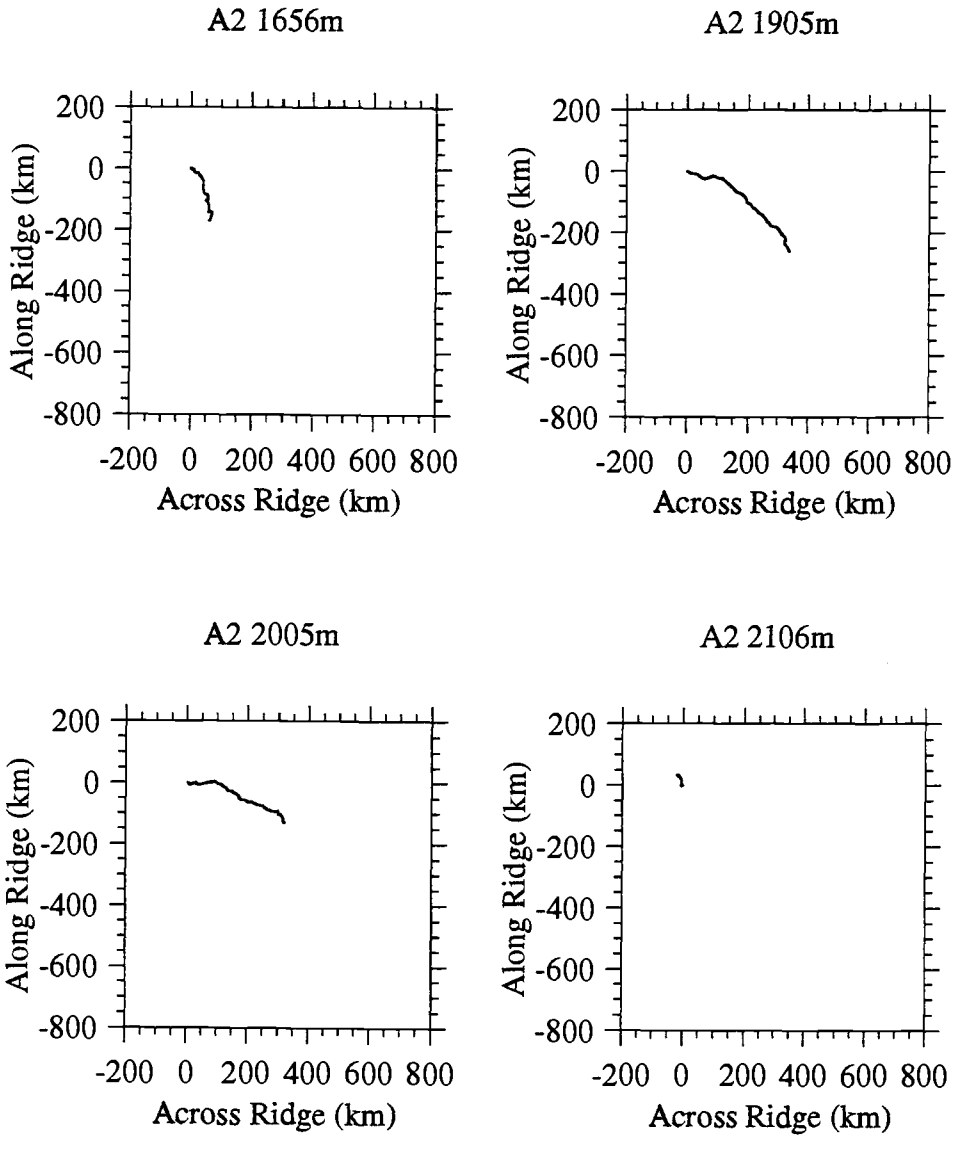

Figure II.35. Progressive vector diagrams (PVD) for horizontal currents (low-pass filtered) at mooring A2 plotted in the along-/across-ridge reference frame. Vectors depict flow velocity past the moored current meter in a horizontal plane. Axis lengths are consistent in Figures II.35 - II.39, and vectors begin at the origin (0,0) of each plot. Record lengths are equivalent to those shown in the corresponding time series (see Figures II.14 - II.34).

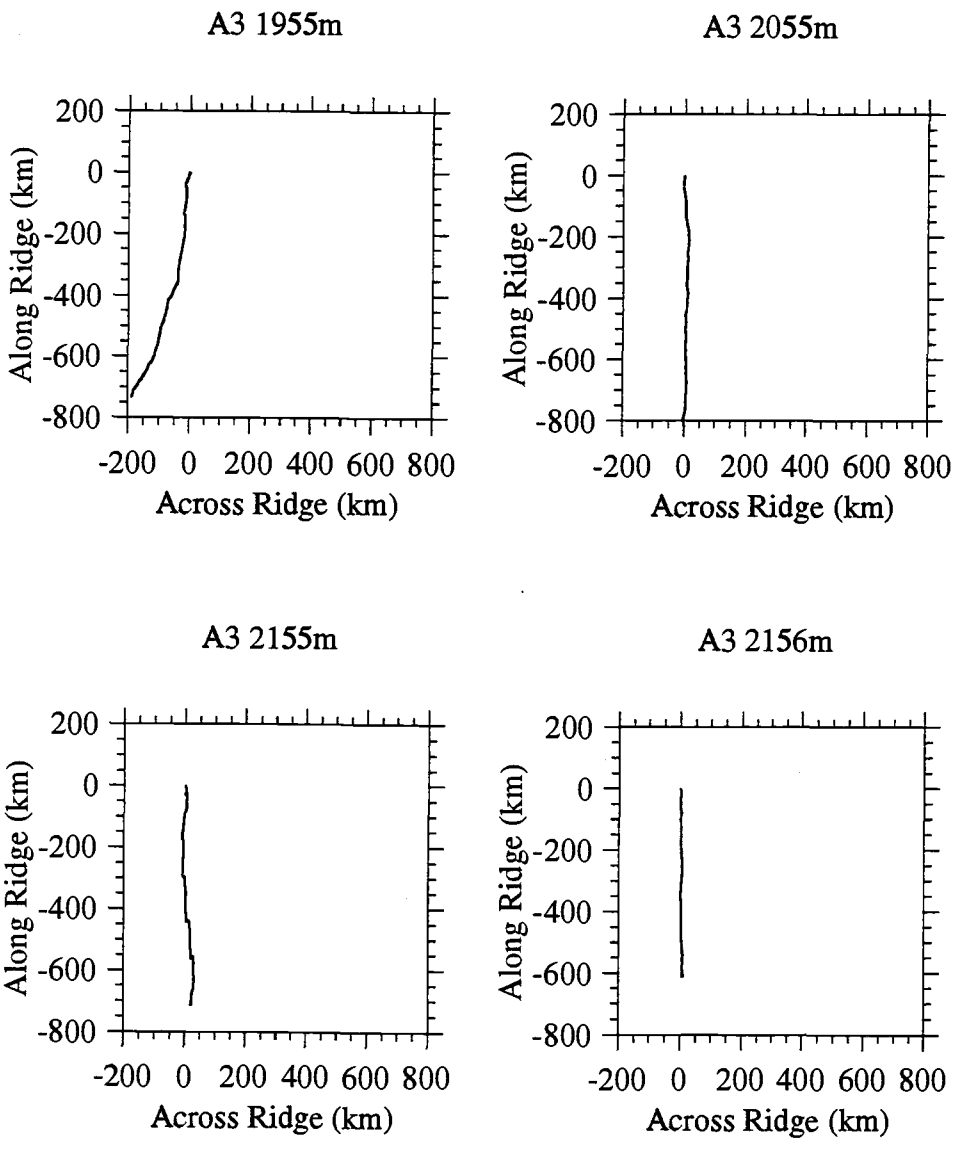

Figure II.36. Progressive vector diagrams (PVD) for horizontal currents (low-pass filtered) at mooring A3 plotted in the along-/across-ridge reference frame. Vectors depict flow velocity past the moored current meter in a horizontal plane. Axis lengths are consistent in Figures II.35 - II.39, and vectors begin at the origin (0,0) of each plot. Record lengths are equivalent to those shown in the corresponding time series (see Figures II.14 - II.34).

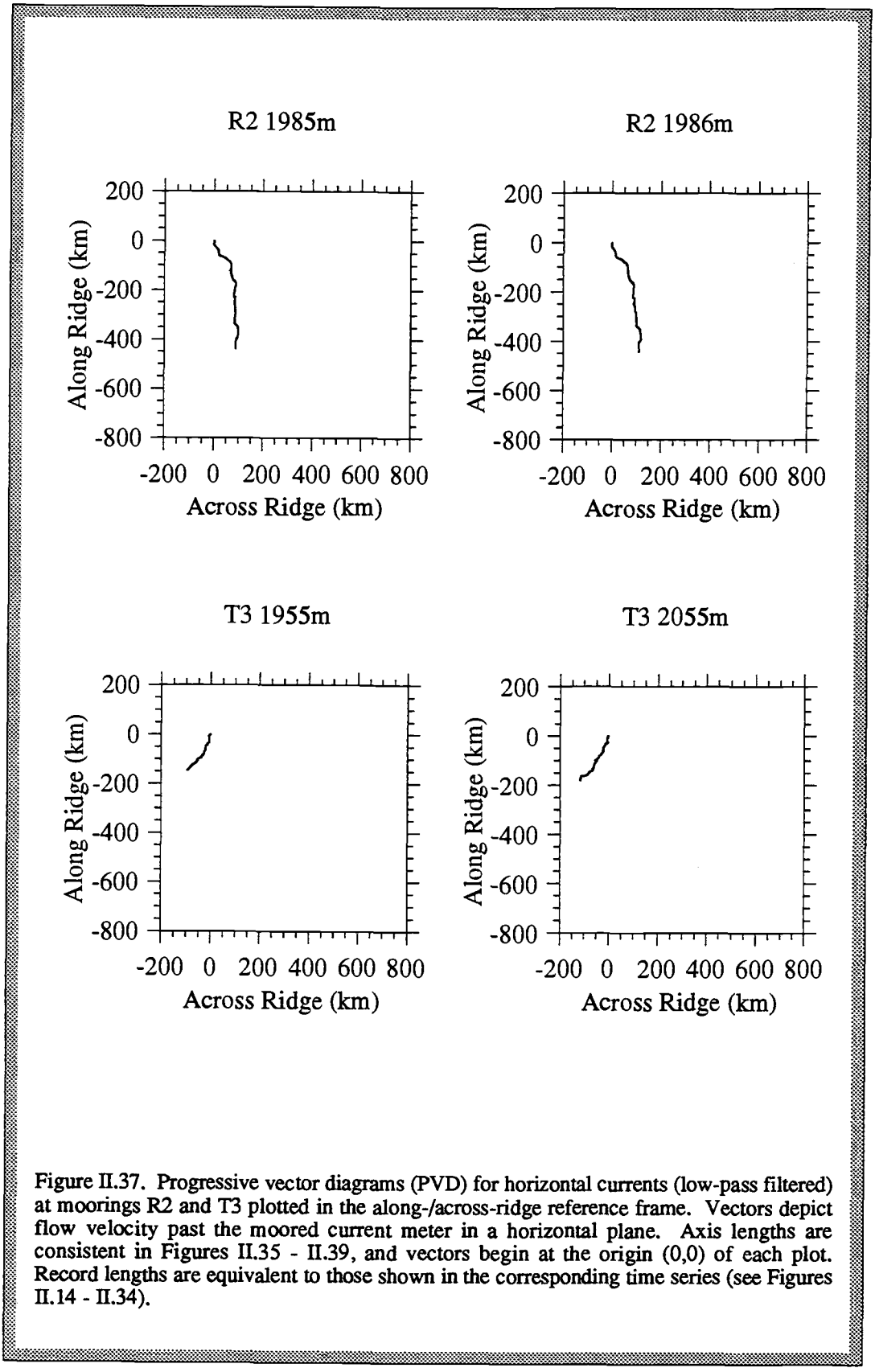

Figure II.37. Progressive vector diagrams (PVD) for horizontal currents (low-pass filtered) at moorings R2 and T3 plotted in the along-/across-ridge reference frame. Vectors depict flow velocity past the moored current meter in a horizontal plane. Axis lengths are consistent in Figures II.35 - II.39, and vectors begin at the origin (0,0) of each plot. Record lengths are equivalent to those shown in the corresponding time series (see Figures II.14 - II.34).

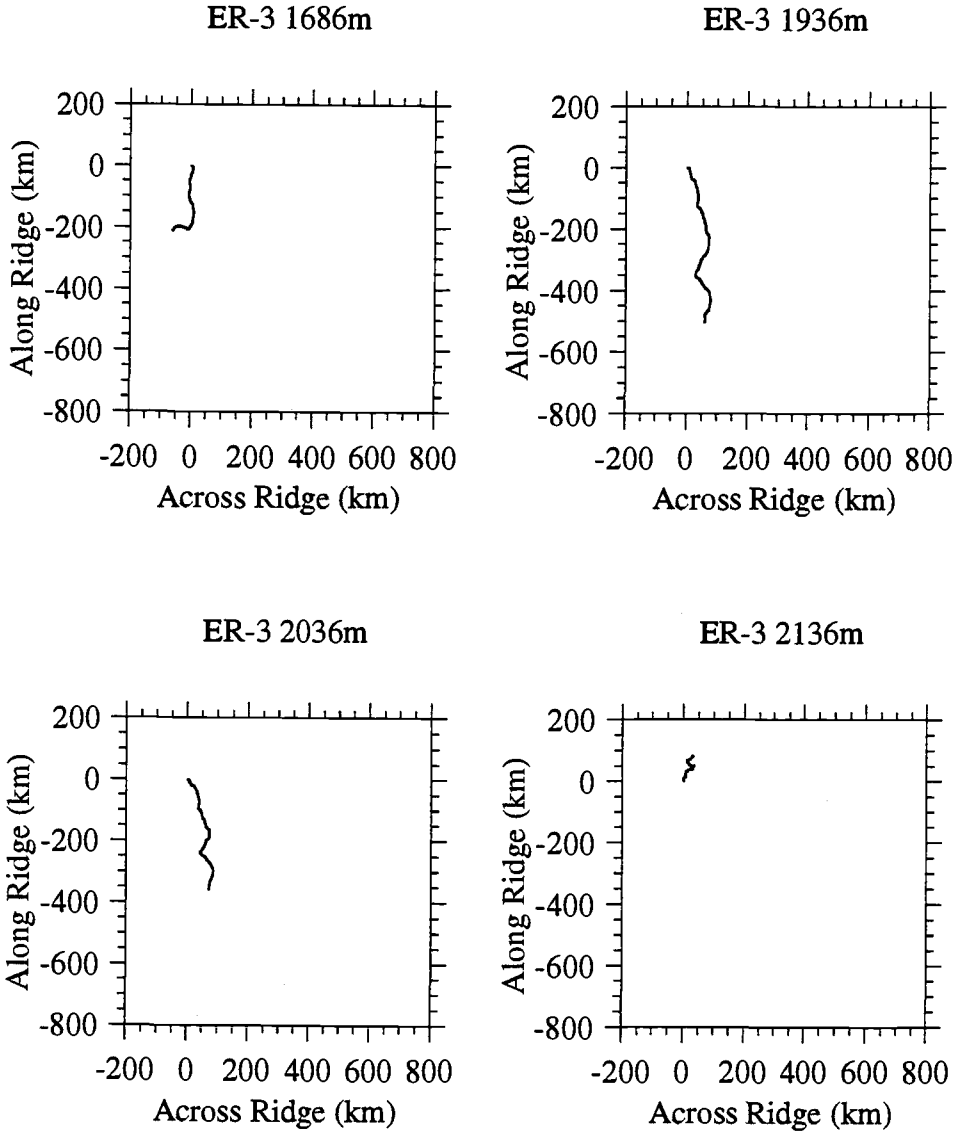

Figure II.38. Progressive vector diagrams (PVD) for horizontal currents (low-pass filtered) at mooring ER-3 plotted in the along-/across-ridge reference frame. Vectors depict flow velocity past the moored current meter in a horizontal plane. Axis lengths are consistent in Figures II.35 - II.39, and vectors begin at the origin (0,0) of each plot. Record lengths are equivalent to those shown in the corresponding time series (see Figures II.14 - II.34).

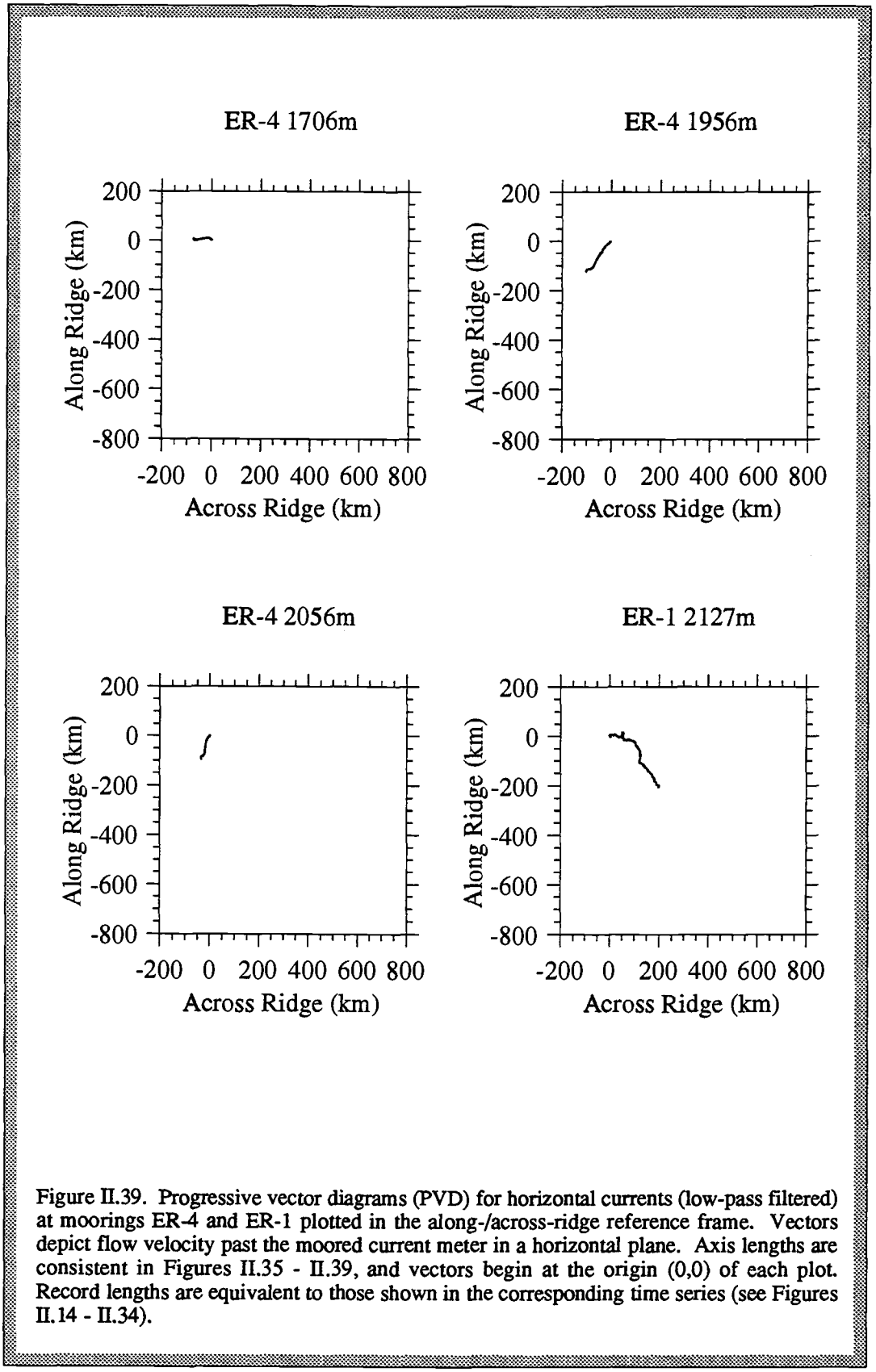

Figure II.39. Progressive vector diagrams (PVD) for horizontal currents (low-pass filtered) at moorings ER-4 and ER-1 plotted in the along-/across-ridge reference frame. Vectors depict flow velocity past the moored current meter in a horizontal plane. Axis lengths are consistent in Figures II.35 - II.39, and vectors begin at the origin (0,0) of each plot. Record lengths are equivalent to those shown in the corresponding time series (see Figures II.14 - II.34).

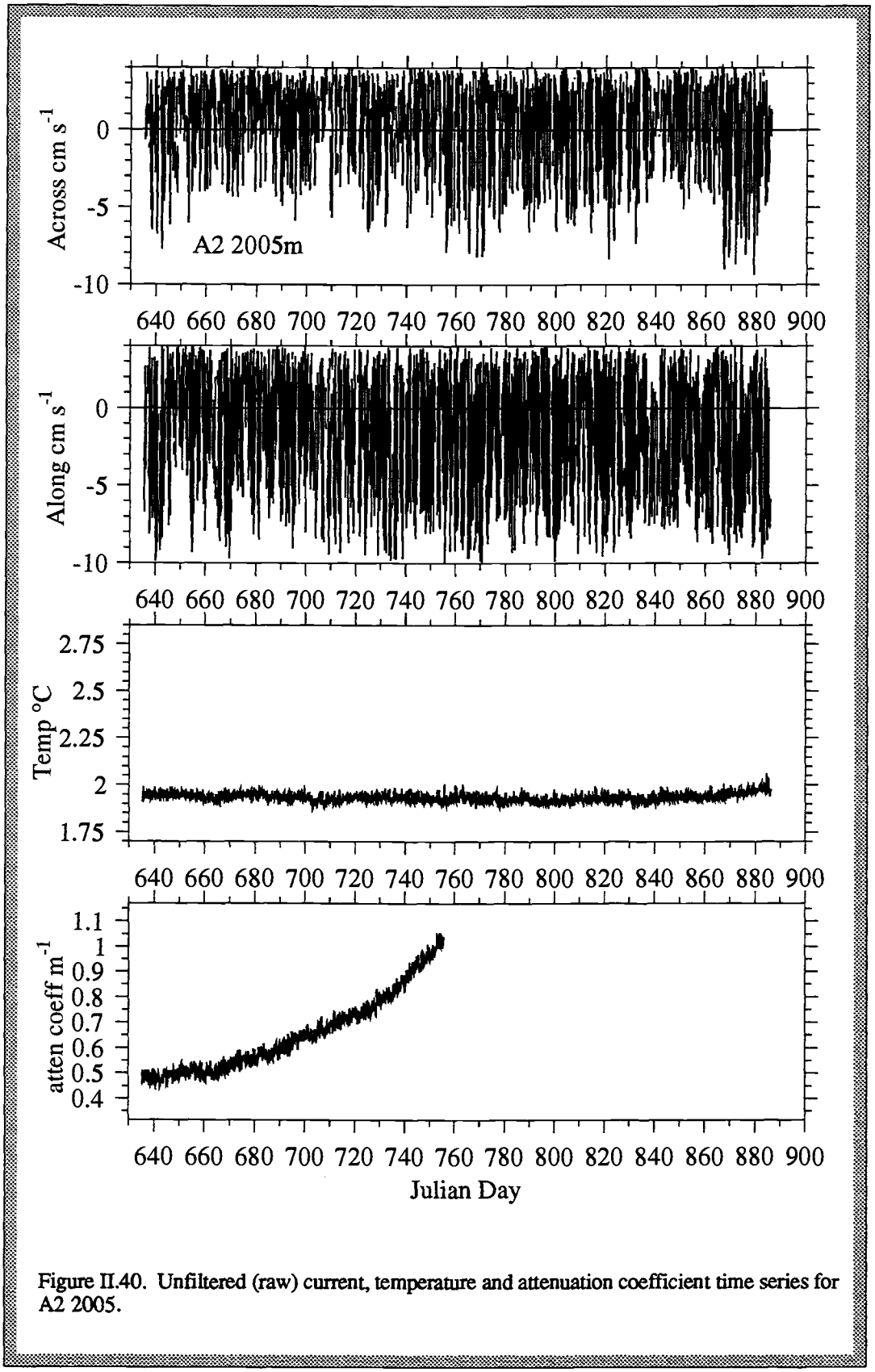

Figure II.40. Unfiltered (raw) current, temperature and attenuation coefficient time series for A2 2005.

Light attenuation and temperature as hydrothermal plume indicators.

In order to decipher complex, deep-sea plume behavior, attenuation coefficient and temperature will be treated as tracers of the hydrothermal plume. It is therefore essential to evaluate the validity of this assumption, as well as the relationship between these parameters. There are several lines of evidence to support the assertion that, within and beneath the non-buoyant plume, changes in temperature and attenuation coefficient are correlated and reflect hydrothermal influence.

Temperature - attenuation coefficient relationships

Data collected at plume-core sites A2 2005, ER-3 1936 and R2 1986 show significant linear correlation ($r^2 > 0.5$) between attenuation coefficient and temperature over the frequency range, ω where $0.1 < \omega < 1$cpd (Figure II.41). Coherence of the two time series is particularly strong and in-phase over higher, tidal/inertial frequencies (see section entitled *Cross-spectra*), however, the present regression analysis, based on band-passed time series, is useful because it visually establishes the fundamental association of these signals which share a common hydrothermal origin. The positive slopes of the regression lines in Figures II.41 and II.42 (except panels for A2 1656 and A3 2156) indicate that higher turbidity is associated with warmer water. Since the source of this deep-sea heat is hydrothermal, it can be inferred that the fine particles measured by the transmissometer are also of hydrothermal origin. Implications of the slope variations in Figures II.41 and II.42, which extend over all frequencies, are discussed at length in the section titled **Implications**. The main point here is that temperature and attenuation coefficient are significantly, positively, linearly correlated - and this supports the validity of using these two parameters as tracers of the neutrally buoyant hydrothermal plume.

Attenuation coefficient trends

The trend of decreasing light transmission over time, observed only in records obtained within or beneath the neutrally buoyant plume, suggests that the trend itself is produced by exposure to hydrothermal material. Above-plume transmissometers, in contrast to those influenced by the plume, reflect background, or non-hydrothermal, water column characteristics. At depths near 1700 m the attenuation coefficient is low (< 0.45 m^{-1}) and stable over time (Figures II.16, II.28 and II.32). This pattern persists for each of three consecutive deployments, A2 1656, ER-3 1686 and ER-4 1706.

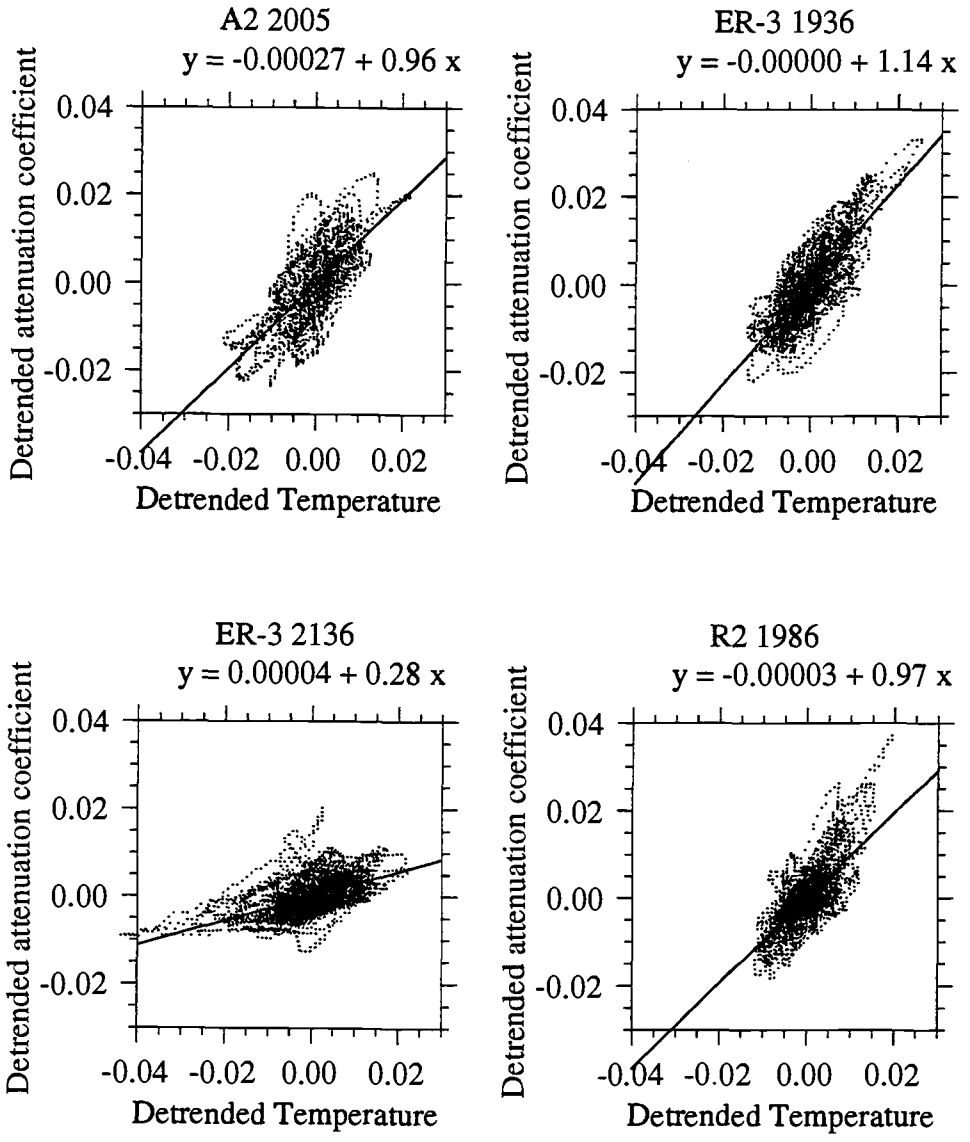

Figure II.41. Relationship between attenuation coefficient (m^{-1}) and temperature (°C) for transmissometer/current meter pairs moored at Endeavour Ridge. Equations for the linear regression appear above each plot. Correlation coefficients (r^2 values) for the regressions are as follows: A2 2005 0.509; ER-3 1936 0.615; ER-3 2136 0.297; and R2 1986 0.510. To make these data comparable in frequency structure, the temperature time series has been detrended by the same method used to detrend the attenuation coefficient time series. A filter which smoothes over a 10-day interval was used to generate the trend for each time series; the trend was in turn subtracted from the low-pass filtered data. Data plot as ellipses oriented along a family of positively sloping lines.

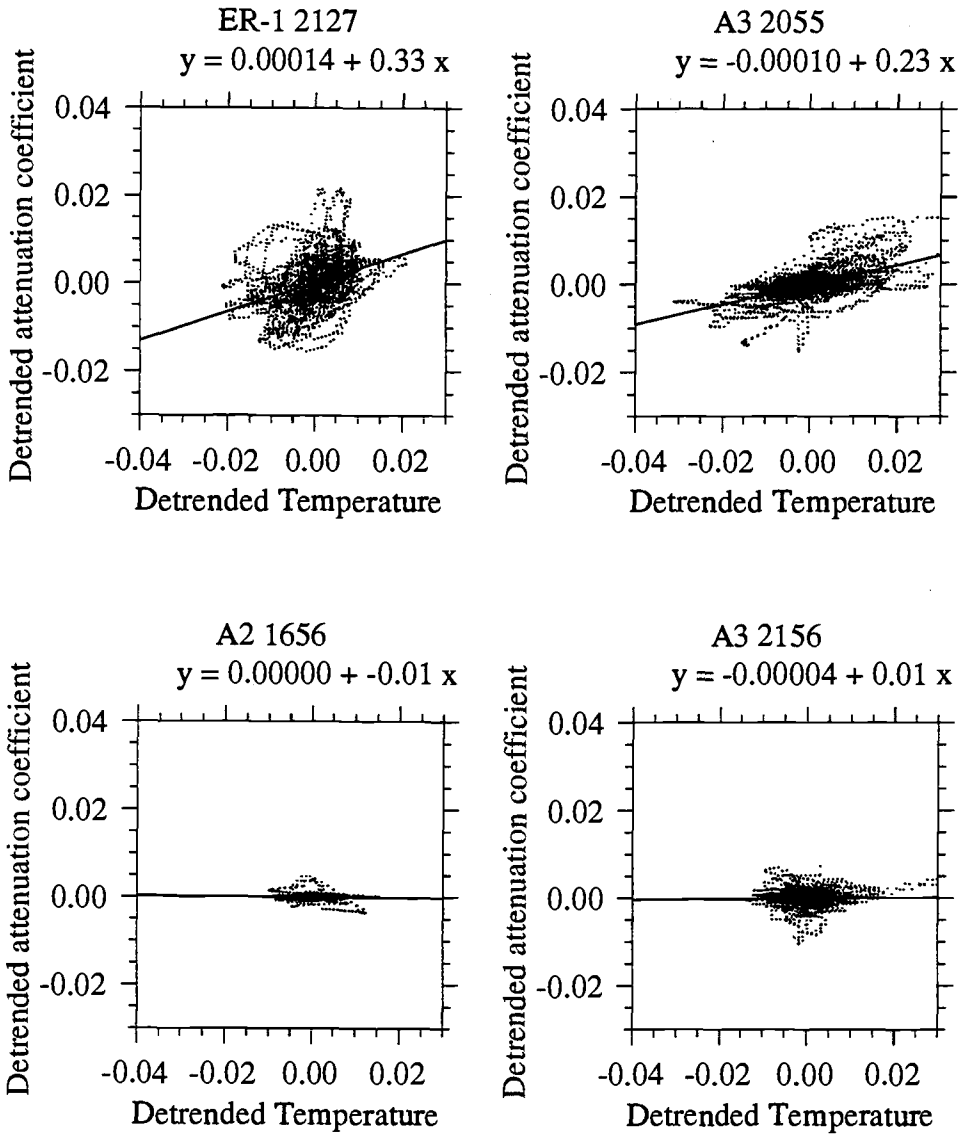

Figure II.42. Relationship between attenuation coefficient (m^{-1}) and temperature (°C) for transmissometer/current meter pairs moored at Endeavour Ridge. Equations for the linear regression appear above each plot. Correlation coefficients (r^2 values) for the regressions are as follows: ER-1 2127 0.157; A3 2055 0.338; A2 1656 0.0016; and A3 2156 0.00058. To make these data comparable in frequency structure, the temperature time series has been detrended by the same method used to detrend the attenuation coefficient time series. A filter which smoothes over a 10-day interval was used to generate the trend for each time series; the trend was in turn subtracted from the low-pass filtered data. Data plot as ellipses oriented along a family of positively sloping lines.

As examples of the contrast between above-plume and in-plume records, the maximum range of attenuation coefficient values over a single deployment is 0.03 m^{-1} during ER-3 1686, in contrast to the 1936 m record (Figure II.9) on the same mooring which has a maximum range of approximately 0.50 m^{-1}, most of which reflects the trend. The range is 0.01 m^{-1} for A2 1656 (Figure II.16) and > 0.50 m^{-1} for A2 2005 (Figure II.5). The low, above-plume values are comparable to the Endeavour Ridge regional light attenuation minimum of 0.40 m^{-1} that occurs between 1000 and 1500 m (Baker and Massoth, 1987). In towed transmissometer surveys, these authors found light attenuation anomalies of 0.02 - 0.11 m^{-1} in the neutrally buoyant plume at Endeavour Ridge. Our maximum, whole-deployment attenuation coefficient range near 1700 m corresponds to the low end of Baker and Massoth's anomaly range.

Transmissometers moored within and beneath the plume produced records with trends of decreasing light transmission (increasing attenuation coefficient) over time (Figures II.4 - II.10). In the case of the short, 2-month deployment, ER-4, a trend is absent (Figures II.11 - II.12). This supports a hypothesis that the trend reflects build-up of plume-derived material on the lenses. The material may be inorganic or organic in composition and may accumulate by deposition, growth or some combination of processes, but in any case, detectable clouding is a gradual, time-dependent process which apparently takes longer than two months. The rate at which clouding progresses may reflect the degree to which a particular instrument is exposed to material in the neutrally buoyant plume, an idea that will be explored later. Uncorrected attenuation coefficients span a range from approximately 0.25 to 1.15 m^{-1} over the 3 year record. The most pronounced trend for an individual deployment is +0.6 m^{-1} over ~ 125 days (ER-2, A2 2005) (Figure II.5).

A word of caution is warranted regarding comparison of records from different transmissometers. Offsets in baselines (or initial values in the case of trended records) may reflect instrumental bias rather than true variations in the concentration of suspended particles (see Figures II.14 - II.34). One obvious reason for concern is that steps were not taken to intercalibrate the transmissometers during pre- or post-deployment individual calibrations. In theory, data from properly calibrated transmissometers should be comparable, and I believe that, with respect to variability, ours are. However, due in part to the unexpected lens clouding, premature instrument

failure, and the small range of light transmission values, one cannot be certain that the absolute values of attenuation coefficient are accurate.

Moreover, some aspects of the data suggest that the record offsets are artificial. The plume-effected, trended, attenuation coefficient records have initial values in the range of 0.35 - 0.65 m^{-1}, however all but two are ≤ 0.4 m^{-1} (Figures II.4 - II.12) . The exceptions the slightly elevated (0.5 m^{-1}) initial value for ER-2 mooring A2 2005 m and distinctly elevated (0.6 m^{-1}) value for ER-3 1936 m. Because these two instruments were close to the vent field and within the plume core, it might be reasonable to expect sustained elevations in the fine particle load. Yet it would be a somewhat unlikely coincidence that the magnitude of this elevation would change so dramatically *between* deployments ER-2 (A2), ER-3, and ER-4 when there is no evidence for such jumps *within* each record. The offset between ER-3 and ER-4 plume-core instruments (Figures II.9 and II.11) exceeds 0.25 m^{-1}, and this is about five times the greatest offset noted within a single instrument record. Additional evidence that the elevated ER-3 1936 m record reflects an instrumental bias is that the transmissometer record obtained 200 meters below it does not have an elevated baseline (compare Figures II.9 and II.10). A persistently elevated fine-particle load within the plume might be expected to extend to the deeper level via particle aggregation and settling, yet no such intensification is evident.

Another reason to question the validity of the elevated attenuation coefficient at ER-3 1936 is that it is inconsistent with evidence presented in the **Implications** section that the rate of lens clouding is related to the concentration of fine particles. For instance, the overall shape of the trend is steeper for instruments in the plume core (A2 2005 and ER-3 1936, Figures II.5 and II.9), and more gradual for a deeper transmissometer (ER-3 2136, Figure II.10) and for instruments moored farther from the vent field (A3 2055 & 2156 and R2 1986, Figures II.6, II.7 and II.8). If the ambient particle concentration was highest at ER-3 1936 (as predicted from the high initial attenuation coefficient), the shape of the trend initially would be steeper (i.e. the first derivative of the curve describing the trend would be higher), and the instrument should have clouded and failed rapidly. This is not what was observed, for A2 2005 bears the distinction of having the steepest initial trend, and most rapid failure, despite the fact that the initial attenuation coefficient is significantly less than at ER-3 1936.

Later, more subtle implications of the shape of the attenuation coefficient trends are discussed, but here I reiterate that the presence of the trend alone in records from plume-influenced depths supports the use of attenuation coefficient as a hydrothermal plume indicator.

Attenuation coefficient variance

Fluctuations in the low-pass filtered, detrended attenuation coefficient time series (shown in the lower panels of Figures II.4 - II.12) increase in amplitude closer to the vent-field source and closer to the depth of the plume core (Figure II.43). This pattern of variance is further evidence that the light attenuation record reflects hydrothermal influence. Variance, defined as the square of the standard deviation of each time series, provides a measure of the spread of values around the mean. (The means are zero for detrended records.) The higher the variance, the more scattered are values of suspended particle concentration. Variance is lower in the ER-1 record than for the subsequent plume-core records. This first mooring was farther from the vent field than later, central moorings (A2, ER-3 and ER-4), and the single transmissometer on it, only 80 meters above bottom, was well beneath the plume core. The factor of six difference in the variance between records 200 m apart during the ER-3 deployment, demonstrates the association between increased variance and proximity to the plume core. The highest variances, recorded at plume-core level during the ER-4 experiment, may reflect ordinary plume variability enhanced by particle flux variations related to higher upper water column productivity during the summer months (see the section called *Seasonality*). The decrease in variance with distance from the vent field is shown in Figure II.43 by comparison of A2 2005, A3 2055 and R2 1986.

Higher variability in the fine-particle field close to the vent field and within the plume core reflects inhomogeneities in suspended particle concentrations where hydrothermal plume is strongest, in contrast to more uniform particle distributions farther afield where hydrothermal signals are weaker. This pattern supports the assertion that the attenuation coefficient, and even more specifically the variability of this parameter, are water column hydrothermal indicators.

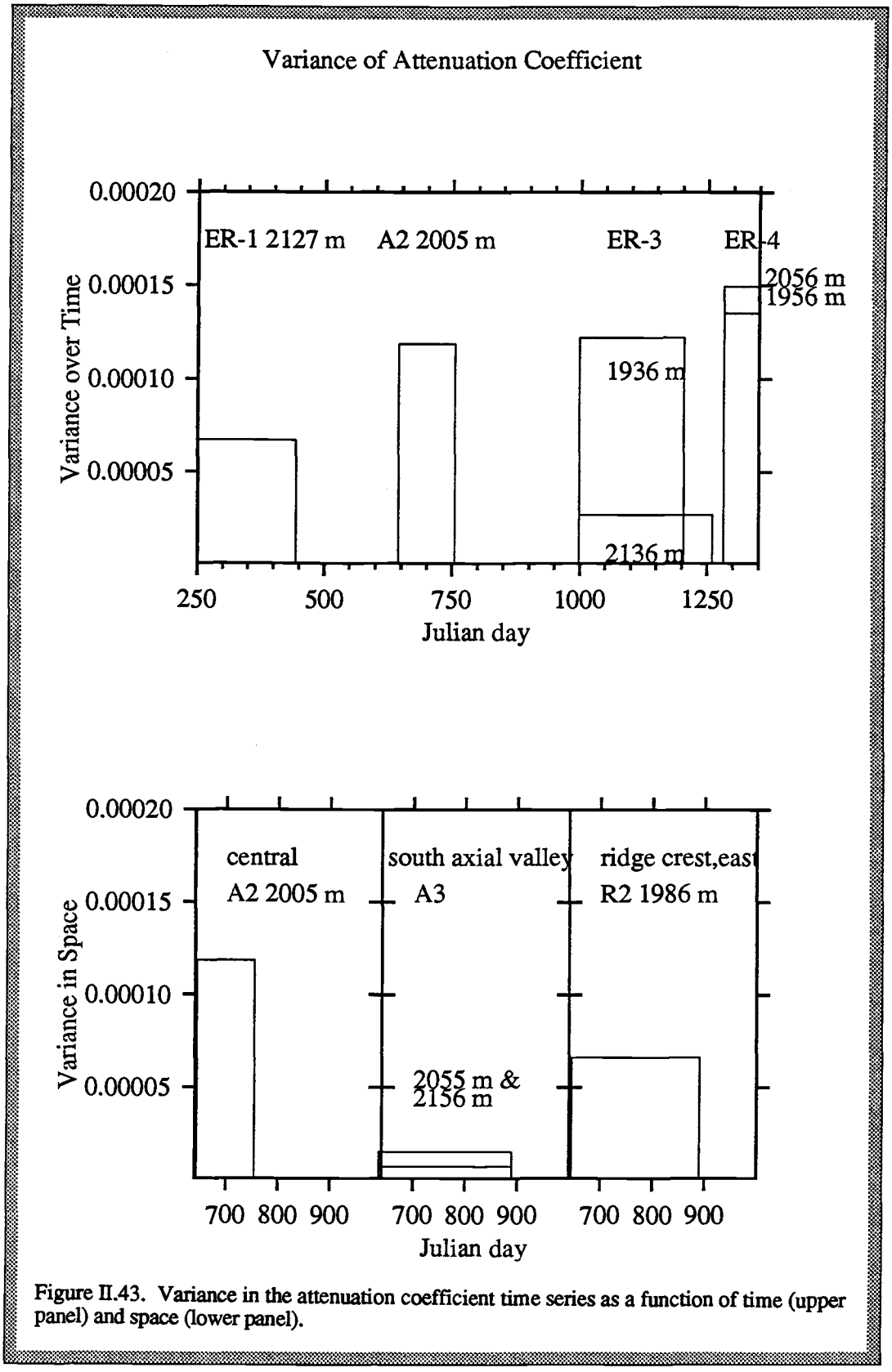

Figure II.43. Variance in the attenuation coefficient time series as a function of time (upper panel) and space (lower panel).

Toward a conceptual plume model

With the goal of developing a conceptual model of hydrothermal plume behaviour, several hypotheses which might explain the observed variance pattern, as well as account for other experimental results, are depicted schematically in Figure II.44. The introduction of these ideas here is offered as a framework in which to think about the observations to come. Following presentation of spectral analyses, and discussion of temporal and spatial variability, I will return to these hypotheses and evaluate their plausibility.

Local inhomogeneities in a hydrothermal plume tracer may be due to one or more of the following four causes:

1. Advection, either horizontal or vertical
2. Changes in vent output, either in quantity or thermal/chemical properties
3. Mixing of two or more hydrothermal fluids, distinguished by different properties, or originating at physically separate sites
4. Water column processes (physical, chemical, biological) which change the concentration/flux of the tracer

The following examples illustrate how these processes could produce variations in the neutrally buoyant plume recorded by a moored sensor:

1. First, consider a simplified neutrally buoyant plume to be three-dimensional streamer which originates above the vent field, assumes a more-or-less channeled form, and extends laterally away, spreading in three dimensions with distance from the source (Figure II.44a). The boundaries of the plume, as defined by thermal and light attenuation anomalies, are well-defined above the vent field, but blur, due to mixing and diffusion, farther afield. The gradients of temperature and particle concentration within the plume itself may be constant or variable. Now superimpose advection on this image of a relatively well-behaved feature. Changes in horizontal current velocity, especially rotary motions, would bring the plume into and out of contact with a fixed sensor, producing corresponding variability in the resultant time series. In the near field, where the plume boundaries, and possibly internal gradients, are strongest, variance in the tracer signal would be highest.

Other ways advection could produce variability include: incomplete mixing in the isopycnal layer along which the plume spreads; formation of detached, particle-rich

eddies by turbulent entrainment during buoyant plume rise; and vertical transport caused by internal waves.

2. Perhaps emission of hydrothermal fluids from the vent field is not constant. Episodic pulses of hydrothermal fluid into the water column would produce patchiness in the neutrally buoyant plume (Figure II.44b). If the emitted volume of hydrothermal fluid is, in fact, stable, the temperature or the chemistry of the effluent may be temporally variable, producing a similar pattern.

3. There may exist more than one vent field in the vicinity of the mooring(s). Variable water-column mixing of chemically, thermally distinct, or even similar, plumes could generate inhomogeneities (Figure II.44d). A variation on this theme involves combination of different types of vent output: one from high-temperature black smokers that is particle-laden and rises buoyantly hundreds of meters, the other from seafloor fissures that produce lower temperature, less turbid fluids, and more diffuse flow (Figure II.44c).

4. Finally, dilution with ambient sea water would cause changes in plume temperature and particle concentration. Furthermore, various particle transformation processes can alter the total particle concentration as well as the partitioning of hydrothermal material among dissolved, finely particulate (suspended), and coarsely particulate (settling) fractions (Figure II.44e). These transformations include chemical precipitation of dissolved components, physical aggregation of small particles into larger ones, scavenging of dissolved components onto particles, particle removal via settling or biological ingestion, particle dissolution/disaggregation, and biological repackaging of fine material into fecal pellets. The changing abundance of fine particles (monitored optically by the transmissometer) and large particles (collected in sediment traps) depends on the rates of these simultaneous processes, which in turn depend on chemical kinetics, physical properties of the material, and water-column biological activity. Particle transformation effects are potentially the most complex of the four variance-producing processes.

Figure II.44. Schematic representation of processes which influence the deep-sea distribution of particles and heat in a neutrally buoyant hydrothermal plume. Though illustrated in separate panels, these processes occur simultaneously.
a. Advection, the sum of rotary tidal and inertial motions, superimposed on the mean along and across-ridge currents, guides the plume past the moored sensors. Vertical current shear is depicted by filled arrows of varying length.
b. Temporal changes in the output volume may result in a patchy water-column distribution of particles and heat that advect past the mooring. Compositional changes, which may include variability in both effluent temperature and chemistry are also indicated by contrasting patterns in plume shading.
c. Mixing to varying degrees of hydrothermal effluent from high-temperature, black smokers and more diffuse, relatively particle-depleted sources may determine the ratio of suspended particles to heat at a particular moored sensor.
d. Mixing of effluent plumes originating at two separate vent fields makes it difficult to determine the role of lateral advection in transporting hydrothermal material. Note that the mooring is in a position which is influenced by both plumes. The two plumes may be compositionally similar or distinct.
e. Particle transformation processes regulate both the fine-particle advected flux and the settling particle flux. Processes illustrated include settling of large particles close to the vent field, dilution of effluent with ambient seawater, accelerated removal of hydrothermal material by settling, "sticky", organic particles from the upper water-column, aggregation of fine material, bacterial transformations (e.g. Mn scavenging by bacterial capsules or bacterially-mediated dissolution), scavenging of dissolved components (e.g. adsorption of P and V by iron oxyhydroxides), zooplankton feeding and fecal pellet production.

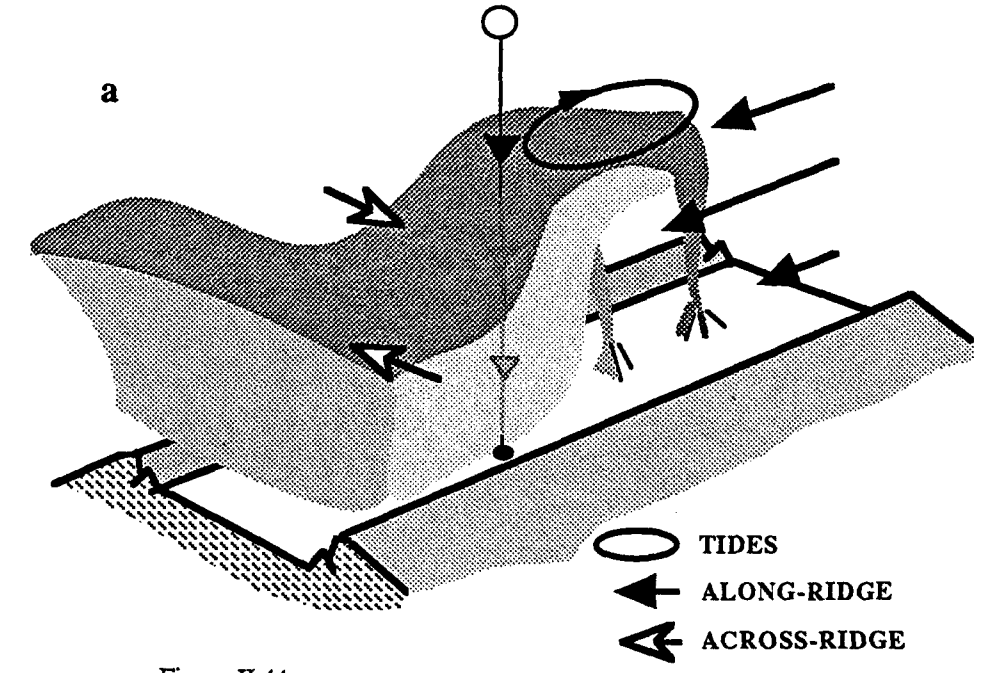

Figure II.44a.

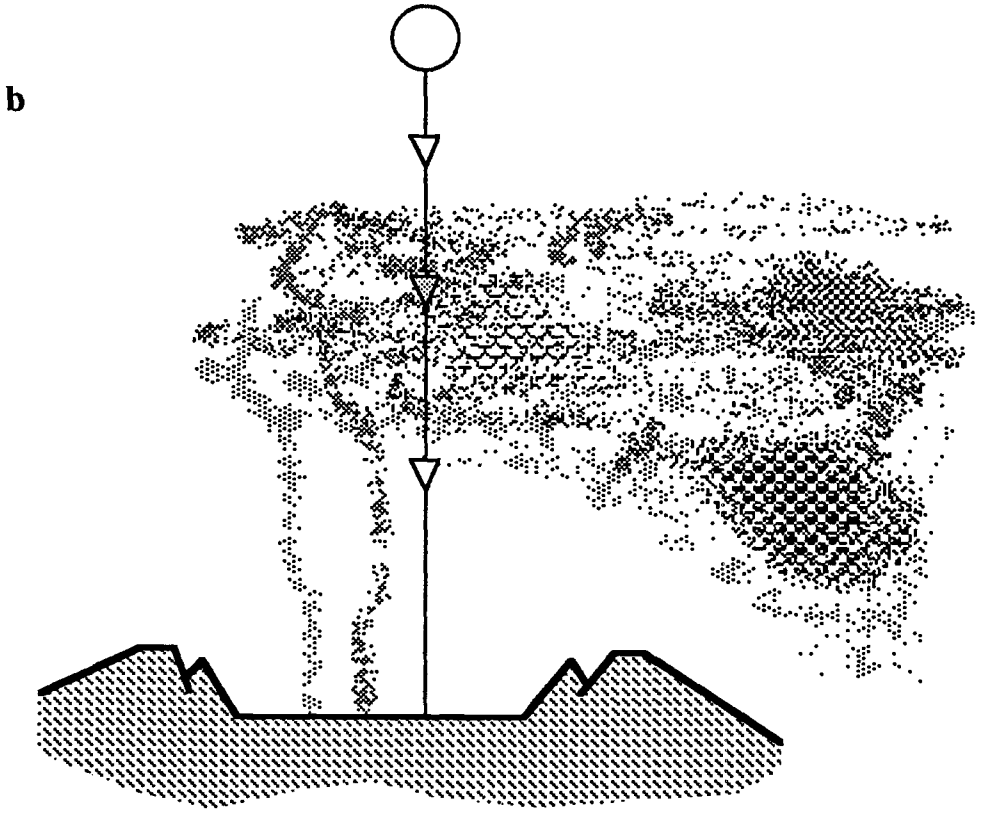

Figure II.44b.

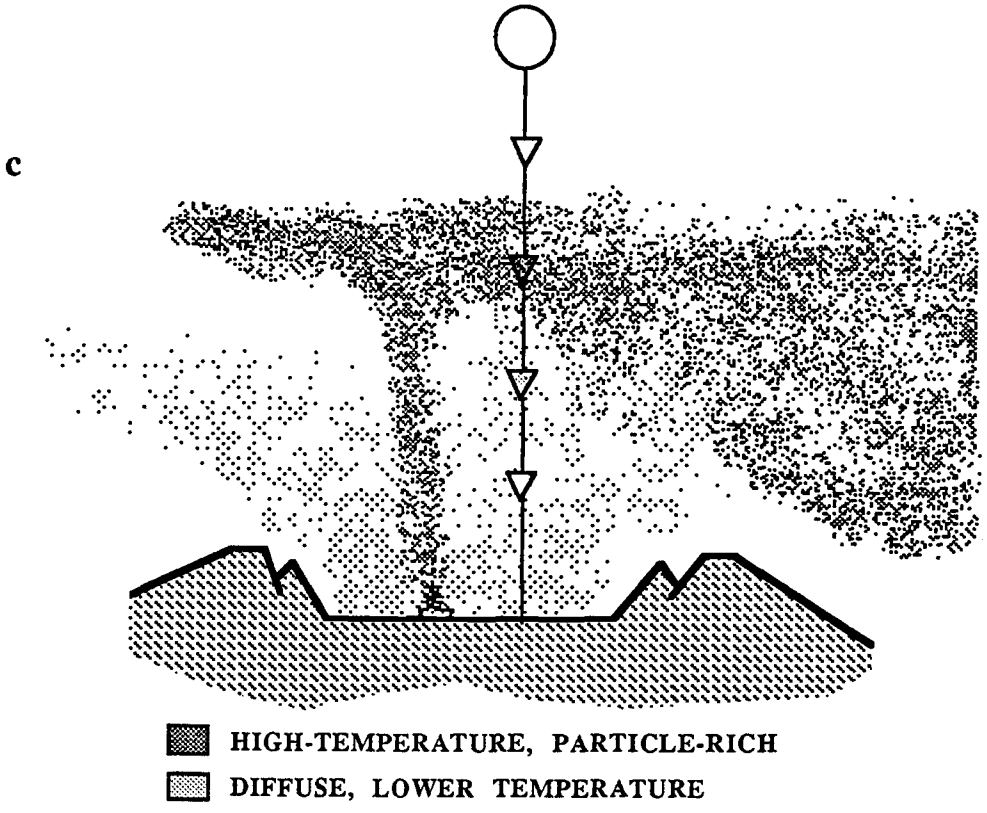

Figure II.44c.

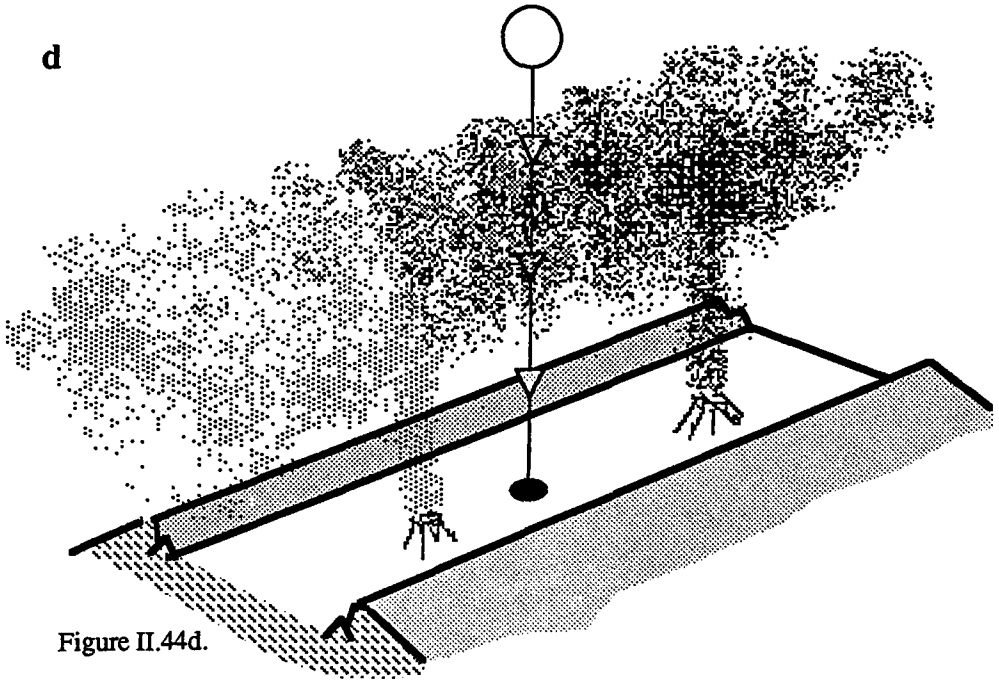

Figure II.44d.

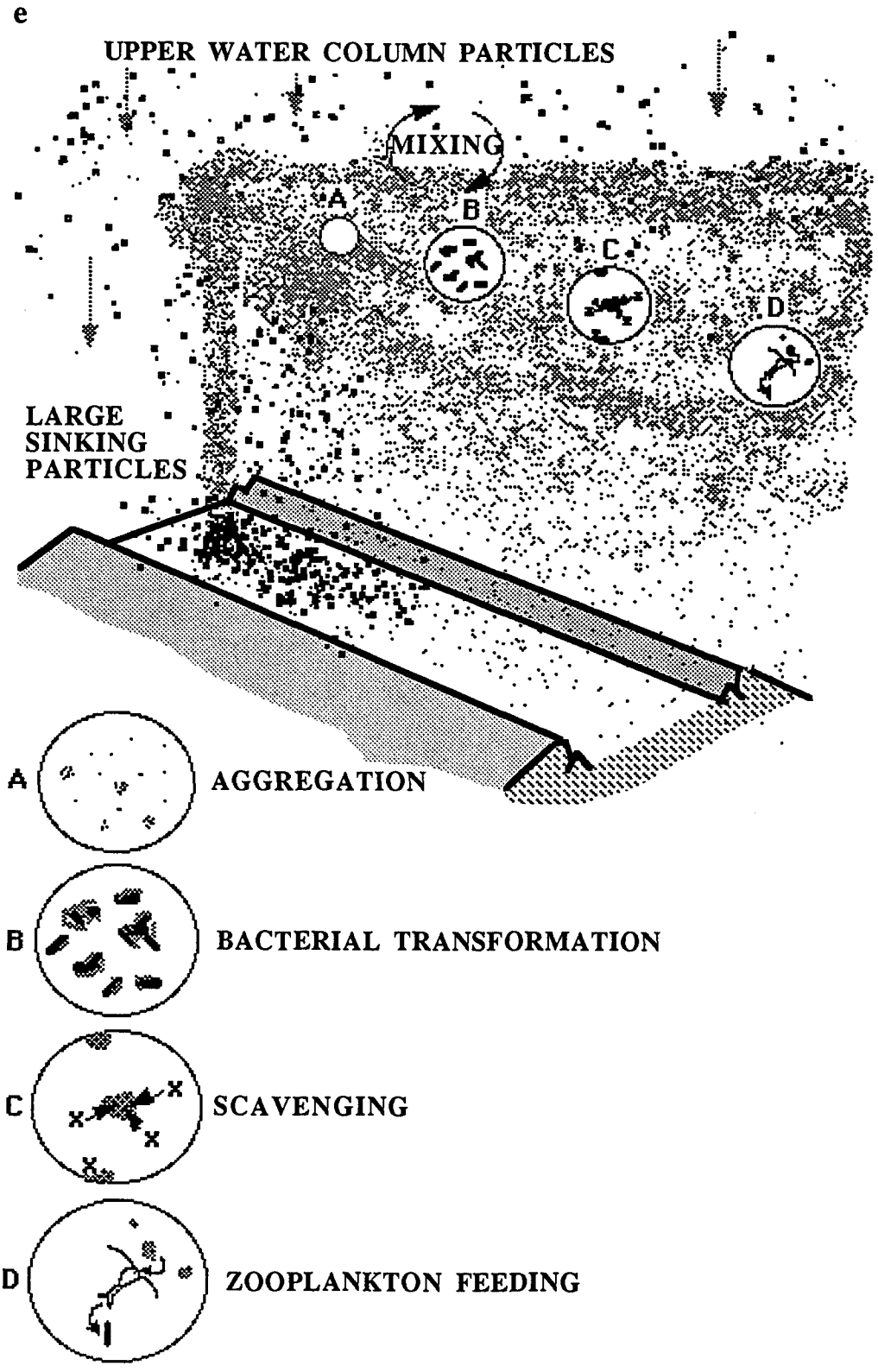

Figure II.44e.

Spectral analysis - evaluating the role of flow

In a previous section three lines of evidence supported the assertion that attenuation coefficient and temperature are indicators of the hydrothermal plume. In this section the role of currents in dispersing hydrothermal effluent is examined. If flow is an important factor in guiding the plume, one would expect a well-defined relationship between current velocity and attenuation coefficient or temperature. Scatter plots and linear regressions similar to those used earlier to evaluate the relationship between attenuation coefficient and temperature are inadequate to evaluate flow/plume tracer relationships, principally because values of the two orthogonal components of current velocity and either temperature or attenuation coefficient are difficult to depict on a two-dimensional graph. Because detrending of the temperature time series is not necessary, I use these records to test the relationship between current velocity and hydrothermal plume distribution. Gray-scale PVDs suggest that there is a predictable pattern between flow and temperature: flow in the vent-to-mooring direction is warmer, as expected (see, for example, Figures II.45 and II.46). A more thorough, statistical, approach is cross-spectral analysis which shows the linear correlation between two time series over giver frequency bands. Prior to a more complete discussion of cross-spectral analyses, I introduce the rationale for calculating more fundamental energy density spectra.

Rationale for evaluating parameters in the frequency domain

Spectral analysis of flow, temperature, and light attenuation data aids in comparison of the physical conditions during each instrument deployment. The spectra (Fourier transform of the autocovariance function) show how variance is distributed with frequency. With respect to flow, I generated spectra of across and along-ridge flow, as well as rotary spectra which show variance distribution for clockwise (CW) and counterclockwise (CCW) rotational flow. For temperature and light attenuation, I report coherency (with each other and with flow), as well as the usual spectral density function. The intent of this analysis is to present evidence that bears on the following hypotheses:

1. Plume-guiding horizontal flow is neither steady nor uniform; temporal and spatial current variability is reflected in the distribution of hydrothermal particles and heat within kilometers of the vent field.

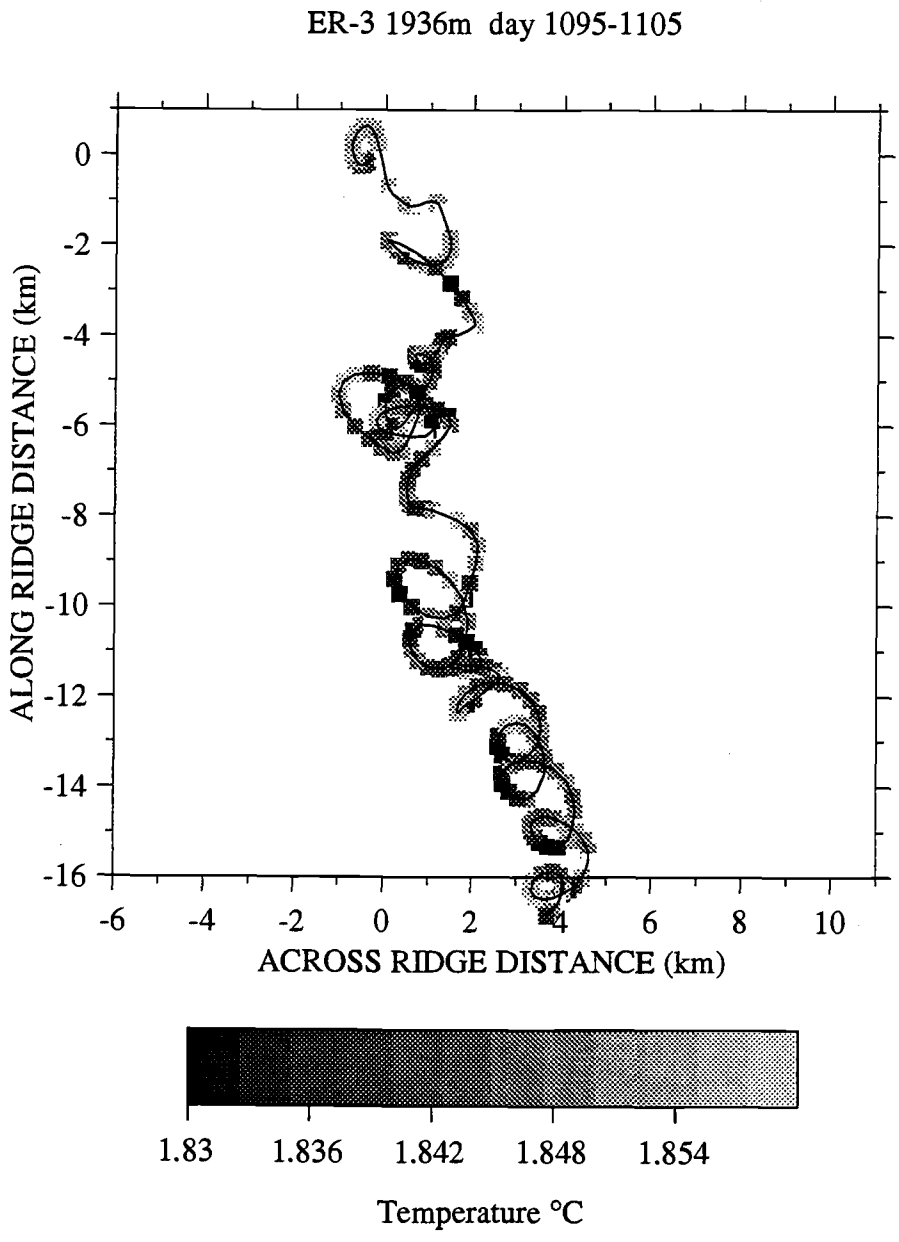

Figure II.45. Grey-scale PVD constructed from unfiltered current meter and temperature data from 1 to 10 January 1987 during the ER-3 1936 deployment. Vector begins at the origin. Squares represent hourly measurements, and darker shades indicate relatively cooler temperatures. Clockwise loops in the PVD reflect the dominant inertial oscillations. The warming and cooling pattern reflects advective transport of hydrothermal emissions alternately toward and away from the mooring which was located approximately 0.5 km northeast of the vent field (see Figure II.2).

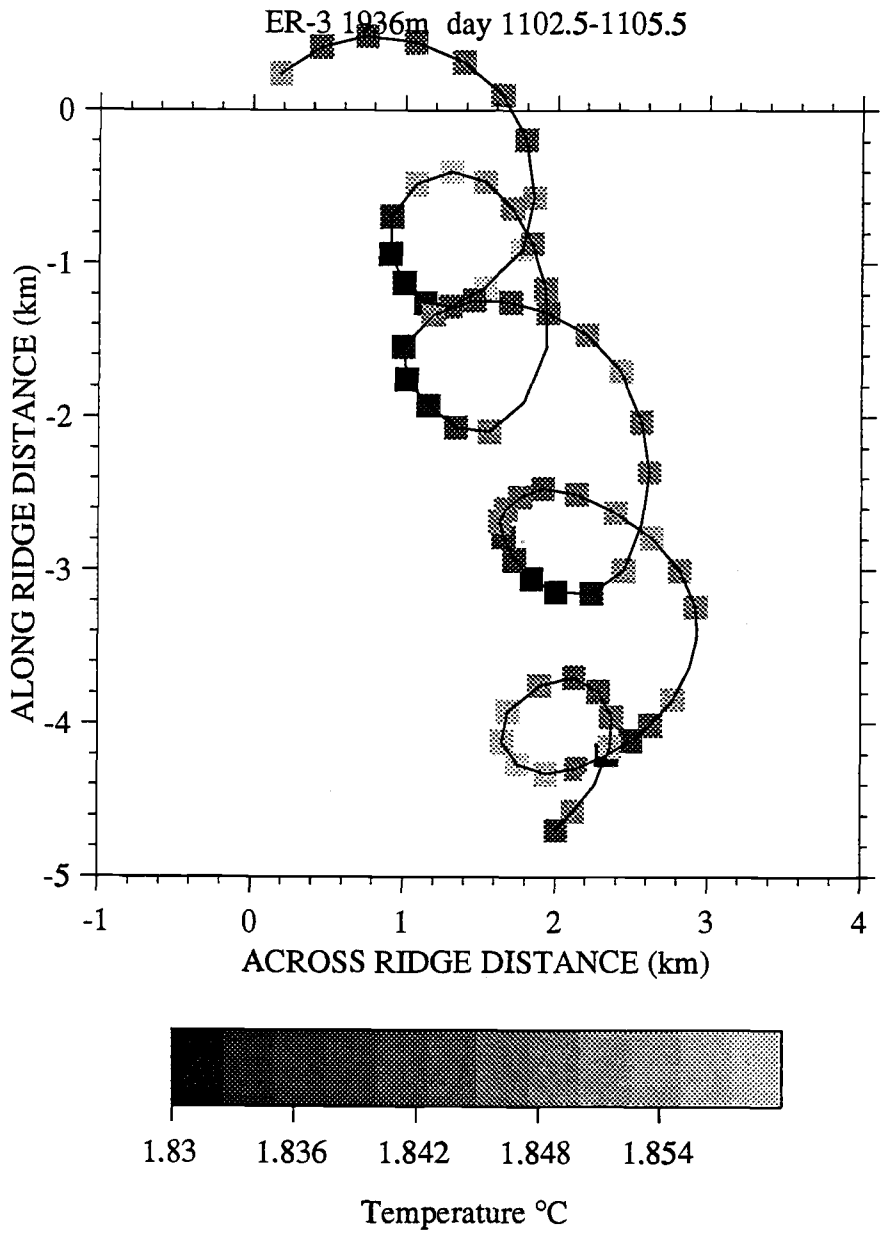

Figure II.46. Grey-scale PVD constructed from unfiltered current meter and temperature data from 7 to 10 January 1987 during the ER-3 1936 deployment. Vector begins at the origin. Squares represent hourly measurements, and darker shades indicate relatively cooler temperatures. Clockwise loops in the PVD reflect the dominant inertial oscillations. The warming and cooling pattern reflects advective transport of hydrothermal emissions alternately toward and away from the mooring which was located approximately 0.5 km northeast of the vent field (see Figure II.2).

2. Variability in flow, and consequently the flux of heat and particles, is concentrated in specific frequency bands that correspond to identifiable forcing processes.

3. The particle population that dominates the light attenuation signal is of hydrothermal origin. Although temperature is a conservative tracer and particle concentration is non-conservative, their distributions are linked in the near-field study area due to the strong influence of advective transport.

4. The influence of hydrothermal emissions in the water column decreases with horizontal distance from the vent field source and vertically with distance from the plume core.

5. Not all features of the temperature and attenuation coefficient spectra can be explained by horizontal advection, indicating that additional processes (e.g. variations in vent output, particle transformations and removal, biological uptake) may be important factors in regulating the oceanic fluxes of hydrothermal material.

The spectra enhance our ability to compare flow and temperature records over a range of depths, a range of distances from the vent field, and over time. This comparison is essential to testing for uniformity, or lack thereof, in the flow field. Spectra, because they provide information in the frequency domain, can be used to compare time series even in cases where there is considerable uncertainty in the true values of a given parameter due to instrumental effects. With the exception of the flow/temperature and flow/attenuation coefficient cross spectra, emphasis in the spectral analysis is on frequencies lower than the diurnal tidal oscillation (one cycle per day). The reason for this focus is that pronounced semi-diurnal, diurnal and inertial peaks are ubiquitous features of the spectra. These peaks are the result of well-understood physical processes, and while some discussion of the relative energy at these frequencies in space and over time is useful, an earlier paper by Thomson et al. (1990) provides an in-depth study of high-frequency energy in the near-inertial band (0.0621 cycles per hour, locally).

Results of the spectral analyses, along with other evidence, will be used later to constrain temporal and spatial variability of hydrothermal particle flux. As a foundation for these specific discussions, the general features of the flow component, rotary, and temperature spectra are reported in the following sections.

General features of the flow and rotary spectra

For purposes of this discussion, I partition the spectra into three frequency ranges:

1) 0 - 0.8 cycles per day (cpd) which includes frequencies lower than the diurnal tide (referred to here as sub-tidal);

2) 0.8 - 2.1 cpd which includes the principal diurnal and semi-diurnal tidal frequencies as well as the inertial band (which I will call tidal-range); and

3) 2.1-12 cpd which includes frequencies higher than the semi-diurnal tidal oscillation and is bounded at the upper end by the Nyquist frequency, the highest resolvable frequency (12 cpd for our hourly measurements). The third (highest) frequency range will not be discussed except to say that energy in these frequency bands reflects internal wave motions, and that energy in this range decreases exponentially with increasing frequency.

Interpretation of the spectra of flow data must take into account the quality of the raw time series data. To varying degrees, the raw data are incomplete. When flow velocity drops below the current meter threshold speed, about 1.7 cm/s, missing values are logged in the time series. Table II.3 shows the fraction of missing data points in each current meter record relative to the record length in percentage ranges. Since evaluation of the spectral density function requires that one begin with measurements at unit intervals of time, a cubic spline interpolation was used to fill in the gaps in the data. An alternative method is to replace missing values with some chosen value, for instance, midway between the rotor stall speed and zero (approximately 0.8 cm/s). One record, ER-1 2127 m, was treated in this way. Little difference is observed in the resultant spectra based on either approach. Still, no method of filling in gappy data is completely satisfactory. Therefore, I place more confidence in spectra obtained from more complete data. The problem of gappy data is not a consideration in the interpretation of temperature or attenuation coefficient spectra because these time series are discrete and continuous.

Table II.3. Missing data values in raw flow time series

% missing values	records
< 10	ER-1 2127; A3 1955; R2 1985
10-20	A2 1655,1905; R2 1986; ER-3 1686,1936,2036; ER-4 1956
20-30	A2 1656,2005
30-40	A3 2055; T3 1955; ER-4 1706
40-50	T3 2055
>50*	A3 2155,2156; ER-3 2136; ER-4 1956

* A2 2105, 2106 functioned for only one month (approx. 10% of the deployment) prior to failure, and so are excluded from this analysis.

Spectra for the four most complete plume-core current meter records, and the beneath-plume ER-1 2127 record, are shown in Figures II.47 - II.51. The peaks corresponding to the diurnal, inertial, and semi-diurnal frequencies are pronounced and statistically significant at the 95% confidence level in both (across and along-ridge) flow spectra and in the clockwise rotary spectra. The inertial peak, however, disappears in the counterclockwise rotary spectra. This is expected since, due to the Coriolis effect, flow turns to the right (rotates clockwise) in the Northern hemisphere, and the inertial oscillation reflects this motion. In the tidal-range, the semi-diurnal peak is highest in most of the rotary spectra. An exception to this occurs in ER-3 and ER-4 where maximum energy in the clockwise spectra is in the inertial peak. There is typically more energy in the tidal bands along-ridge than across-ridge, and higher energy in the clockwise rotations than in the counterclockwise direction. Over the tidal frequencies the spectral energy density maxima are in most cases < 100 $(cm/s)^2/cpd$. These values are comparable to those reported by Cannon et al.(1991).

In the sub-tidal range, energy typically increases with decreasing frequency both in the Cartesian and rotary spectra. In most cases the low-frequency energy maximum is less than 10 $(cm/s)^2/cpd$ which is roughly an order of magnitude less than the tidal range maximum. The features of the low-frequency spectra vary considerably.

Figure II.47. Energy density spectra for along-ridge and across-ridge currents, temperature, and clockwise (CW) and counterclockwise (CCW) rotational flow at ER-1 2127 m. The log-log axes measure frequency on the abscissa and spectral energy density on the ordinate. Confidence limits of 95% are shown for 28 degrees of freedom; bandwidth is 0.04651.

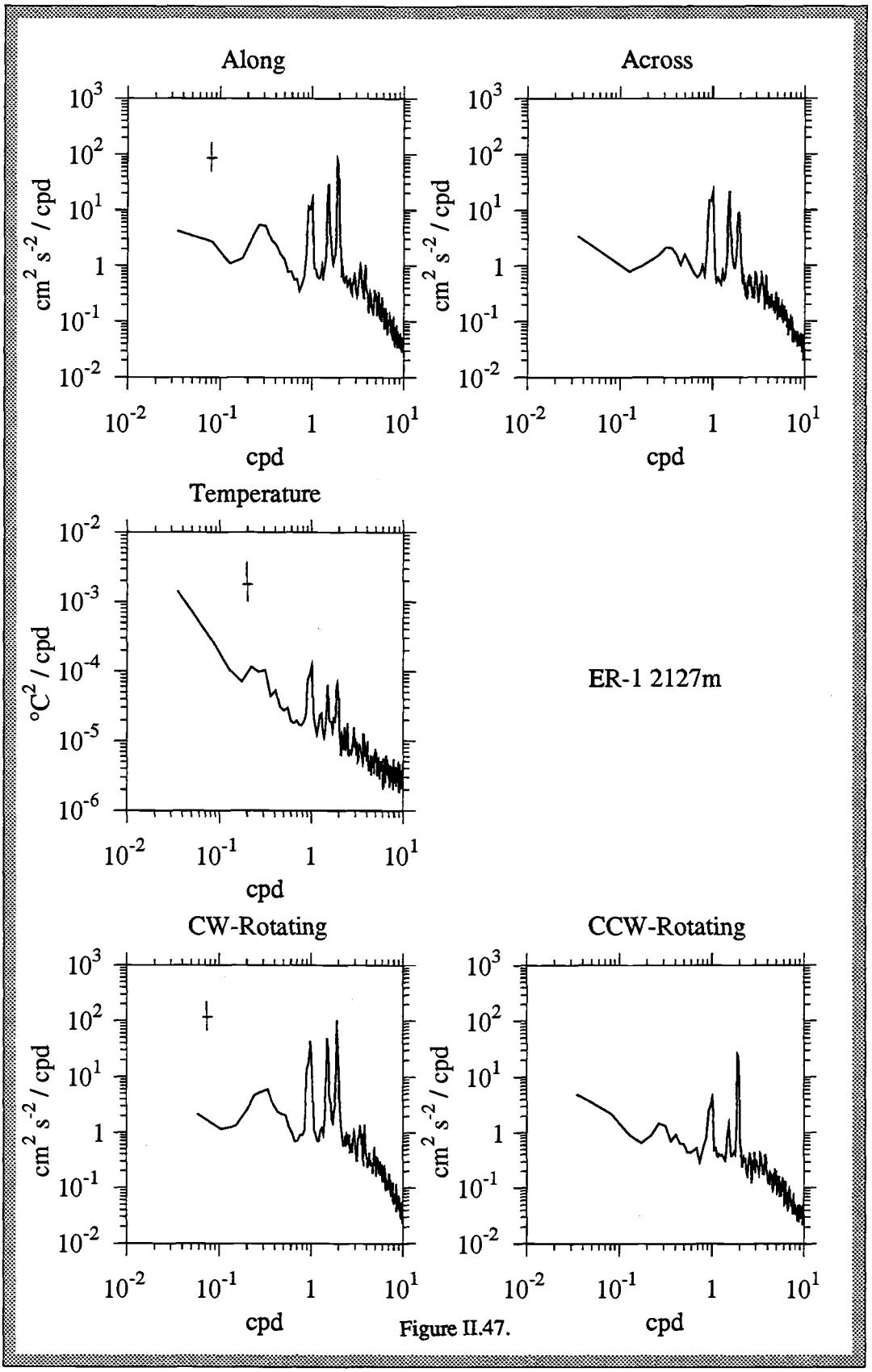
Along
Across
Temperature
ER-1 2127m
CW-Rotating
CCW-Rotating
cm² s⁻² / cpd
°C² / cpd
cpd
10³
10²
10¹
1
10⁻¹
10⁻²
10⁻³
10⁻⁴
10⁻⁵
10⁻⁶

Figure II.47.

Figure II.48. Energy density spectra for along-ridge and across-ridge currents, temperature, and clockwise (CW) and counterclockwise (CCW) rotational flow at A2 1905 m. The log-log axes measure frequency on the abscissa and spectral energy density on the ordinate. Confidence limits of 95% are shown for 24 degrees of freedom; bandwidth is 0.04651.

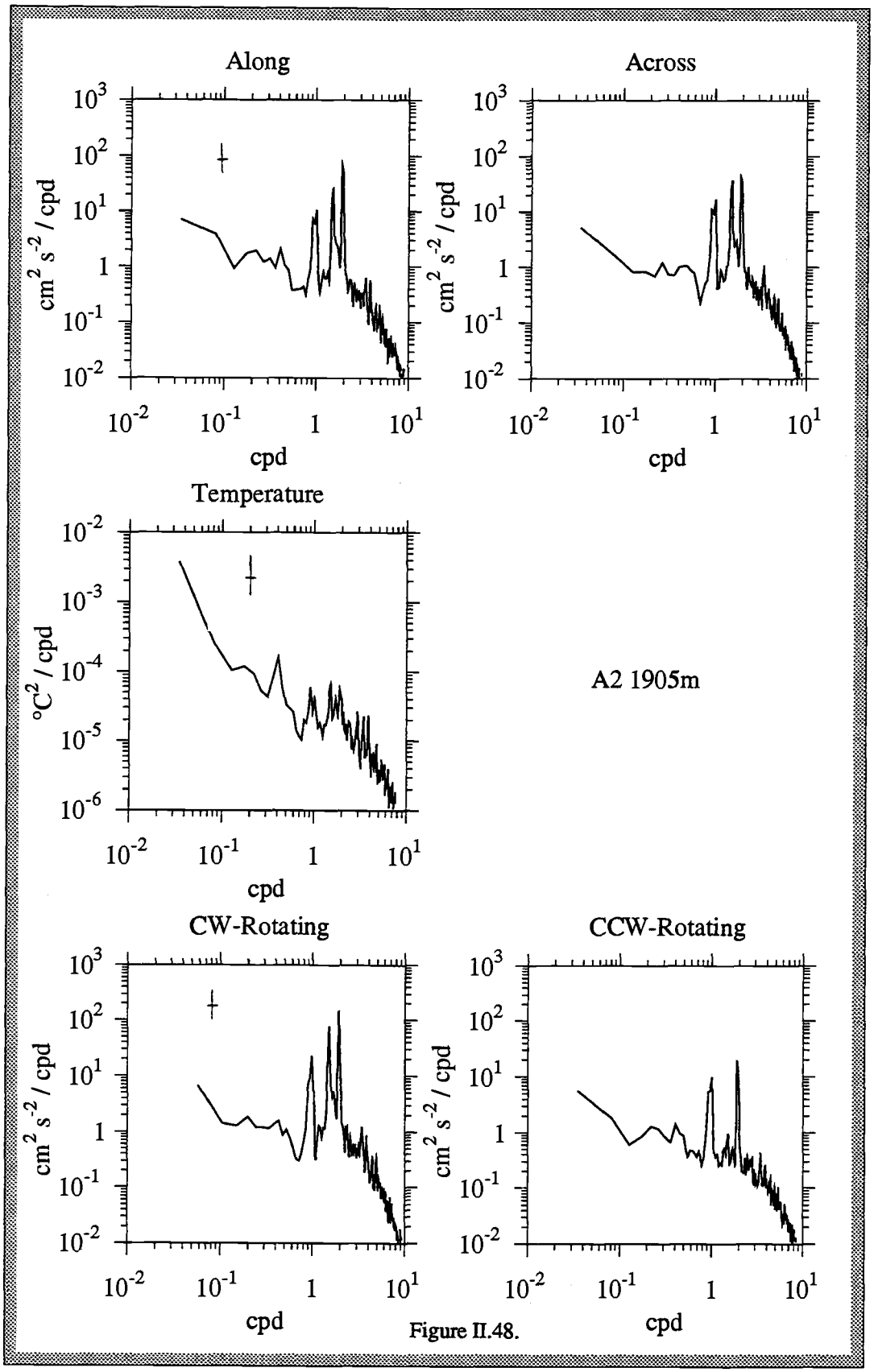
Along
Across
Temperature
CW-Rotating
CCW-Rotating
A2 1905m
cm² s⁻² / cpd
°C² / cpd
cpd
10³
10²
10¹
1
10⁻¹
10⁻²
10⁻³
10⁻⁴
10⁻⁵
10⁻⁶

Figure II.48.

Figure II.49. Energy density spectra for along-ridge and across-ridge currents, temperature, and clockwise (CW) and counterclockwise (CCW) rotational flow at A3 1955 m. The log-log axes measure frequency on the abscissa and spectral energy density on the ordinate. Confidence limits of 95% are shown for 24 degrees of freedom; bandwidth is 0.04651.

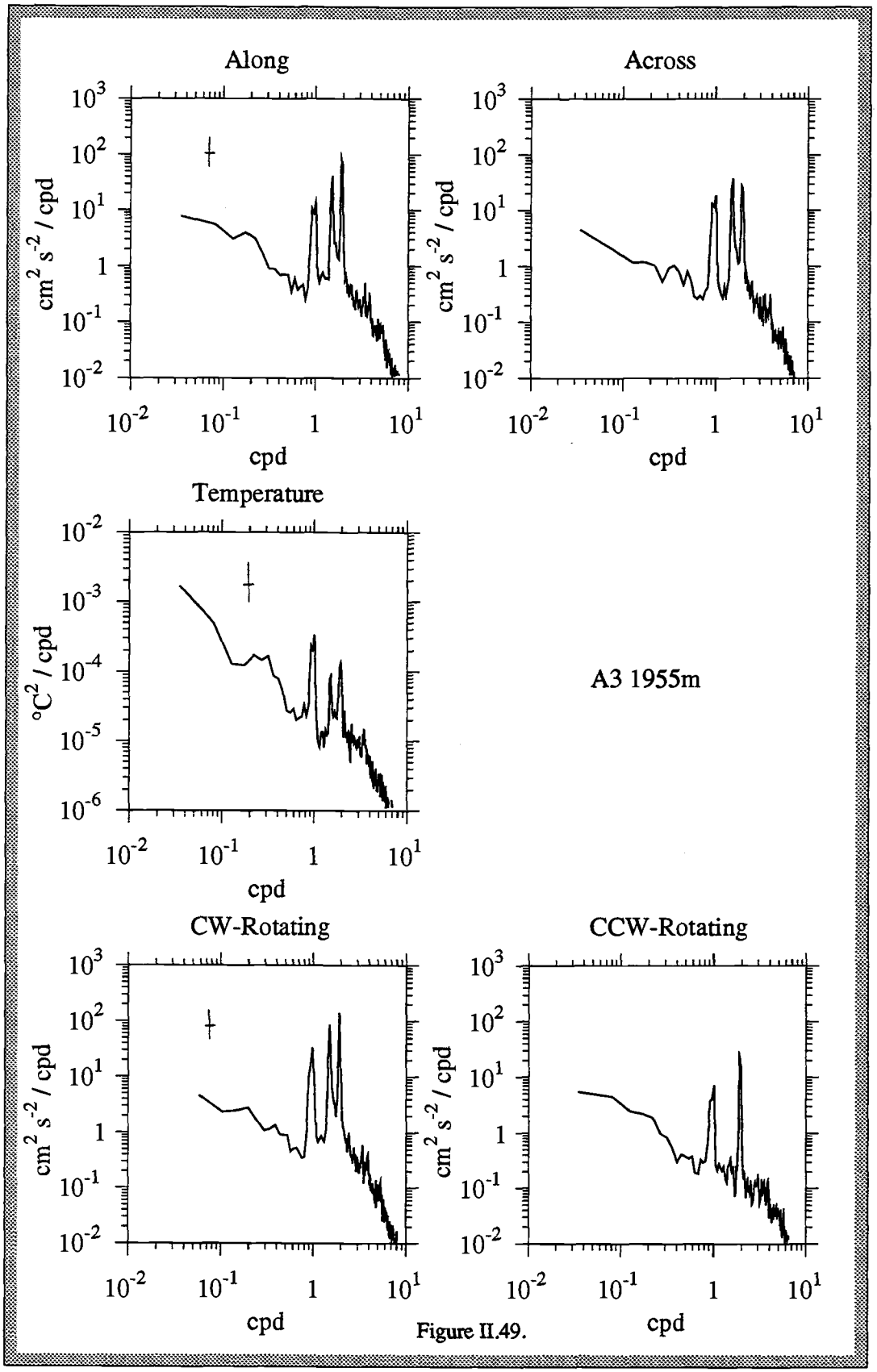
Along
Across
Temperature
CW-Rotating
CCW-Rotating
A3 1955m
cm² s⁻² / cpd
°C² / cpd
cpd
10³
10²
10¹
1
10⁻¹
10⁻²
10⁻³
10⁻⁴
10⁻⁵
10⁻⁶

Figure II.49.

Figure II.50. Energy density spectra for along-ridge and across-ridge currents, temperature, and clockwise (CW) and counterclockwise (CCW) rotational flow at R2 1985 m. The log-log axes measure frequency on the abscissa and spectral energy density on the ordinate. Confidence limits of 95% are shown for 24 degrees of freedom; bandwidth is 0.04651.

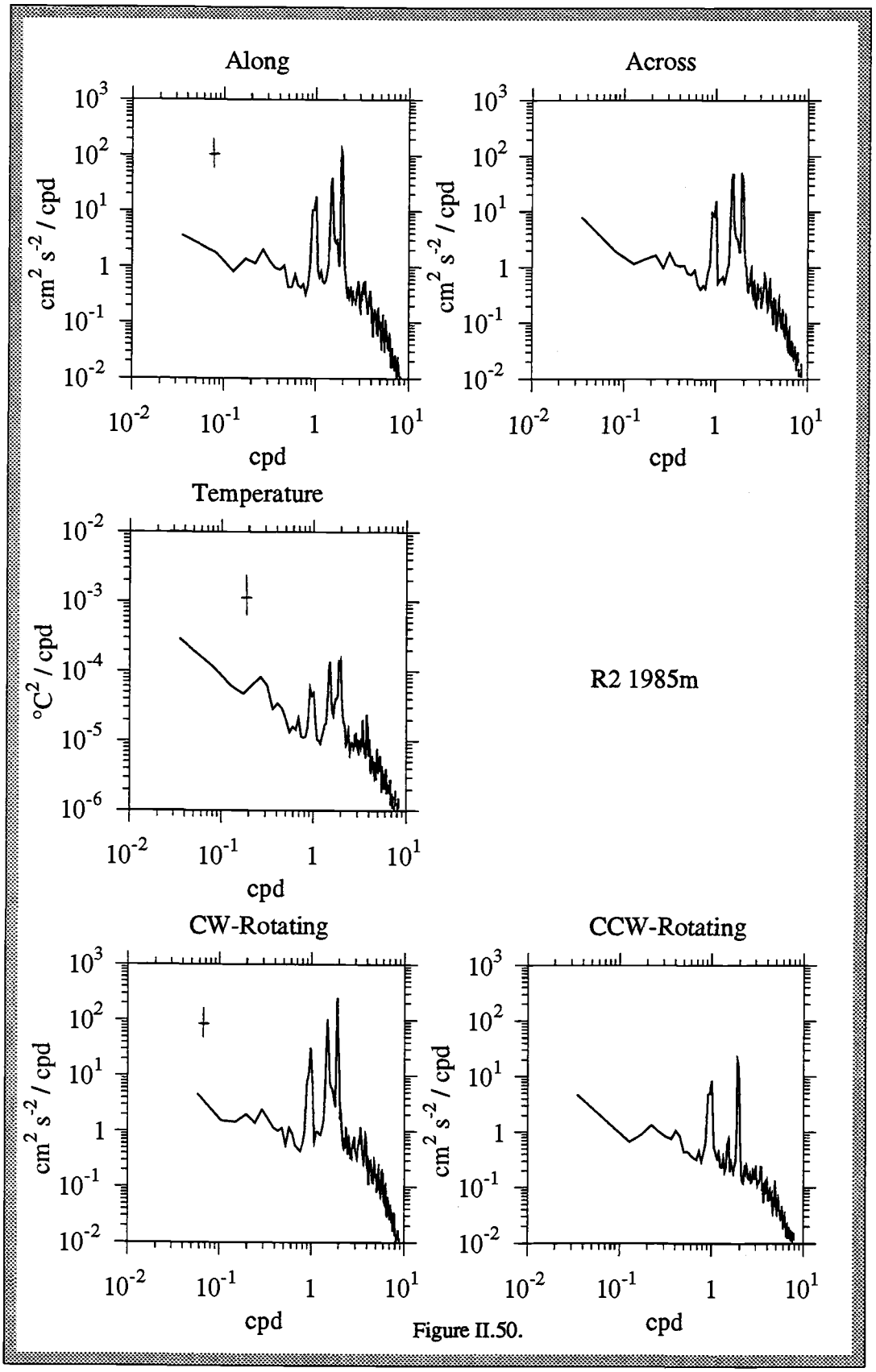
Along
Across
Temperature
CW-Rotating
CCW-Rotating
R2 1985m
cm² s⁻² / cpd
°C² / cpd
cpd

Figure II.50.

Figure II.51. Energy density spectra for along-ridge and across-ridge currents, temperature, and clockwise (CW) and counterclockwise (CCW) rotational flow at ER-3 1936 m. The log-log axes measure frequency on the abscissa and spectral energy density on the ordinate. Confidence limits of 95% are shown for 24 degrees of freedom; bandwidth is 0.04651.

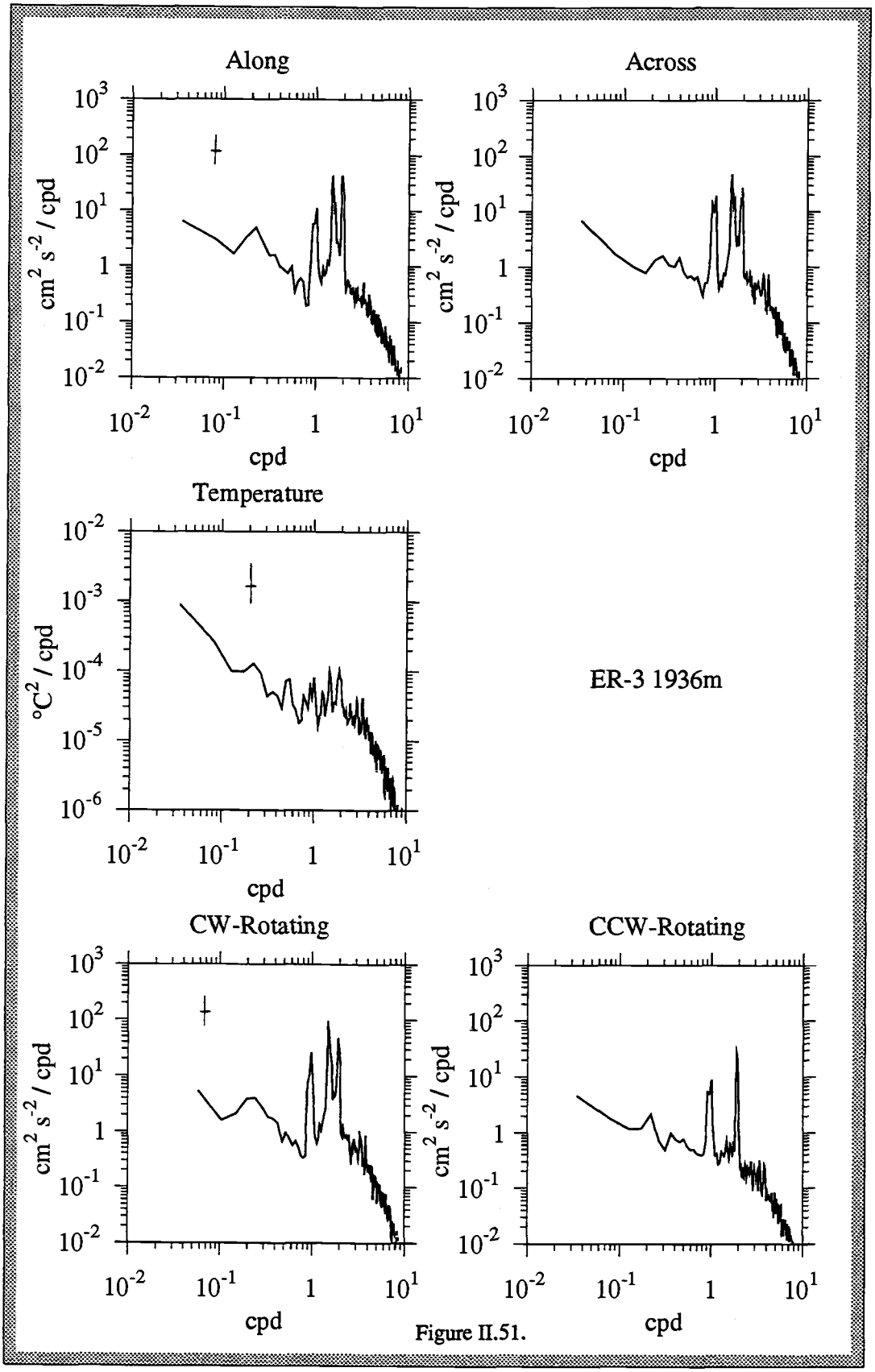
Along
Across
Temperature
CW-Rotating
CCW-Rotating
ER-3 1936m
cm² s⁻² / cpd
°C² / cpd
cpd
10³
10²
10¹
1
10⁻¹
10⁻²
10⁻³
10⁻⁴
10⁻⁵
10⁻⁶

Figure II.51.

In some flow and rotary spectra, significant peaks are observed at frequencies corresponding to periods of 2.5-4 days. In many of these cases, however, the significance is questionable. In contrast to Cannon et al. (1991), I do not find strong spectral evidence for 4-day oscillations. Results of their current meter deployments over five years at the southern end of the Juan de Fuca Ridge indicated that 4-5 day, periodic, clockwise rotations were prominent, especially within the rift valley and near the seafloor close to the ridge axis. Winter intensification and the clockwise rotation led these authors to suggest that the motion was storm induced.

General features of the temperature spectra

Temperature, unlike many dissolved and particulate tracers, is conservative and, theoretically, an unambiguous hydrothermal indicator. Two shortcomings of our data, however, make it difficult to use records of temperature over time from moored instruments directly to decipher plume behavior. First, our data do not permit calculation of potential temperature anomalies on an isopycnal because we lack synchronous records of background (non-hydrothermal) potential temperature and salinity. (The conductivity channel on the Aanderaa data loggers was used to log light transmission data.) Second, while relative variations in temperature recorded by each instrument are reasonably accurate, the absolute temperature values are questionable; thus, it is difficult to compare individual temperature time series.

Comparison of spectra based on the temperature time series is one way to address these problems. Distribution of variance with respect to frequency depends negligibly on instrumental response. (Note that in Figure II.52 the A3 2155 and 2156 temperature spectra, as well as R2 1985 and 1986, are nearly identical, whereas the corresponding temperature time series, Figures II.22, 23 and II.24, 25, are dramatically offset.) Patterns of the spectral energy density functions for temperature can not only be compared with each other, but also with flow and rotary spectra, thereby allowing semi-quantitative evaluation of the role played by advective processes in the distribution of hydrothermal fluids. Spectra of attenuation coefficient records may also be useful in this regard, however, their utility is limited by the presence of long-period trends (or trend removal effects, i.e. the elimination of low-frequency energy), the fact that many of these records are truncated due to instrument failure, and the consideration of non-conservative particle dynamics.

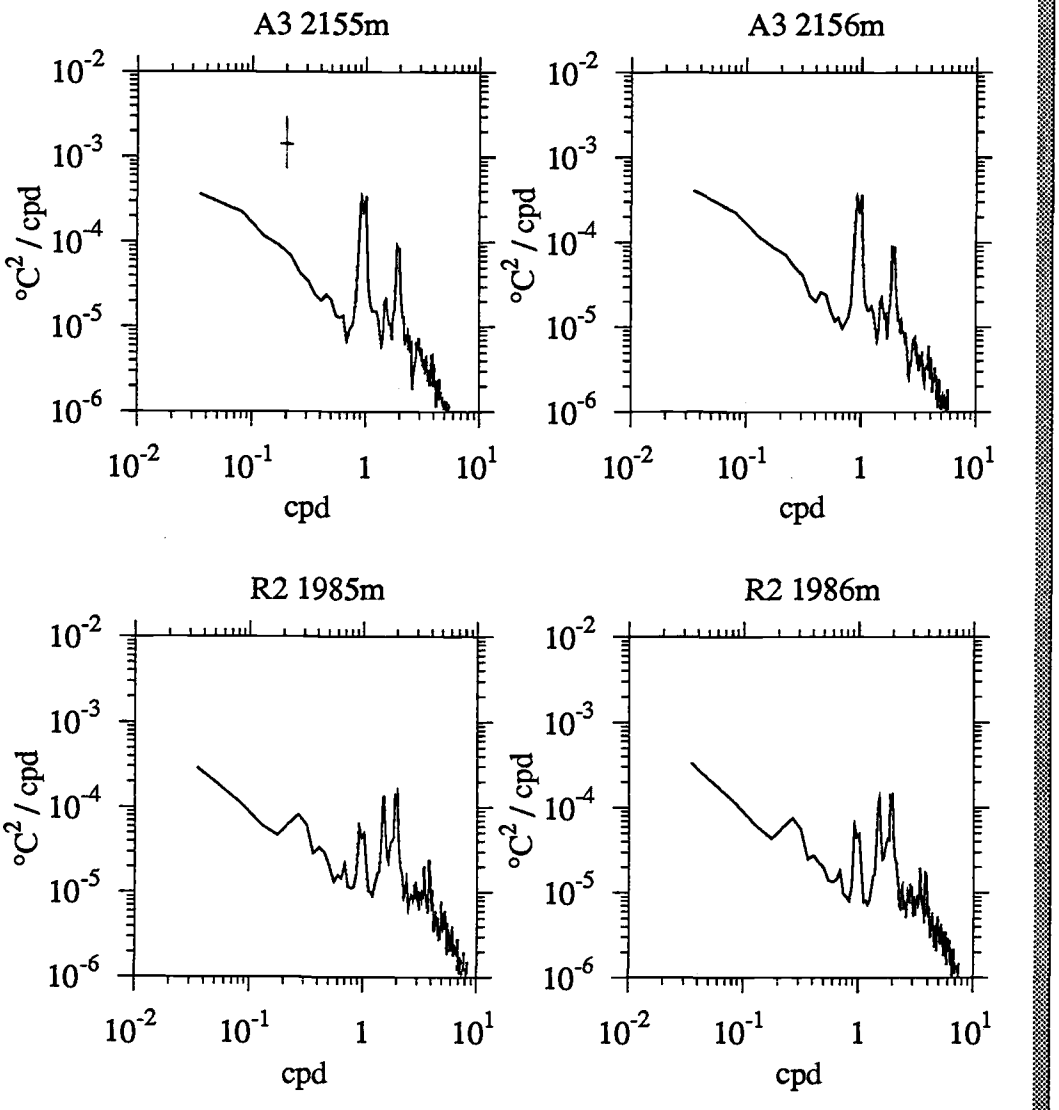

Figure II.52. Energy density spectra for temperature at A3 2155, 2156 and R2 1985, 1986. The log-log axes measure frequency on the abscissa and spectral energy density on the ordinate. Confidence limits of 95% are shown for 24 degrees of freedom; bandwidth is 0.04651.

As with the spectra of across and along-ridge flow, energy density in the temperature spectra (Figures II.47 - II.51) increases with decreasing frequency. Multiple significant peaks occur over the full frequency range of 0-12 cpd, and compared to the flow spectra, the diurnal, inertial, and semi-diurnal tidal peaks are far less energetic relative to other frequencies in the temperature spectra.

Cross-spectra

One application of cross-spectral analysis is to rigorously test the coherence of attenuation coefficient and temperature, the correlation of which was established previously for a specific frequency band. Figure II.53 shows the cross-spectrum for attenuation and temperature at ER-3 1936, at which we obtained the longest records of both parameters in the near-vent, plume-core area. Highly significant in-phase peaks over a broad range of frequencies demonstrate coherence. I later show that the slope of the attenuation/temperature relationship is relatively constant over all frequencies in a single record, yet changes dramatically between records, an observation relevant to the evaluation of the four variance-producing processes described earlier.

Representative cross-spectra of along and across-ridge flow with temperature are shown in Figures II.54 - II.59. Though the absolute value of the resultant cross-correlation coefficients at zero lag are low, it is clear from the numerous significant spectral peaks that the current velocity components and temperature are coherent at the 95% confidence level at frequencies up to five cycles per day. The most energetic frequencies corresponding to the tides and inertial oscillation are coherent in all records, however coherence at higher and lower frequencies is also typical. Phase angles associated with coherent frequencies are generally consistent with what is expected based on the locations of the moorings relative to the vent field (refer to Figure II.2). For example, the along-ridge flow and the temperature recorded at A3 1955 m are out of phase (phase closer to 180° than to 0°) where there is significant coherence (Figure II.54). This means that positive along-ridge flow (20°T, generally northward) is associated with cooler water, while negative along-ridge flow (200°T, generally southward) is linked to warmer water. Mooring A3 was located in the axial valley, several kilometers south of the vent field, and this result reflects advection of the hydrothermal plume to the south. In the case of R2 1985 (Figure II.57), the observed coherency is in-phase (values close to zero), implying that positive across-ridge flow (110°T, generally eastward) is associated with warmer water. Again this result is

Figure II.53. Cross-spectrum of attenuation coefficient and temperature time series for ER-3 1936 showing in-phase coherence, particularly pronounced at frequencies ≤ inertial oscillation. Both raw time series were linearly detrended to compensate for the trend which introduces artificial low-frequency in the attenuation coefficient record.
Frequency is measured in cycles per day (cpd) on the abscissa in all three panels. The upper panel shows the two energy density spectra overlain; the solid line is attenuation coefficient, and the dashed line is temperature. The central panel is the cross-spectrum. Peaks extending above the horizontal dashed line indicate significant correlation at those frequencies. Confidence limits of 95% are shown for 16 degrees of freedom. The lower panel shows phase relationships; points with vertical bars correspond to significant peaks in the central panel. Phase angles of zero degrees (or near 0°) mean that the two parameters changed in unison (i.e. they are in-phase). Phase angles of ±180° mean that the two time series are out of phase, that is, as one increases, the other decreases; the sign of the angle indicates which series leads or lags.

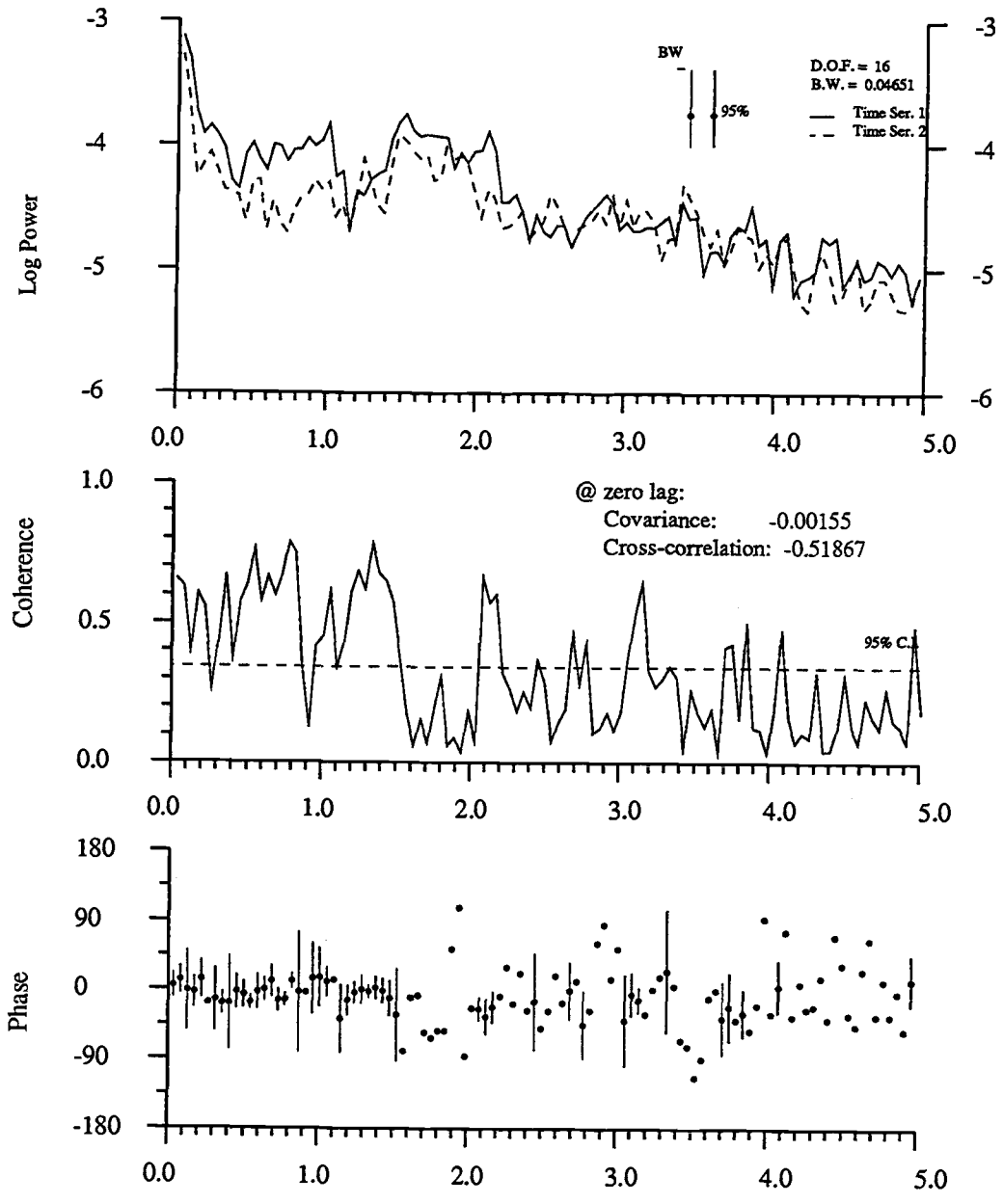
Log Power
-3
-4
-5
-6
BW
95%
D.O.F. = 16
B.W. = 0.04651
Time Ser. 1
Time Ser. 2
0.0
1.0
2.0
3.0
4.0
5.0
Coherence
1.0
0.5
0.0
@ zero lag:
Covariance: -0.00155
Cross-correlation: -0.51867
95% C.L.
Phase
180
90
0
-90
-180

Figure II.53.

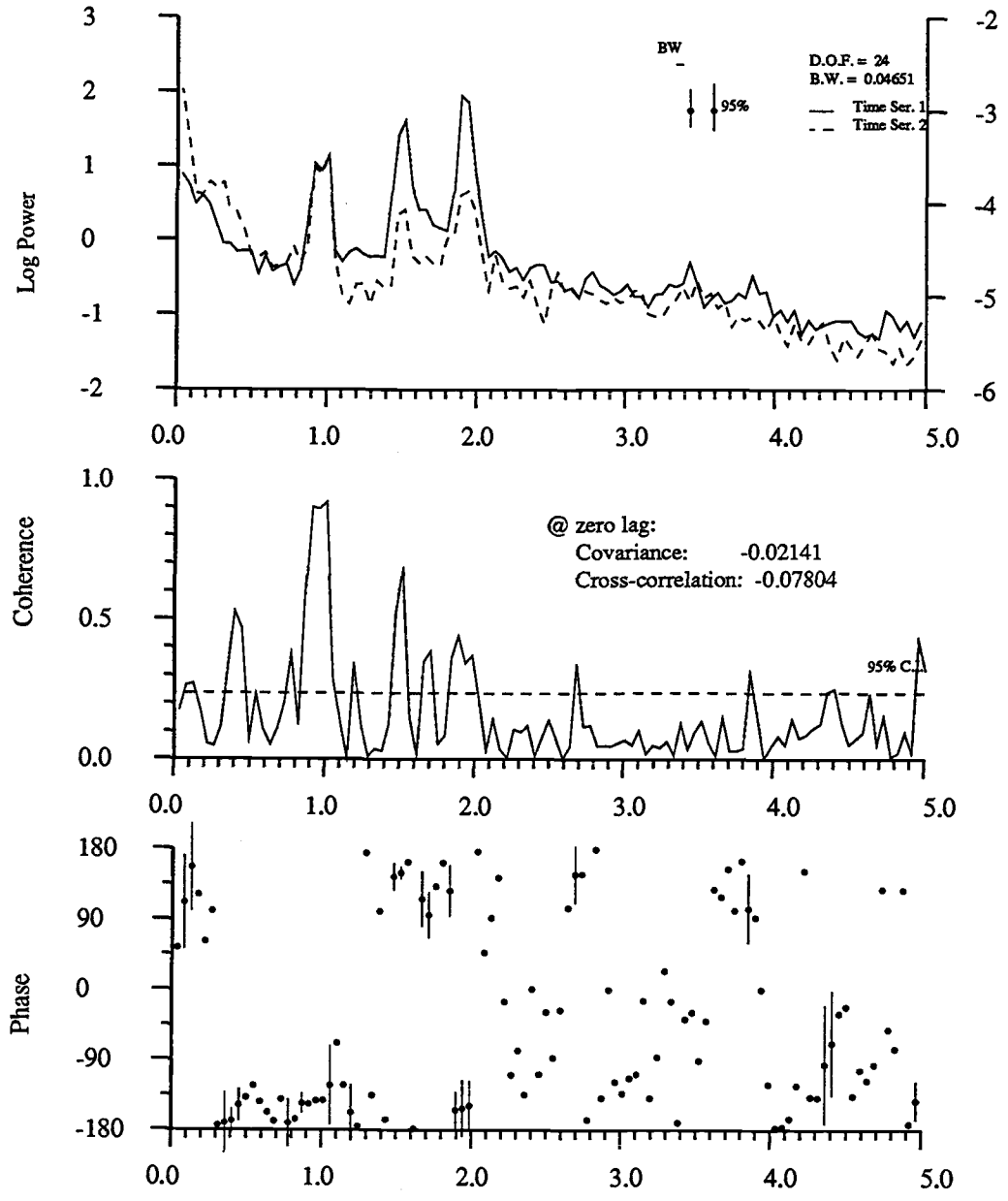

Figure II.54. Cross-spectrum of unfiltered along-ridge current and temperature for A3 1955 m. Confidence limits of 95% are shown for 24 degrees of freedom. Individual spectra are plotted together above the cross-spectrum, with phase information plotted below. See caption for Figure II.53.

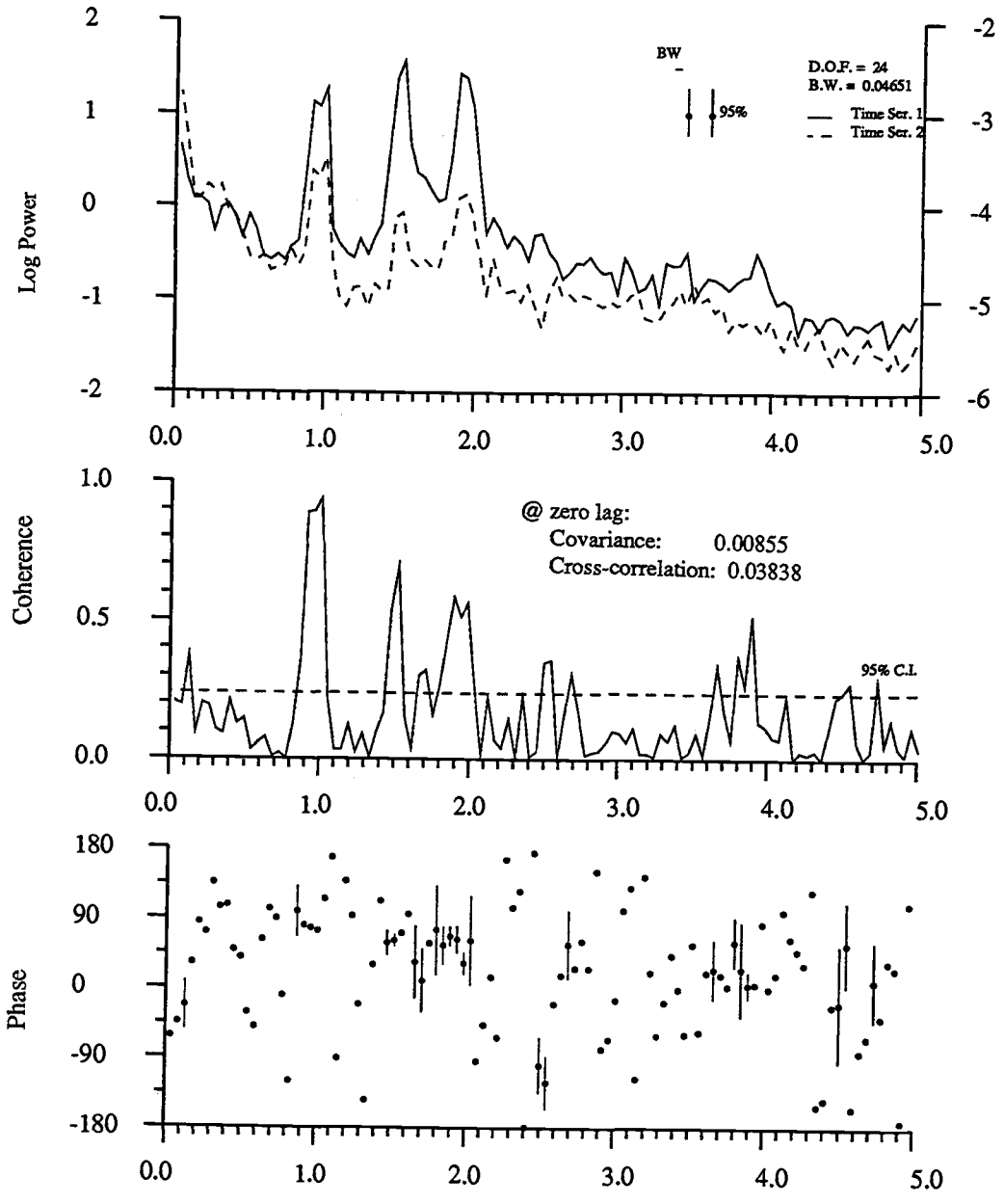

Figure II.55. Cross-spectrum of unfiltered across-ridge current and temperature for A3 1955 m. Confidence limits of 95% are shown for 24 degrees of freedom. Individual spectra are plotted together above the cross-spectrum, with phase information plotted below. See caption for Figure II.53.

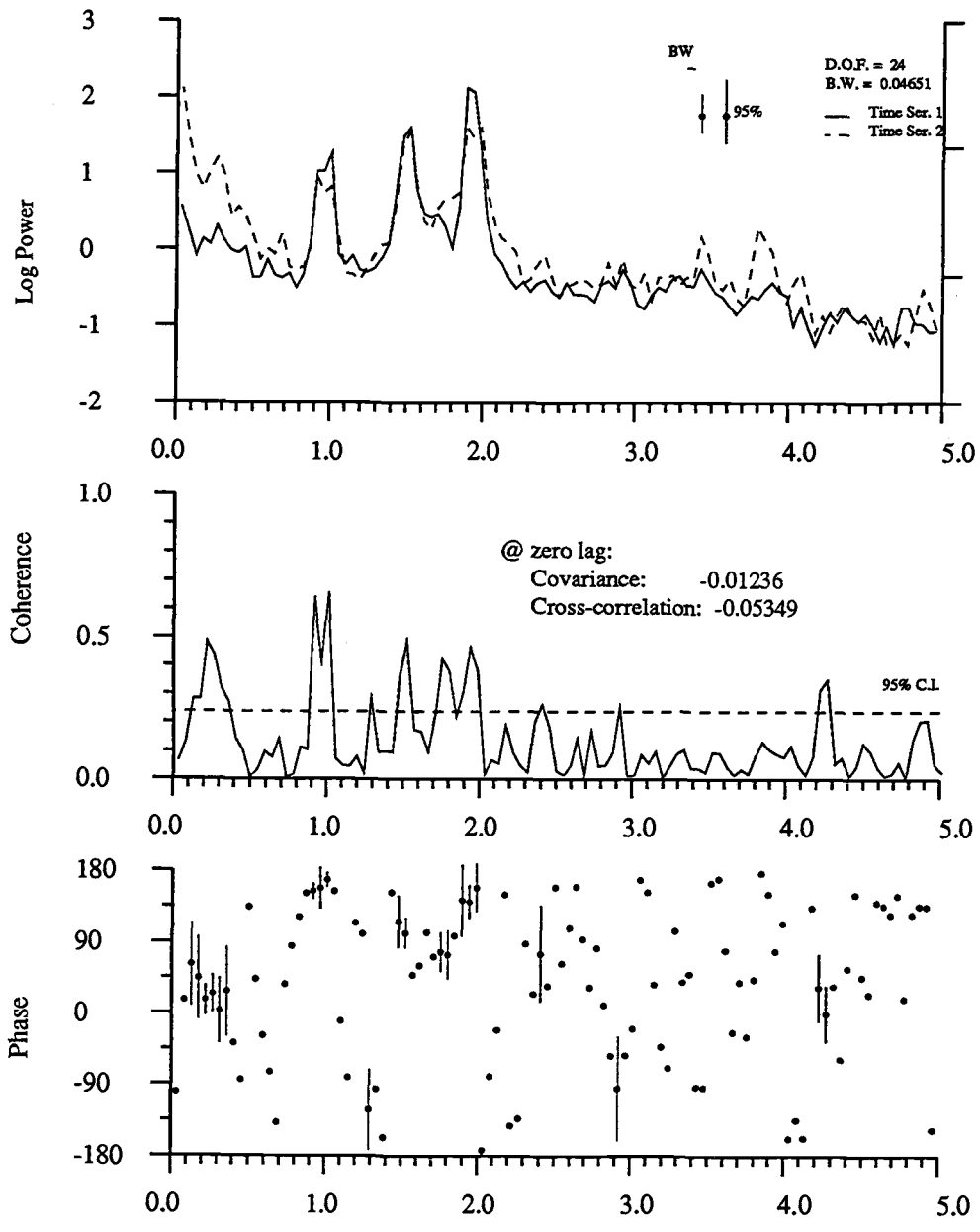

Figure II.56. Cross-spectrum of unfiltered along-ridge current and temperature for R2 1985 m. Confidence limits of 95% are shown for 24 degrees of freedom. Individual spectra are plotted together above the cross-spectrum, with phase information plotted below. See caption for Figure II.53.

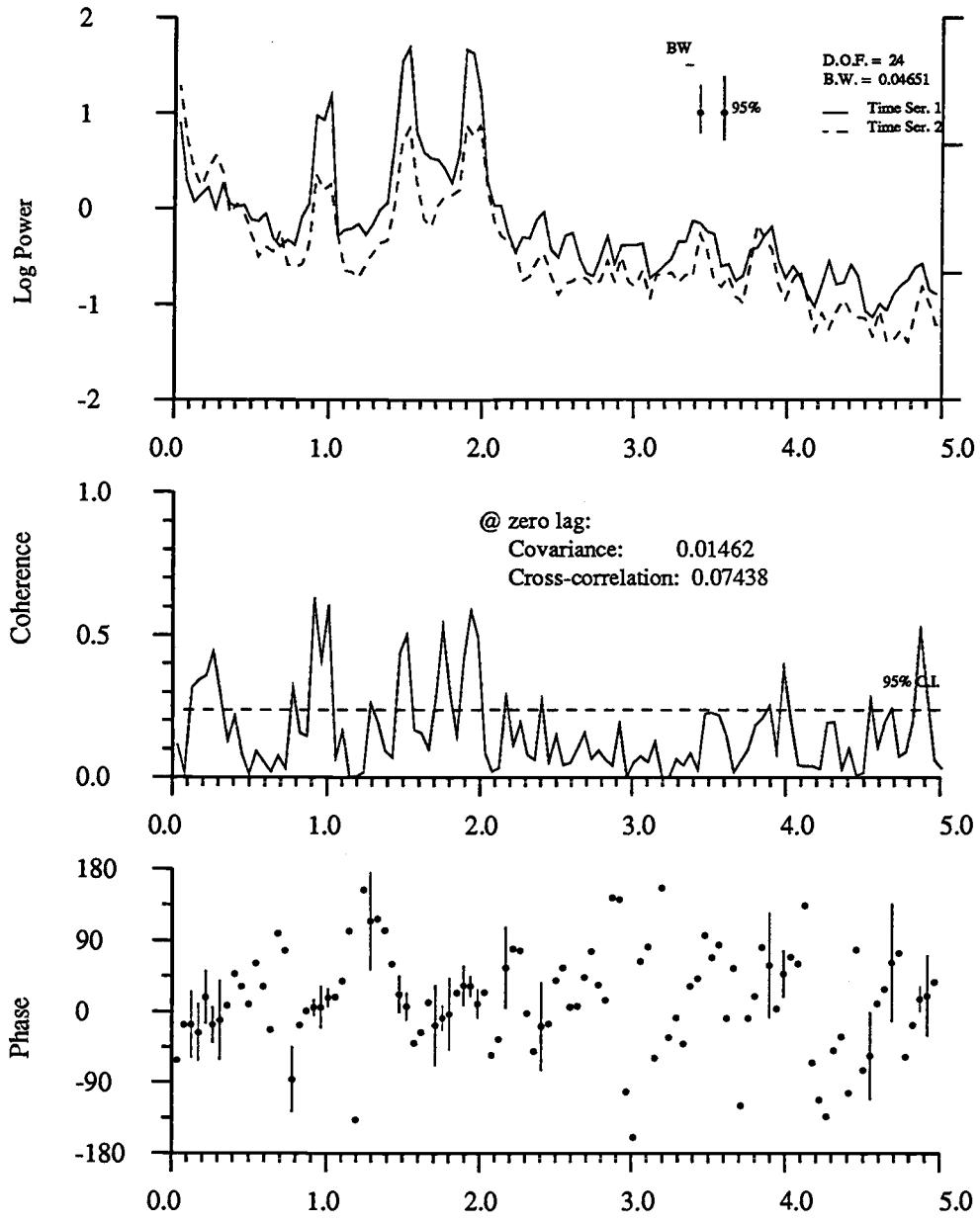

Figure II.57. Cross-spectrum of unfiltered across-ridge current and temperature for R2 1985 m. Confidence limits of 95% are shown for 24 degrees of freedom. Individual spectra are plotted together above the cross-spectrum, with phase information plotted below. See caption for Figure II.53.

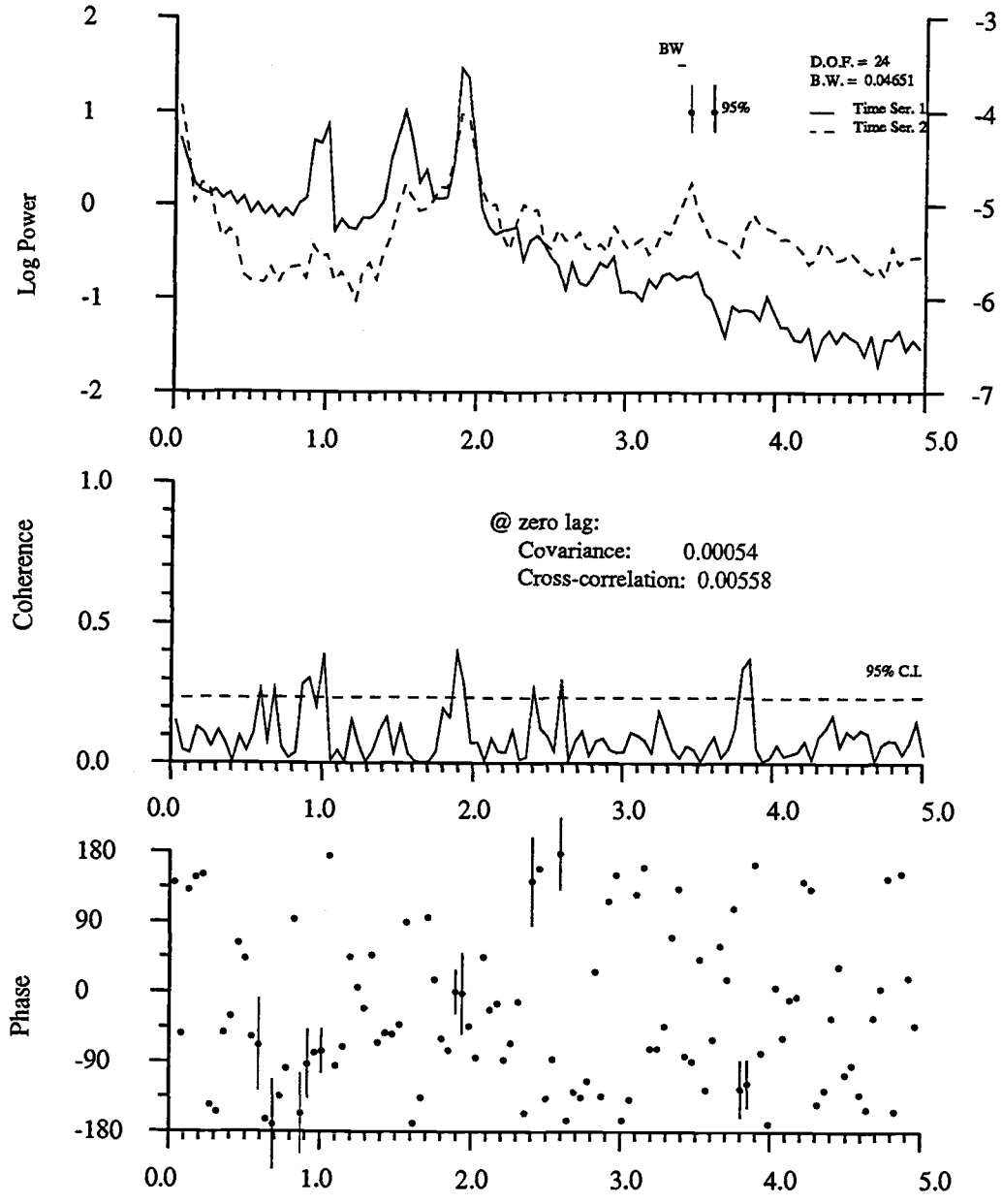

Figure II.58. Cross-spectrum of unfiltered along-ridge current and temperature for T3 2055 m. Confidence limits of 95% are shown for 24 degrees of freedom. Individual spectra are plotted together above the cross-spectrum, with phase information plotted below. See caption for Figure II.53.

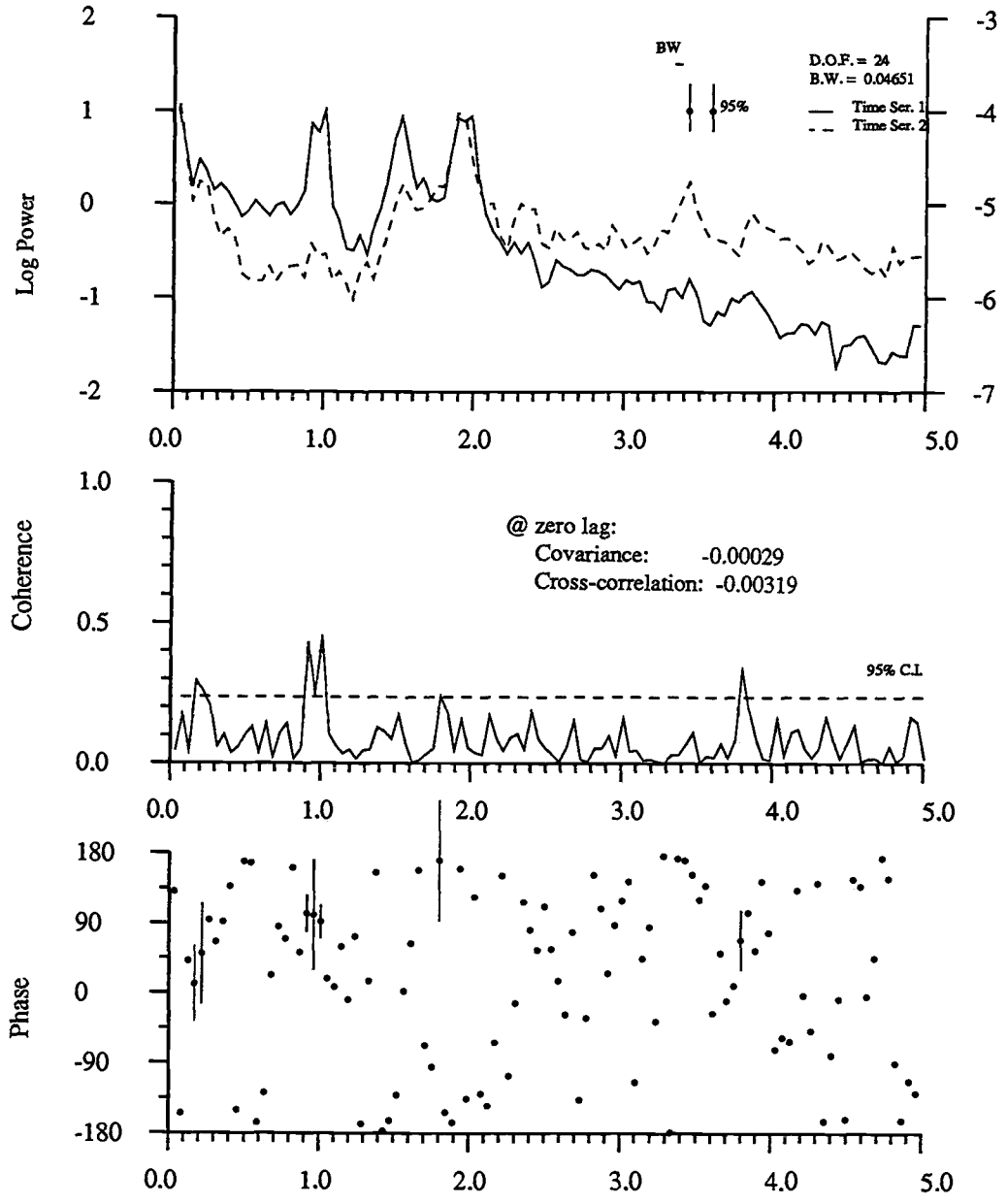

Figure II.59. Cross-spectrum of unfiltered across-ridge current and temperature for T3 2055 m. Confidence limits of 95% are shown for 24 degrees of freedom. Individual spectra are plotted together above the cross-spectrum, with phase information plotted below. See caption for Figure II.53.

consistent with the directional relationship of R2 and the vent field: R2 was on the eastern ridge crest adjacent to the vent field. The relationship between flow and temperature deteriorates with distance from the vents field. The cross-correlation coefficient between flow and temperature decreases at T3 by an order of magnitude from the near-field values (Figures II.58 and II.59).

These observations support the assertion that flow is an important factor in distributing hydrothermal effluent. Moreover, the weaker coupling of flow and temperature in the far-field can be interpreted in two, non-mutually exclusive ways: 1. The temperature anomaly in the distal plume decreases due to mixing and diffusion, hence subduing any temperature fluctuation induced by velocity changes. 2. Tidal-range rotary motions, which have spatial scales of < 2 km, account for most of the covariance between flow and temperature, and therefore the coherence is stronger in near-field records (i.e those obtained within about 2 km of the vent field). The first effect almost certainly occurs, and the second effect is likely, based on the high-amplitude tidal-range peaks in the cross-spectra.

Another application of cross-spectral analysis is testing the uniformity of flow in the study region. Interpretation of the light attenuation, temperture and settling particle flux records is strongly dependent on the degree of horizontal or vertical shear between the sensors. Rough seafloor topography at a spreading ridge can alter flow (Thomson et al., 1990) and thereby reduce spatial flow coherence. Figures II.60 - II.75 show the cross-spectra and cross-correlation coefficients for along and across-ridge components of flow for selected instrument pairs. At depths corresponding to the neutrally buoyant plume, both along and across-ridge flow at A2 1905 and R2 1985 (Figures II.60 and II.61) are highly correlated (cross-correlation = 0.86, 0.82 for along and across-ridge flow respectively), in-phase, and coherent at tidal-range frequencies. Comparison of flow at A2 1905 and A3 1955 (Figures II.62 and II.63) gives similar results: cross-correlation = 0.73, 0.69 for along and across-ridge currents, which are also in phase. These observations suggest that within several kilometers of the central, near-vent-field mooring, horizontal flow at plume depths is uniform. That this tight coupling of across/across-ridge and along/along-ridge pairs weakens with distance between moorings is not surprising. The cross-correlation over about 15 km between A2 2005 and T3 2055 is 0.50 and 0.34 for along and across-ridge flow (Figures II.64 and II.65), however coherence is still remarkably close to one, and relatively in-phase,

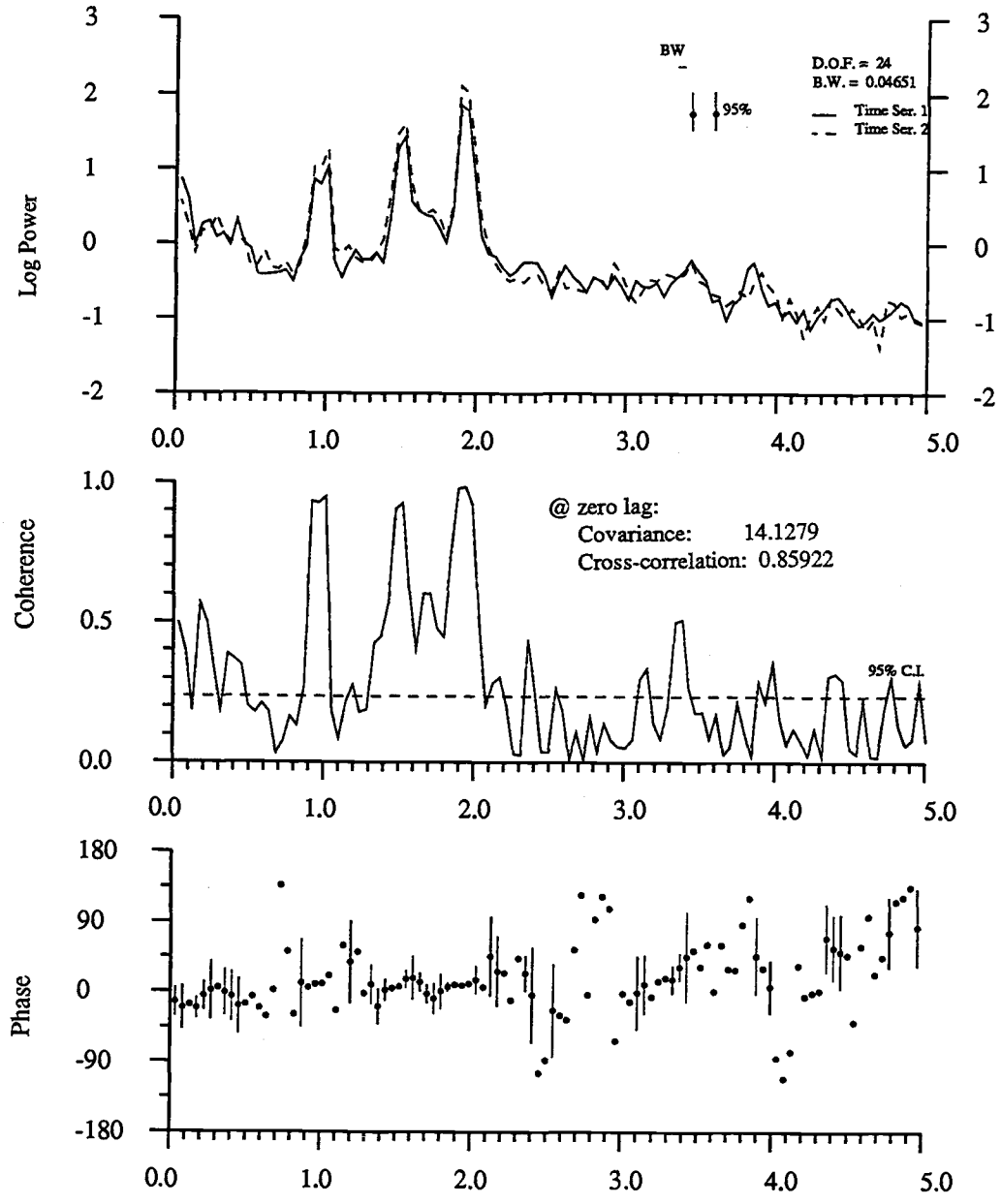

Figure II.60. Cross-spectrum of unfiltered along-ridge flow at A2 1905 and R2 1985. Confidence limits of 95% are shown for 24 degrees of freedom. Above the cross-spectrum, individual energy density spectra are shown; below are phase values. See caption for Figure II.53.

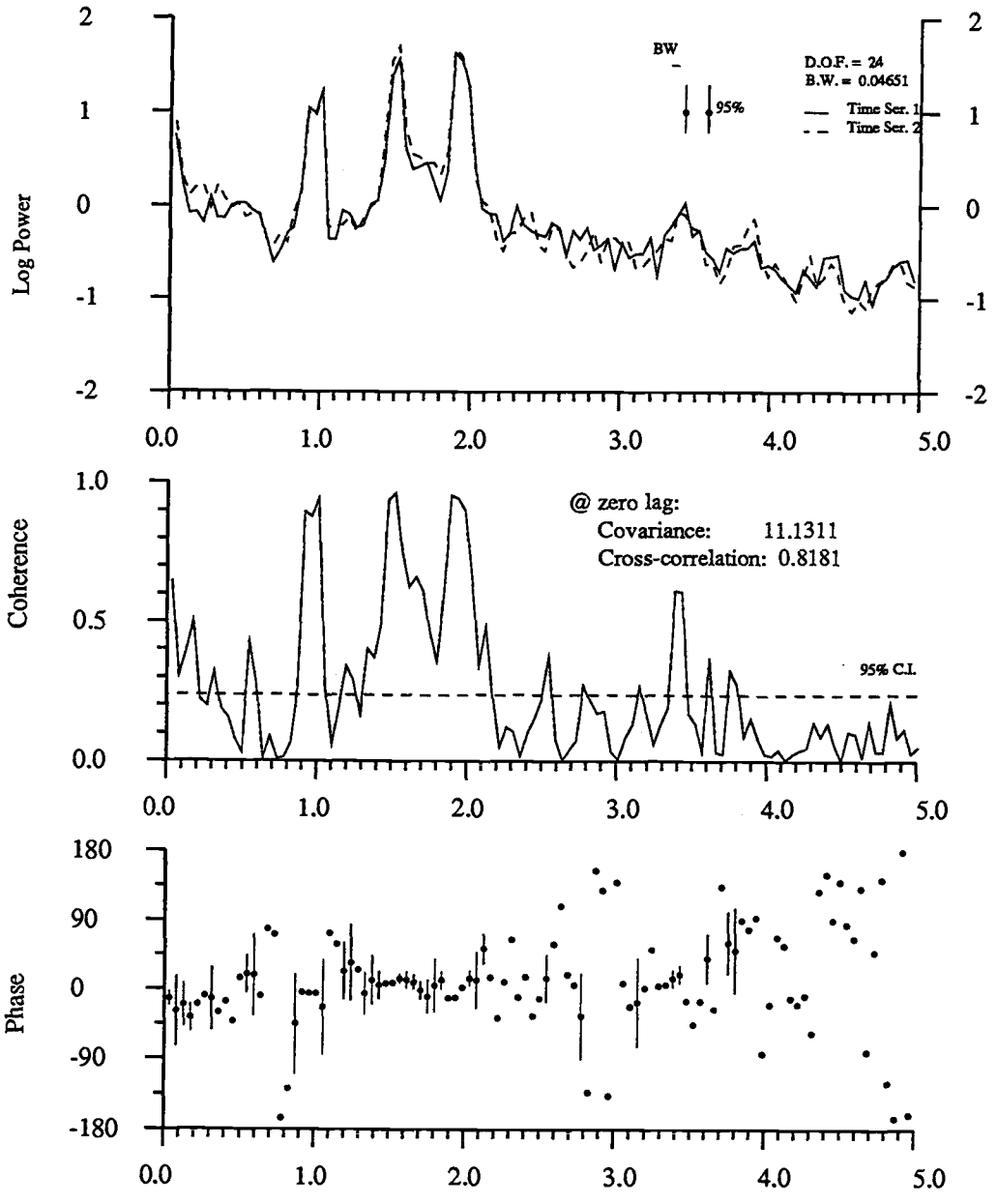

Figure II.61. Cross-spectrum of unfiltered across-ridge flow at A2 1905 and R2 1985. Confidence limits of 95% are shown for 24 degrees of freedom. Above the cross-spectrum, individual energy density spectra are shown; below are phase values. See caption for Figure II.53.

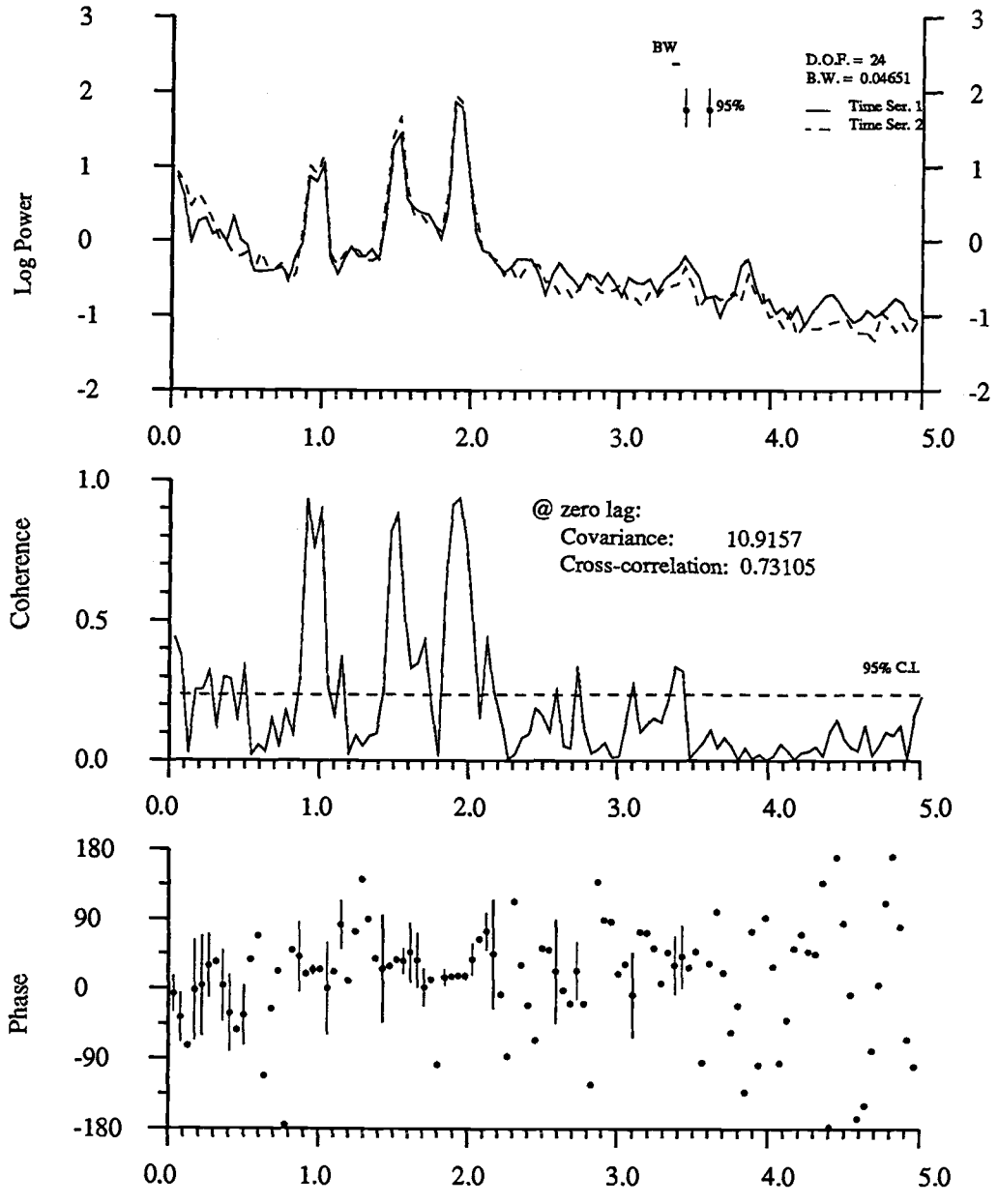

Figure II.62. Cross-spectrum of unfiltered along-ridge flow at A2 1905 and A3 1955. Confidence limits of 95% are shown for 24 degrees of freedom. Above the cross-spectrum, individual energy density spectra are shown; below are phase values. See caption for Figure II.53.

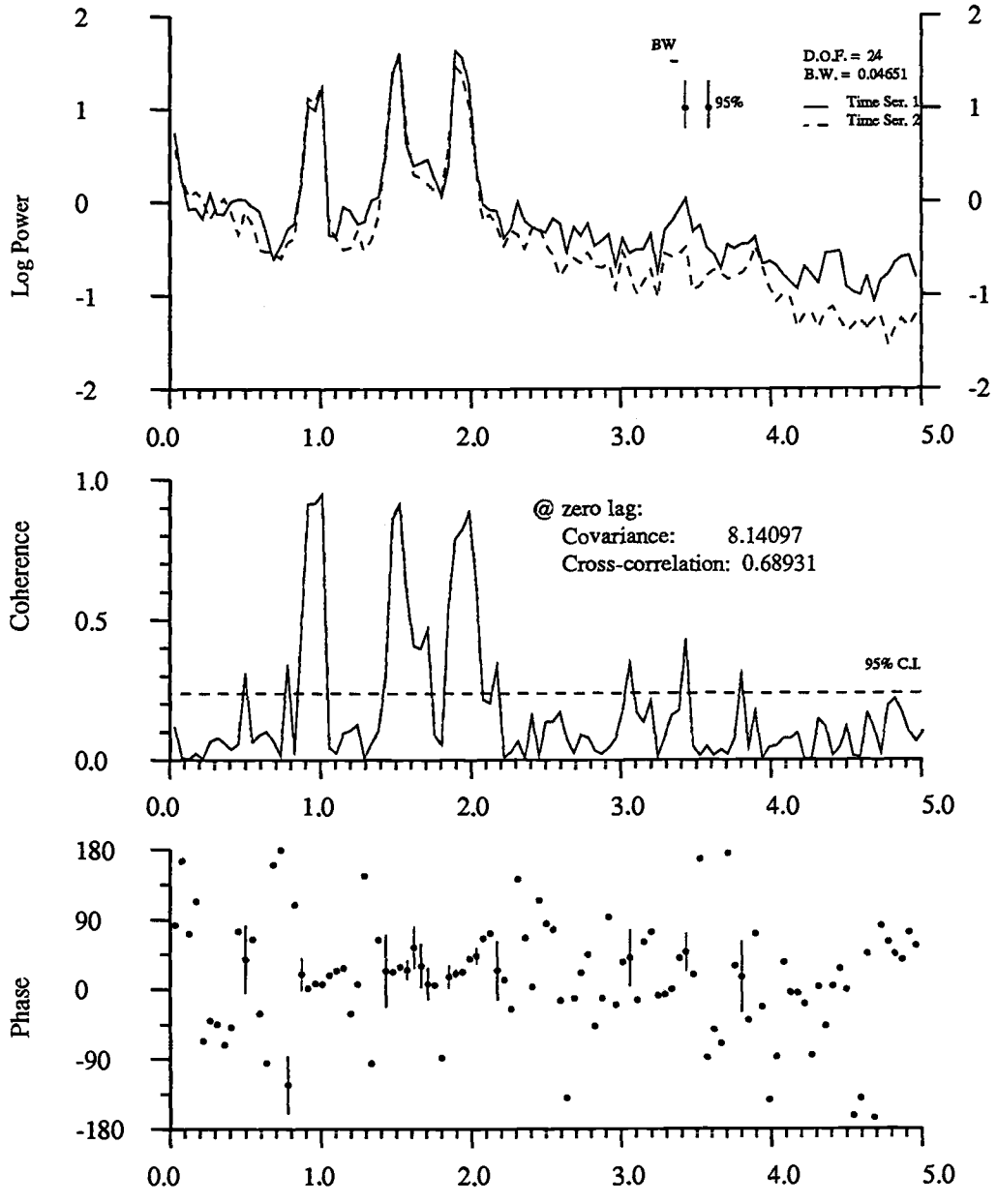

Figure II.63. Cross-spectrum of unfiltered across-ridge flow at A2 1905 and A3 1955. Confidence limits of 95% are shown for 24 degrees of freedom. Above the cross-spectrum, individual energy density spectra are shown; below are phase values. See caption for Figure II.53.

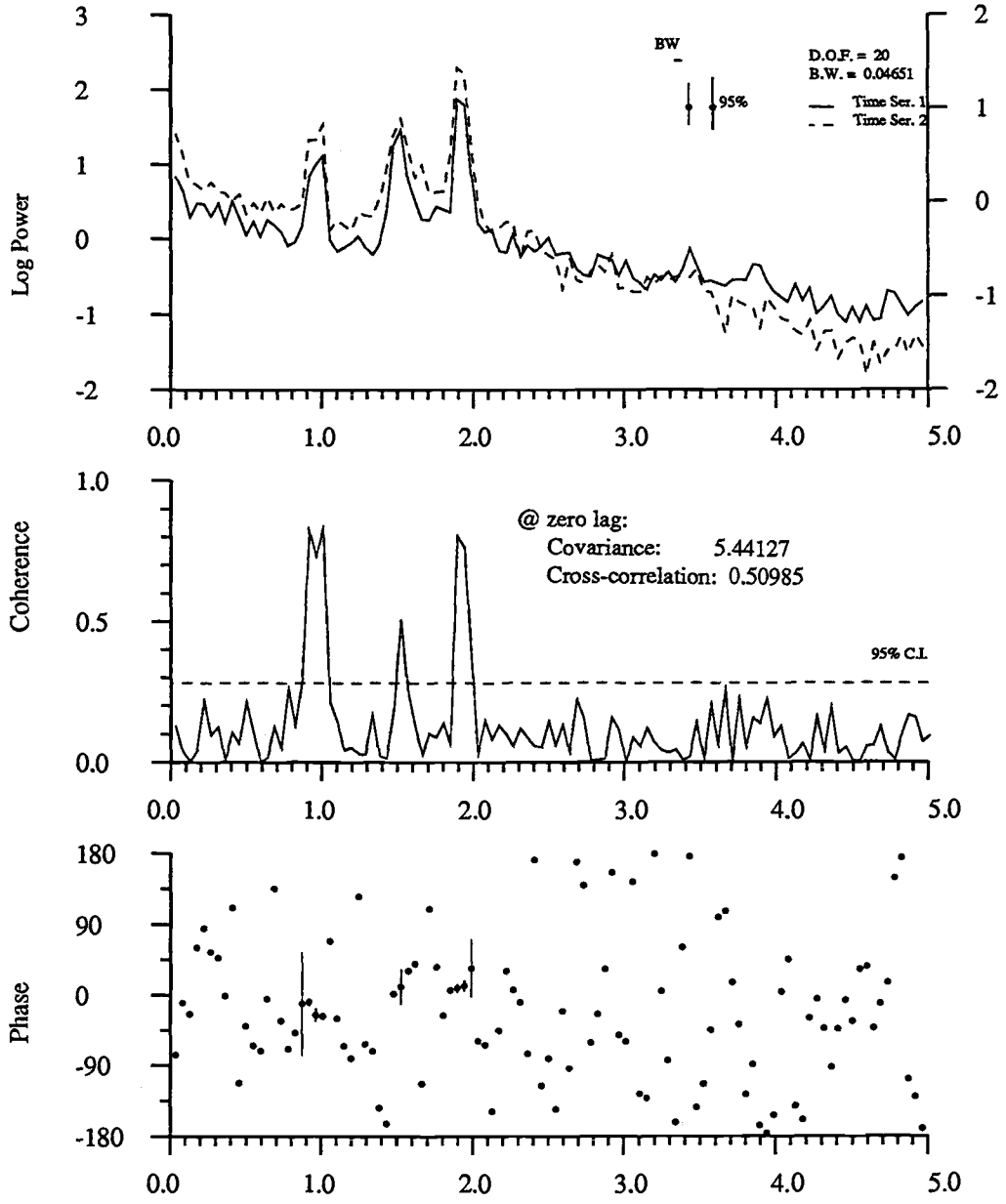

Figure II.64. Cross-spectrum of unfiltered along-ridge flow at A2 2005 and T3 2055. Confidence limits of 95% are shown for 20 degrees of freedom. Above the cross-spectrum, individual energy density spectra are shown; below are phase values. See caption for Figure II.53.

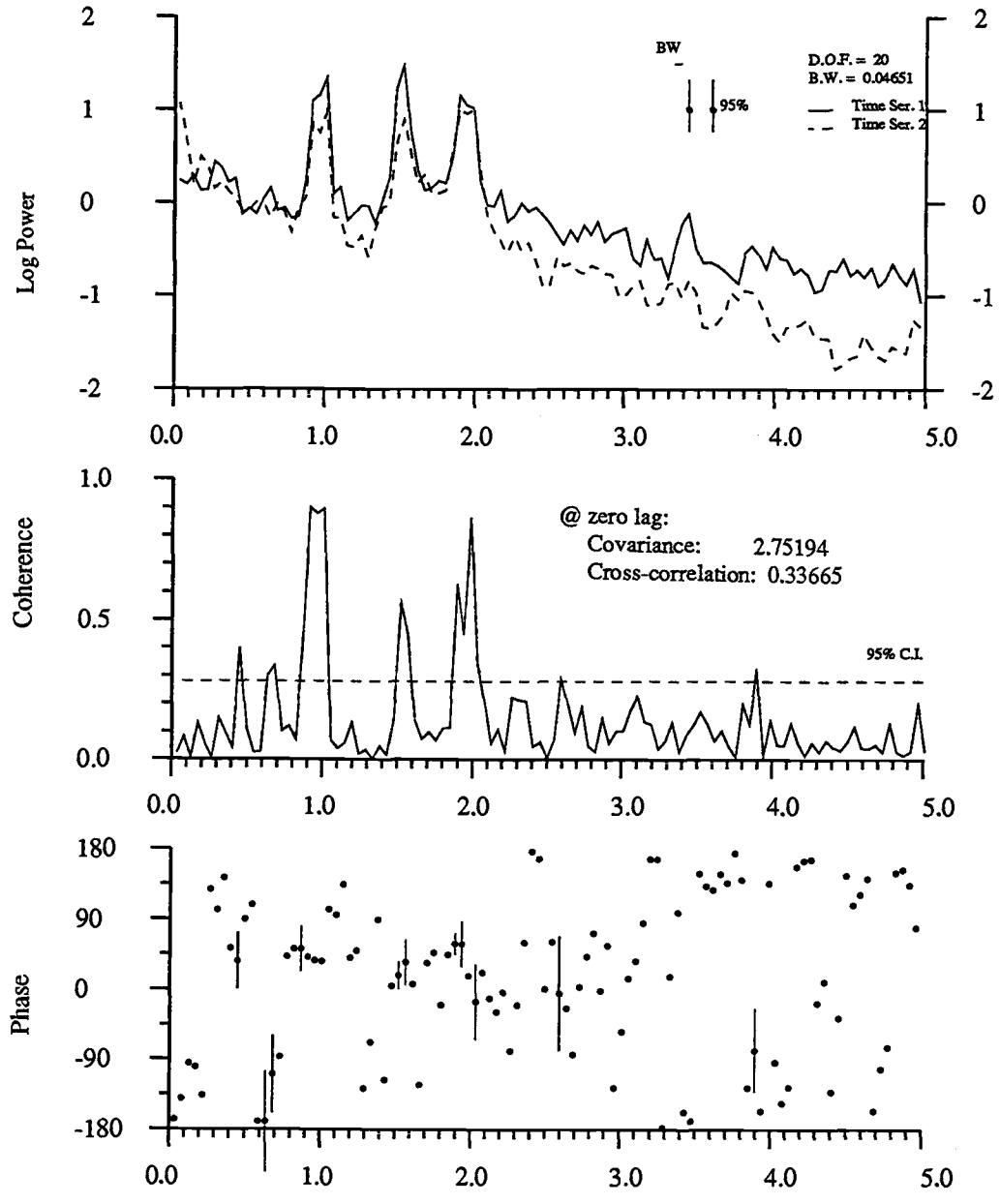

Figure II.65. Cross-spectrum of unfiltered across-ridge flow at A2 2005 and T3 2055. Confidence limits of 95% are shown for 20 degrees of freedom. Above the cross-spectrum, individual energy density spectra are shown; below are phase values. See caption for Figure II.53.

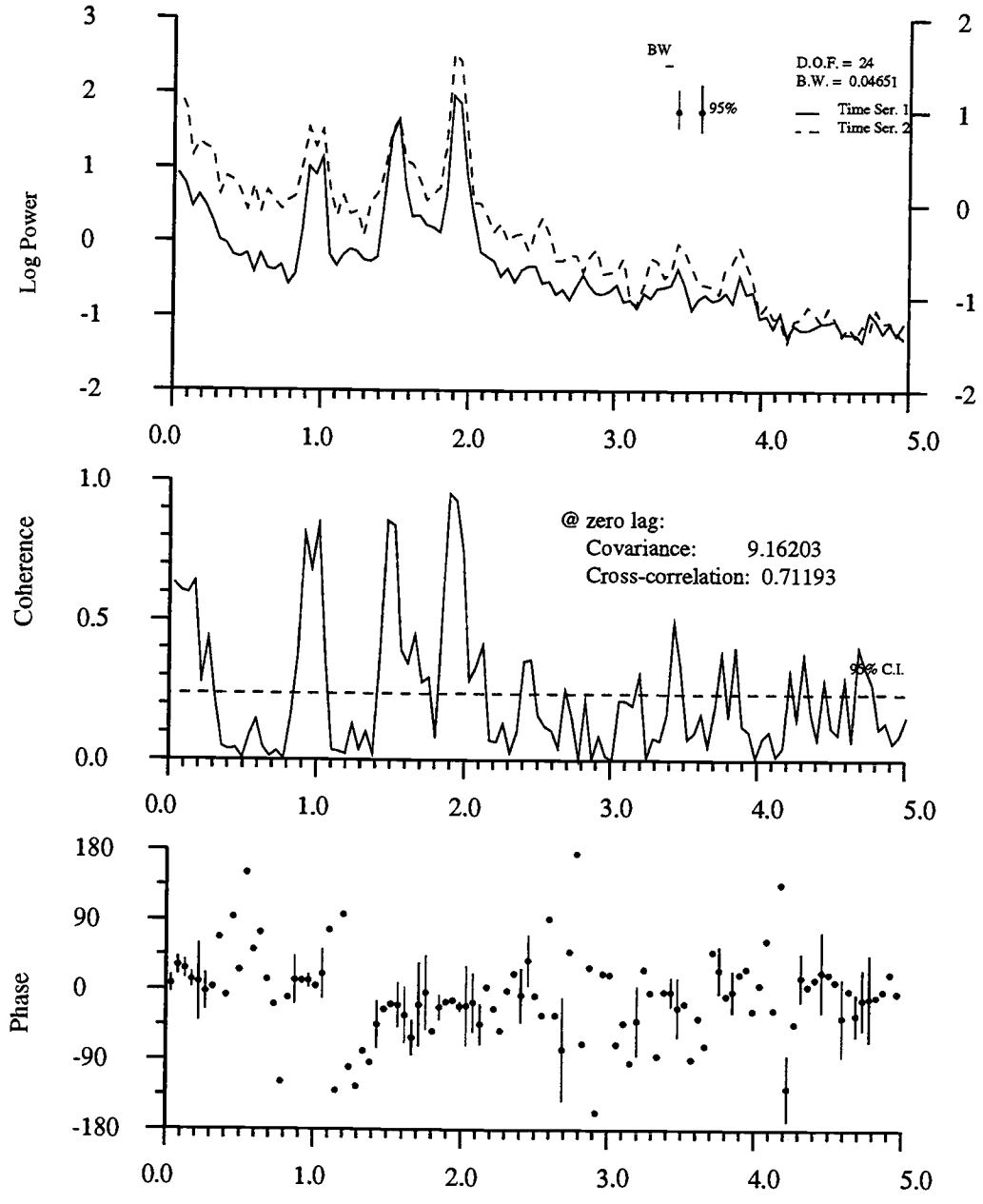

Figure II.66. Cross-spectrum of unfiltered along-ridge flow at A3 1955 and A3 2055. Confidence limits of 95% are shown for 24 degrees of freedom. Above the cross-spectrum, individual energy density spectra are shown; below are phase values. See caption for Figure II.53.

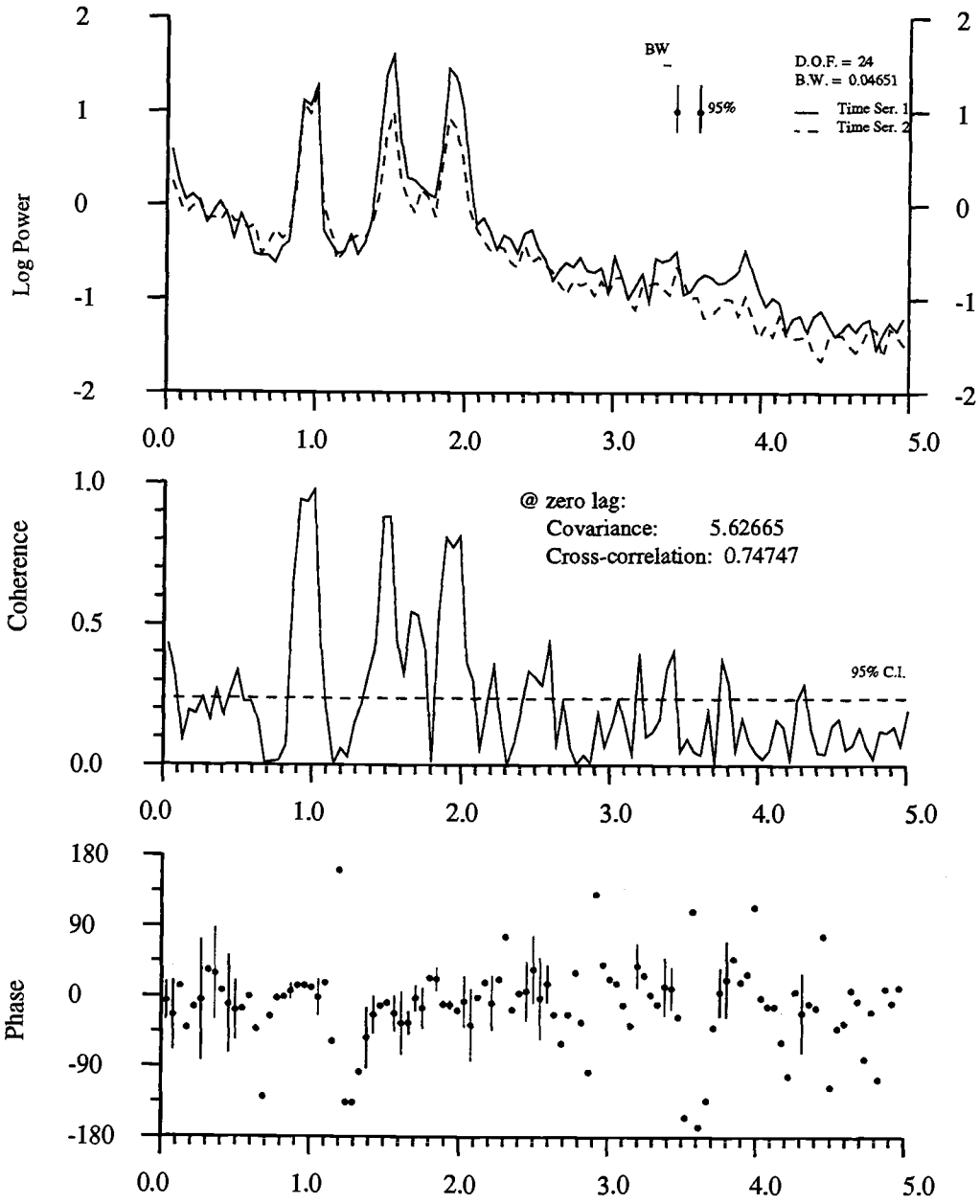

Figure II.67. Cross-spectrum of unfiltered across-ridge flow at A3 1955 and A3 2055. Confidence limits of 95% are shown for 24 degrees of freedom. Above the cross-spectrum, individual energy density spectra are shown; below are phase values. See caption for Figure II.53.

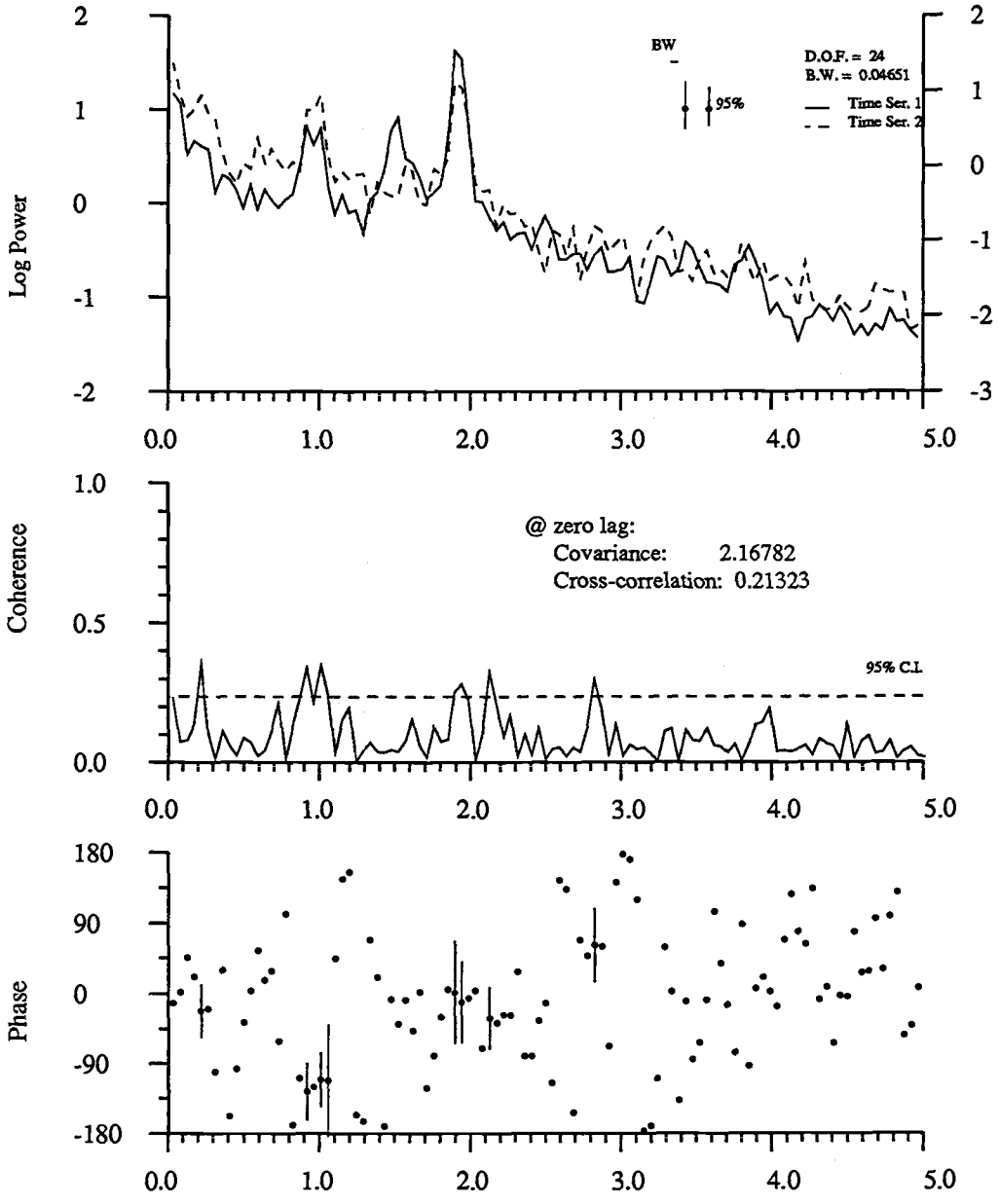

Figure II.68. Cross-spectrum of unfiltered along-ridge flow at A3 2055 and A3 2155. Confidence limits of 95% are shown for 24 degrees of freedom. Above the cross-spectrum, individual energy density spectra are shown; below are phase values. See caption for Figure II.53.

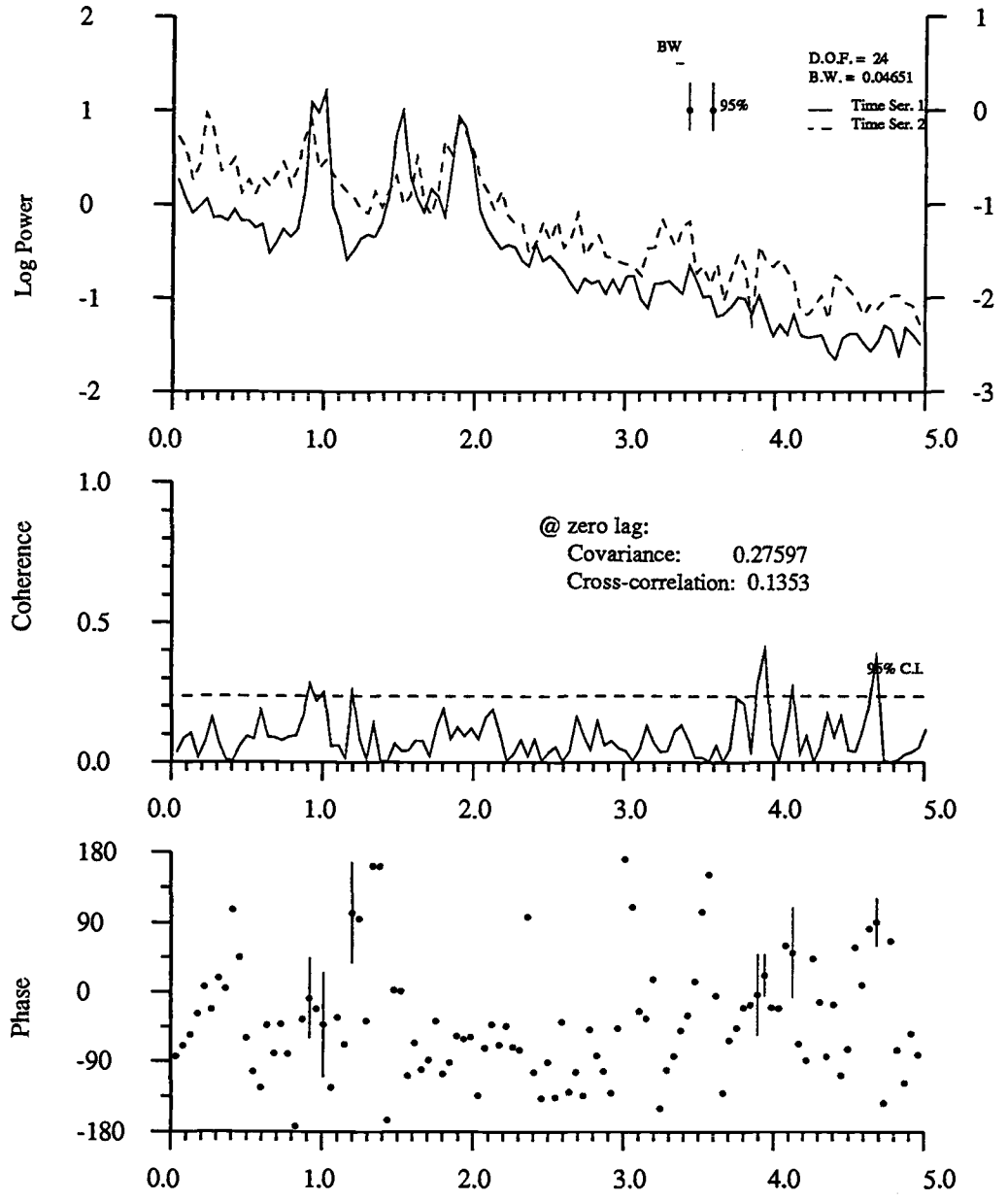

Figure II.69. Cross-spectrum of unfiltered across-ridge flow at A3 2055 and A3 2155. Confidence limits of 95% are shown for 24 degrees of freedom. Above the cross-spectrum, individual energy density spectra are shown; below are phase values. See caption for Figure II.53.

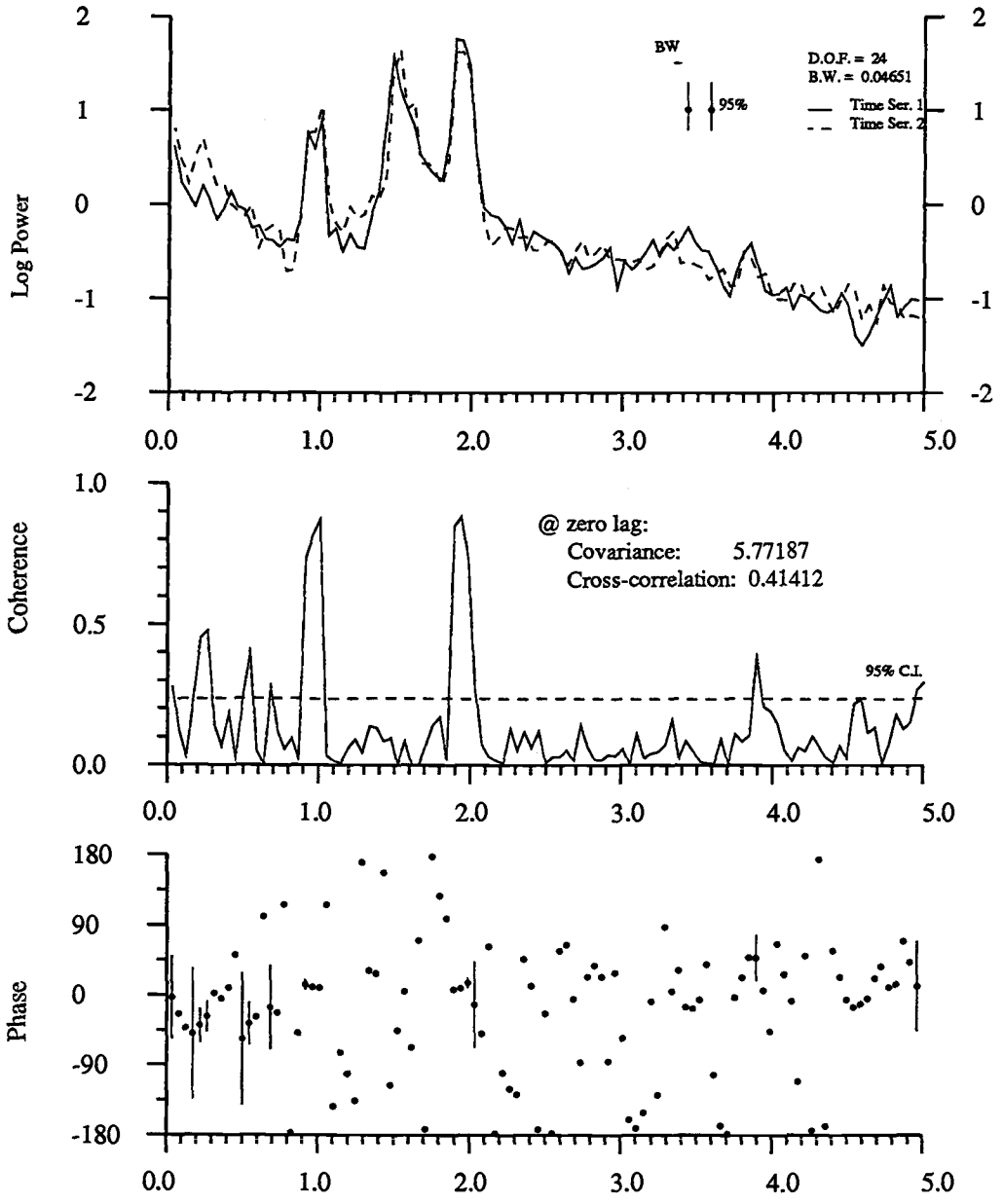

Figure II.70. Cross-spectrum of unfiltered along-ridge flow at ER-3 1686 and ER-3 1936. Confidence limits of 95% are shown for 24 degrees of freedom. Above the cross-spectrum, individual energy density spectra are shown; below are phase values. See caption for Figure II.53.

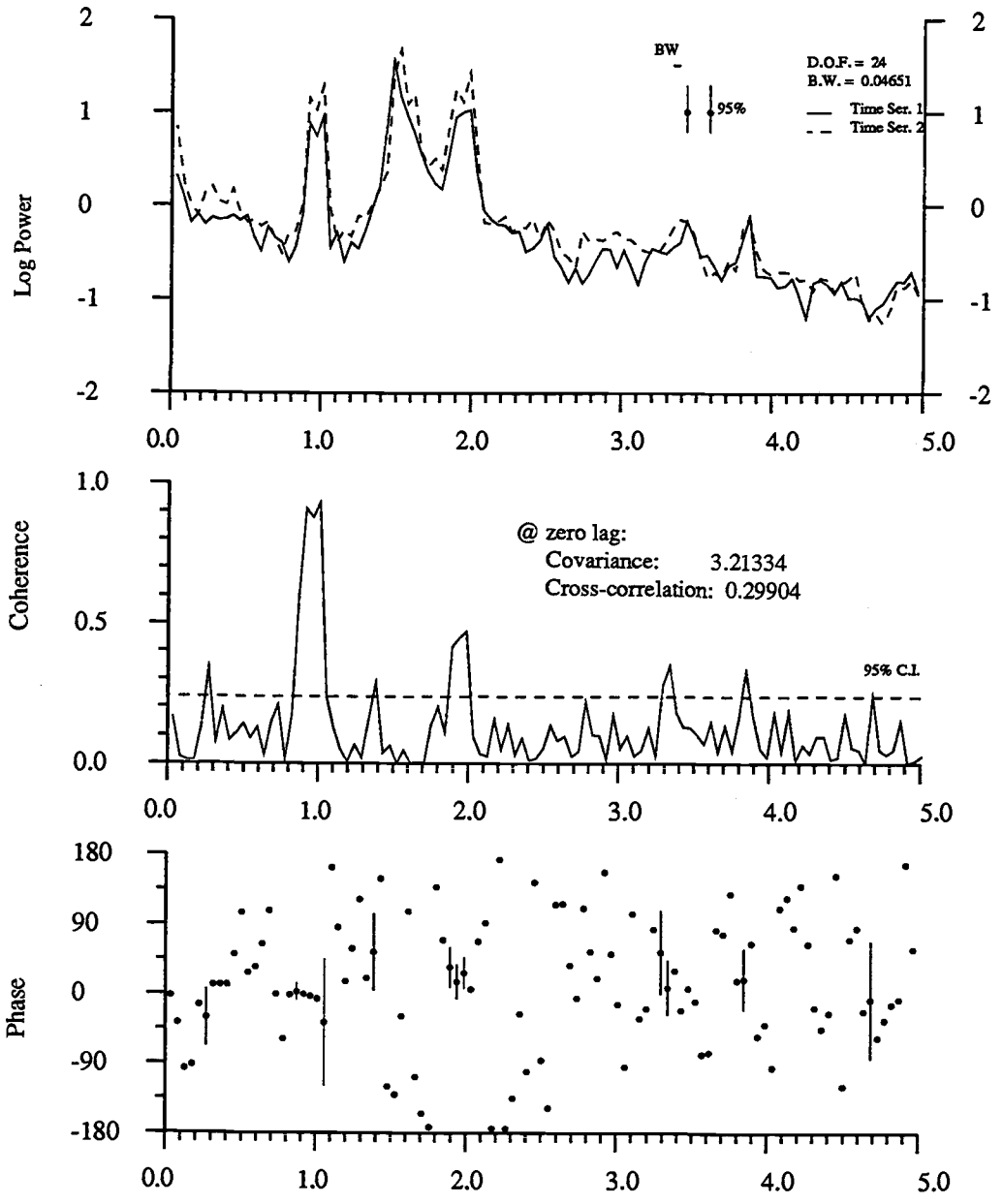

Figure II.71. Cross-spectrum of unfiltered across-ridge flow at ER-3 1686 and ER-3 1936. Confidence limits of 95% are shown for 24 degrees of freedom. Above the cross-spectrum, individual energy density spectra are shown; below are phase values. See caption for Figure II.53.

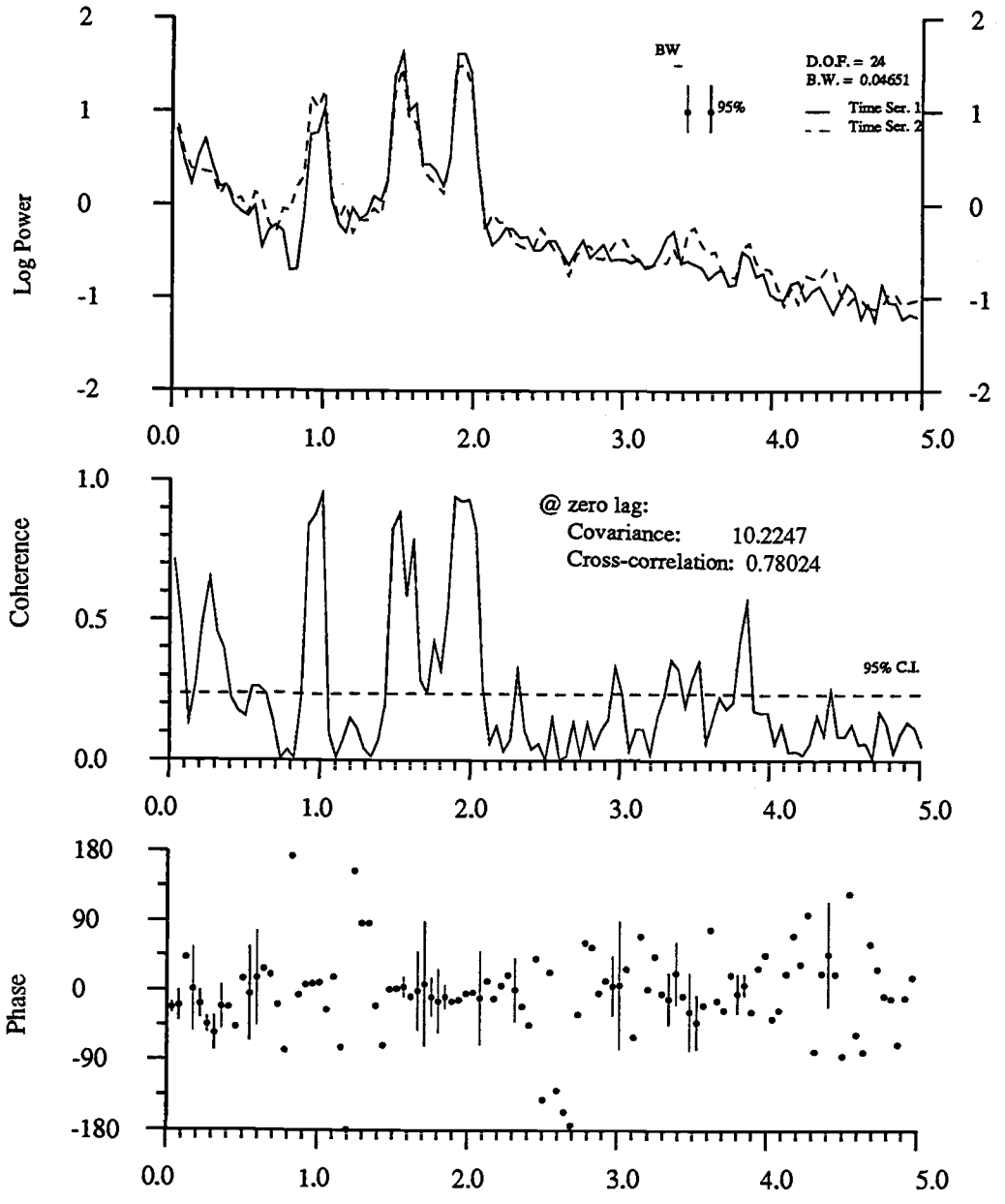

Figure II.72. Cross-spectrum of unfiltered along-ridge flow at ER-3 1936 and ER-3 2036. Confidence limits of 95% are shown for 24 degrees of freedom. Above the cross-spectrum, individual energy density spectra are shown; below are phase values. See caption for Figure II.53.

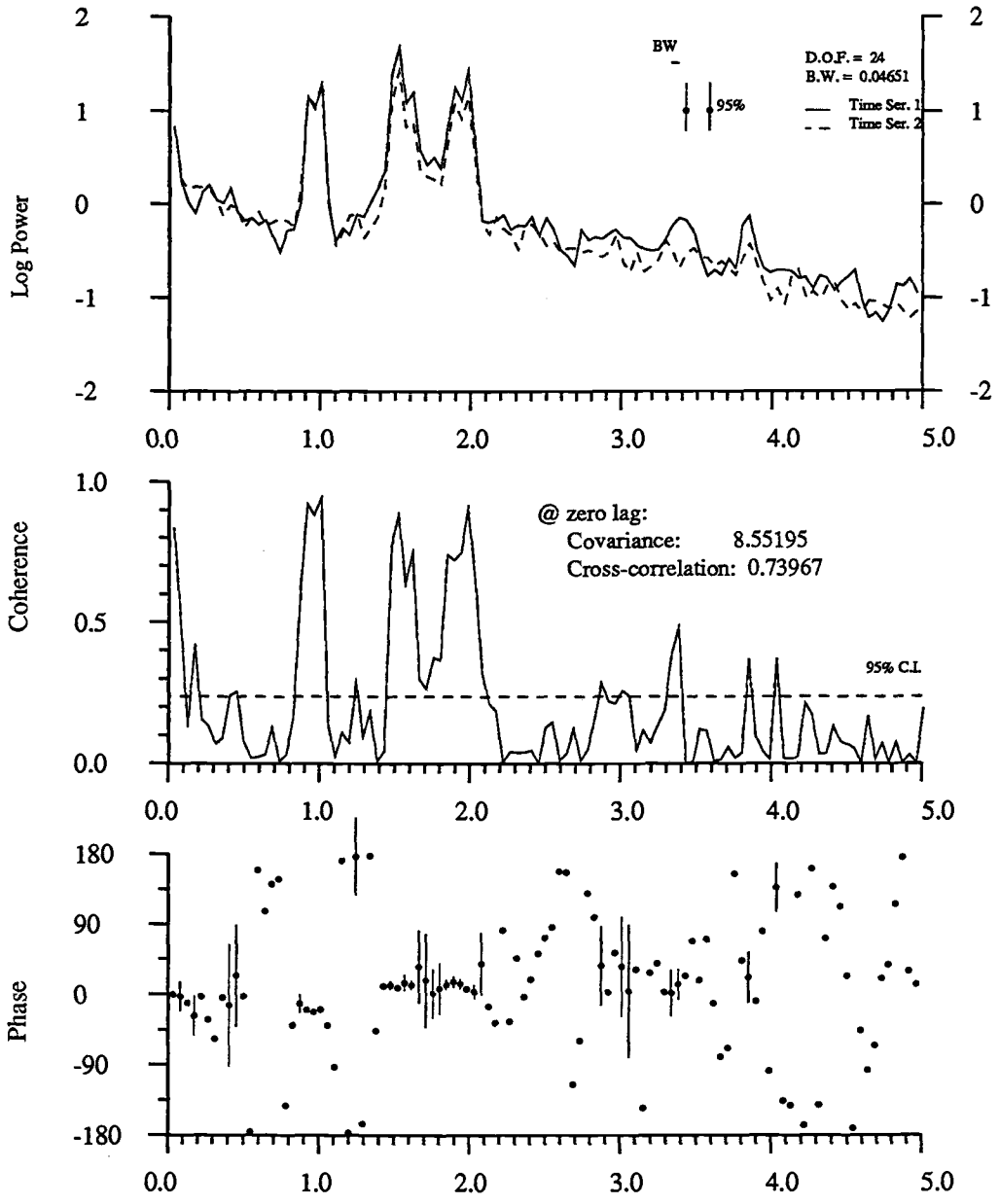

Figure II.73. Cross-spectrum of unfiltered across-ridge flow at ER-3 1936 and ER-3 2036. Confidence limits of 95% are shown for 24 degrees of freedom. Above the cross-spectrum, individual energy density spectra are shown; below are phase values. See caption for Figure II.53.

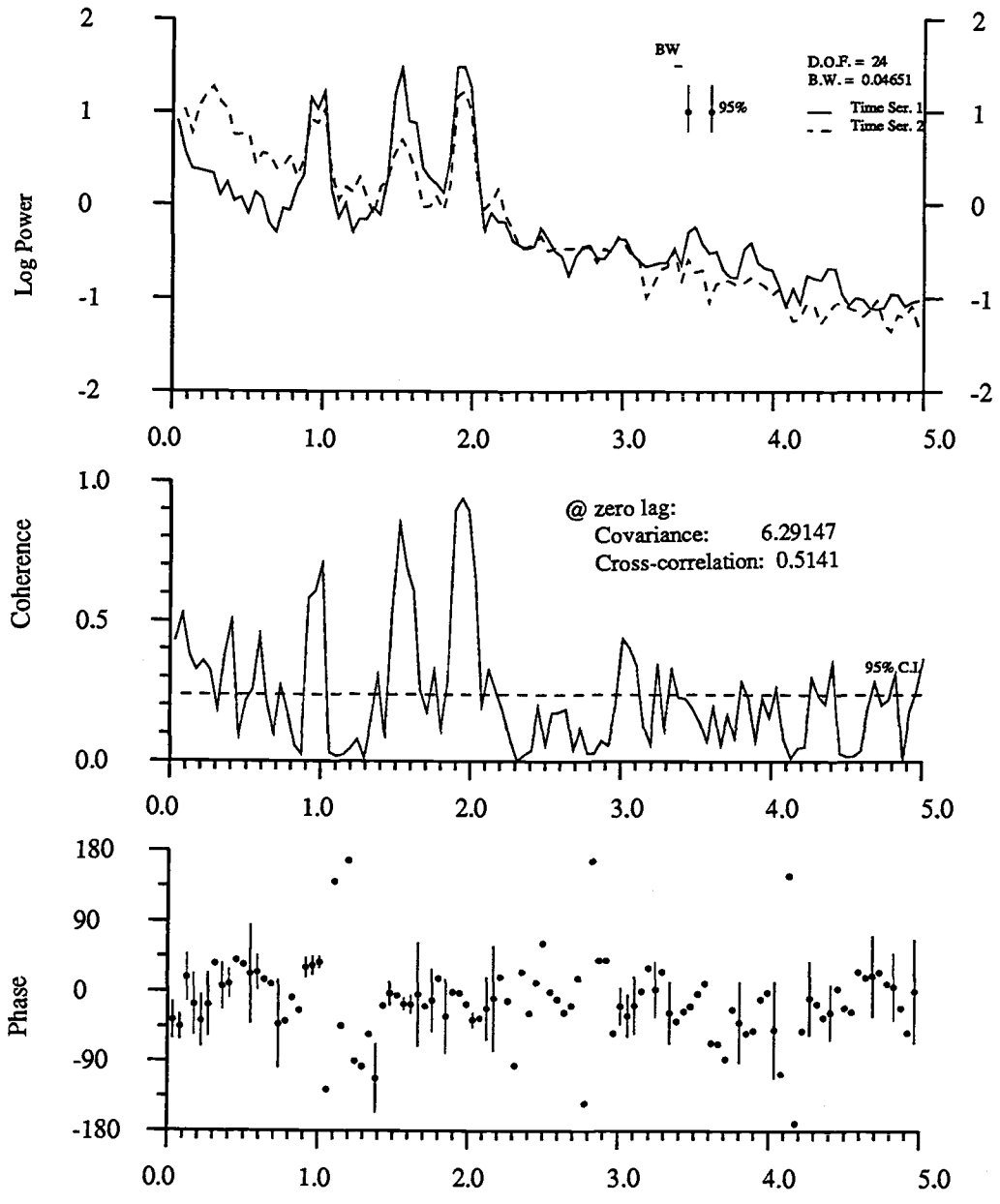

Figure II.74. Cross-spectrum of unfiltered along-ridge flow at ER-3 2036 and ER-3 2136. Confidence limits of 95% are shown for 24 degrees of freedom. Above the cross-spectrum, individual energy density spectra are shown; below are phase values. See caption for Figure II.53.

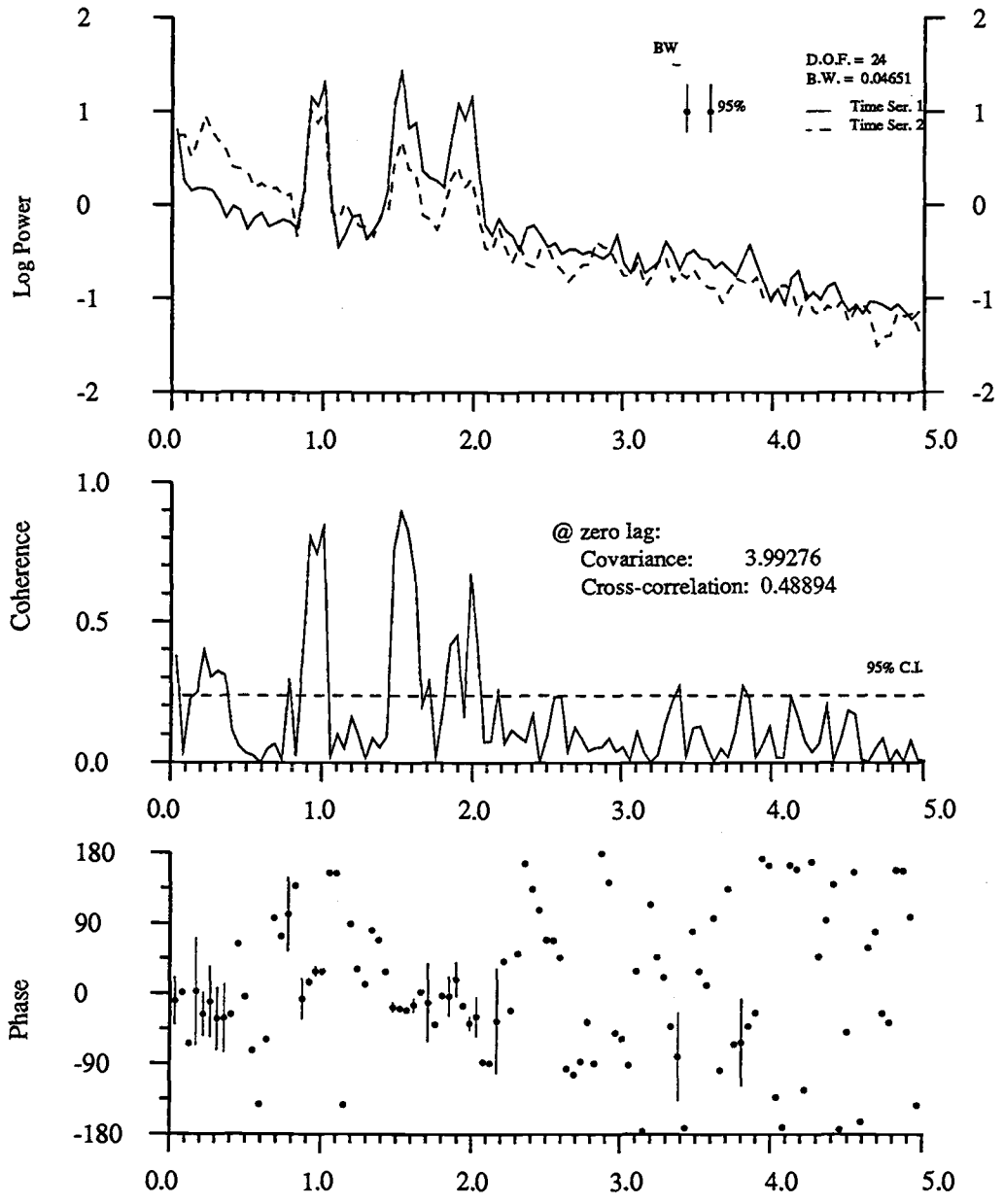

Figure II.75. Cross-spectrum of unfiltered across-ridge flow at ER-3 2036 and ER-3 2136. Confidence limits of 95% are shown for 24 degrees of freedom. Above the cross-spectrum, individual energy density spectra are shown; below are phase values. See caption for Figure II.53.

at the tidal and inertial frequencies. The non-uniformity in the horizontal flow field over the 15 km distance between moorings is evidence of horizontal shear, the implications of which I will later touch on.

Vertical uniformity of horizontal currents depends on depth. Between 1955 and 2055 m at A3, both across and along-ridge flow are highly coherent and in-phase over a wide range of frequencies (Figures II.66 and II.67). The cross-correlation coefficients are 0.71 and 0.75 for along and across-ridge currents. In contrast, over the next 100 m interval, from 2055 to 2155 m, coherence is low; cross-correlation values are 0.22 and 0.13 (Figures II.68 and II.69). Over the depth ranges between instruments on the ER-3 mooring, the strongest coherence is between flow at 1936 and 2036 m (cross-correlation coefficients are 0.78 and 0.74 for along and across-ridge currents, Figures II.72 and II.73), but is significantly lower over the next deeper 100 m-interval (Figures II.74 and II.75), and far lower between 1686 and 1936 m (Figures II.70 and II.71). Other indications of non-uniformity in flow with depth are based on comparisons of PVDs, and this shear is discussed in the section on *Patterns with depth* to follow. Thomson et al. (1989) in surveys with an acoustic Doppler current profiler (ADCP) found persistent shear in horizontal velocities near the top of the Endeavour Ridge neutrally buoyant plume, with vertical changes in speed of approximately 5 cm/s over depths of 100 m. Vertical shear may influence the trajectory of sinking particles, the distribution of solutes, and possibly zooplanktonic distributions (see **Implications**).

Temporal variability in the hydrothermal plume

In the previous sections I established that temperature and attenuation coefficient measured by moored instruments provide information about hydrothermal plume variability. Four factors that may produce variance in plume signals were described. Spectral analysis was introduced as a tool for identifying time scales of important physical processes and comparing records from various instruments. Coherence of temperature and flow velocity support the assertion that near the vent field, horizontal advection regulates the distribution of plume-carried particles and heat. In the sections that follow I bring together direct observations from flow, temperature, and attenuation time series, results of spectral analysis, and evidence from sediment traps to quantify periodic and episodic variability in the hydrothermal plume over time. The discussion proceeds from high- (semi-diurnal) to low- (interannual) frequency.

High-frequency (tidal and inertial) variations

High-frequency variability associated with tidal and inertial oscillations is visible in plots of the unfiltered current meter records (Figure II.40), PVDs (Figures II.3, II.45 and II.46), and energy density spectra (Figures II.47 - II.51). The four dominant tide-producing force constituents are the semi-diurnal principal lunar M_2 and the principal solar S_2, and the diurnal luni-solar K_1 and principal lunar O_1. The relative sizes of these constituents in the order given are 100:47:58:42 (Pond and Pickard, 1983), however tides and tidal currents can be quite different due to baroclinic effects. Near-inertial motions, comparable in magnitude to the M_2 currents, are confined to the frequency band 0.060 - 0.067 cycles per hour (equivalent to about 1.5 cpd and corresponding to a period of approximately 16 hours), which is between the diurnal and semi-diurnal frequencies. An in-depth treatment of the near inertial motions, as well as the tidal constituents, is given in Thomson et al. (1990). In this more general treatment I use the term tidal-range frequencies to include the combined, relatively high-frequency semi-diurnal and diurnal tidal oscillations, as well as inertial motions.

The tidal-range motions are rotary, and, in general, the major axes of ellipses traced by the rotating vector are oriented parallel to the ridge axis (20°T) for the semi-diurnal currents and roughly across-ridge for the diurnal flow. The rotation of the majority of the tidal vectors at Endeavour Ridge, and by definition the inertial flow, is clockwise. The effect of these regular oscillations is to physically expand the area influenced by the neutrally buoyant plume above the vent field by roughly one or two

kilometers. Each of our central vent field moorings, ER-1, ER-2 (A2), ER-3 and ER-4, and possibly the ridge-crest mooring and axial valley moorings ER-2 (R2) and (A3), were within the region where tidal effects are likely to be important in controlling local variability in hydrothermal parameters.

Pronounced high-frequency variability in the raw temperature and attenuation coefficient time series (the removal of which was discussed in the **Methods** section called Data processing) prompts the hypothesis that this variability is due to horizontal advection. Cross-spectral analysis confirms that temperature and flow are most highly coherent at tidal-range frequencies. This evidence supports the hypothesis that tidal advection is a pervasive cause of variance in the hydrothermal plume temperature and fine-particle fields.

In summary, although tidal-range fluctuations were removed in order to resolve additional, less energetic variability in our records, it is important to recognize that the tidally-induced motions are of primary importance in dispersing hydrothermal heat and particles in the zone close to the spreading ridge. Relatively small-scale rotary flow accounts for much of the high-frequency temporal variability and resultant inhomogeneity in the near-vent hydrothermal particle and thermal fields. Further support for this hypothesis are spatial patterns observed in the temperature spectra, and these are discussed in the section on Spatial variability in hydrothermal fluxes.

Two to four-day variations

When a low-pass filter appropriate for removing the tidal and inertial oscillations is applied to the data, oscillations with periods of approximately two days and longer are revealed in the time series (Figures II.14 - II.34). Spectral analysis confirms significant sub-tidal variability of 2-5 day periodicity in some spectra of horizontal flow velocity, temperature and rotary flow, but the pattern is weak (Figures II.47 - II.50). In contrast to the tidal-range frequency peaks, the lower-frequency peaks are not consistently significant at the 95% confidence level. The maximum energy in the currents at these sub-tidal frequencies is typically < 10 $(cm/s)^2/cpd$, approximately an order of magnitude less than the tidal-range frequency maximum. In the case of the temperature spectra, energy associated with these peaks is typically on the order of 10^{-4} $°C^2/cpd$. Four-day energy is particularly strong at ER-1 2127 (Figure

II.47) and ER-3 1936 (Figure II.51), whereas A2 1905 (Figure II.48) shows strong energy at frequency corresponding to a 2.5-day period.

The occurrence of sub-tidal spectral peaks does not adhere to a consistent pattern; the peaks are observed only in some of the flow component and rotary spectra, and their presence seems independent of location relative to the plume core or vent field. Differences among these spectra will be discussed further in the sections on interannual and spatial variability. My results contrast with those of Cannon et al. (1991) who reported much higher variance (up to 100 $(cm/s)^2/cpd$ in clockwise spectra) in broad peaks centered at periods of 4-5 days in all current records below 2000 m near the crest of the southern Juan de Fuca Ridge. These authors found that the 4-day oscillations were more intense in the winter and correlated with maximum wind stress. The implication of this contrast is that storm energy propagating downward from the surface is less of a persistent factor in controlling plume dynamics at Endeavour Ridge than it is along the southern Juan de Fuca Ridge.

Lower-frequency variations

Though energy in most of the flow, rotary, temperature and attenuation coefficient spectra increases at low frequencies, resolution of very low-frequency peaks is limited by record length, and, in the case of light attenuation, by the trend. To evaluate temporal variability of the hydrothermal plume at lower frequencies (periods longer than a week but shorter than a season) I turn to the time series of flow and temperature, as well as settling particle flux data from sediment traps. Evidence of low-frequency variability (event durations >10 days) is observed in time series plots of low-pass filtered records of across and along-ridge flow, temperature and detrended attenuation coefficient. Specific examples include the detrended light attenuation records for A2 2005 (Figure II.5) and ER-4 2056 (Figure II.12), the across and along-ridge flow at ER-3 1936 (Figure II.29), and the temperature records in Figure II.76. To evaluate the importance of this lower-frequency variability, I compare its amplitude to variability at higher frequencies.

Comparison of tidal-range and sub-tidal variability

From the spectra, the amplitude of variations at a particular frequency can be calculated as the square root of the product of the spectral energy density and the frequency. The amplitude of the lowest-frequency temperature variations is 0.003 - 0.008 °C which is typically only half the amplitude of the most energetic temperature fluctuations at tidal-range frequencies (ER-3 1936; Figure II.51). In the case of currents, the relative energies of low-frequency and tidal-frequency variability are dramatically different: the amplitude of the low-frequency variations is characteristically one or two orders of magnitude less than that associated with tides. For example, at A2 1905 along-ridge flow varies by about 0.5 cm/s at 0.03 cpd but up to about 10 cm/s at the semi-diurnal frequency, 2 cpd (Figure II.48).

These observations are consistent with a spatially-defined thermal anomaly (the neutrally buoyant plume) in an advective field characterized by energetic tidal oscillations and, to a lesser extent, low-frequency changes in the mean flow direction (Figure II.44 a). Visualize from above a roughly channeled, streamer-like plume spreading and advecting horizontally away from its source, as previously described. The boundaries of the plume are diffuse due to mixing with the ambient sea water, and there is a thermal gradient across the plume. Mixing and diffusion also generate along-plume gradients. Consider the temperature variations recorded at a fixed point (the moored current meter) when a rotary motion of tidal elliptical dimensions (on the order of 1-2 kilometers) is added to the mean flow. The rotary motion will broaden the across-plume zone that experiences the effects of the plume. As the thermal gradients in the plume are wafted by the fixed sensor they will generate temporally corresponding variability in the temperature record. Long timescale ($\geq$ 10 d) directional changes in the mean flow will also cause temperature variability if the moored instrument is alternately within and outside the plume zone. From the PVDs, it can be seen that such changes do occur. Since typical mean horizontal velocities are about 1 cm/s, much less than the tidal velocities (up to 15 cm/s), the amplitude of the low-frequency current variability should be less than that at tidal frequencies, and indeed it is (compare Figures II.40 and II.18).

One explanation for temperature variability at low frequencies is that directional changes in the mean flow tend to expose the sensor to the temperature extrema; the

current meter tends to be either within the zone of plume influence, or well outside it. Another way of stating this is that low-frequency changes in the mean current determine the plume location (whereas, at least locally, tidal rotations are small, superimposed oscillations that have no net effect on the distribution of hydrothermal effluent). An example of the low-frequency response occurs near the end of the ER-3 2036 record. Low-frequency directional changes in flow, principally in the across-ridge component occur in the last 100 days of the deployment. At approximately day 1190, across-ridge flow changes sign from negative to positive, then back to negative again at about day 1230 (Figure II.30 and the PVD in Figure II.38, lower left panel). Along-ridge flow over this time period generally remains negative. A corresponding increase, then decrease, in temperature is observed (Figure II.30), apparently reflecting the transport of hydrothermally-heated water from the vent field eastward across the axial valley toward the mooring. It is not possible to determine if the warm water originated at the primary vent field or one farther north, however this consideration is irrelevant to the demonstration of the association between longer-period advective variability and local change in hydrothermal plume intensity.

In contrast to the ER-3 2036 example, records from A3 2055 suggest that an explanation other than directional change accounts for the longer-period temperature fluctuations at that site. Flow during the A3 deployment at 2055 m depth followed the axial valley to the southwest (PVD, Figure II.36, upper right panel), and while the flow direction was quite stable and in the vent field-to-mooring direction, current speed did fluctuate (see along-ridge flow in Figure II.21). The corresponding temperature record shows low-frequency variability comparable in magnitude to ER-3 2036 (> 0.05°C) (Figure II.76). In this case, the pattern might be explained by the efficiency with which currents bring hydrothermal effluent past the sensor. Rapid transport with little mixing might produce high temperatures; conversely, slower transport might allow time for more heat diffusion and mixing, resulting in lower temperatures. Even the opposite interpretation is logical: high velocities might enhance mixing and decrease temperature, while low velocities could enhance retention of heat in the advecting water mass. However, the data do not convincingly support either explanation. In the first part of the A3 2055 record, there appears to be an association of lower (less negative) along-ridge velocity with higher temperatures, but later, midway through the deployment, temperature and velocity show no obvious coupling, even though the pattern of velocity fluctuations is persistent over the whole deployment period.

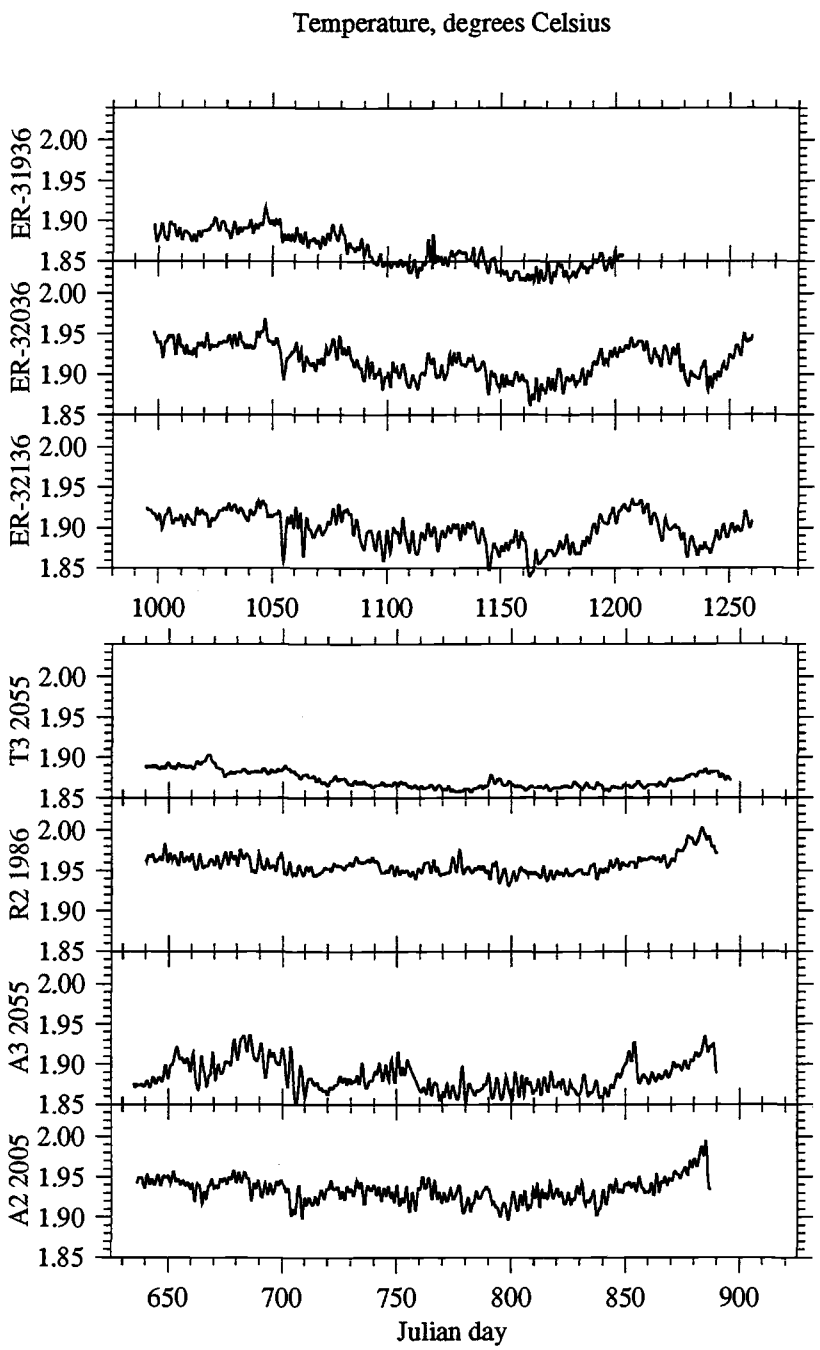

Figure II.76 . Low-pass filtered temperature time series within or beneath the plume for ER-3 and ER-2 moorings.

So while low-frequency advection seems to influence plume behavior near the vent field during the ER-3 experiment, the contrasting ER-2 A3 example above suggests that at distances greater than 2 km from the vent field, low-frequency temperature variability in is brought about by factors other than horizontal advection. Alternative explanations for the ER-2 A3 observations (other than drift in the thermistor output) include 1) temporal changes in quantity or temperature of vent output; 2) spatial variability in flow over the 2 -3 km from the vent field to the mooring that could produce inhomogeneities in the thermal field; and 3) time-variable mixing of hydrothermal effluent from high and low-temperature venting or from more than one vent field. Of these possibilities my data least support (2) and (3). Horizontal current inhomogeneity is minimal within several kilometers of the vent field as shown by high cross-correlation between flow at moorings A2 and A3 (Figures II.62 and II.63). With regard to the third hypothesis, the depth at which the temperature variations were observed, 2055 m, is more than 150 m above the seafloor, above the region most influenced by diffuse venting. Moreover, mooring A3 was positioned 2.5 km south of the primary Endeavour Ridge vent field, far from any other known vent field on the ridge segment. Although I am unable to test the remaining (first) hypothesis, by process of elimination, it appears tenable. From this analysis, I conclude that advection contributes to, but is not the sole cause of low-frequency variability in the neutrally buoyant plume.

Long-term temperature variability

Temperature records are particularly useful for identifying lower-frequency hydrothermal plume variability because, unlike sediment trap data which is temporally constrained by sample cup intervals, temperature records are continuous over longer deployment periods. However, instrumental offsets in the absolute temperature values far exceed the true variability in temperature signals which can be attributed to hydrothermal effects. Potential temperature anomalies measured in the plume core are typically +0.10°C (Thomson et al., 1990). In contrast, offsets between instruments moored only one meter apart were 0.68°C (A3 2155 and 2156 m) and 0.79°C (R2 1985 and 1986 m). The maximum range of temperature measured at each of these instruments was only 0.11°C. I believe, therefore, that the absolute accuracy of these

and the other temperature records is questionable, although relative changes of the signal within each record are valid.

In the discussion that follows, I assume that instrumental drift is negligible, and, consequently, that changes in temperature over time at a single location reflect changes in the local intensity of the hydrothermal plume. Temperature measured at sites T3 and R2 shows little evidence of long-period temperature variability (Figure II.76). However, at A3 some low-frequency fluctuations of approximately 50-day duration and 0.08°C amplitude are observed. Similar trends are found in the ER-3 temperature records.

Bearing on the hypothesis that the dynamics of the neutrally buoyant plume and the settling flux of hydrothermal particles are strongly coupled, I ask: Do periods of high hydrothermal settling particle flux at a given site correspond to periods when the presence of the neutrally buoyant plume is strong? In other words: Are the horizontal fluxes of fine particles and heat coupled temporally to the settling hydrothermal particle flux? That the answers to these questions are not necessarily affirmative can be appreciated by considering the analogous atmospheric condition of clouds unaccompanied by precipitation at a given time and location.

A simple approach to testing the temporal coupling of the neutrally buoyant plume and the flux of settling particles is to evaluate temperature signals averaged over sediment trap cup periods. An association of warmer conditions and higher hydrothermal settling particle flux would support such coupling. Despite the pronounced contrasts among temperature records from different instruments, the mean temperatures for each cup period over which a single current meter was deployed vary little (Table II.4). For example, the mean temperatures for each of the four cup periods at ER-1 2127 m are nearly identical at 1.92 - 1.93°C. At A2 1905 m the mean temperatures for the five cup periods range from 1.79 to 1.86°C. One hundred meters deeper, the range is even narrower: 1.92-1.94°C. One year later at the near vent field mooring ER-3, the cup period temperature ranges were 0.05, 0.04 and 0.03°C at the three plume-affected depths, 1936, 2036 and 2136 m. Even with increasing distance from the active vent field, cup-averaged temperatures are tightly clustered. At mooring A3 the maximum temperature range at any of the three plume affected depths was

0.03°C at 2055 m. At R2 and T3 the maximum single-instrument ranges were 0.03 and 0.05°C.

Table II.4. Temperature, averaged over sediment trap cup periods

Mooring/ depth (m)	cup period	Mean T (°C)	SD (±)	Mooring/ depth (m)	cup period	Mean T (°C)	SD (±)
ER-1	2	1.93	0.03	ER-3	2	1.89	0.01
2127	3	1.93	0.01	1936	3	1.86	0.02
	4	1.93	0.02		4	1.84	0.02
	5	1.92	0.01		5	1.86	0.02
					1	1.87	0.02
ER-2 A2	2	1.80	0.07				
1905	3	1.79	0.03	ER-3	2	1.94	0.02
	4	1.83	0.01	2036	3	1.91	0.02
	5	1.84	0.01		4	1.90	0.02
	1	1.86	0.02		5	1.92	0.02
					1	1.93	0.02
ER-2 A2	2	1.94	0.02				
2005	3	1.93	0.02	ER-3	2	1.91	0.01
	4	1.93	0.02	2136	3	1.90	0.02
	5	1.92	0.02		4	1.88	0.02
	1	1.94	0.02		5	1.90	0.02
					1	1.90	0.02
ER-2 A3	2	1.94	0.02				
1955	3	1.92	0.02				
	4	1.91	0.02				
	5	1.90	0.01				
	1	1.92	0.02				
ER-2 A3	2	1.90	0.02				
2055	3	1.88	0.02				
	4	1.88	0.02				
	5	1.87	0.01				
	1	1.89	0.02				
ER-2 R2	2	2.75	0.01				
1985	3	2.75	0.01				
	4	2.75	0.01				
	5	2.74	0.01				
	1	2.77	0.02				
ER-2 R2	2	1.96	0.01				
1986	3	1.95	0.01				
	4	1.95	0.01				
	5	1.95	0.01				
	1	1.97	0.02				
ER-2 T3	2	2.00	0.01				
1955	3	1.98	0.01				
	4	1.97	0.01				
	5	1.97	0.01				
	1	1.97	0.01				
ER-2 T3	2	1.89	0.01				
2055	3	1.87	0.01				
	4	1.86	0.01				
	5	1.86	0.01				
	1	1.87	0.01				

Though the differences in the cup-averaged temperatures are small, they are statistically different at very high confidence levels according to Student's t-test. The index, t, is directly proportional to the difference in the means but indirectly proportional to the square root of an expression that depends on the standard deviations and the number of observations. Consequently, with our large data sets and low standard deviations, even small differences in the temperature means of 0.01°C are significant at > 0.99 confidence levels.

Given that the observed changes in the cup-averaged means are significant, non-identical means can be interpreted as further evidence for local low-frequency temperature variations in water column above Endeavour Ridge. In the case of ER-1 2127 m, the nearly identical means suggest that the intensity of local hydrothermal influence was relatively constant over the deployment period. In contrast, the cup-averaged settling hydrothermal particle flux at the deepest trap on the mooring, only a meter above the current meter, varied by over a factor of two between the cups with the lowest and highest fluxes of hydrothermal elements (Dymond and Roth, 1988). Further evidence of variability in the settling hydrothermal particle flux is compositional variability among cups as given by Fe/S and Fe/Mn ratios discussed in Dymond and Roth (1988). The contrast of apparent three-month-averaged thermal stability in the water column and temporal differences in the hydrothermal flux into the sediment trap might be taken as evidence that the removal of large, settling hydrothermal particles from the plume is not coupled to the horizontal fluxes of heat and fine particles. But because these measurements were made only about 80 meters above the seafloor, they are not representative of conditions in the neutrally buoyant plume.

Data collected at plume depths during the ER-2 experiment do support a relationship between settling hydrothermal particle flux and local temperature and fine-particle distributions in the neutrally buoyant plume. Cup periods of high hydrothermal particle flux correspond to periods with the highest mean temperatures. As indicated by the hydrothermal copper flux (discussed at length in the next section), at A2 1950 and 2050 m cup 1 had the highest hydrothermal flux, followed by cup 2. At A2 2150 m cup 2 was highest. At A3 2050 m cup 2 had the highest hydrothermal signal. Comparison of these estimates of hydrothermal inputs to the sediment traps with cup-averaged temperatures in Table II.4 indicates that near the vent field, in the axial valley,

there is an association of higher temperature and enhanced hydrothermal particle settling. Farther afield, at mooring T3 the temperature/copper flux association breaks down; the cup period during which the highest copper flux was measured was not the warmest.

Returning to the question of the source of variability in settling hydrothermal particle flux at ER-1, I note that the timing of changes in settling hydrothermal particle flux at the ER-1 mooring suggests a seasonal relationship. Hydrothermal particle flux at depth may be linked to upper water column productivity cycles. Cup 5 with the highest hydrothermal flux collected particles over the period from 8 June to 9 August 1985, in theory, a time of high upper ocean primary production and resultant flux of settling biogenic material. Cup three with the lowest hydrothermal flux spanned the period 8 December 1984 to 8 March 1985, which is a winter, low-productivity season. A scavenging model of sorts would explain this pattern. The removal of hydrothermal particles from the neutrally buoyant plume may be enhanced by the rain of "sticky" organic debris from above, a mechanism similar to cleansing of dust from the air by raindrops. Strong evidence for seasonality is found in sediment trap data from the two subsequent mooring deployments, ER-2 and ER-3, and this is examined in the next section.

At ER-1, however, evidence from sediment trap data to support this seasonal effect is weak. The period of highest above-plume organic carbon flux is not coincident with the timing of highest hydrothermal settling particle flux (Dymond and Roth, 1988). The flow record from 2127 m does not suggest that high cup 5 hydrothermal inputs can be attributed to directional orientation of horizontal flow (Figure II.14). However, as will be shown later, horizontal flow at plume-core depths (which was not measured during this deployment) can differ substantially from flow at other depths. The possibility that vent output was higher, or at least enriched in hydrothermal elements, during cup 5 can neither be proven or dismissed, but as indicated previously, temperature was not elevated during this period (JD 525-587, Figure II.14). This example is an excellent illustration of the difficulty encountered in attempting to reconstruct time-integrated effects of advection that influence measured settling particle fluxes from sparse (in this case, one) point measurements of flow.

Unlike the ER-1 record, subsequent plume-depth temperature records do exhibit changes among cup periods, however these changes are not readily explained by horizontal advection. During the ER-2 experiment cup 2 spanned the period 6 October to 23 November 1985, and cup 1 was open for one week at the end of September, beginning of October 1985 *and* from 15 April to 12 June 1986. So cup 2 represents an autumn period, while cup 1 largely represents a spring sampling (see Table II.2). At A2 1905 and 2005, cup 1 had the highest temperature (tied with cup 2 at 2005 m). At A3 1955 and 2055, the highest temperature were recorded in cup 2 (tied with other cups at 2155 and 2156 m). At R2 1985 and 1986, cup 1 was warmest, and at T3 1955 and 2055, cup 2 was warmest. In light of the mooring positions (refer to Figure II.2), and the location of the primary vent field, these observations collectively suggest that during the fall of 1985, the plume followed a generally southward trajectory, while generally eastward flow prevailed during the spring of 1986. The PVDs from A2 1905 and 2005 m (Figure II.35, upper right and lower left panels) contradict this hypothesis, for they show eastward flow in the fall and southward flow in the spring. The PVD from A3 (Figure II.36) shows a trend to the southwest along the axial valley in the fall, and more westward in the spring, particularly at 1955 m. At R2, flow during both time periods has a strong southward component, but it appears to follow the ridge crest more closely in the spring, while veering slightly eastward in the fall. At T3, flow is generally southward in the fall, but westward in the spring (Figure II.37). Recent evidence which suggests that thermal plumes may originate at other vent fields along the Endeavour Segment (Thomson et al., 1992b) complicates interpretation of these records. However, if the primary vent field was the dominant source of heat in the neutrally buoyant plume at the time of the measurements, flow records obtained during the ER-2 experiment do not support the hypothesis that cup-averaged temperatures reflect long-term trends in physical transport of the plume by currents.

To summarize: Small, but statistically significant variations in mean temperature reflect the degree to which the neutrally buoyant plume influences a given mooring and depth during the collection interval for each sediment trap cup. The cup-averaged temperatures do not obviously reflect long-term advection patterns, but in some near-field instances there appears to be an association of higher temperature with elevated flux of settling hydrothermal particles. I suggest that these somewhat confusing observations might reflect persistent patchiness in the neutrally buoyant plume that

would tend to obscure the flow/temperature relationship. Such inhomogeneity could reflect multiple plumes originating at separate vent fields.

Variations in settling particle flux

Sediment trap data offer further evidence of low-frequency variability in hydrothermal particle flux. Temporal resolution of the settling particle flux, as determined by sample cup collection periods, varies between two weeks (in the ER-4 deployment) and three months (in ER-1). The maximum variation in total settling particle flux measured at depths ≥ 1950 m is by a factor of 47 between 0.121 mg/cm^2/yr during the 48-day, A2 1950 m cup 4 period (JD 740-788) and 5.724 mg/cm^2/yr during the 48-day A2 2150 m cup 2 period (JD 644-692) (Figures II.77 and II.78, bottom panels). Variation by cup period in total particle flux in any single trap ranges from a factor of 1.4 (T3 2050 m) to a factor of 17 (A2 1950 m). In the deepest 300 m of the water column, within 15 km of an active vent field, the flux of settling particles varies significantly on time scales of weeks to months. Values of total settling particle flux, however, provide little information on the cause of the variability; the composition of the particulate material must be considered.

Dymond and Roth (1988) use normative analysis to determine the proportion of the total particle flux that is of hydrothermal origin. On an annual basis, only about 18% of the total settling particle flux at 1950 m (33% at 2100 m) is hydrothermal, with the remainder representing biogenic and aluminosilicate material. **[biogenic+Al-Si = CaCO3 + opal + 2.5(C-org) + 100/8(Al)]** Using this normative calculation, the compositional data for A2 1950, 2050 and 2150 m suggest that 31, 60 and 58% of the flux is hydrothermal respectively. At 2150 m for the ER-3 and ER-4 deployments the hydrothermal flux was 11 and 2.4%. Although the hydrothermal flux is often smaller than the combined biogenic and aluminosilicate contribution, it shows high temporal variability. Within several kilometers of the vent field, the hydrothermal flux spans several orders of magnitude from 8 μg/cm^2/yr at A3 2050 m to 2670 μg/cm^2/yr at A2 2150 m.

An alternative approach to compare the settling hydrothermal flux over sediment trap cup periods uses copper as an indicator of hydrothermal input. Relatively small

Figure II.77. Plume-core settling particle fluxes by sediment trap cup period as a function of time at moorings close to the vent field. The bottom panel is the total particle flux, while the three components above represent terrestrial (Al), biogenic (C_{org}), and hydrothermal (Cu) inputs. From left to right, the first 5 histogram bars correspond to experiment ER-2, the second 5 to ER-3, and the 5 narrow bars to the right correspond to ER-4. Dates are noted on the Cu panel.

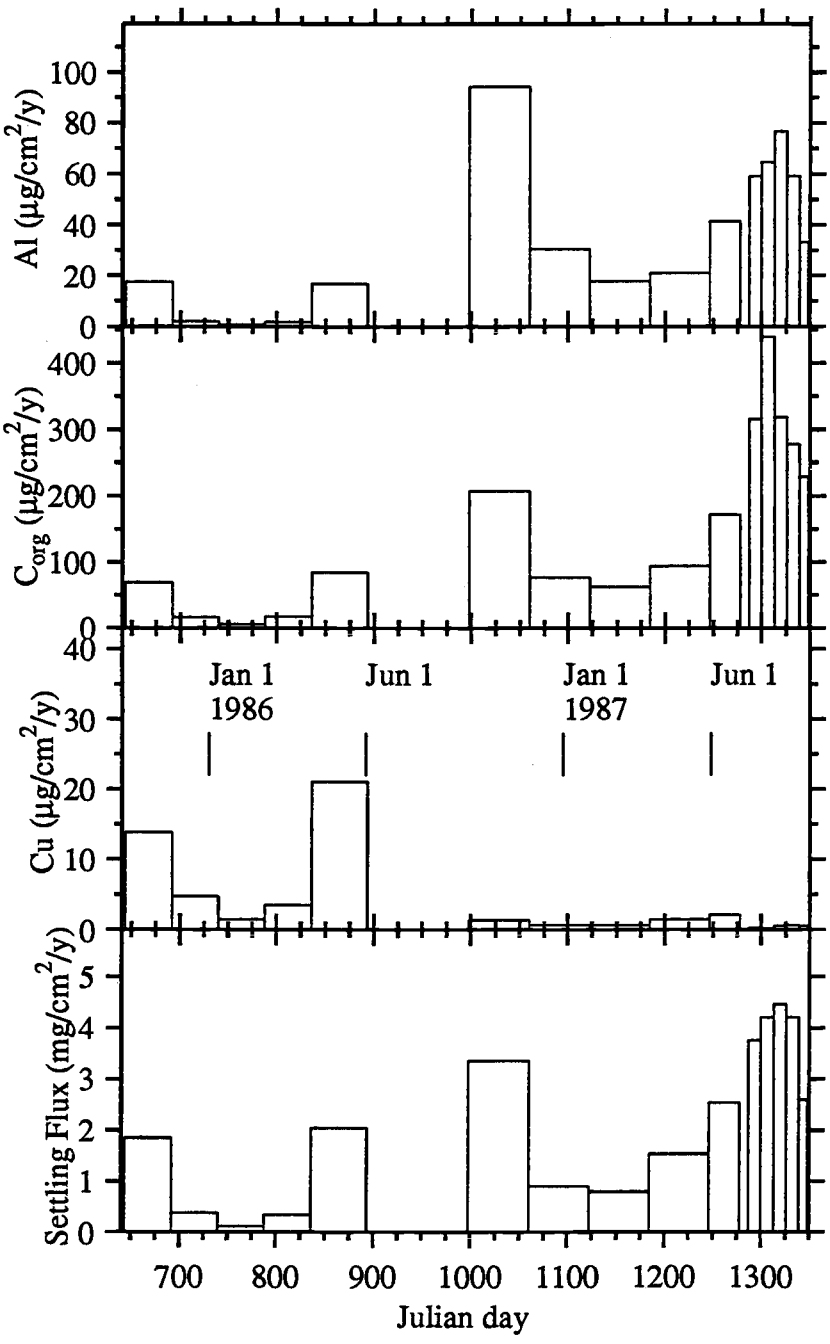
Data for A2, ER-3 and ER-4 at 1950 m
Al (µg/cm²/y)
100
80
60
40
20
0
C_org (µg/cm²/y)
400
300
200
100
0
Jan 1
1986
Jun 1
Jan 1
1987
Jun 1
Cu (µg/cm²/y)
40
30
20
10
0
Settling Flux (mg/cm²/y)
5
4
3
2
1
0
700
800
900
1000
1100
1200
1300
Julian day

Figure II.77.

Figure II.78. Beneath-plume settling particle fluxes by sediment trap cup period as a function of time at moorings close to the vent field. The bottom panel is the total particle flux, while the three components above represent terrestrial (Al), biogenic (C_{org}), and hydrothermal (Cu) inputs. From left to right, the first 5 histogram bars correspond to experiment ER-2, the second 5 to ER-3, and the 5 narrow bars to the right correspond to ER-4. Dates are noted on the Cu panel.

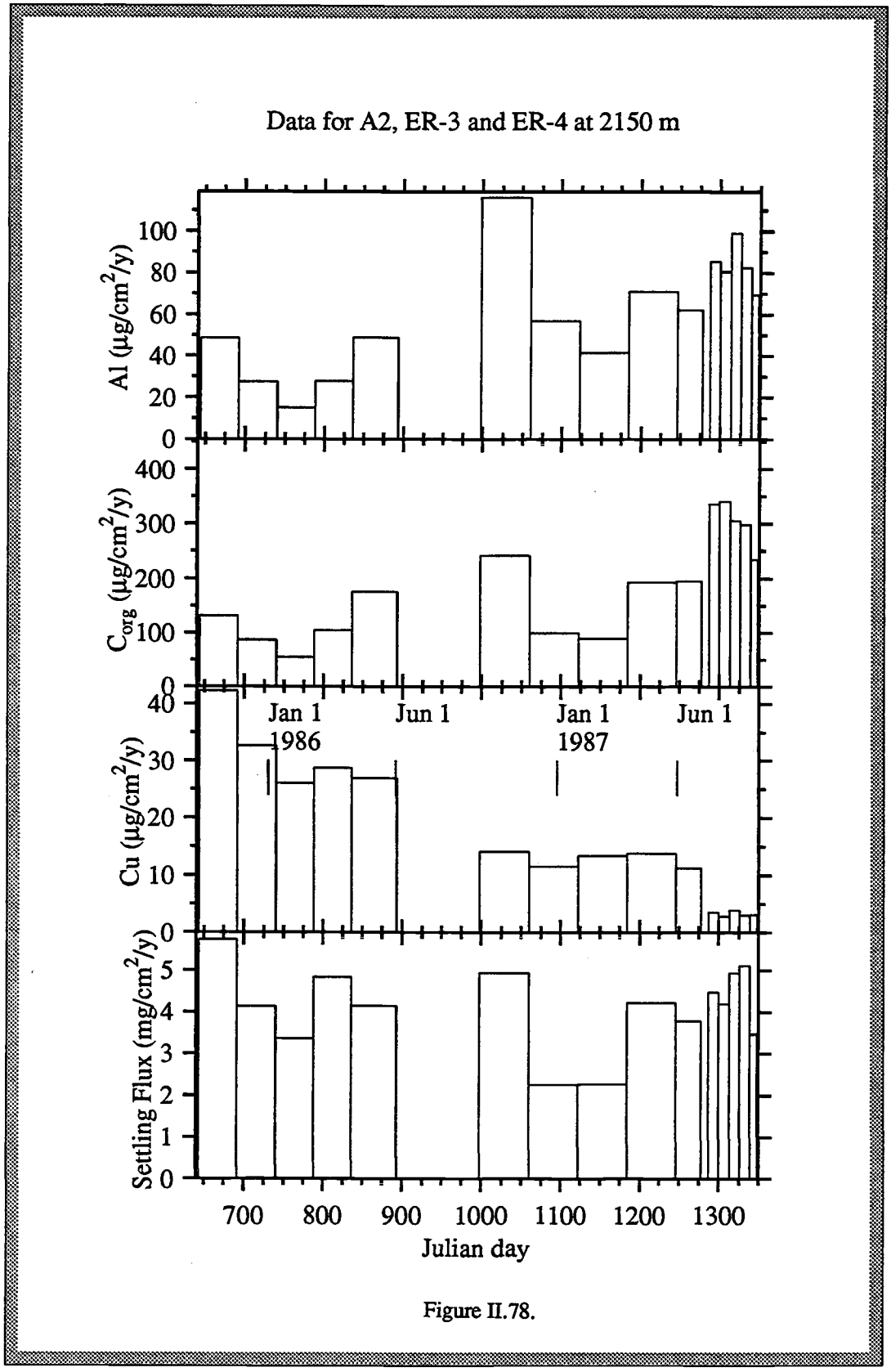
Data for A2, ER-3 and ER-4 at 2150 m
Al (µg/cm²/y)
100
80
60
40
20
0
C_org (µg/cm²/y)
400
300
200
100
0
Cu (µg/cm²/y)
40
30
20
10
0
Settling Flux (mg/cm²/y)
5
4
3
2
1
0
Jan 1
1986
Jun 1
Jan 1
1987
Jun 1
700
800
900
1000
1100
1200
1300
Julian day

Figure II.78.

contributions to the total copper flux from biogenic and aluminosilicate sources are calculated and subtracted to yield fluxes of hydrothermal copper. Previous sediment trap investigations have shown that dissolved copper is removed from seawater through scavenging by organic particles (Fischer et al., 1986). My calculation assumes that the rate at which dissolved copper is scavenged by organic material is the same for both plume-entrained, chemosynthetic and photosynthetic-based organic particles originating above the plume. The Cu/Al ratio in aluminosilicates is assumed to be 6.7×10^{-4}, according to the crustal abundances of elements published in Taylor (1964). The Cu flux from aluminosilicates is calculated as the product of this ratio and the flux of Al at the depth of interest. The Cu from biogenic sources is calculated in a two-step process. First, the above-plume biogenic Cu is calculated as the difference between the total Cu flux above plume (approximately 1700 m) and the aluminosilicate Cu. Second, I compute the in-plume biogenic Cu as the product of the above-plume ratio of biogenic Cu to organic carbon and the in-plume organic carbon. Finally, the hydrothermal Cu is calculated as the total Cu flux minus the biogenic and aluminosilicate Cu at the depth of interest.

In the form of an equation:

$Cu_h = Cu_t - Cu_b - Cu_a$

where

subscripts h, t, b, and a refer to hydrothermal, total, biogenic, and aluminosilicate;

$Cu_a = (Cu/Al)_a * Al = (6.7 * 10^{-4}) * Al$;

$Cu_b = \{Cu_b/C\text{-}org\}_{(above\text{-}plume)} * C\text{-}org_{(plume)}$

$= \{[Cu_t - Cu_a] / C\text{-}org\}_{(above\text{-}plume)} * C\text{-}org_{(plume)}$;

where

C-org refers to organic carbon

and

Cu_t is measured.

Table II.5. Temporal variation in copper flux at Endeavour Ridge

Mooring/ depth (m)	Cup	Cu flux ($\mu g/cm^2/yr$)	C-org flux (1700 m)	Vent-to-mooring direction	Current velocity (cm/s)
ER-2 A2	2	13.75	129.2	30°T	
1950	3	4.77	91.8		
	4	1.46	52.8		2.19 156°T
	5	3.48	116.4		
	1	21.00	160.1		2.65 169°T
ER-2 A2	2	47.18	129.2	30°T	
2050	4	17.27	52.8		
	5	11.55	116.4		1.70 135°T
	1	58.33	160.1		1.87 164°T
ER-2 A2	2	42.24	129.2	30°T	poor data
2150	3	32.68	91.8		
	4	26.02	52.8		
	5	28.79	116.4		
	1	26.90	160.1		
ER-2 A3	2	1.40	N/A	200°T	3.90 193°T
2050	3	0.98			
	4	0.58			
	5	0.48			
	1	0.44			4.25 203°T
ER-2 A3	2	1.04	N/A	200°T	
2150	3	0.66			
	4	0.59			
	5	0.57			
	1	0.50			
ER-3	2	1.41	246.8	40°T	
1950	3	0.67	132.9		2.42 187°T
	4	0.68	166.3		
	5	1.47	261.3		
	1	2.07	209.3		3.14 211°T
ER-3	2	14.05	246.8	40°T	poor data
2150	3	11.51	132.9		
	4	13.38	166.3		
	5	13.80	261.3		
	1	11.24	209.3		

Hydrothermal copper accounts for more than 99% of the copper flux in all sediment trap cups at 1950, 2050 and 2150 m on the A2 mooring. During the ER-3 deployment more than 90% of the copper flux at 1950 m and 99% of the copper flux at 2150 m is hydrothermal. At 2050 m at mooring site A3, several kilometers south of the vent field, the deployment-averaged copper flux was still 98% hydrothermal, however the percent hydrothermal Cu by cup period reached a minimum of 70% during cup 1. Of the small amount of copper that is not hydrothermal, our calculations suggest that more than 83% during ER-2 and 60% during ER-3 is of biogenic origin, with only minor aluminosilicate inputs. These results indicate that copper flux is a reliable indicator to compare hydrothermal input in sediment traps moored within and beneath the neutrally buoyant plume.

Significant variability in hydrothermal copper flux among cup periods is an indication of temporal variability in the hydrothermal plume. As shown in Table II.5, at A2 1950 m Cu flux is highest in cup 1 (21 $\mu g/cm^2/yr$) and lowest in cup 4 (1.4 $\mu g/cm^2/yr$). At 2050 m there is a factor of 5 variation among cup periods, with the highest Cu flux, 58 $\mu g/cm^2/yr$, in cup 1, and the lowest, 11.5 $\mu g/cm^2/yr$, in cup 5. At 2150 m the factor by which the copper flux varies is less than 2, with the highest flux 42 $\mu g/cm^2/yr$ in cup 2 and the lowest 26 $\mu g/cm^2/yr$ in cup 4. During the ER-3 experiment, at 1950 m, hydrothermal copper flux varied by a factor of about 3, while at 2150 m the flux was relatively constant but more than a factor of 2 less than during the A2 experiment at the same depth. Even at mooring A3 2050, hydrothermal Cu flux varies by a factor of 3 among cup periods, from 0.44 $\mu g/cm^2/yr$ in cup 1 to 1.4 $\mu g/cm^2/yr$ in cup 2.

I now test whether the differences in settling copper flux are due to advection. Cup-averaged current speeds and directions are compared with corresponding copper fluxes. The following discussion is illustrated graphically in Figure II.79. At the A2 1950 m trap the difference between the flow during the cup period of highest (cup 1) and lowest (cup 4) Cu flux, is that the average current speed during cup 1 was about 0.5 cm/s higher than in cup 4 and it flowed 13° more toward the south. Considering the relative positions of the vent field and the mooring - the mooring was $\approx$ 0.5 km northeast of the vent field - the average current velocity difference cannot explain the differences in settling copper flux. If however, the major source of the copper was a source to the north, for instance, the Fairycastle Site, mean advection could account for

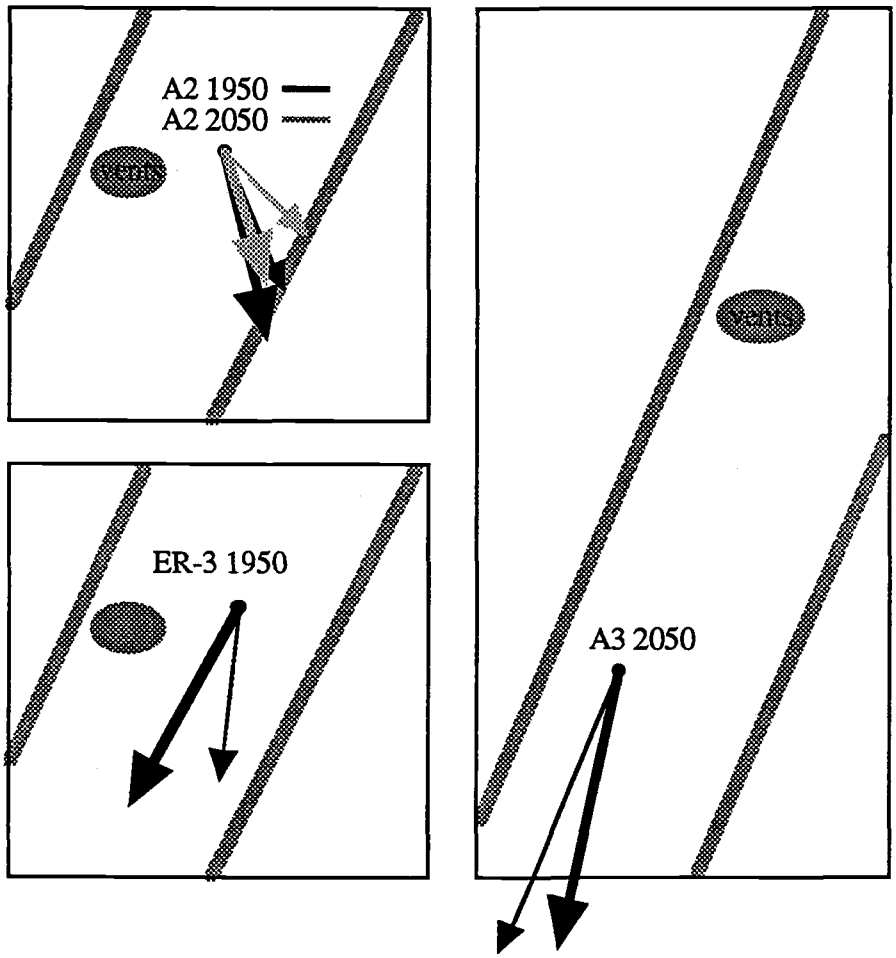

Figure II.79. Summary of the relationship between horizontal flow (averaged over sediment trap cup periods) and settling hydrothermal particle flux at Endeavour Ridge. In each of the three panels, the gray parallel lines represent the boundaries of the 1-km-wide axial valley, the axis of which is oriented 20°T. The shaded ellipse indicates the location of the vent field. The points from which pairs of vectors originate indicate the location of the specified moorings relative to the vent field. The thick vector shows the mean horizontal flow at the specified depth(s) corresponding to the sediment trap cup period of highest Cu flux; conversely, the thin vector represents flow during the period of lowest Cu flux. With respect to transport of hydrothermal material from the vent field to the mooring, the thick and thin vectors are not significantly different.

the copper flux pattern. This however is not likely, and I will demonstrate shortly that there is a more logical explanation.

Applying this mean current analysis to the A2 2050 data, I find a similar situation. Flow during the period of highest Cu flux was only 0.17 cm/s faster and directed 29° more southward than during the period of lowest Cu flux. At ER-3 1950 m, which was positioned only about 200 m east of its predecessor A2, flow was to the southwest during the periods of both highest and lowest Cu flux. The difference is that during the high flux cup (1) flow was more westward by 24° and faster by 0.72 cm/s than in cup 3. During both high and low periods of Cu flux at A3 2050 m, flow was southward and a bit westward at relatively high average current speeds of about 4 cm/s. The minor differences are that during the high flux period mean currents were 0.35 cm/s slower and directed a bit less to the west, i.e. about 10° more to the south.

From the observations illustrated in Figure II.79, one might reason that mean current velocity does not control the distribution of settling hydrothermal particles. This is not strictly true, because advection does determine the **location** of copper-rich plume waters. However, the **removal** of copper from these waters is regulated by another control mechanism: Copper removal is enhanced by the flux of organic particles settling through the horizontally advecting plume. The seasonal variation of upper-ocean biological productivity (indicated in part by above-plume organic carbon flux in Table II.5) is reflected at depth in a corresponding pattern of settling organic material. Copper, which does not come principally from the euphotic zone, exhibits a similar seasonal deep-sea flux pattern. The inference is that the rain of sticky, organic particles through the neutrally buoyant plume, in effect, cleanses the plume of hydrothermal copper. This seasonal effect will be discussed in greater depth later.

Seasonality

The record of settling particle flux shows strong evidence of seasonality in the hydrothermal component. The flux of hydrothermal elements Cu, Zn and Fe increases during times of high upper water column productivity (spring/summer) and decreases during the less productive seasons (Figure II.80 and II.81). The neutrally buoyant plume is far deeper than the depth range where light and nutrient availability generate seasonal patterns of biogenic settling particle flux. I suggest that the hydrothermal

Figure II.80. Plume-core settling particle fluxes, by sediment trap cup period, over ≈ 3 years. Fluxes of Fe, Zn, and Cu are shown in addition to the total particle flux. From left to right in groups of 4, 5, 5 and 5 histogram bars, data are for deployments ER-1, ER-2 A2, ER-3 and ER-4. Dates are noted in the Zn panel.

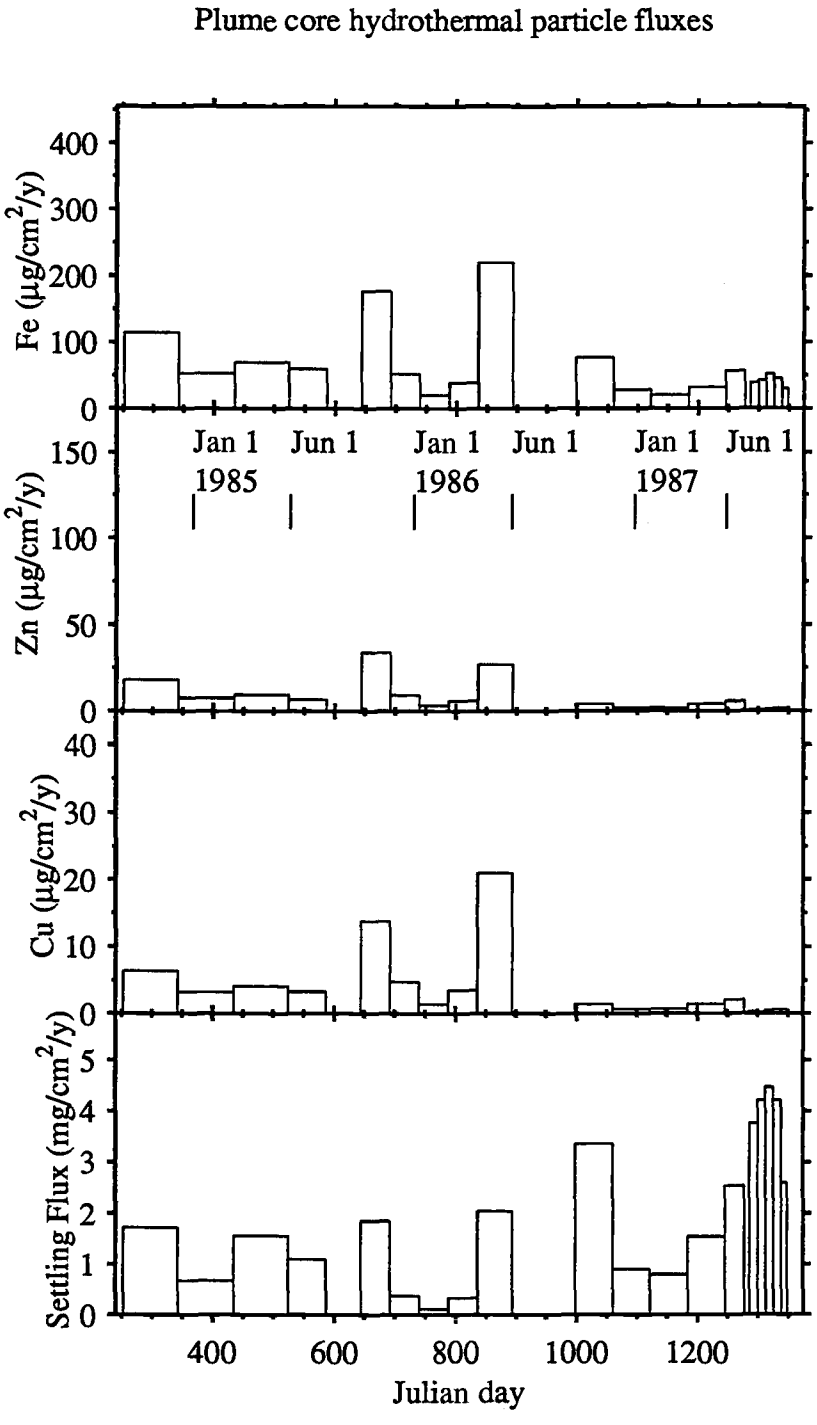
Plume core hydrothermal particle fluxes
Fe (µg/cm²/y)
400
300
200
100
0
Jan 1 1985
Jun 1
Jan 1 1986
Jun 1
Jan 1 1987
Jun 1
Zn (µg/cm²/y)
150
100
50
0
Cu (µg/cm²/y)
40
30
20
10
0
Settling Flux (mg/cm²/y)
5
4
3
2
1
0
400
600
800
1000
1200
Julian day

Figure II.80.

Figure II.81. Beneath-plume settling particle fluxes, by sediment trap cup period, over ≈ 3 years. Fluxes of Fe, Zn, and Cu are shown in addition to the total particle flux. From left to right in groups of 4, 5, 5 and 5 histogram bars, data are for deployments ER-1, ER-2 A2, ER-3 and ER-4. Dates are noted in the Zn panel.

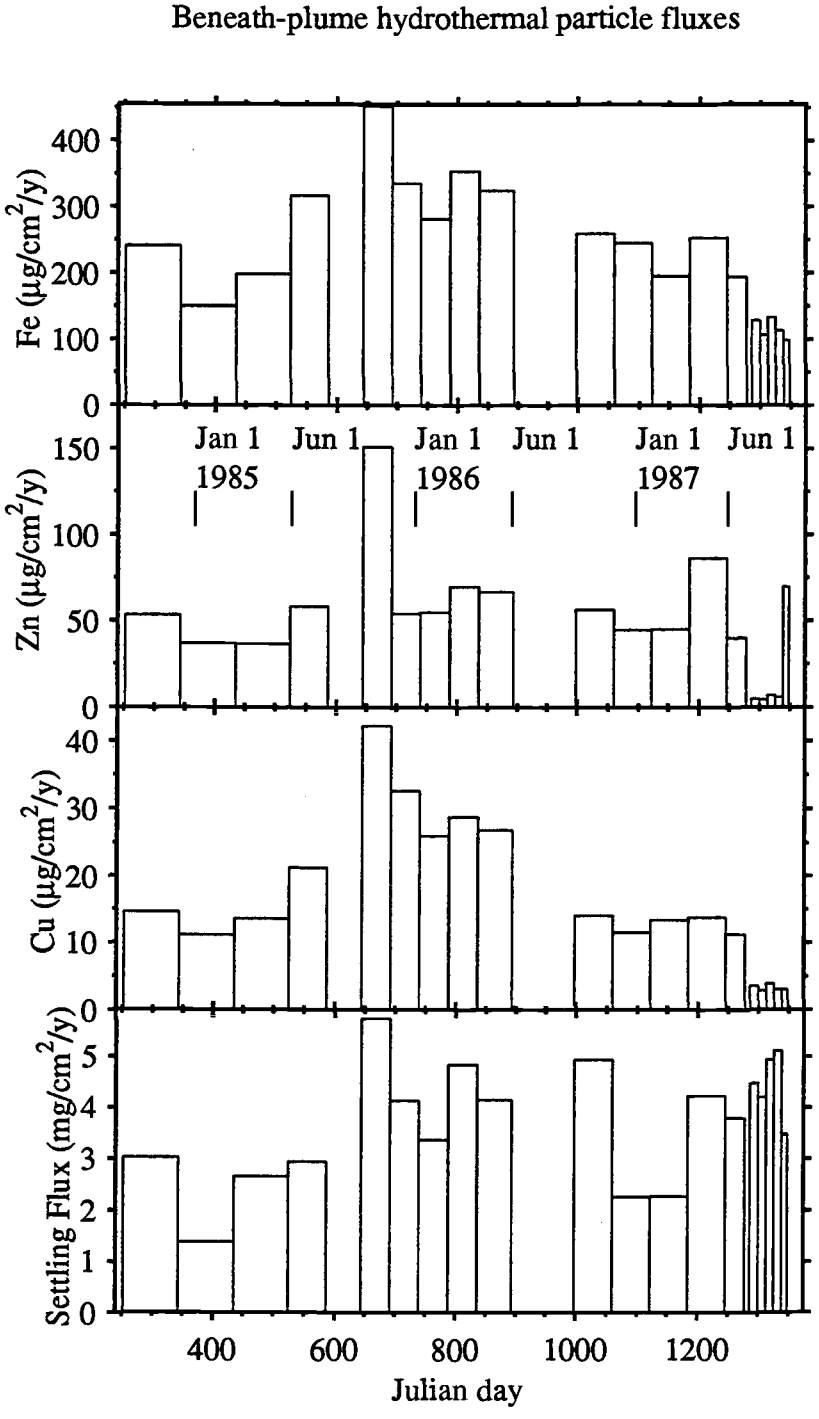
Beneath-plume hydrothermal particle fluxes
Fe (µg/cm²/y)
400
300
200
100
0
Jan 1
1985
Jun 1
Jan 1
1986
Jun 1
Jan 1
1987
Jun 1
Zn (µg/cm²/y)
150
100
50
0
Cu (µg/cm²/y)
40
30
20
10
0
Settling Flux (mg/cm²/y)
5
4
3
2
1
0
400
600
800
1000
1200
Julian day

Figure II.81.

Figure II.82. Horizontal flow, temperature, and attenuation coefficient near the vent field, at plume-core depths, over three consecutive mooring deployments, integrated over sediment trap cup periods to facilitate comparison with the settling flux data shown in Figure II.77. Dates are noted in the bottom panel.

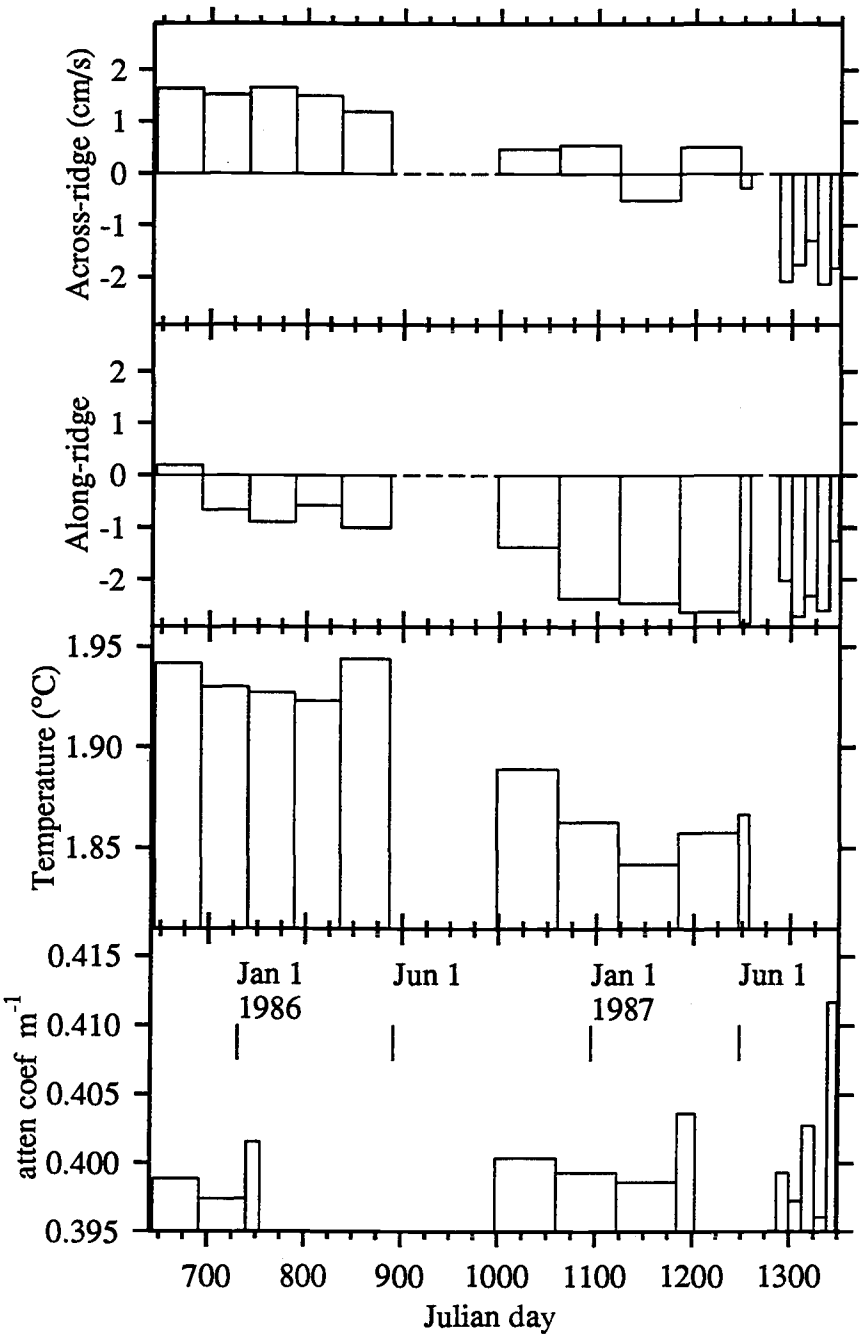
Data for moorings A2 2005, ER-3 1936, ER-4 1956
Across-ridge (cm/s)
2
1
0
-1
-2
Along-ridge
2
1
0
-1
-2
Temperature (°C)
1.95
1.90
1.85
atten coef m-1
0.415
0.410
0.405
0.400
0.395
Jan 1
1986
Jun 1
Jan 1
1987
Jun 1
700
800
900
1000
1100
1200
1300
Julian day

Figure II.82.

particle flux pattern is produced by an enhanced rain of settling biogenic material with an above-plume source through the non-buoyant plume. This high flux of sticky organic material (marine snow) would bind, physically or chemically, with the hydrothermal particles and accelerate their settling to the seafloor.

Abundant support for this hypothesis is available in the literature. This scavenging mechanism is consistent with that described by Deuser (1986) to account for variations in deep-water particle flux in the Sargasso Sea, whereby sedimentation and upper ocean productivity are closely coupled. Bacon et al. (1985) found seasonal variations in radionuclide fluxes at a deep-ocean station which they attribute to scavenging by biogenic particles derived from the overlying surface water. Tyler (1988) reviews experimental results that document seasonal variability in deep-sea particle flux, as well as in physiological response of deep-sea biota to seasonal pulses of sinking, surface-derived, organic matter. Seasonal signals in upper-ocean primary production are rapidly transferred to the deep sea by settling particles, effects of advection and particle transformation notwithstanding, according to Asper et al. (1992).

The settling particle flux varies in both quantity and composition over time. Figures II.82 and II.77 summarize the dynamics and settling particle flux near the plume core over sediment trap cup periods during the ER-2, 3 and 4 experiments. In addition to the total settling particle flux, copper, organic carbon, and aluminum, are plotted and serve as indicators of hydrothermal, biogenic, and detrital fluxes respectively. The lowest overall fluxes were recorded during the ER-2 A2 deployment and correspond to the low productivity winter season (3 cups spanning 23 November 1985 to 27 February 1986). A similar seasonal pattern is also observed in the subsequent ER-3 deployment, although the comparable fluxes are twice as large. The highest fluxes, up to 4.5 $mg/cm^2/y$, were measured during the ER-4 deployment which spanned the highly productive summer season (11 July - 10 September 1987). Indeed, the organic carbon flux is at a maximum over this period. The seasonality of the settling fluxes extends to the aluminum flux also. The coupling of Al and organic carbon may be the result of terrestrial nutrient inputs which fuel primary productivity. Alternatively, indiscriminate scavenging of particulate material by organic-rich marine snow or incorporation into fecal material might explain the link.

The Cu fluxes in the plume core during the ER-3 and ER-4 experiments are very low, up to an order of magnitude lower than the A2 fluxes. The observation that organic carbon flux was up to four times greater during the later experiments does not contradict the hypothesized link between productivity and removal of hydrothermal particles. I interpret this as evidence of limited copper availability during these times as a result of plume advection away from the moorings. The effects of advection on settling hydrothermal particle flux are demonstrated by comparing the flow and flux data within the plume core during the A2 and ER-3 deployments. Recall that the two moorings are, for all practical purposes, in the same position relative to the vent field. Copper flux was an order of magnitude higher during A2 than during ER-3 (Figure II.77), even though organic carbon flux was significantly higher during ER-3. If the seasonal effect was the only determinant of Cu flux, this would present a dilemma. However, note that, although during neither deployment did flow follow a vent-to-mooring course, currents during ER-3 were directed southwest, along-ridge whereas, during A2 flow had a stronger across-ridge, vent-to-mooring trend (Figure II.79). So during A2, more plume-transported Cu was available for scavenging than during ER-3. Mean flow during the ER-4 deployment had a very strong westward component (Figure II.39) which guided the plume from above the vent field in the opposite direction from the mooring, thereby limiting copper availability. The possibility that there was some fundamental difference in plume chemistry between the deployments cannot be ruled out, but assuming there was not, advection is a likely candidate for the control mechanism.

Interestingly, some seasonality is noted in the corresponding current and temperature records at plume depths (Figure II.82). It appears that the dominant flow component, across-ridge for A2 and along-ridge for ER-3, intensifies slightly, and temperature drops slightly, during the winter. It is possible that this intensification moved hydrothermal material farther from the vent field, thereby reducing the near-field temperatures and settling fluxes. During the ER-4 summer, flow is altogether different, with a strong westward component, the significance of which is stated above. Cannon et al. (1991) also found evidence of seasonality in the mid-depth flow above the southern Juan de Fuca Ridge. There, 4-day variance was higher during the winter and spring, and coincided with a pattern of rotating current vectors and maximum surface wind stress.

Beneath the plume, at approximately 2150 m depths, total settling particle flux is enhanced, particularly for ER-2 A2 which is more than 4 times the plume-core flux. The total flux is also slightly higher at the deeper level for the ER-3 experiment. Seasonal patterns in particle flux measured deeper in the plume are similar to the plume core records for Al and organic carbon (Figure II.78). In general, Al, organic carbon and Cu all increase in the deeper traps, however the increase is most dramatic for copper flux (Figure II.83). Temperature at the deeper instruments (Figure II.84) shows the same type of seasonality noted in the records obtained above 2000 m. Flow patterns are similar but the current velocities are lower in the deeper records.

As a final point regarding seasonality, although it seems likely that at least some of the baseline offsets in attenuation coefficient time series are artificial, the possibility that they are real cannot be ruled out. In fact, the observed pattern in above-plume records suggests seasonality. There is some offset in the baselines of above plume records, A2 1656, ER-3 1686 and ER-4 1706, around a value of 0.4 m^{-1} (Figures II.16, II.28 and II.32, bottom panels). A baseline increase of 0.1 m^{-1} over the three-year experiment is of the same magnitude as the high-frequency variability in plume-core records. These subtle changes, if not instrumental, may reflect a seasonality of the upper water column fine-particle field. ER-4, with the highest baseline, was a summer deployment, and perhaps higher surface productivity during this period led to additional inputs of fine particles. A decrease in attenuation coefficient during ER-3 corresponds to the winter, low productivity period (December-March).

Interannual variations

Because the longest record is from the central mooring at plume-core depths, I will use the ER-2 A2, ER-3 and ER-4 data to evaluate longer period hydrothermal plume behavior . These data show distinct interannual differences in the current regime.

At first glance, horizontal flow at the depth of the neutrally buoyant plume seems generally constant over time. The record-averaged current speed for the three plume core instruments A2 2005, ER-3 1936 and ER-4 1956 is comparable at 5.2 ± 2.4, 5.5 ± 2.3 and 5.8 ± 1.6 cm/s respectively. Speeds ranged from the stall speed of

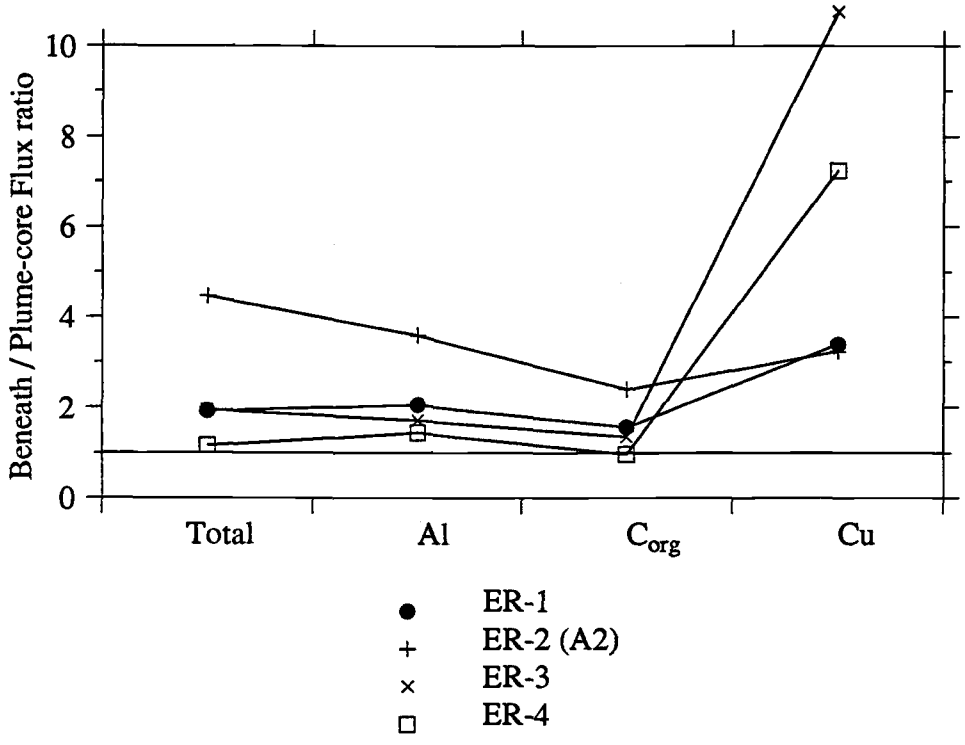

Figure II.83. Ratio of beneath-plume (approx. 2150 m) total settling particle flux, and fluxes of aluminum, organic carbon, and copper, to those measured within the plume core (approx. 1950 m), for 4 Endeavour Ridge mooring deployments. Values greater than one indicate beneath-plume enrichment.

Figure II.84. Horizontal flow, temperature, and attenuation coefficient near the vent field, at plume depths, over three consecutive mooring deployments, integrated over sediment trap cup periods to facilitate comparison with the settling flux data shown in Figure II.78. The data for ER-2 A2 are the same as in II.82, however the data for ER-3 and ER-4 are for deeper instruments here. Note that the depth of the sediment traps in Figure II.78 is deeper than for the current meter records shown here; depths in Figures II.77 and II.82 are more closely matched. Dates are noted in the bottom panel.

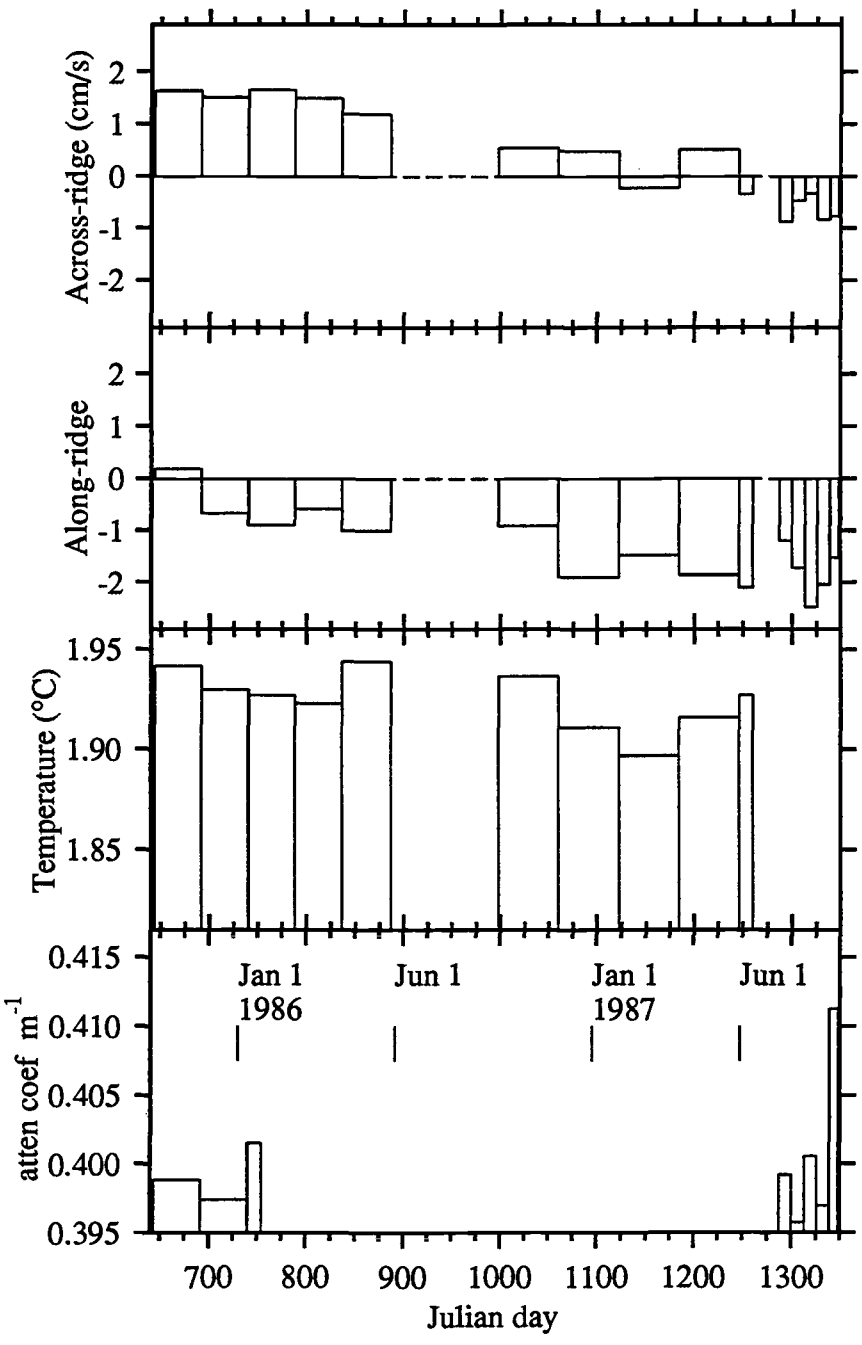
Data for moorings A2 2005, ER-3 2036, ER-4 2056
Across-ridge (cm/s)
2
1
0
-1
-2
Along-ridge
2
1
0
-1
-2
Temperature (°C)
1.95
1.90
1.85
atten coef m-1
0.415
0.410
0.405
0.400
0.395
Jan 1
1986
Jun 1
Jan 1
1987
Jun 1
700
800
900
1000
1100
1200
1300
Julian day

Figure II.84.

the current meter, about 2 cm/s, to nearly 16 cm/s. In all three records, flow had a strong southward, along-ridge component.

Further inspection of the current meter data reveals distinct inter-deployment differences. From progressive vector diagrams (Figure II.85), it is possible to calculate the average velocity during each deployment period which spans 251 days for A2, 266 days for ER-3, and 68 days for ER-4, respectively. It must be emphasized that a PVD does not indicate the path of a particle; it is a record of how velocity changes at a fixed point over time. A parcel of water leaving that fixed point may experience a very different current field, and thus, its path would not be that of the PVD. However, from the PVD, the average speed over some time interval can be calculated as $(x^2+y^2)^{1/2}$/time elapsed. For the three plume-core records, in chronological order, speeds calculated this way are 1.15, 1.73 and 1.37 km per day. This suggests that long-term average transport varies by up to 50%. (On a sediment trap cup-by-cup basis, average speeds over a single deployment vary by more than a factor of two.) It is also notable that the long term transport is not directionally steady. The deployment-averaged direction for the plume-core currents, in chronological order is 133°T, 192°T and 233°T. This means that during A2 transport was over the east ridge crest, during ER-3 it nearly paralleled the ridge axis, and during ER-4 it veered westward (Figure II.85). This analysis demonstrates strong interannual variability in flow which guides the hydrothermal plume.

Settling particle flux data provide independent evidence of long-term variability in the neutrally buoyant plume. Figure II.77 shows that during the ER-3 deployment the total settling particle flux, as well as terrestrial (Al) and biogenic (C_{org}) fluxes were greatly enhanced relative to the ER-2 A2 deployment, however hydrothermal flux (Cu) was an order of magnitude lower. As discussed in the preceding section, dramatic differences in these fluxes during the ER-4 experiment probably reflects a seasonal effect, as opposed to interannual variability. Fluxes of aluminum, organic carbon, copper and total settling particle fluxes within the plume measured for three other deployments relative to the ER-2 (A2) fluxes are shown in Figure II.86.

In summary, the currents which guide the neutrally buoyant plume are neither directionally stable nor constant in speed over time scales of years. Settling particle flux at the Endeavour Ridge study site varies interannually in response to variability of

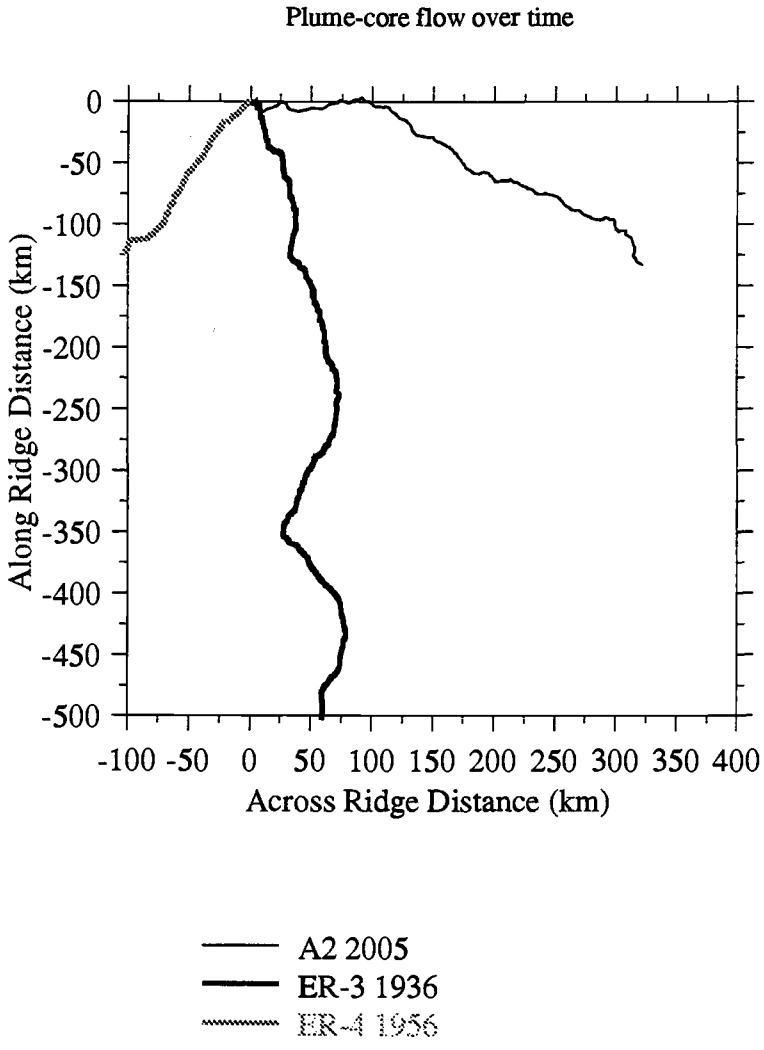

Figure II.85. PVDs for A2 2005, ER-3 1936, and ER-4 1956 deployments. Vectors begin at the origin. See text for record lengths.

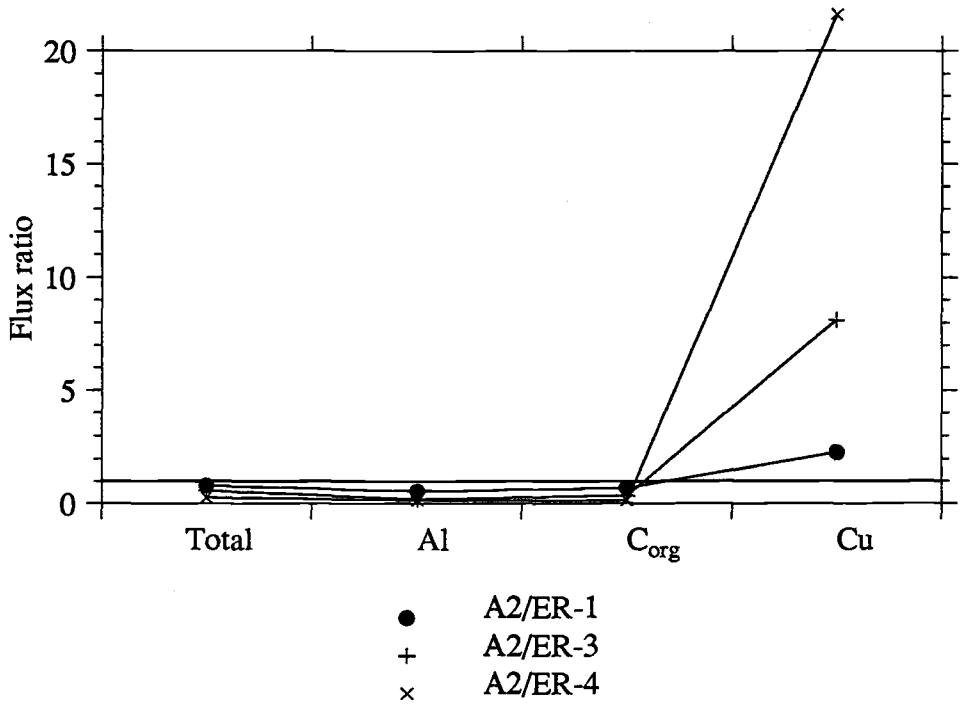

Figure II.86. Ratio of ER-2 (A2) total settling particle flux, and fluxes of aluminum, organic carbon, and copper, to those measured within the plume core (approx. 1950 m), for the other three Endeavour Ridge mooring deployments. Values greater than one indicate that the fluxes during ER-2 (A2) were enriched in that element relative to the other deployment. The ER-2 deployment was a time of higher hydrothermal flux but relatively lower flux of settling particles from other sources (i.e. low terrigenous and biogenic fluxes).

both upper water column particle-forming processes, and horizontal advection of the neutrally buoyant plume. The flux of non-hydrothermal material from above the plume modifies removal of hydrothermal components from the advecting plume.

Other types of temporal variability

Scales of temporal variability for which there is some evidence in our records, but which are not discussed in-depth in this manuscript, include very high-frequency (2.1-11 cpd) fluctuations, and apparently episodic changes in a given parameter. High-frequency vertical motions caused by internal waves may transport thermal or suspended particle gradients past a sensor. Temperature fluctuations at high frequencies are not highly correlated with horizontal velocity fluctuations forced by vertical internal wave motions (Figures II.87 - II.89). The few high-frequency peaks in the cross-spectra of flow and temperature may reflect this forcing or, alternatively, random correlation.

Non-periodic, i.e. episodic, changes in plume signals may be important in understanding the oceanic implications of hydrothermal venting. Baker et al. (1987) discovered a dramatic megaplume above a southern Juan de Fuca Ridge vent field. This feature, discovered during water column surveys of hydrothermal activity along the ridge crest, was eddy-like, 700 m thick, and 20 km in diameter. The geometry of the plume, along with mineralogic and hydrographic evidence, suggest it was the result of a brief, massive injection of hydrothermal fluid, and that the feature was only days old when it was sampled. It was centered 700 m above the seafloor, and was separated by a 50-m layer from a lower, chemically distinct hydrothermal plume thought to be a steady-state feature more typical of hydrothermal plumes sampled elsewhere. The megaplume may be the expression of an incremental seafloor-spreading event, and could equal the annual output of 20-2000 350°C black smokers compositionally similar to those at 21°N on the East Pacific Rise. A second megaplume was found in a later survey, and Baker et al. (1989) calculated that the associated fluxes of heat and mass were two orders of magnitude greater than the steady-state fluxes at Endeavour Ridge. While I found no evidence of comparable phenomena at Endeavour Ridge, the possibility of such episodic venting cannot be ruled out and should be considered in models of deep-sea hydrothermal plumes.

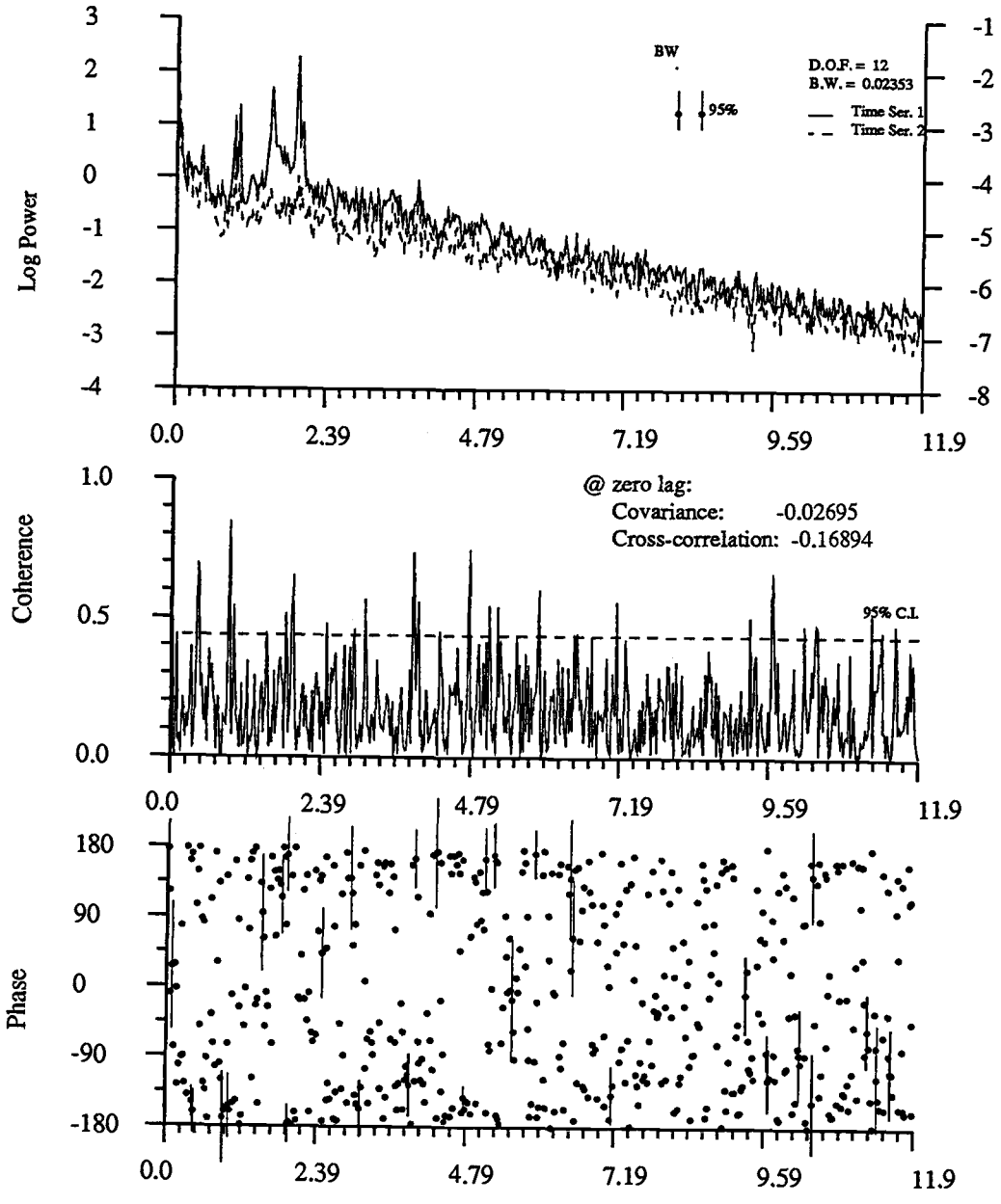

Figure II.87. Cross-spectrum for along-ridge flow and temperature at A2 1905 plotted out to the Nyquist frequency, showing a few significant high-frequency peaks in the portion of the spectra that corresponds to internal waves (2.1-12 cpd).

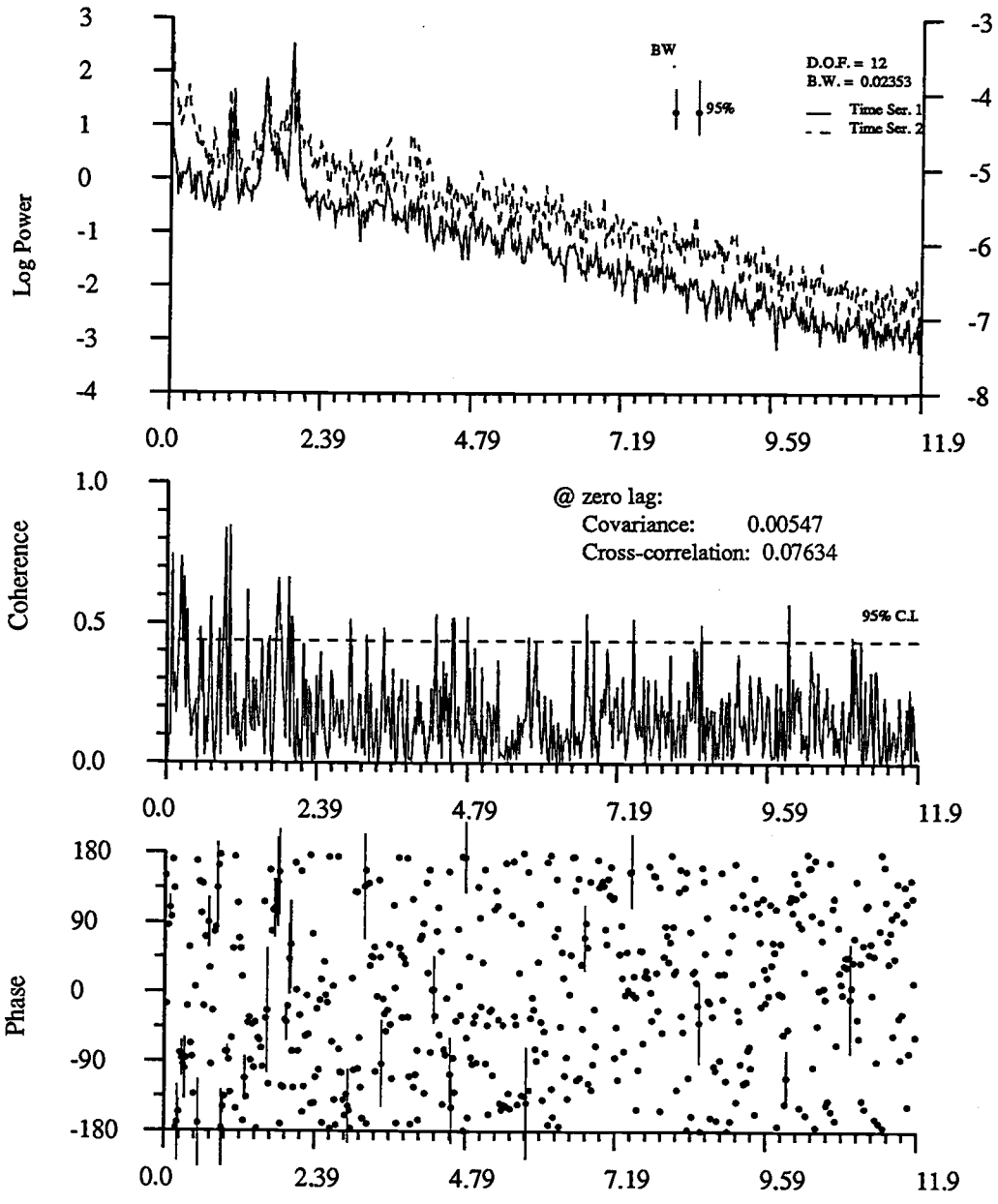

Figure II.88. Cross-spectrum for along-ridge flow and temperature at R2 1985 plotted out to the Nyquist frequency, showing a few significant high-frequency peaks in the portion of the spectra that corresponds to internal waves (2.1-12 cpd). R2 1985 was selected for this analysis because it is one of the plume-core records with the fewest missing current meter data points.

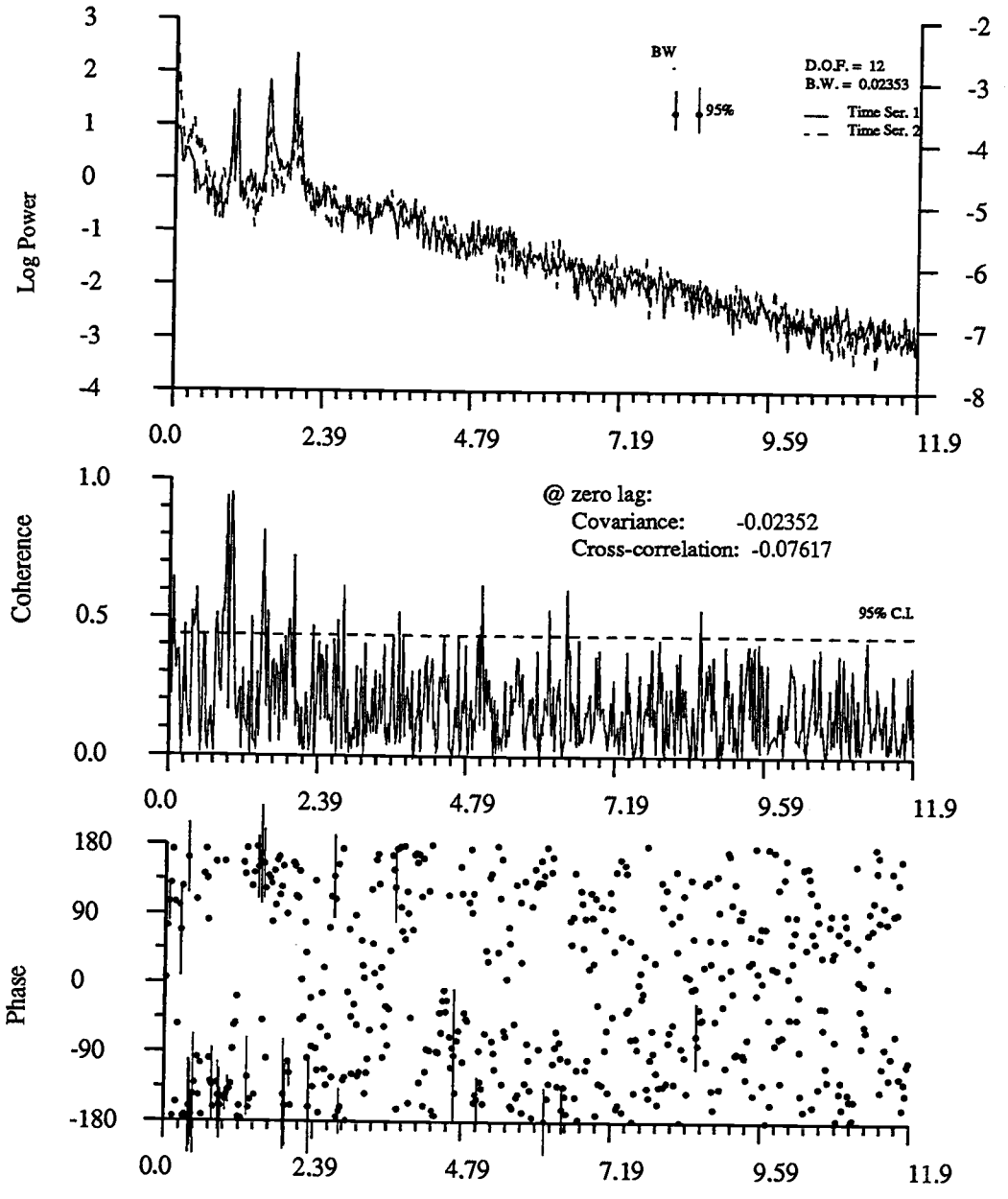

Figure II.89. Cross-spectrum for along-ridge flow and temperature at A3 1955 plotted out to the Nyquist frequency, showing a few significant high-frequency peaks in the portion of the spectra that corresponds to internal waves (2.1-12 cpd). A3 1955 was selected for this analysis because it is one of the plume-core records with the fewest missing current meter data points.

On much smaller scales, abrupt changes in our temperature and attenuation records evidence of possible episodicity. Examples include:

1) the decrease in temperature of about 0.15°C over 12 days beginning at JD 660 at A2 1905 (Figure II.17). Temperature stays low for about 25 days, then rises gradually over the remaining 200 days of the deployment. The onset of this feature appears to be associated with a change in flow direction shown more clearly in Figure II.90. Currents rotated anticlockwise then clockwise, as along-ridge flow changed from negative to positive and back to negative, while across-ridge flow was consistently positive. The temperature minima occur when across and along-ridge flow are at their maximum positive value. Paradoxically, this association suggests that the mooring was located southwest of the vent field. According to our best estimate (see Thomson et al., 1990), mooring A2 was positioned northeast of the primary vent field. Another vent field has been found northeast of the primary vent field, however high-temperature hydrothermal venting there is much less intense, or possibly non existent. Diffuse seafloor venting would not be expected to dominate the temperature time series recorded 300 m above bottom. Two possible explanations for the pattern, if not instrumental or due to navigational error, are: a) The temperature or volume of hydrothermal fluid emitted from the vents decreased suddenly, then gradually increased; and b) Clockwise tidal rotations, not included in Figure II.17 or II.90, are the mechanism by which the hydrothermal plume sweeps past the mooring. I reject the first hypothesis because no synchronous temperature decreases are found in records from any of the other nearby instruments (A2 2005, R2 1986, A3 1955). The second, tidal ellipse, hypothesis is also unsatisfying for two reasons: 1. The mooring was less than one kilometer from the vent field, close enough for the hydrothermal effects to be detected via tidal advection regardless of the mean flow trajectory; and 2. Although there are other times during the deployment when mean flow was similar to what it was during the prominent temperature decrease (e.g. JD 702, JD 850), and the magnitude of tidal oscillations is reasonably steady over time, those periods are not marked by similar temperature decreases. The onset of the temperature decrease appears to be related to the rapid change in current direction. However, since current velocity returned to its pre-event values soon after the event while temperature only very slowly returned to its initial value of around 1.85°C, I believe the temperature data reflect an instrumental problem. Note that the lowest-frequency energy in the temperature spectra for A2 1905

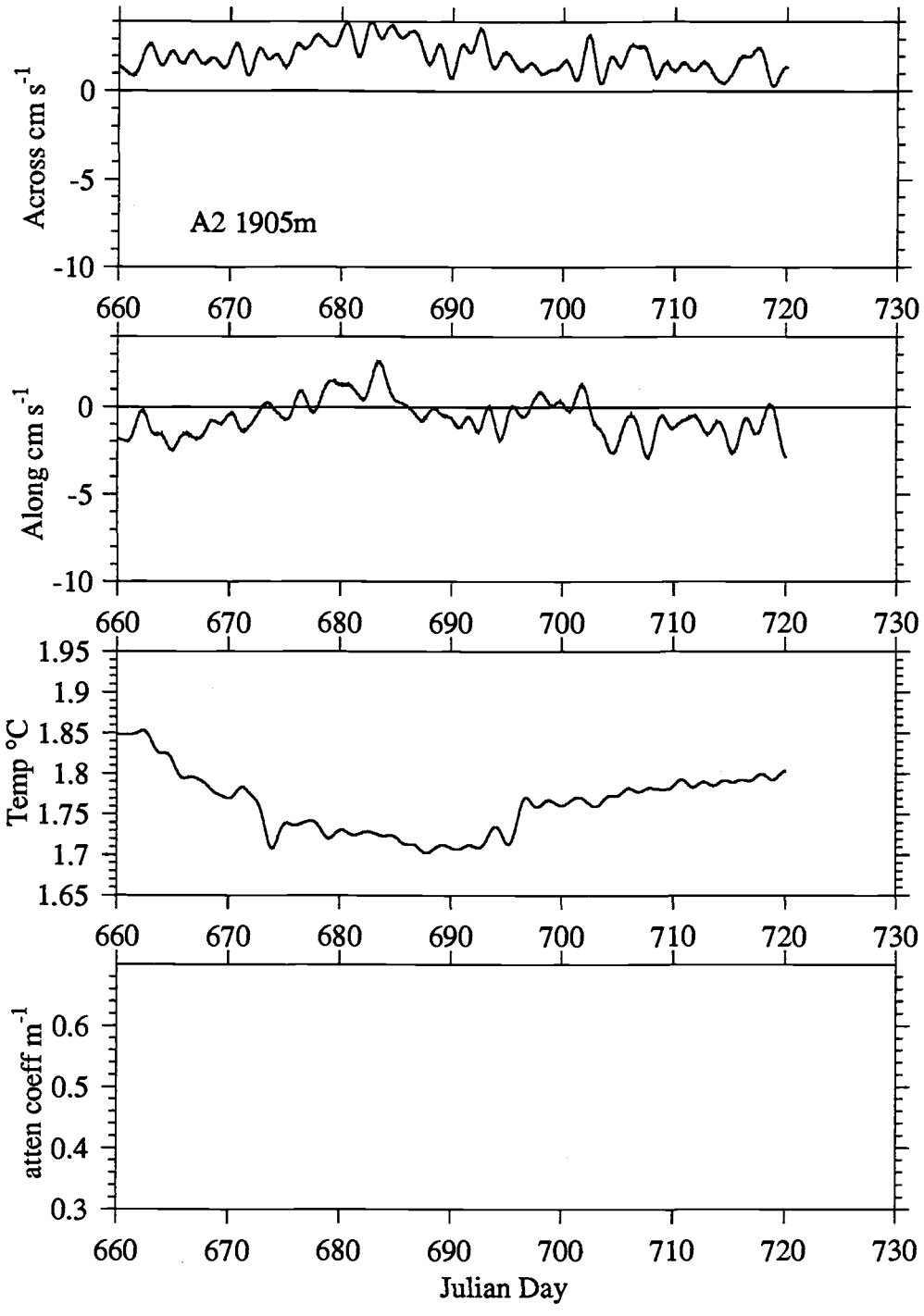

Figure II.90. Expanded-scale view of a portion of the A2 1905 time series focusing on particular physical events discussed in the text.

(Figure II.48) is the highest of any plotted in Figures II.47-51 and II.52, reflecting the 200-day temperature trend.

2) the small increases in both temperature and attenuation coefficient beginning at JD 703 at A3 2156 (Figure II.23). The amplitude of these changes is small (< 0.03°C and 0.01 m^{-1}) and the duration of the event is less than two days (Figure II.91). Because the mooring was south, along-ridge of the vent field, increases in hydrothermal signals should be associated with stronger negative along-ridge flow. At the onset of the event, however, along-ridge flow was weakening, becoming less negative. This seems paradoxical until one notes that across-ridge flow changed signs. This change indicates that the plume swept across the ridge rotating anticlockwise from west to east. During this rotation, when across-ridge flow was zero, the plume was alligned along the axial valley, directly toward the mooring, thus explaining the increases in temperature and attenuation.

3) small increases in temperature and attenuation, two at JD 775,777 and three over the interval JD 792-802 in the R2 1986 records (Figure II.25). The amplitude of the increases was ≤ 0.04°C and < 0.05 m^{-1}, and the events lasted 2-3 days (Figure II.92). These five features are all clearly associated with simultaneous increases in positive across-ridge flow and weakening of negative along-ridge flow. This is precisely what is predicted considering the mooring location which is on the ridge crest to the east of the vent field.

4) "rabbit ear" peaks in temperature and attenuation at JD 1118 and 1120 at ER-3 1936 (Figure II.29). These two-day events have amplitudes of ≤ 0.04°C and < 0.05 m^{-1}, and appear to be realted to sign changes in across-ridge flow (Figure II.93). Warmer, particle-rich water is advected past the mooring when the plume rotates anticlockwise from the west to the east side of the ridge. Mooring ER-3 was east and north of the vent field.

5) the brief dip in the temperature of about 0.04°C which reaches a minimum at JD 1055 and lasts for several days at ER-3 2036 (Figure II.30). Cooler conditions correspond to intensification of negative along-ridge flow that transports hydrothermal effluent more rapidly away from the mooring which is northeast of the vent field (Figure II.94).

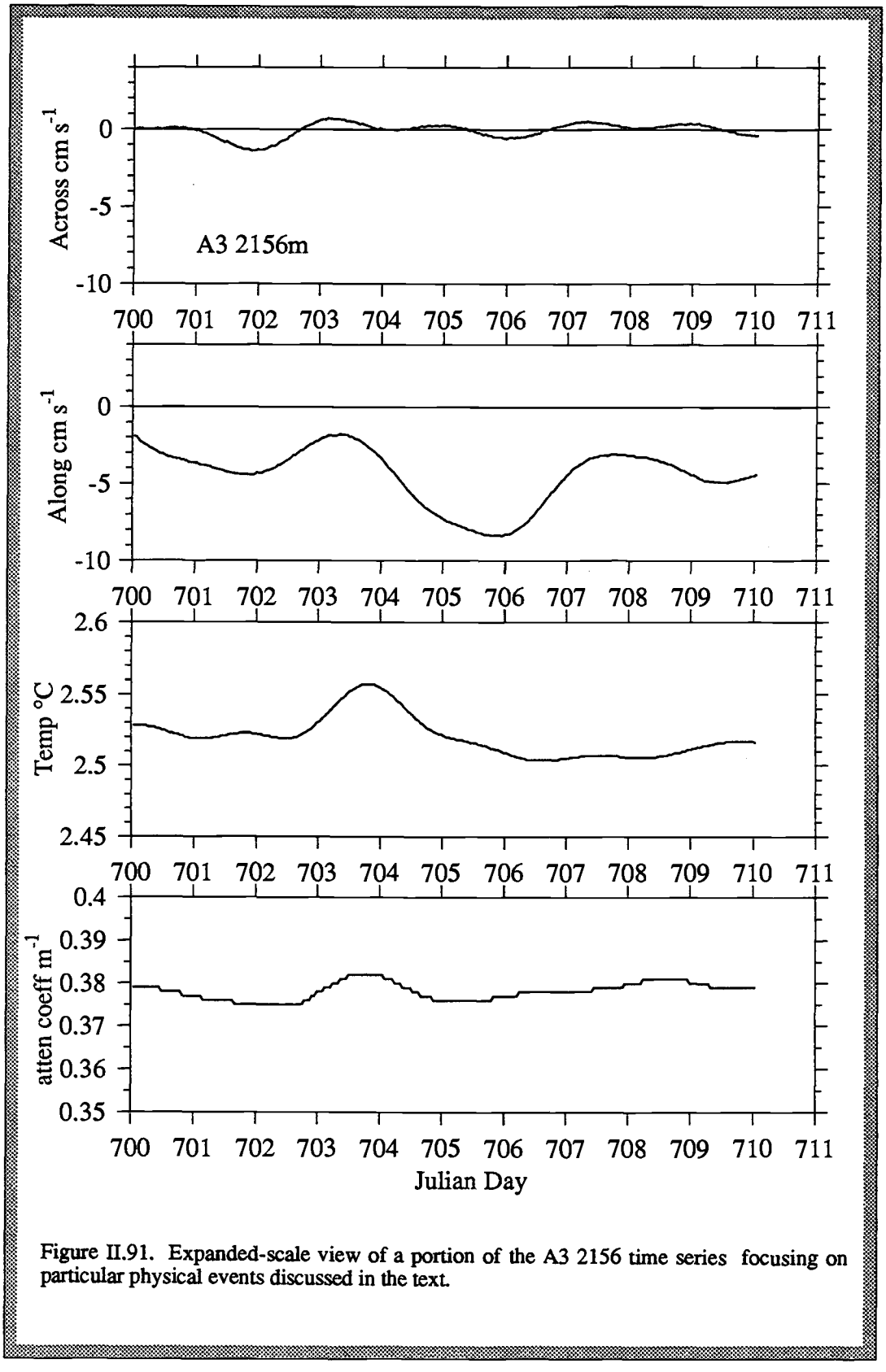

Figure II.91. Expanded-scale view of a portion of the A3 2156 time series focusing on particular physical events discussed in the text.

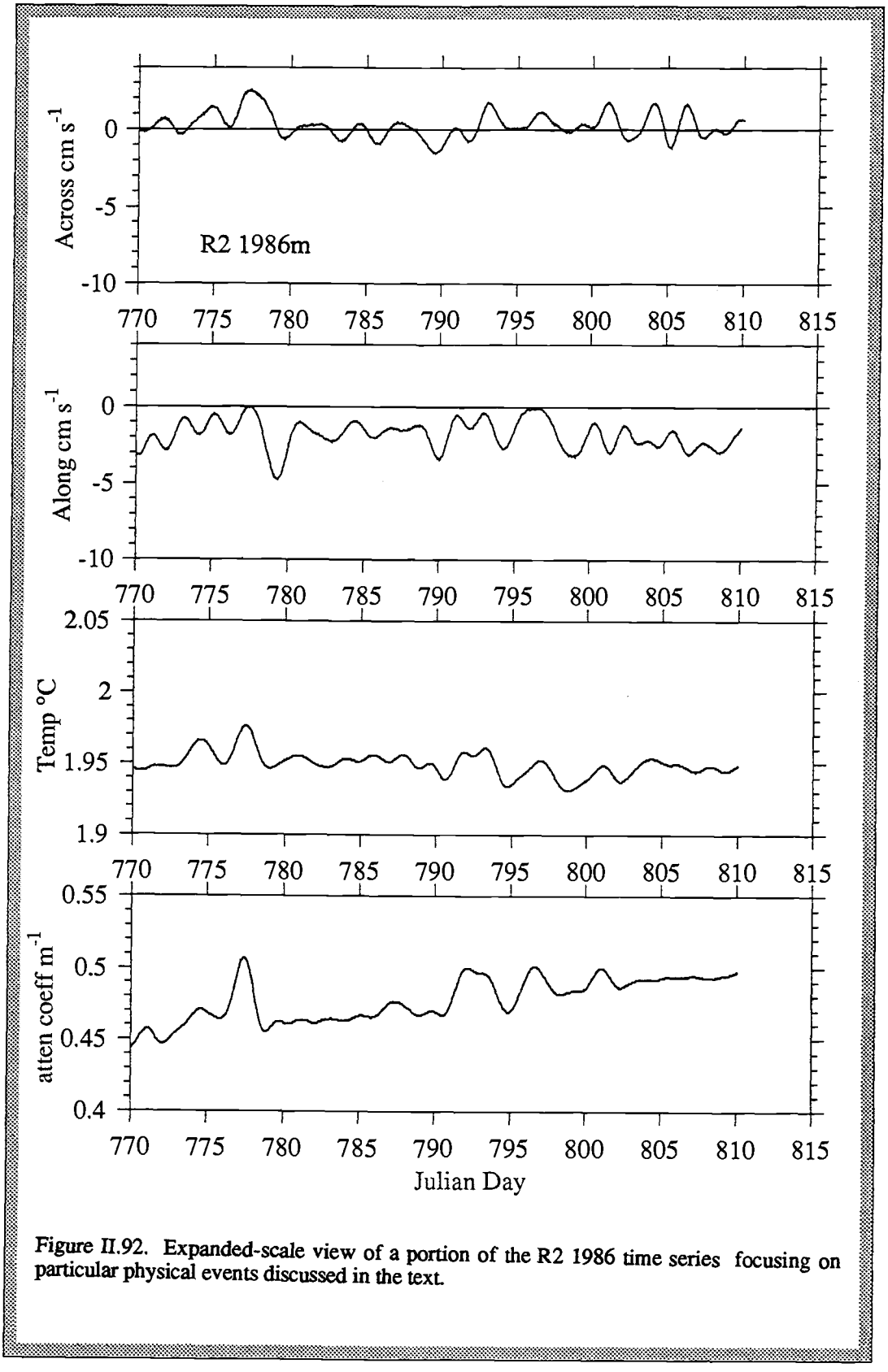

Figure II.92. Expanded-scale view of a portion of the R2 1986 time series focusing on particular physical events discussed in the text.

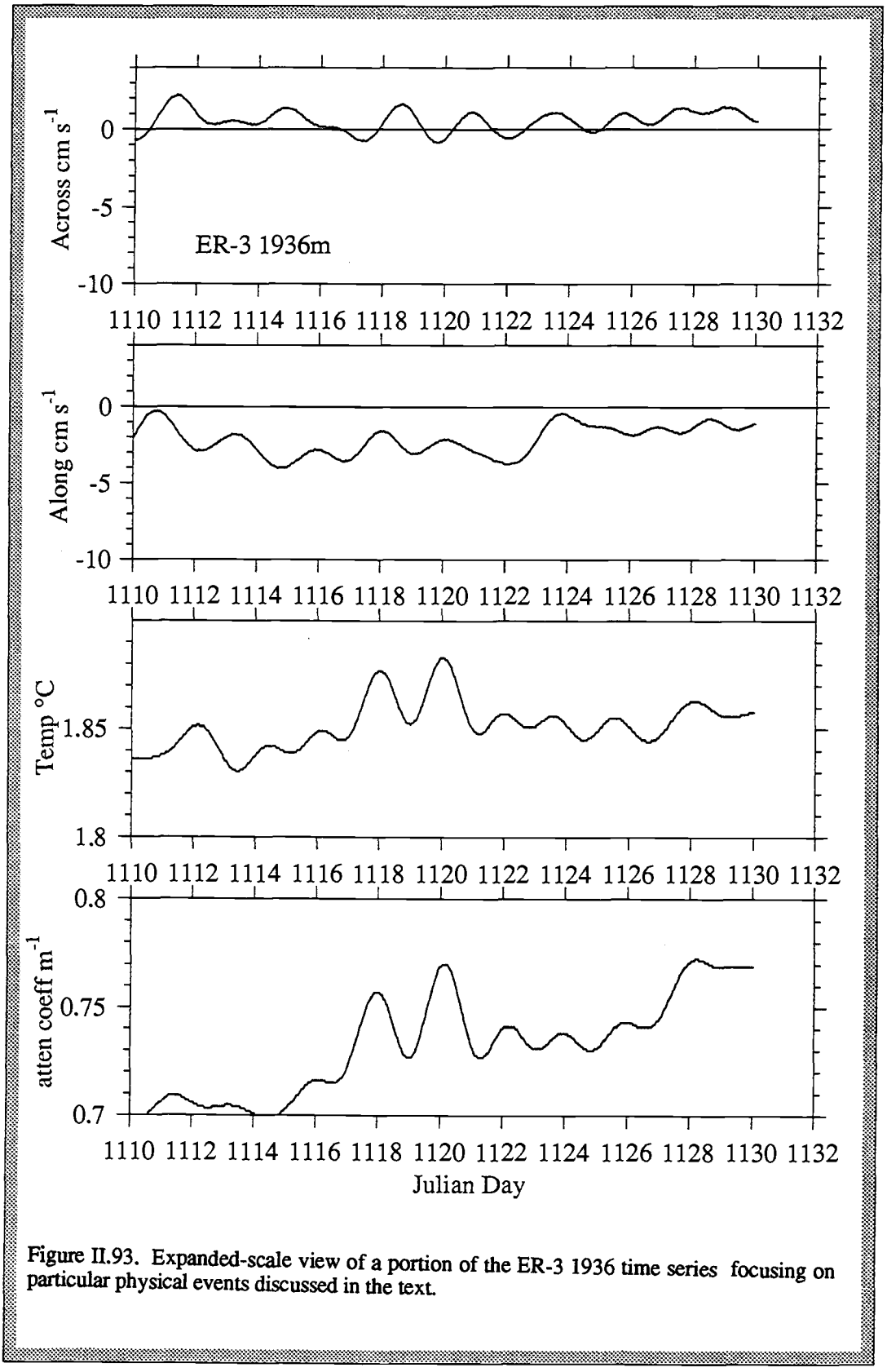

Figure II.93. Expanded-scale view of a portion of the ER-3 1936 time series focusing on particular physical events discussed in the text.

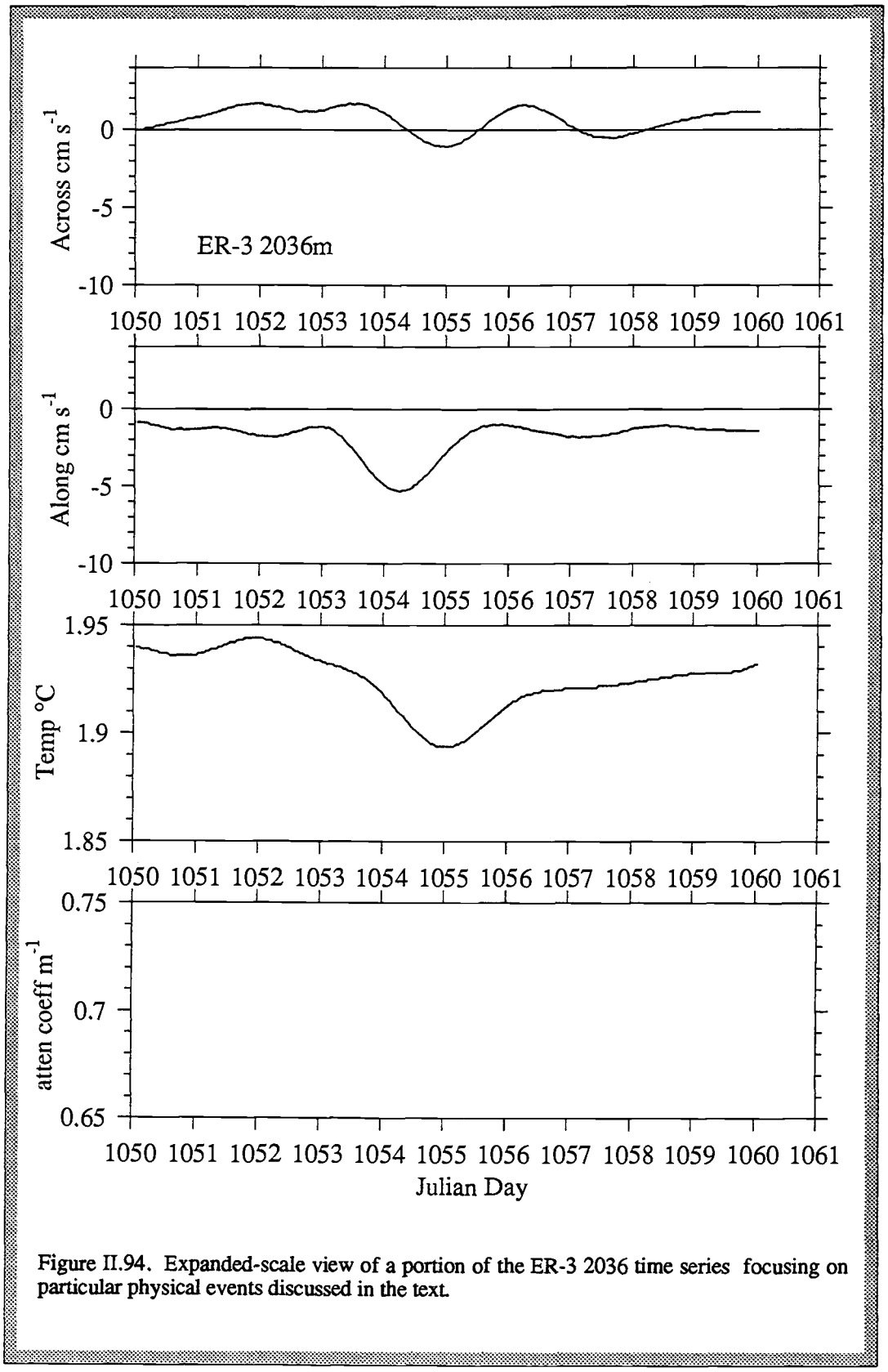

Figure II.94. Expanded-scale view of a portion of the ER-3 2036 time series focusing on particular physical events discussed in the text.

6) two elevations in attenuation coefficient of 0.07 m^{-1} lasting approximately one day each, beginning at JD 1322 in the records from ER-4 1956 and 2056 (Figures II.33 and II.34). These attenuation increases appear to correspond to decreases in negative across-ridge flow (Figure II.95 and II.96). Less negative along-ridge flow implies that transport of hydrothermal fluids was less intensely away from the mooring. The PVD in Figure II.39 (upper right panel) shows that during the entire ER-4 deployment flow was consistently away from the mooring. When the current speed was reduced, there was a higher concentration of fine particles closer to the vent field and available for tidal transport past the mooring.

All but one of the six examples of events discussed above can be accounted for by horizontal advection. Because the events I discussed are not periodic features in the time series, they are in that sense episodic. However, this designation is based on a limited record length. While the demonstration of how various types of changes in current velocity can produce variations in hydrothermal influence at a moored instrument is useful, these examples do not constitute evidence of episodicity in hydrothermal venting. Any episodicity demonstrated is in regard to current velocity or local hydrothermal plume intensity. Moreover, the amplitude of each event is small, and the duration short, relative to the variance and record length of the corresponding time series.

Spatial variability in hydrothermal fluxes

Understanding the dynamics of the Endeavour Ridge neutrally buoyant plume requires evaluation of spatial as well as temporal patterns. In previous sections of this manuscript I have presented some evidence of spatial patterns in neutrally buoyant, fine-particle, hydrothermal plume. To recapitulate:

1. The positive trend in attenuation coefficient, although a result of optical fouling, is most pronounced in the plume core records and is an indicator of hydrothermal, fine particle distribution in the water column.

2. Increases in amplitude of high-frequency variations in attenuation closer to the vent field and to the plume core indicate that the fine particle concentration is more variable in the near-field and becomes more homogenous with distance.

3. The flow field is relatively uniform between near-field instruments at the same depth during a single deployment (e.g. A2, R2 and A3 during the ER-2 experiment);

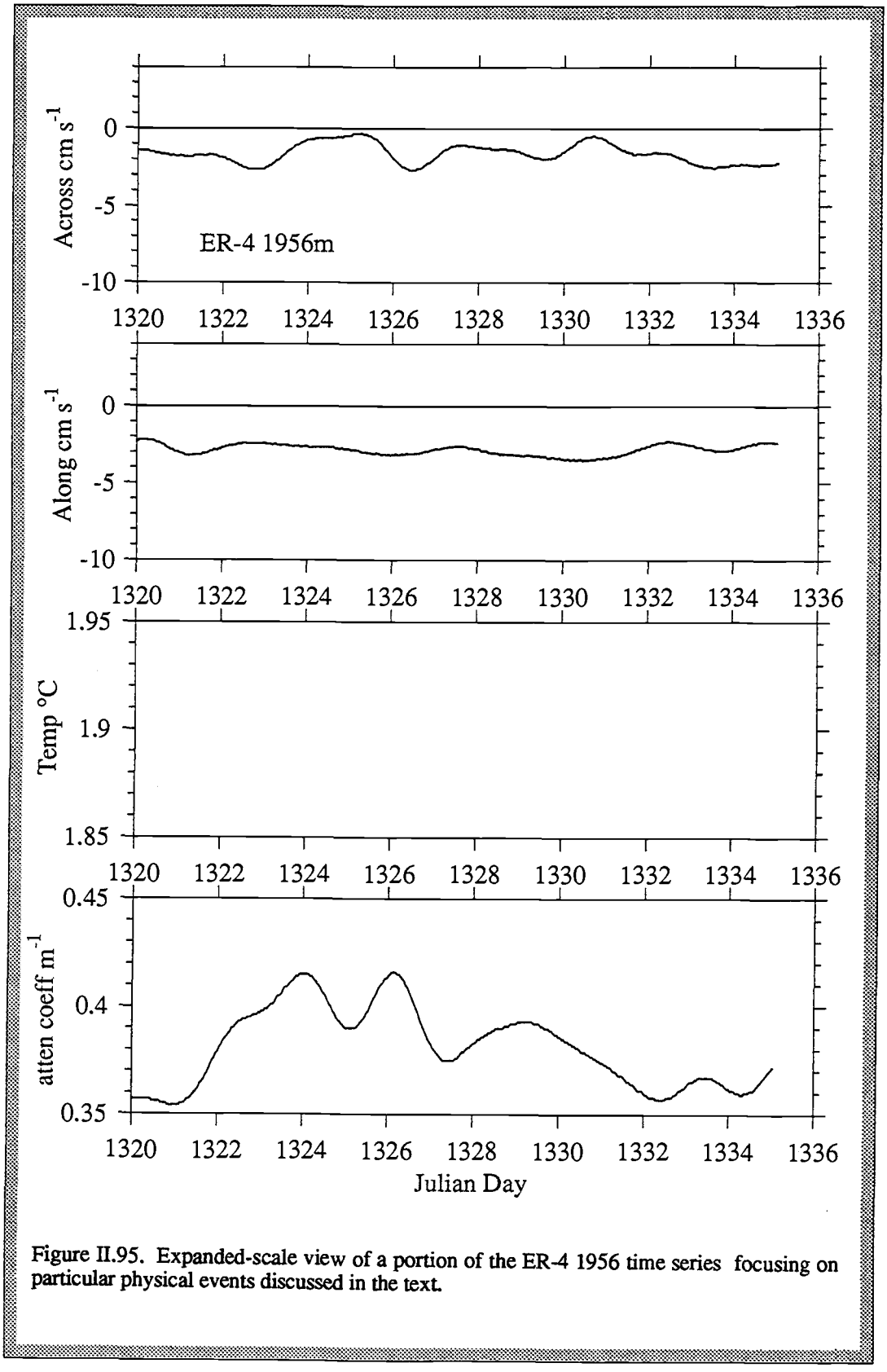

Figure II.95. Expanded-scale view of a portion of the ER-4 1956 time series focusing on particular physical events discussed in the text.

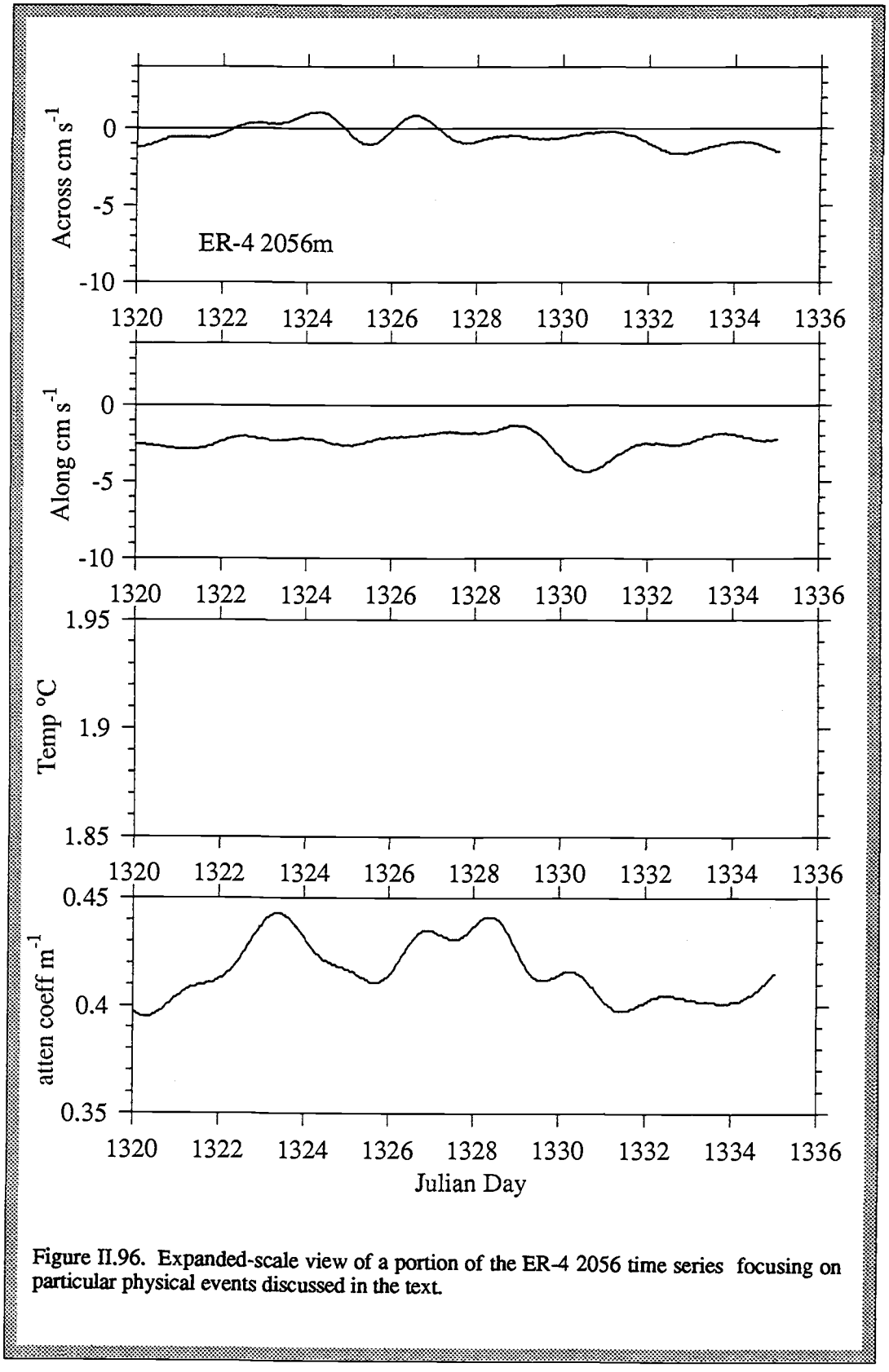

Figure II.96. Expanded-scale view of a portion of the ER-4 2056 time series focusing on particular physical events discussed in the text.

however, cross-spectral analysis suggests shear in the horizontal velocities with depth and distance from the vent field.

In the two sections that follow, I draw principally on current meter and sediment trap data to expand our discussion of spatial patterns in the flow field and settling particle flux in the vicinity of the hydrothermal plume. A fundamental question I address is: How does the settling flux of hydrothermal particles change with distance from the vent field and with depth in the water column?

Patterns with depth

In addition to fluctuations in horizontal velocities over time, the currents above Endeavour Ridge also vary spatially. Comparison of PVDs over a range of depths at a single location reveals a pattern of current shear. For example at A2, PVDs show trajectories that rotate over 180° anticlockwise from above the plume to beneath it (including A2 2106, an attenuated record not shown in Figure II.97). At 1656 m, the overall transport is to the southwest along the trend of the axial valley. At 1905 m, probably within the upper region of the neutrally buoyant plume, the average velocity was 1.75 km/day in the direction 160°T, about twice the average speed above the plume. One hundred meters below, at 2005 m, in what is probably the plume core, average flow direction is more to the east, approximately 135°T at 1.2 km/day. For the first two months, flow is almost directly eastward, then takes a turn to the southeast. A surprising change is noted at 2106 m: for the one month record obtained at this depth flow is northward at just under 1 km/day. The northward flow may be a local, topographically-induced effect (R. Thomson, personal communication). These observations suggest that settling particles follow a complex, three-dimensional, possibly helical path as they descend through the water column. Vertical shear within the plume, as determined from the PVDs at 1905 and 2005 m is 0.55 km/day and 25° per 100 m. The changes in velocity over a range of depths may serve to contain settling hydrothermal material in a zone close to the vent field. If the depth profile of the current vector was more uniform, perhaps at least more directionally consistent, the hydrothermal plume would be dispersed farther from its origin.

Some evidence of this helical transport pattern is observed in subsequent deployments at this site. The above plume PVD at ER-3 1686 m shows a fish hook shape, trending southwest along the axial valley for most of the deployment period until

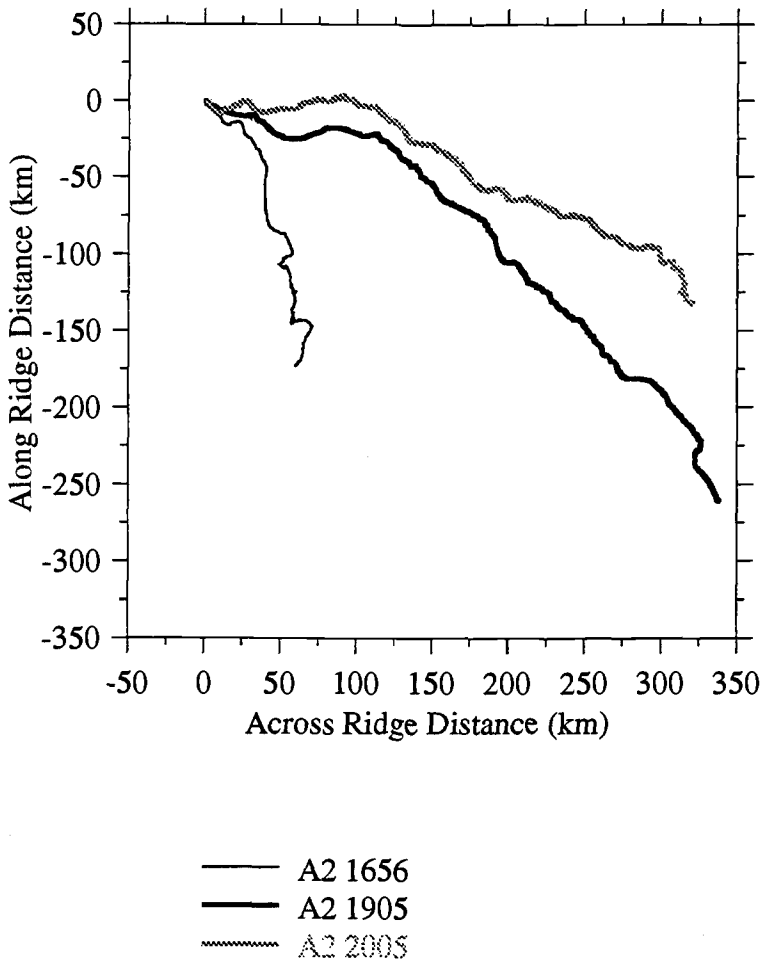

Figure II.97. PVDs at mooring ER-2 A2 at the depths specified over the entire deployment period. Vectors begin at the origin. Refer to Table II.1 for record lengths.

early March when flow did a nearly 90 degree turn and continued to the northwest for the final three months of the record (Figure II.98). Average speed was 0.85 km/day. At 1936 m the flow was simpler in trend, southwest, along-ridge, at about 1.77 km/day. During cups 3, 4 and 5 (late November to late May) speed exceeded 1.6 km/day over each consecutive 2-month interval. At 2036 m, the PVD is very similar in trend to the instrument record obtained 100 m above, but the average velocity was considerably lower, about 1.28 km/day. One hundred meters deeper, flow is directionally complex. As in the case of the deepest current meter record on A2, we find a strong northward component of flow at ER-3 2136 m. During cups 3, 4 and 5 flow direction is highly variable and produces chaotic patterns in the PVD.

Above-plume (1706 m) currents during the summertime ER-4 deployment show flow oriented predominantly westward, with northward flow at the beginning and end of the record (Figure II.99). Over the 2-month deployment, the average velocity was 0.84 km/day. In the plume core, at 1956 m, flow to the southwest (225°T) averages 1.31 km/day. At 2056, also likely to be within the plume, flow is similar, but the trend is more to the south, approximately following the ridge axis at 1.59 km/day. This is the deepest record on the ER-4 mooring, yet based on the three current meters there is still evidence of the helical, anticlockwise pattern.

The cause of the helical pattern, which persists over more than two years, is unclear, however it may be important in restricting the transport of hydrothermal material away from the vent field. Particles settling through the vertical velocity shear would follow a downward spiraling trajectory. The consequence of this is that particles would be advected horizontally away from the vent field more slowly than they would if the vertical profile of currents consisted of equivalent speeds that were, in contrast, uniform in direction with depth. In this way, advective patterns may serve as a physical focusing mechanism for settling hydrothermal particles.

In addition to changes in horizontal current velocity with depth, the flux and composition of settling hydrothermal particles also varies with depth. Hydrothermal particle flux increases dramatically with depth beneath the plume core (Figures II.80 and II.81), and this pattern is discussed at length in Dymond and Roth (1988) and Roth and Dymond (1989). Changes in composition of the hydrothermal material with depth, as well as among mooring deployments, are demonstrated by comparison of ratios of

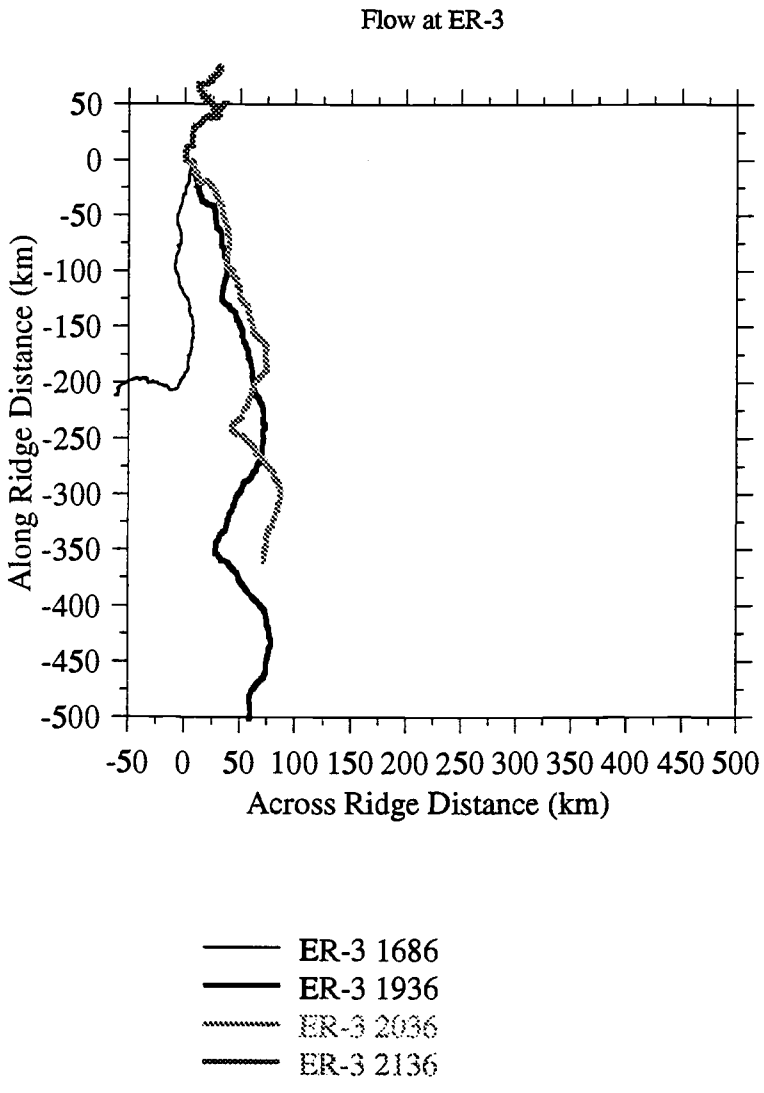

Figure II.98. PVDs at mooring ER-3 at the depths specified over the entire deployment period. Vectors begin at the origin. Refer to Table II.1 for record lengths.

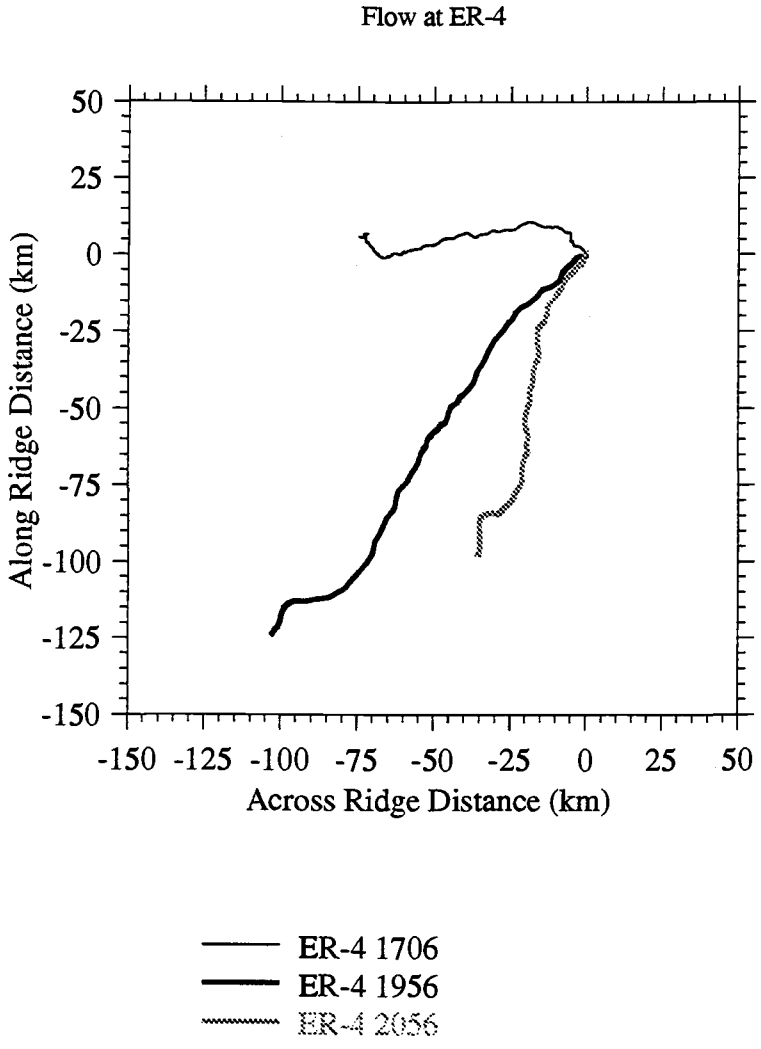

Figure II.99. PVDs at mooring ER-4 at the depths specified over the entire deployment period. Vectors begin at the origin. Refer to Table II.1 for record lengths.

iron flux to the flux of other hydrothermal elements (Table II.6). Decrease in the Fe/Cu and Fe/Zn ratios between the plume-core (1950 m) and beneath the plume (2150 m) reflect an increase in large, rapidly settling, copper and zinc-bearing sulfide particles closer to the seafloor. Variations in the Fe/Mn ratio may reflect relative inputs from high-temperature, Fe-rich, and lower-temperature, Mn-rich hydrothermal effluent. Fe/Mn decreases with depth during the ER-1, ER-4, and possibly the A2 deployments, suggesting that the particle flux in the deeper traps is influenced by low-temperature, diffuse venting. Changing Fe/S ratios indicate more fundamental changes in the source or sub-seafloor circulation of hydrothermal fluid.

Table II.6. Settling particle flux ratios and fluxes ($\mu g/cm^2/yr$) within and beneath the Endeavour Ridge plume.

Mooring/ depth	Fe/Cu	Fe/Zn	Fe/Mn	Fe/S	Fe	Cu	Zn	Mn	S
ER-1 1950	17.4	6.4	47.9	0.5	74.8	4.3	11.7	1.6	150
ER-1 2100	15.0	4.8	41.9	0.5	219	14.6	45.1	5.2	441
A2 1950	11.2	6.6	84.8	N/A	109	9.7	16.6	1.3	N/A
A2 2050	10.9	5.4	113.3	0.6	390	35.7	72.0	3.4	678
A2 2150	11.3	4.5	64.1	0.4	355	31.4	79.0	5.5	939
ER-3 1950	34.3	12.5	39.6	1.0	41.2	1.2	3.3	1.0	39
ER-3 2150	18.0	4.2	40.6	0.5	232	12.9	55.5	5.7	457
ER-4 1950	90.7	36.1	24.4	1.4	40.8	0.45	1.1	1.7	28
ER-4 2150	35.3	5.6	1.9	1.0	115	3.3	20.6	61.1	111

Patterns with distance from vent source

Another fundamental observation is a pattern of increasing hydrothermal settling particle flux closer to the vent field. Patterns of flux versus distance during the ER-2 deployment for total settling particle flux, fluxes of hydrothermal elements and a hydrothermal element ratio are shown in Figure II.100 . Total settling particle flux is relatively uniform (plume-core fluxes = 3.0, 2.4, 2.3 and 3.0 $mg/cm^2/y$ for A2, A3, R2 and T3), whereas hydrothermal fluxes decreases dramatically within two kilometers of the vent field. For example copper flux within the plume core was 36, 0.75, 0.25 and 0.16 $\mu g/cm^2/y$ respectively at moorings A2, A3, R2 and T3. Similar patterns are exhibited by iron and zinc. Manganese, however, does not readily

Figure II.100. Plume-core settling particle flux as a function of distance from the vent field. Data are from the four ER-2 moorings within 15 km of the vent field. Top panel shows components for which flux is either constant or increases with distance from the vent field; bottom panel shows elemental fluxes that decrease with distance. Note that left and right y-axes pertain to different components. Data for each mooring are directly beneath the corresponding mooring name listed along the top of the plot.

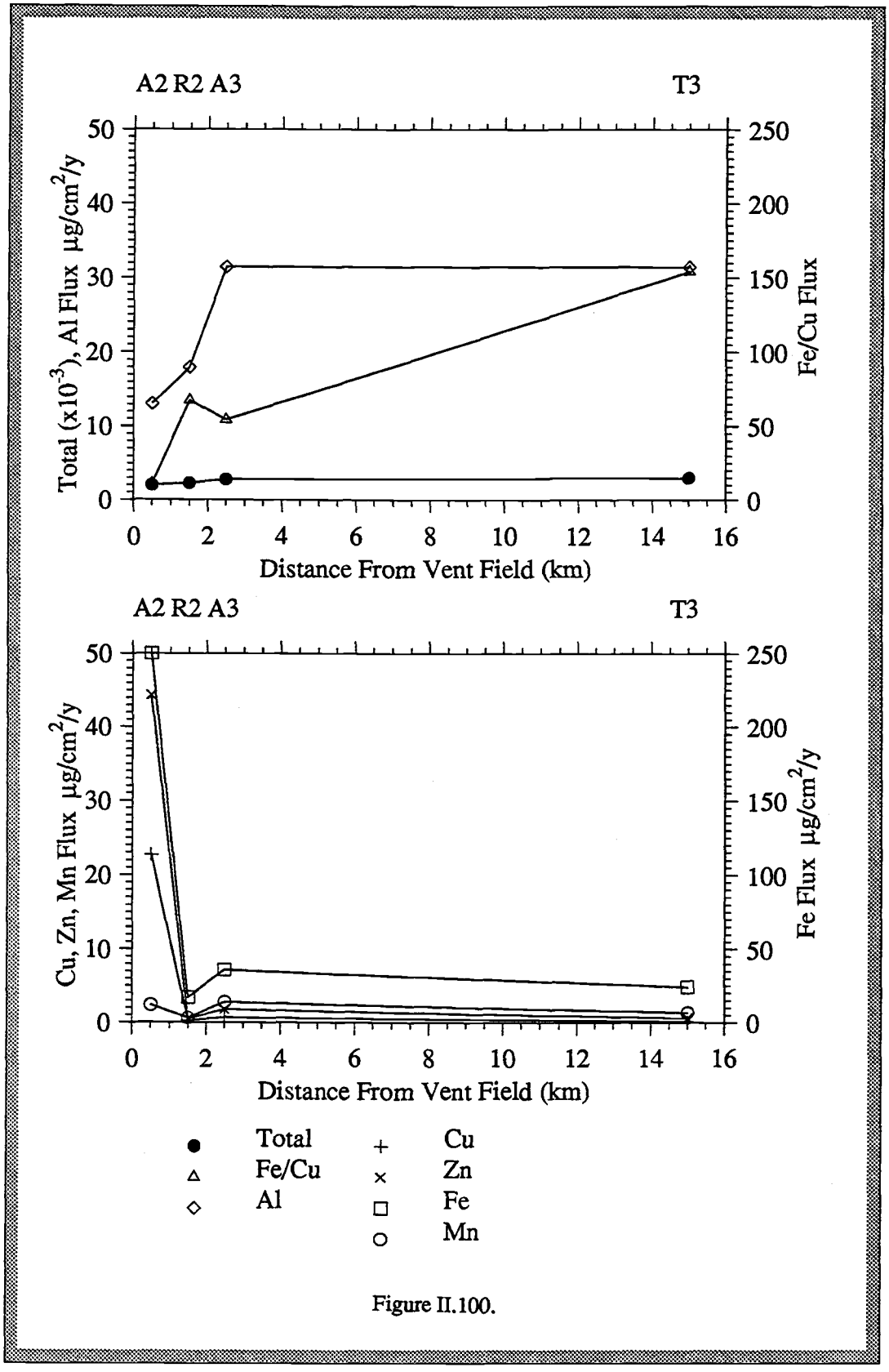

Figure II.100.

precipitate after injection into the ocean and behaves almost conservatively over the 15 km. The Fe/Cu ratio increases with distance, reflecting near-vent removal of Cu via rapidly sinking, large sulfide particles. The pattern observed for Al is more difficult to explain. I believe it reflects near-vent removal of Al, rather than an increase with distance from the vent field. The removal process may be biologically mediated as I will discuss in the **Implications**.

The relative spatial changes in settling particle fluxes by sediment trap cup periods are illustrated in Figures II.101 and II.102.

Comparison of flow patterns at the three, non-vent field sites of the ER-2 array shows distinct spatial variability. The currents measured at the southern axial valley site, A3, were comparatively uniform with depth and unidirectional over the ER-2 deployment (Figure II.103). An anticlockwise rotation with depth, although visible in records from 1955, 2055 and 2155 m, is much more mild than is the case for the near-vent field, A2 sites. At 1955 m the PVD shows a southwestward trend with average speed just over 3 km/day. The record from 2055 m is similar, but oriented more to the south, parallel to the ridge axis, at an average speed of 2.64 km/day. These plume-depth, average speeds are the highest recorded in the ER-2 array, and may indicate that advective particle transport becomes more efficient along the spreading ridge axis with distance from the vent field. The deepest record is also ridge-parallel, but the average velocity is only 1.86 km/day. There is no evidence of northward flow or the complexity noted in the deep records closer to the vent field in the previous section.

The current measured at the eastern ridge-crest station, R2 1986 m, was generally ridge- parallel at an average speed of 1.88 km/day, but showed intermittent excursions to the southeast (Figure II.37, upper right panel).

At the distal site, T3, flow records obtained at 1955 and 2055 m are similar (Figure II.37, lower two panels). At both depths, flow is directed 225°T at approximately 0.58 km/day, although some turns in the PVD persist for roughly 2-4 weeks. Compared to values from the A3 instruments, these relatively low average velocities recorded 15 km away from the vent field suggest that off-axis, and perhaps somewhere between a distance of several to ten kilometers from the vent field, horizontal advective particle transport drops about 80%.

Figure II.101. Schematic map showing the spatial relationships between the 1-km-wide axial valley, the vent field, the 4 ER-2 moorings (located at filled triangles), and the settling particle fluxes by sediment trap cup period (cup duration = 48 days). The order of the settling fluxes is the same in all four histogram sets, although only the diagram at T3 is labeled. Vertical axes for fluxes of a particular component are of equivalent length.

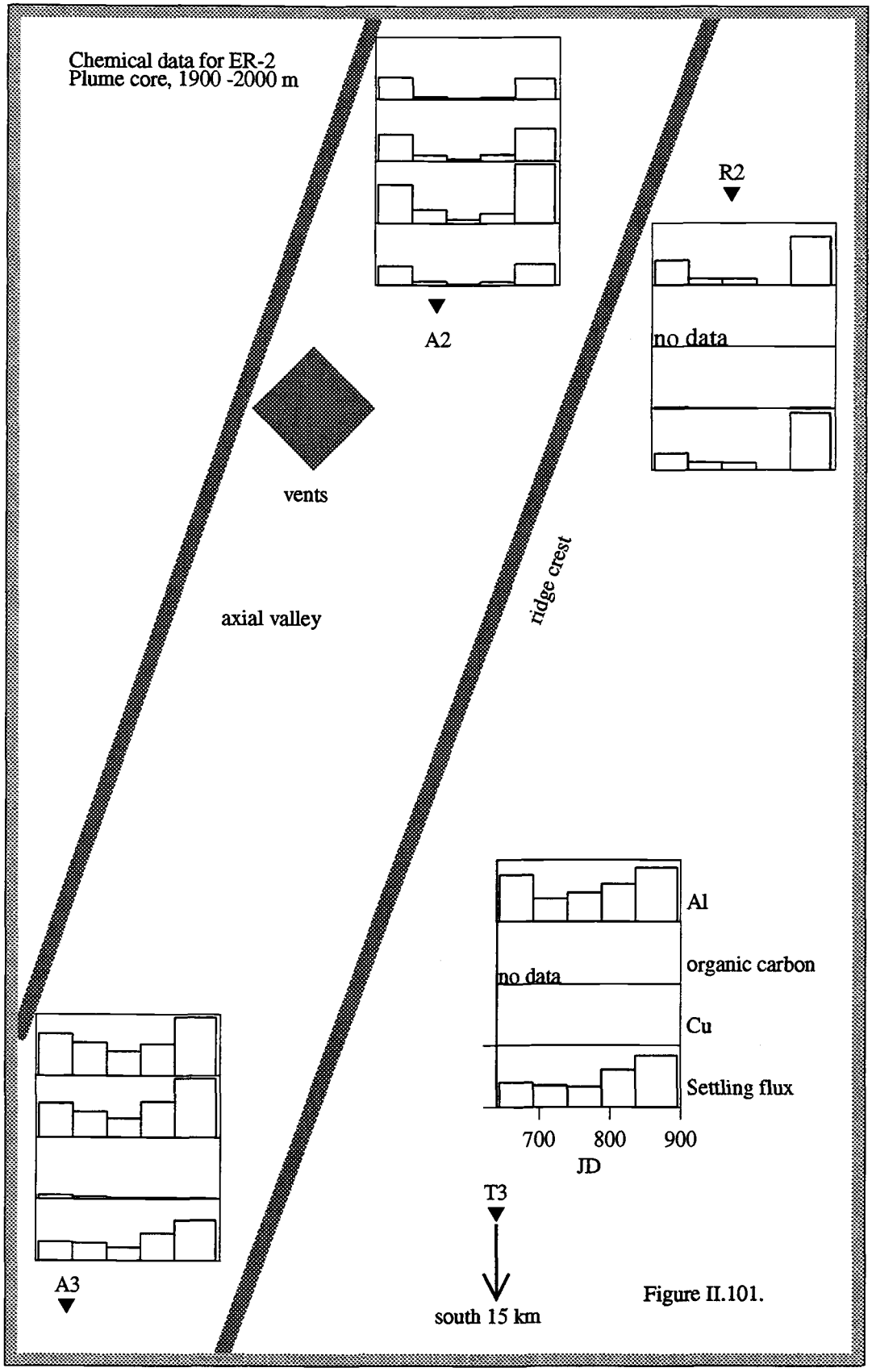

Figure II.101.

Figure II.102. Schematic map showing the spatial relationships between the 1-km-wide axial valley, the vent field, the 4 ER-2 moorings (located at filled triangles), and the settling hydrothermal particle fluxes by sediment trap cup period (cup duration = 48 days). The order of the settling fluxes is the same in all four histogram sets, although only the diagram at T3 is labeled. Vertical axes for fluxes of a particular component are of equivalent length.

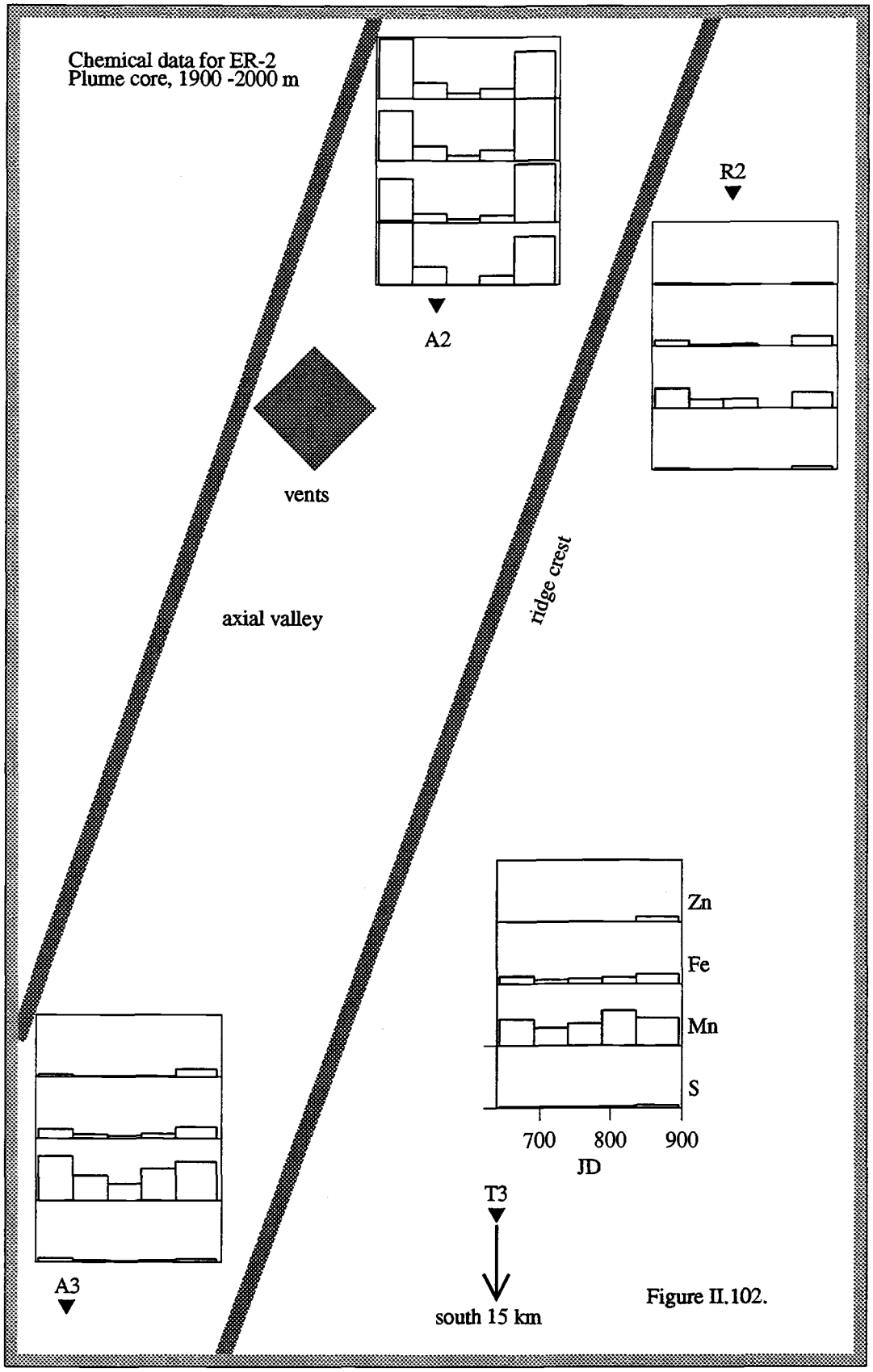

Figure II.102.

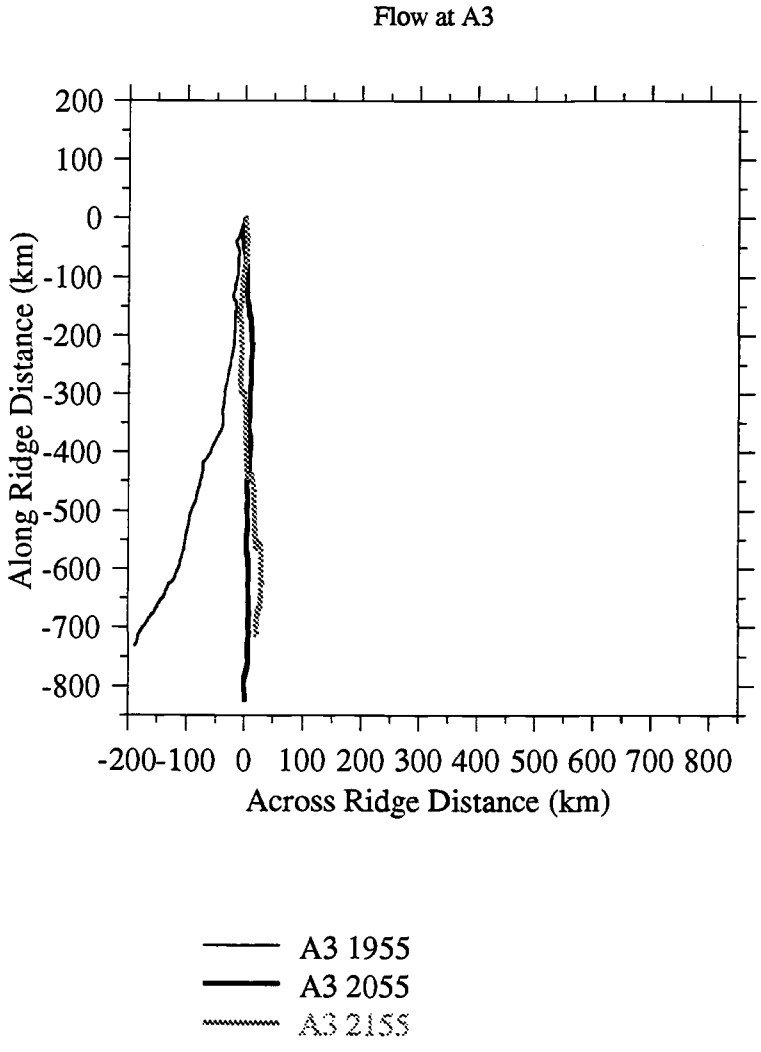

Figure II.103. PVDs at mooring ER-2 A3 at the depths specified over the entire deployment period. Vectors begin at the origin. Refer to Table II.1 for record lengths.

Summary

The validity of using attenuation coefficient, as well as temperature, recorded by moored sensors in the vicinity of a seafloor vent field as hydrothermal plume indicators is supported by three lines of evidence. Within and beneath the non-buoyant plume, changes in temperature and attenuation coefficient are significantly, positively correlated and reflect hydrothermal influence. Trends of increasing attenuation coefficient over time recorded by transmissometers moored only within the zone of plume influence are caused by gradual clouding of the optical lens which appears to reflect high concentrations of fine hydrothermal particles. Because band-passed attenuation coefficient variance increases with proximity to the vent field and to the plume core, I suggest that hydrothermal, fine-particle distribution in the near-field is patchy but becomes more uniform with distance.

I propose that inhomogeneities in temperature, dissolved tracer, and particle fields can be accounted for by one or more of the following processes: 1) advection; 2) pulsations in vent output; 3) mixing of distinct hydrothermal fluids; and 4) water column transformations, in the case of chemical components.

The influence of advection is evident over time scales of hours to years, but the most energetic and persistent variability occurs at tidal-range frequencies in records of both unfiltered current velocity and temperature. This high-frequency variability is due to rotary motions with horizontal scales of 1-2 km that reflect diurnal and semi-diurnal tides, as well as inertial oscillations. Cross-spectral analysis demonstrates that horizontal flow and temperature fluctuations are coherent and in-phase at sub-tidal, tidal-range, and very high frequencies; the cross-correlation decreases with distance from the vent field. This result supports the hypothesis that within several kilometers of the vent field advection is a dominant plume-guiding influence. Furthermore, coherence between currents recorded at different instruments indicates that the near-field horizontal flow field is relatively uniform, but shows evidence of inhomogeneity over distances of about 10 km. Vertical shear in horizontal flow within the plume core is weak, but quite dramatic above and beneath the plume.

Lower-frequency variability in flow and temperature is less energetic and less ubiquitous in the time series and spectra than are tidal and inertial fluctuations. Significant peaks corresponding to periods of 2-5 days, and thought to reflect downward propagating storm energy appear only in some spectra. Even in the absence of significant lower-frequency spectral peaks, energy increases with decreasing frequency. Fluctuations with periods > 10 days are visible in many of the temperature time series. In an example from the plume-core during ER-3, comparison of the flow and temperature time series support the hypothesis that low-frequency changes in flow direction account for the low-frequency temperature variations. In contrast, another example from the earlier ER-2 A3 mooring shows that even where mean advection is directionally steady, temperature varies over low-frequencies, suggesting that mean current velocity is not the only factor causing temperature variation at a fixed point at the depth of the neutrally buoyant plume. In this particular case, using the process of elimination, I assert that vent output changes, which can also alter the height of plume rise, may be the most reasonable explanation for the temperature variability. More generally, this example emphasizes the need to consider all four variance-producing factors when interpreting patterns in the time series of hydrothermal indicators.

Sediment trap results further document low-frequency variability over time scales of weeks to months in both total and hydrothermal particle fluxes. Using copper as an indicator of hydrothermal flux, I find that advection and seasonal settling particle flux patterns co-regulate the removal of hydrothermal elements from the plume. Mean flow determines the location of the plume, hence **availability** of hydrothermal copper; seasonal fluxes of organic particles from the upper ocean control copper **removal** via a scavenging-like, plume-cleansing mechanism. The deep-sea expression of upper-ocean seasonality is most obvious in the particle flux data, but seasonal changes in the physical oceanographic regime (most notably, wintertime current intensification) may enhance the effects of upper ocean productivity cycles.

Advection and sedimentation both vary interannually. At plume-core depths the mean current velocity varied by 50% in speed and 100° in direction among three deployments spanning two years. Total settling particle flux at 1950 m within one kilometer of the vent field varied by a factor of 3.7, copper flux by a factor of 22, and organic carbon by more than a factor of 7 on a trap-averaged basis over four deployments in three years.

The data suggest that the relationship between removal of large, hydrothermal particles via settling and horizontal fluxes of heat and fine particles is not constant. During the first Endeavour Ridge experiment, mean temperature in the plume and the settling flux of hydrothermal particles below are not obviously linked; variation in temperature averaged over sediment trap cup periods is insignificant, but hydrothermal settling particle flux varies dramatically. Yet in subsequent experiments, there is an apparent association of higher temperature with enhanced settling hydrothermal particle flux within several kilometers of the vent field, suggesting that horizontal transport of heat and fine particles in the plume is linked to settling hydrothermal particle flux. The signs of the temperature changes, however, are not predictable from the velocity data based on the relative positions of the vent field and moorings. The weak or absent relationship between mean current velocity and mean temperature (or hydrothermal settling particle flux) at low frequencies is further evidence for thermal inhomogeneity within the plume.

Regarding other scales of temporal variability, there is some evidence for very high-frequency plume variability which may be related to internal waves, and also numerous examples of small-amplitude, episodic changes in attenuation coefficient and temperature in the neutrally buoyant plume, most of which appear to be related to horizontal advection.

Spatial characteristics of hydrothermal plume dynamics include an anticlockwise rotary pattern of current velocity over depth at a single mooring site, higher mean horizontal current velocity within the axial valley, and subdued mean horizontal velocity about 15 km from the vent field. The most prominent spatial patterns with respect to settling hydrothermal particle flux are dramatic increases beneath the plume and decreases with distance from the vent field.

Implications

Results of our three-year, moored-instrument experiment at Endeavour Ridge quantify local variability in horizontal flow, temperature, suspended particle concentration and settling particle flux above an area of hydrothermal venting. The data presented here suggest that the behavior of water column hydrothermal plumes is far more complex than originally thought and that factors in addition to temporal variability in vent output significantly contribute to temporal and spatial plume variability. Since plume dynamics bear directly on the interpretation of physical, chemical and biological oceanographic data collected in the vicinity of active vent fields, understanding of temporal and spatial variability of these deep-sea features is critical. In this section I discuss implications of my results that are relevant to development or refinement of hydrothermal plume models. I also compare my findings to those of other investigators and consider the implications of their observations for interpretation of our data.

Implications of water-column particle/heat relationships

Though attenuation coefficient and temperature are closely coupled, as shown by linear regression and cross-spectral analysis, the relationship between these parameters is apparently not spatially consistent. The slopes of the regression lines in Figures II.41 and II.42 vary from close to zero to 1.14 $m^{-1}/°C$, and this indicates that the record-averaged particle-to-heat ratio varies from location to location. Even within a single record, this ratio varies. In Figure II.104, a time series plot of this ratio for band-passed A2 2005 data, pronounced 2-10 day oscillations are persistent. The variability is, to some extent, a function of frequency, but is even more determined by instrument position. Figures II.105 and II.106 show the slope of the attenuation coefficient/temperature relationship as a function of frequency at eight locations. The intra-record variability is matched or exceeded in magnitude by inter-record variability.

Possible mechanisms to account for these observations include: 1. Particle concentration changes. Temperature is conservative whereas particle concentration can change in response to precipitation, aggregation, scavenging (processes that form particles), as well as settling, dissolution, biological uptake (particle removal processes). 2. Mixing, to varying degrees, of two or more hydrothermal plumes which have distinct heat/particle proportions. The end-member fluids may originate from

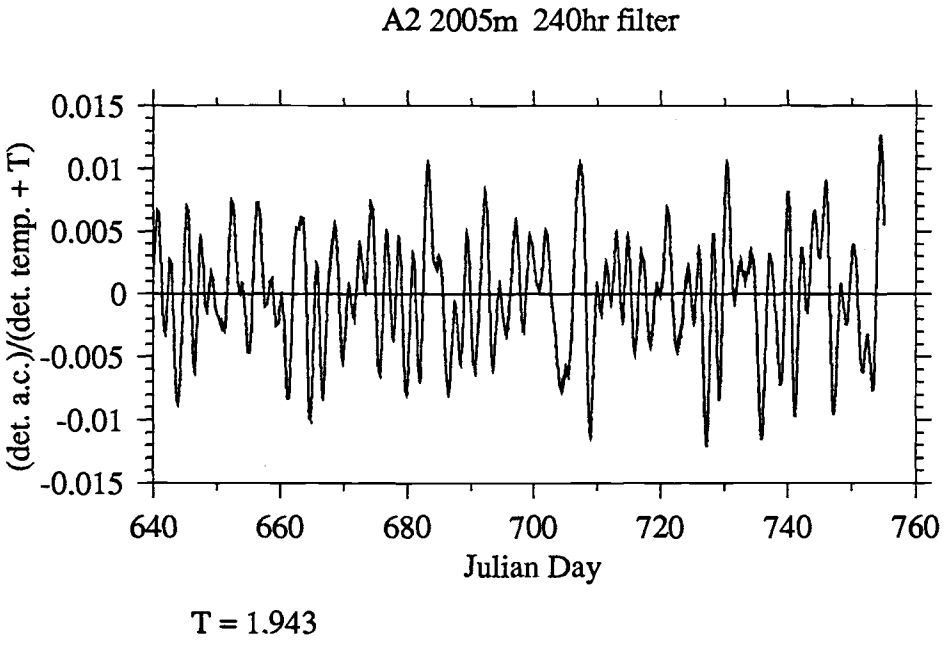

Figure II.104. Time series plot of attenuation coefficient/temperature ratio for A2 2005 showing variability in the suspended particle/heat ratio in the neutrally buoyant hydrothermal plume. Data are low-pass filtered and detrended with a 240-hour cutoff filter (as in Figures II.41 - II.42). Since detrending by our curve subtraction method generates time series with zero means, a constant value, T=1.943, which is the initial value in the temperature time series, was added to each element of the detrended temperature record in order to avoid division by zero.

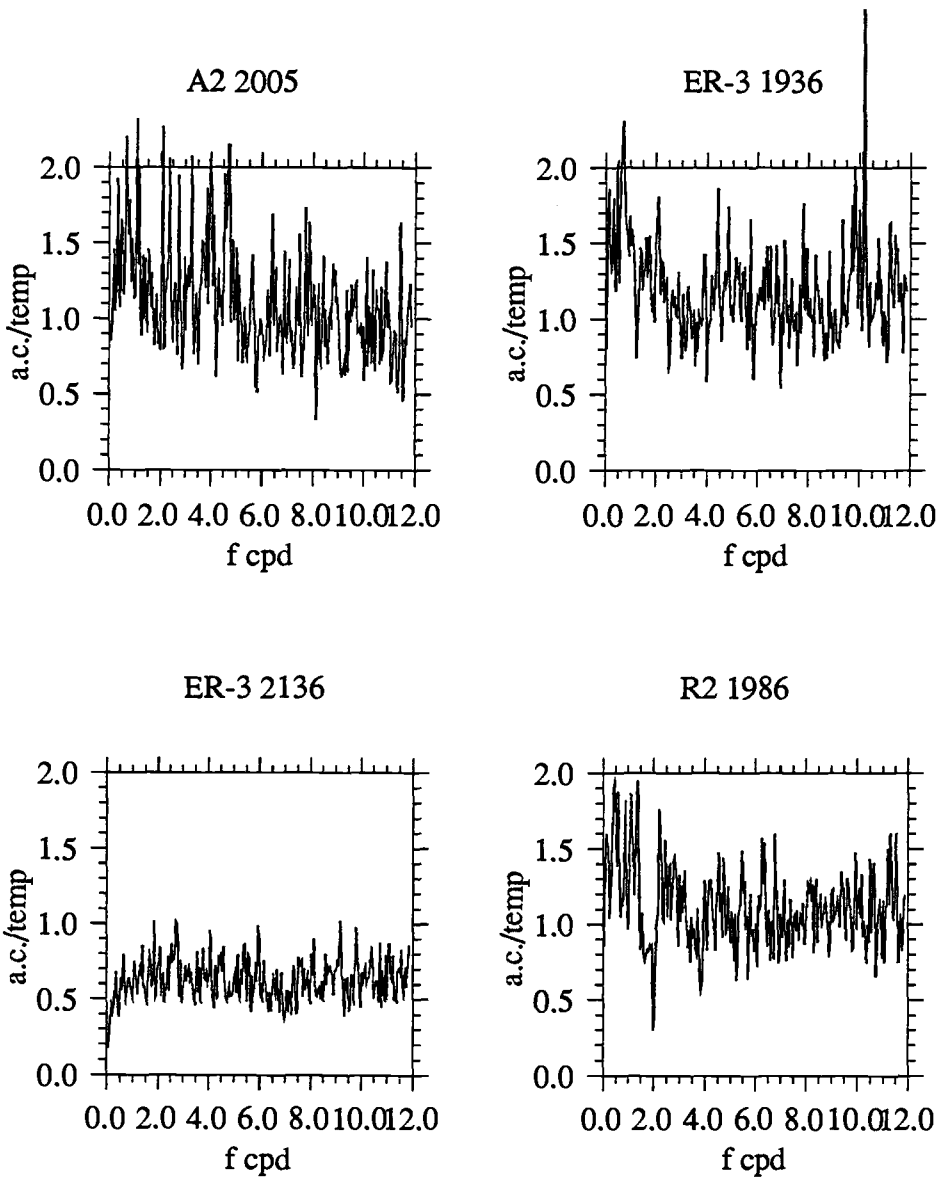

Figure II.105. The ratio of the attenuation coefficient and temperature spectra for the records evaluated in Figure II.41. These plots are based on unfiltered records, and show the slope of the attenuation coefficient/temperature relationship as a function of frequency (f, in the x-axis label is written as the Greek letter omega in the text). Units of the y-axes are $m^{-1}/°C$.

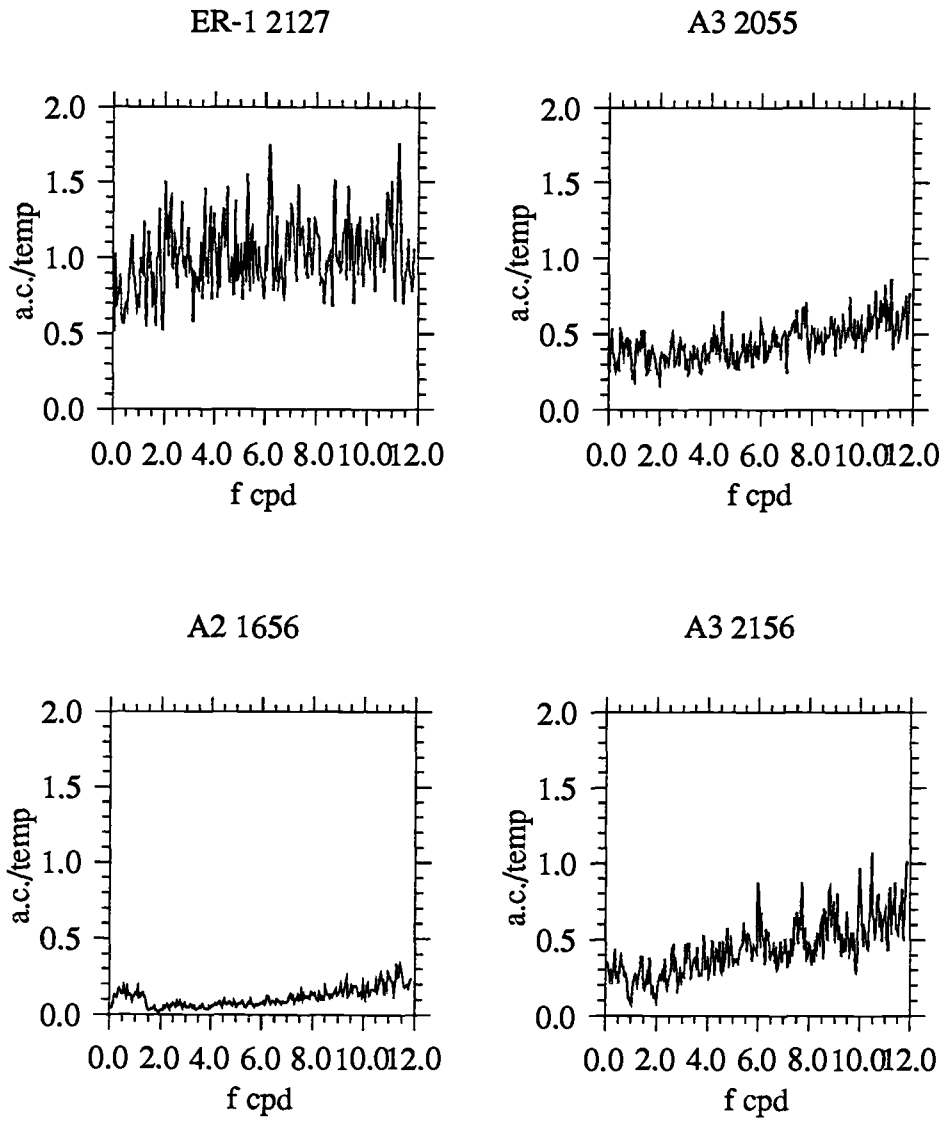

Figure II.106. The ratio of the attenuation coefficient and temperature spectra for the records evaluated in Figure II.42. These plots are based on unfiltered records, and show the slope of the attenuation coefficient/temperature relationship as a function of frequency (f, in the x-axis label is written as the Greek letter omega in the text). Units of the y-axes are $m^{-1}/°C$.

different types of venting within a single vent field, or from geographically separate vent fields. 3. Temporal variability in the characteristics of the vented fluid. These may be changes in the particle/heat ratio of the effluent, or changes in the chemistry, hence, the particle-forming potential of the fluid. Support for each of these three mechanisms is found in our data or inferred from the findings of other investigators.

1. Particle concentration changes

Freshly vented hydrothermal fluid is simultaneously diluted by ambient sea water and subjected to a variety of particle-forming and removal processes. Baker and Massoth (1987) reported typical temperature anomalies of 0.02-0.05 °C that were uniform 10-15 km downcurrent in the neutrally-buoyant plume above the southern Juan de Fuca Ridge. In contrast, these authors found that attenuation coefficient anomalies were non-uniform along the plume. Particle concentration is non-conservative, and it changes not only with mixing but with other time-dependent processes that include precipitation, settling, aggregation, dissolution, etc. Using a radon-helium clock, Kadko et al. (1990) determined the removal sequence of selected plume components and confirmed that age of the plume (the length of time it has been in the water column) is one factor that determines its composition. My data have demonstrated that the currents which transport the Endeavour Ridge plume are highly variable in both speed and direction. Given such complex flow, it is likely that the age of a parcel of neutrally buoyant plume water that passes a stationary instrument could vary considerably, depending on the path it has taken from the vent field to the mooring. Because particle formation and removal occur in the advecting plume, the age and mixing history of the hydrothermal fluids are important determinants of the suspended particle/heat relationship.

Slopes of the linear relationship between attenuation coefficient and temperature may reflect changing particle concentrations. I expect particle-forming and removal processes to reduce particle concentrations in the aging plume. The low particle/heat ratio at plume core depths but several kilometers downstream of the vent field at A3 2055 (Figure II.42, upper right panel) probably reflects removal of particles via settling from the advecting plume. In contrast, the slope of the regression line for the A2 2005 m record in the plume core and closer to the vent field is more than four times higher.

One might think that particle removal could also account for the apparently reduced slope of the regression line for A3 2156 (Figure II.42, lower right panel). In fact, however, correlation between these two parameters is not statistically significant ($r^2 \approx 0.0006$), so the slope of the line is meaningless. The lack of correlation, in addition to the narrow range of attenuation coefficient values, at this location and also above the plume at site A2 1656 (Figure II.42, lower left panel) suggest that changes in the fine, suspended-particle concentrations are negligible (or optically undetectable) in both places. The difference between the source of particles in these two cases is indicated by the broader range of temperature values at A3 2156 (Figure II.42, lower right panel) which reflects hydrothermal influence.

2. Mixing

The pattern of weaker correlation between attenuation coefficient and temperature beneath the plume (depths > 2100 m) and several kilometers away from the vent field - ER-3 2136, ER-1 2127 and A3 2055 - (Figures II.41, lower right, and II.42 upper two panels) can be explained by a mixing scenario. Turbulent mixing of fluids with distinct particle/heat relationships could render detection of one constant relationship impossible. In the case of the deepest instruments, closest to the seafloor, the likely scenario is based on two types of venting that occur in close proximity to each other: High-temperature black smokers emit particle-laden plumes that ascend buoyantly hundreds of meters. Lower-temperature, more diffuse emissions primarily influence deeper zones of the water column and, in contrast to black smokers, contribute significant heat but fewer particles (Schultz et al., 1992). Baker and Massoth (1987) found evidence of heat input from warm springs, i.e. diffuse venting at both Endeavour Ridge and the Southern Symmetrical Segment of the Juan de Fuca Ridge. They report that the ratio of attenuation coefficient and temperature anomalies is reduced in the lower 100 m of the water column relative to values obtained for the neutrally buoyant plume above 2100 m .

The temperature/attenuation coefficient relationships, in concert with settling particle flux and absolute temperature data, provide evidence to support the mixing hypothesis. The plume-core A2 2005, ER-3 1936 and R2 1986 regression line slopes are comparable, in contrast to the deeper ER-1 2136 slope which exhibits a trend of lower particle/heat ratio (Figure II.41). The slope of the regression line for the ER-1 2127 data in Figure II.42, upper left panel, is similarly low. These near-vent field,

beneath-plume measurements, exhibit on average an attenuation/temperature ratio about one-third that shown in plume-core records, and the correlation coefficients are < 0.5.

Two independent data sets (from sediment traps and temperature records) suggest that anomalously high heat, rather than a dearth of particles, at the deeper level account for this trend. Sediment trap data from the ER-3 deployment show that the total settling particle flux was almost a factor of two greater in the 2150 m trap than at 1950 m (3.474 mg/cm^2/y vs. 1.774 mg/cm^2/y). The large-particle settling flux does not necessarily correspond to the fine-particle (< 10 μm), suspended-particle load measured by the transmissometers, yet it is likely that the two are related. This relationship could be a direct or an inverse proportionality, or, the two particle-size populations may be independent. Consider, first, the following two lines of reasoning: 1. The fine and coarse particle populations are directly proportional. Large, settling particles are typically aggregates of finer material. Hence, a more concentrated region of source material (fine particles) should yield an enhanced flux of larger particles. 2. Alternatively, the fine and coarse particle populations are inversely related. If repackaging of fine particles into larger particles accelerates removal of suspended material from the water column, an association of lower attenuation coefficient (clearer water) and enhanced settling particle flux below would be expected. If the first line of reasoning is correct, I expect, based on the sediment trap data, that the particle concentration at ER-3 2136 m is at least as high, if not higher, than at 200 m above. To account for the lower attenuation coefficient/temperature ratio at 2136 m, it is necessary to identify a source of additional heat. Diffuse venting would be a likely source of the excess heat near the seafloor. In fact, comparison of non-detrended temperature records for ER-3 1936 and ER-3 2136 show warmer conditions at the deeper level (Figure II.107). If the second (inverse) relationship between the particle size classes is correct, there is no need to invoke an additional heat source. However, since the temperature data do indicate input of additional heat, the diffuse venting/black smoker mixing scenario emerges as a plausible explanation.

If the fine and coarse particle populations are completely independent, the settling particle flux data are not particularly relevant to evaluating the cause of the higher heat/particle relationship at depth. However I must then account for either a lower concentration of fine particles, or an additional heat source near the seafloor. In the vicinity of a hydrothermal vent field which emits a particle-laden plume from which

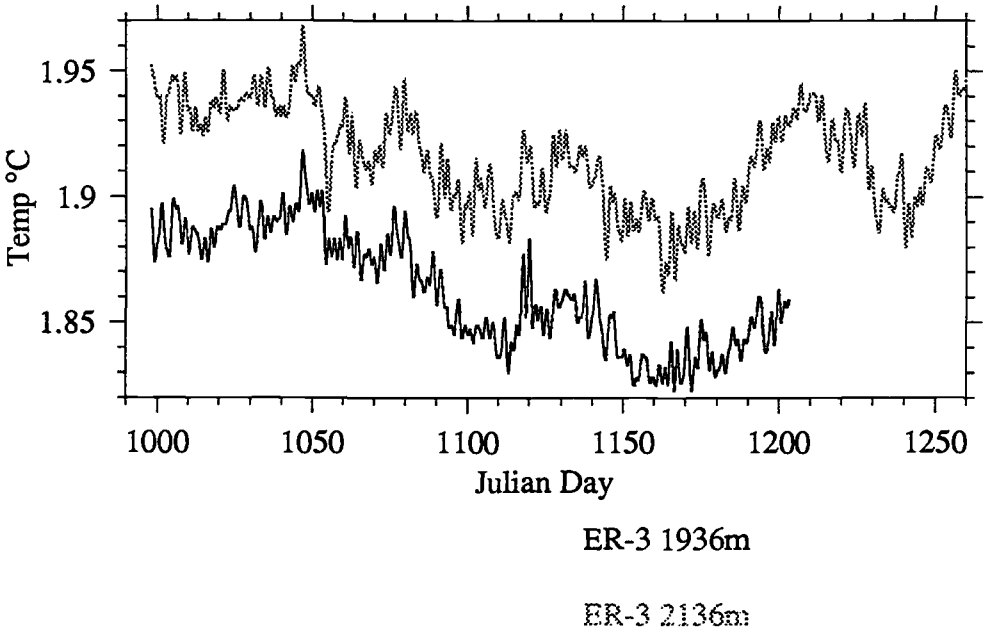

Figure II.107. Low-pass filtered temperature time series from ER-3 1936 and 2136, showing higher temperature at the deeper instrument.

particles are continuously settling, the additional heat explanation seems more likely, and the probable source of this heat is diffuse venting. I draw on results from Baker et al. (1985) who surveyed an 18-km long segment of the southern Juan de Fuca Ridge and defined numerous hydrothermal plumes based on light-scattering measurements. They found that maximum fine-particle concentrations occurred 30-120 m above bottom (mab) which is well below plume-core depth. If similar conditions prevail at Endeavour Ridge, the fine-particle concentration at ER-3 2136 (about 60 mab) would be higher than at 260 mab, irrespective of the large-particle/fine-particle relationship discussed above, and an additional heat source would be required.

Another type of water column mixing scenario would combine fluids originating at different vent fields. This second type of mixing may be more applicable to explaining the reduced attenuation coefficient/temperature ratio at A3 2055 which is at plume-core depth, hence, above the level where diffuse heat input would be strongest. It is not known whether individual neutrally buoyant plumes bear characteristic particle/heat signatures, however it has been established that the particle composition of plumes from different vent fields is distinct and can be used to track specific plumes several tens of kilometers from their source (Feely et al., 1992). Variability in plume particle chemistry suggests that the chemistry of the vent effluent from which the particles form is also variable. Butterfield et al. (1989) reported significant heterogeneity in fluid composition from vents within the primary Endeavour Ridge vent field, and Lilley et al. (1989) measured considerable inter-vent differences in volatile (methane, hydrogen, carbon dioxide) concentrations. The chemistry of the vent effluent reflects, in part, the temperature at which sub-seafloor water/rock reactions occur, and this in turn probably determines the exit temperatures of the fluids which are known to be different at different vent fields. Consequently, it is plausible that the temperature/particle concentration ratio of the neutrally buoyant plume varies from site to site. Baker et al. (1985) documented temporal and spatial variability in particle loadings along the axis of the southern Juan de Fuca Ridge which they attribute this to inputs from discrete vent fields. As was mentioned in **Background and Clarification of terms**, evidence exists for several active vent fields on Endeavour Ridge. Some of our moorings, ER-1 and A2 particularly, were positioned very close to the location reported for the northern, secondary vent field (Robigou et al., 1989), and consequently may have been influenced both by the plume emanating from the vigorous primary vent field and by emissions from this secondary field.

3. Temporal variations

The hypothesis that the particle/heat relationship in any one neutrally buoyant plume measured at a fixed location varies over time merits consideration. Such variability could result from temporal variation in the temperature and chemistry of the source fluid, or from temporal variations in the advective flow that guides the neutrally buoyant plume. Fluctuations in the flow and temperature of the vented fluids from Endeavour Ridge over time scales of hours to about one month have been documented at individual vents within the vent field by time lapse video (McDuff and Delaney, 1989), measurements of emitted radiation (Smith and Delaney, 1989) and employment of thermocouples (Delaney et al., 1989). This variability could extend up into the neutrally buoyant plume which integrates the output from individual vents. Alternatively, temporal variability in the plume-guiding flow field could account for changes in the attenuation coefficient/temperature ratio measured in our Eulerian experiment. The observation that the temporal variability of the particle/heat ratio (Figure II.104) is similar to that of the current components supports the hypothesis that advective flow plays a role in generating the time-variable ratio.

In the preceding paragraphs, I have presented evidence and drawn on the work of other investigators to evaluate the likelihood of the processes that apparently play a role in controlling the particle/heat relationship of the neutrally buoyant hydrothermal plume. Our results indicate that evolution of the plume and concomitant particle removal, mixing of source fluids, temporal changes in the composition and temperature of the vent emissions, and complex flow patterns all are probable, simultaneously occurring, controlling factors and should, therefore, be included in plume models.

Implications of the attenuation coefficient trends

Although transmissometer lens clouding was an unforeseen problem in our study, it is possible to extract some useful information from the resultant trends that affect the time series. The shapes of individual attenuation coefficient trends discussed in the section called *Attenuation coefficient trends* may reflect the intensity of sustained ambient hydrothermal particle concentration. Evidence that lens clouding is related to turbidity is empirical. Transmissometers closest to the vent field and closest to the plume core (≈ 1900 m depth) which harbors elevated hydrothermal particle concentrations cloud most rapidly. In contrast, light attenuation records obtained

farther from the area of strongest plume influence (for example, at site A3, Figures II.6 and II.7, and in the upper water column at about 1700 m, Figures II.16, II.28 and II.32), or deployed for short intervals (for example ER-4, Figures II.11 and II.12) show little or no trend. This suggests that the rate of lens clouding is proportional to the concentration of hydrothermal material, i.e. the more turbid the water the faster the lens will cloud. Steep, rapidly increasing attenuation coefficient curves and truncation due to instrument failure probably reflect instrumental exposure to the most intense particle plumes. Regardless of the functionality of this relationship, the fact that there are differences in the shapes of the curves (the trends) suggest that there are differences in the long-term average ambient particle concentrations measured by the transmissometers. In the A2 2005 record, the rapid increase of attenuation coefficient commences immediately, whereas for the more distal ER-2 moorings (A3 and R2) and the subsequent ER-3 moorings, a more gradual increase follows a relatively constant initial period of up to approximately three months. The records from ER-4 show a hint of an increasing trend, though these records are not long enough to ascertain the form of the trend.

I hypothesize that the sharp, persistent increase in the attenuation coefficient time series at A2 2005 reflects a period of intense hydrothermal particle transport past this site. The average temperature recorded at A2 2005 was approximately 0.05°C higher than that recorded at ER-3 1936, and this supports the hypothesis that the hydrothermal plume was more intense at this depth and time. In fact, physical conditions favored enhanced transport of hydrothermal material past the A2 2005 transmissometer because the across-ridge flow (vent-field to mooring) was the dominant component (Figure II.35, lower left panel); during the ER-3 deployment flow at 1936 m was predominantly along-ridge (Figure II.38, upper right panel). Mooring A2, ER-3 and ER-4 were positioned within the axial valley, but slightly east of the vent field (see Figure II.2). Another indication of heightened hydrothermal influence at A2 2005 is the high copper flux measured in our sediment traps at 1950 and 2150 m during this deployment (Figures II.77 and II.78). At A2 1950 m the Cu flux is an order of magnitude higher than during ER-3 or ER-4; at 2150 m it is three times greater than in the comparable trap on ER-3 and 10 times greater than the ER-4 trap. Although it is thought that sediment traps measure predominantly large particles and transmissometers record the fine particle field, both classes of particles are associated with the hydrothermal plume. In fact, large particles form by aggregation, and alternatively fine

particles can form by disaggregation, so the particle size classes are probably coupled. The preceding evidence supports a hydrothermal cause for the attenuation trends and the assertion that the shape of the trend reflects hydrothermal plume intensity.

Implications of attenuation coefficient and temperature variance patterns

In the section on *Attenuation coefficient variance* I described a pattern of increasing variance in band-passed attenuation coefficient with proximity to the plume core and to the vent field. Here I evaluate possible causes for this pattern which bear on our conceptual plume model. In the following section I discuss biological implications of the spatial distribution of variance.

Support for a hypothesis that physical transport plays an important role in producing the observed variance pattern comes both from our experimental results and from observations of plume behavior made during the course of multiple shipboard surveys. The first indication that changes in flow direction are related to attenuation coefficient variability comes from the observation that variance in low-pass filtered attenuation coefficient occurs at frequencies similar to fluctuations in both along and across-ridge, low-pass filtered current speed. For some records, changes in flow direction can be related to changes in attenuation coefficient. At ER-4 2056 m there is a general association of positive across-ridge flow (eastward) with elevated attenuation coefficient, and stronger (negative, or southward) along-ridge flow with suppressed attenuation (Figure II.108). Considering the relative positions of the mooring and the vent field, this observation suggests that the local distribution of suspended hydrothermal particles is controlled by flow patterns. When currents transport plume material from the vent field toward the mooring, attenuation coefficient increases. However, when currents guide the plume along the axial valley, i.e. not in the direction of ER-4, particle concentration and, hence, attenuation, decrease at the mooring.

Previously I demonstrated that temperature and attenuation coefficient are highly correlated at tidal/inertial frequencies. Thus, observations about temperature can be used to infer control mechanisms for the fine-particle field. One way to show the relationship between high-frequency flow and hydrothermal heat distribution is to construct a PVD on which is superimposed a gray-scale indicator of temperature. Such an image based on unfiltered temperature and currents is shown in Figures II.45 and II.46 for ten-day and three-day segments of the ER-3 1936 deployment. The

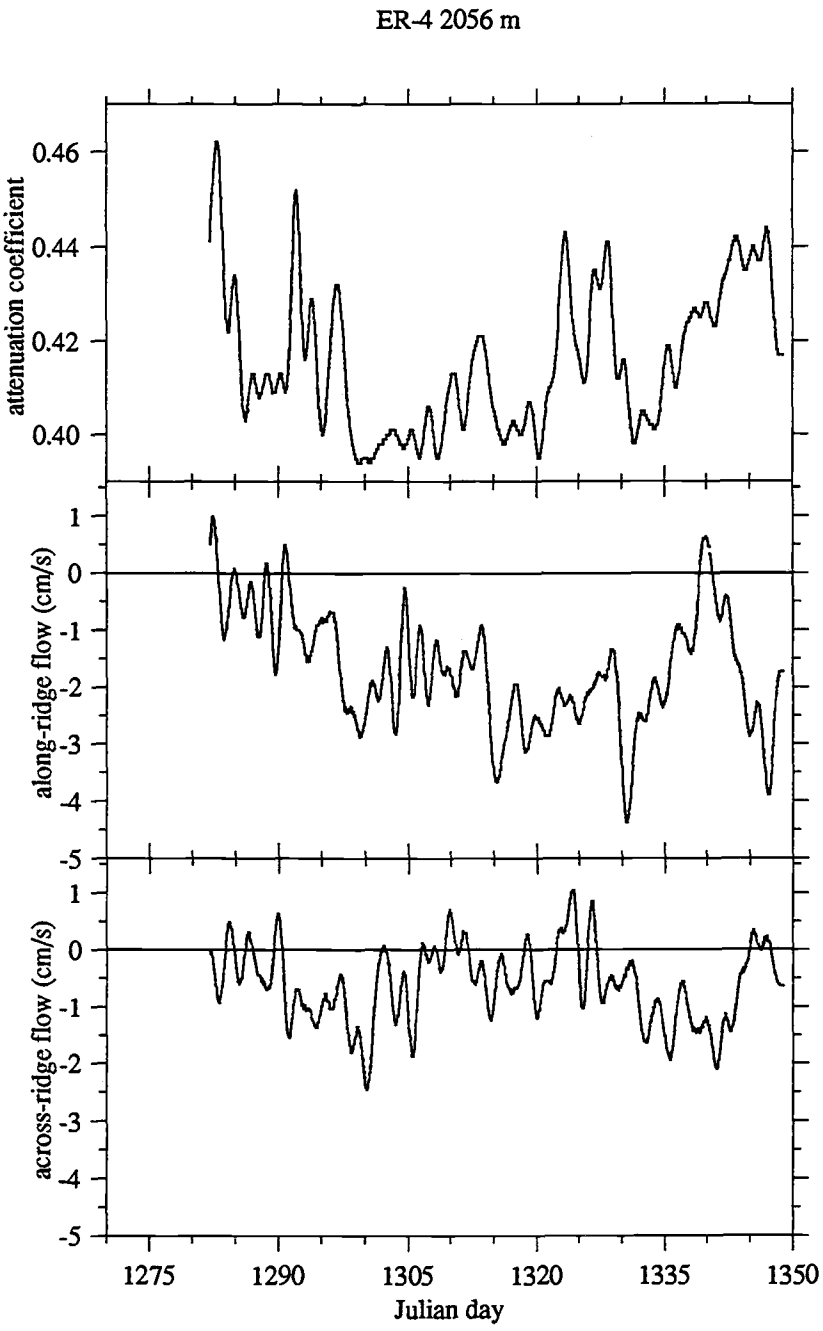

Figure II.108. Low-pass filtered attenuation coefficient, along and across-ridge currents at ER-4 2056.

association of warmer temperature with positive across-ridge flow and cooler conditions with negative across-ridge flow is expected because the mooring was located east of the vent field.

The evidence above points to advection as a primary determinant of the heat and fine-particle fields. But why are these hydrothermal tracer concentrations more variable close to the vent field and close to the plume core? The probable answer is that the highest thermal and hydrothermal particle gradients occur close to the vent field and close to the boundaries of the neutrally buoyant plume. During shipboard towed-sensor surveys we have observed a channeled form of the plume extending radially away from the vent field. Heat and particle gradients in such a feature advected to and fro past fixed sensors could produce the signal variability we observed. The relationship between gradients and variance extends downward to the seafloor. Attenuation coefficient variance at ER-3 2136 beneath the plume core but near the vent field is relatively low. I propose that the subdued variance reflects the conditions closer to the seafloor where persistently elevated hydrothermal particle concentration may be maintained by diffuse venting and fallout from the spreading plume.

In summary, variance patterns imply that within several kilometers of the vent field horizontal advection at plume depths regulates deep-sea hydrothermal plume behavior. Within 100 m of the seafloor diffuse hydrothermal inputs also contribute to the thermal and fine-particle fields. The variance patterns are also indicative of patchiness in the near-field hydrothermal tracer distributions. Interpretation of data collected in some plume-sampling programs clearly requires consideration of these inhomogeneities. Future investigations should be designed to address plume patchiness, or alternatively, to sample in such a manner as to spatially integrate over the patchiness, for example, by towing a sensor over several kilometers, possibly in a convoluted path and/or sampling at a high rate.

Biological implications of hydrothermal plume patchiness

The ecological implications of variability in the hydrothermal suspended-particle field include patchiness of possibly biologically important plume-carried nutrients, toxic hydrothermal components, or even entrained, plume-specific larval or mature fauna in the area close to the plume core. Early findings of suspended particulate organic material (Comita et al., 1984) and microorganisms (Winn et al., 1986) in the buoyant

portions of hydrothermal plumes, and macrozooplankton in the water just above an active vent field (Smith et al., 1985) were followed by publications that suggested or documented biological activity in association with the neutrally buoyant hydrothermal plume. Roth and Dymond (1989) published evidence that chemosynthetic organic material was transported in the advecting plume. Cowen et al. (1990) showed that scavenging rates of dissolved hydrothermal Mn in the plume are microbially mediated and change as the plume ages.

It has been hypothesized that larvae of benthic invertebrates and other zooplankton living at vent fields are transported by hydrothermal plumes, thereby enabling colonization of new vent habitats. Preliminary data of Mullineaux et al. (1991) show that the hydrothermal plume above the Cleft Segment of the Juan de Fuca Ridge contains substantial numbers of larvae of a wide variety of benthic taxa. It follows from the present observations of advectively generated patchiness in suspended particle concentrations, that the distribution of passive larvae in the hydrothermal plume would also be patchy due to physical transport.

Thomson et al. (1991) discovered an intense acoustic scattering layer at the top of the Endeavour Ridge plume and hypothesized that this reflected enhanced zooplankton populations. Probing further, Thomson et al. (1992a) found a 100-m-thick acoustic scattering layer near the top of the neutrally-buoyant plume, and beneath this, a layer of anomalously low backscatter intensity corresponding to the depths of the fine-particle-rich hydrothermal plume. A simultaneous biological sampling program (Burd et al., 1992) documented high concentrations of macrozooplankton at depths immediately above the top of the plume. Thomson et al. (1992a) assert that the acoustic backscatter anomalies reflect zooplankton biomass distributions and suggest that the cause of the zooplankton layering is related to the availability of nutrients near the top of the plume and, conversely, the presence of hydrothermal toxins within the main body of the plume. Their observation that a deep layer exhibiting anomalously high backscatter is present at a station more than 10 km from the vent field suggests that the observed patterns of zooplankton distributions extend laterally into regions where the concentrations of hydrothermal particles, as well as heat and dissolved components, are greatly reduced as a result of particle settling, as well as mixing and dilution, in the spreading plume.

In contrast to the zone immediately above the plume, the plume core (defined by light attenuation anomalies and non-linearity of the potential temperature-salinity relationship) was almost devoid of the large zooplankton. Burd et al. (1992) reported low biomass, ascertained from zooplankton trawls, coincident with small negative anomalies of acoustic backscatter (3-7 dB; 2-5 times less than background) in the core of the Endeavour Ridge plume. Because the acoustic frequency used in this study (150 kHz) and the mesh size of the nets preclude detection of animals/particles < 1mm, this result translates, for purposes of the present hydrothermal particle investigation, to a finding that the neutrally buoyant plume core is a zone where large particles are rare. This is consistent with anomalously low settling particle fluxes measured at plume depths by our sediment traps (Roth and Dymond, 1989). More on this later.

The effects of hydrothermal venting on vertical zooplankton distributions apparently extend far above the neutrally buoyant plume. Burd et al. (1992) point out that the depth profiles of acoustic backscatter (macrozooplankton concentration) in the water column in the vicinity of the ridge crest are notably different from profiles of zooplankton abundance reported in areas of the open ocean not influenced by vents. The differences are not restricted to depths near the neutrally buoyant plume, rather they extend up to mid-water column (approximately 500 m) depths. Specific structural features of the acoustic backscatter profiles may reflect vertical migration, predation dynamics, or functional separation of zooplankton populations.

If the food source for zooplankton populations found in a persistent layer above the plume is contained within the plume itself, as suggested by Thomson et al. (1992a), it is possible that these animals maintain their positions in a layer above the patchy plume and feed opportunistically when currents guide nutritious blobs beneath them. This hypothesis is predicated by the assumption that the zooplankton practice chemotaxis, and some mechanism by which they could maintain their position relative to the plume below. Current shear could be this mechanism. Thomson et al. (1989) conducted acoustic Doppler current profiler (ADCP) investigations at Endeavour Ridge and found that the top of the plume was a region of enhanced current shear. I also presented evidence from our moored current meters of vertical shear. Haury et al. (1990) found experimentally that turbulent shear flow tends to broaden the vertical distributions of some zooplankton species, resulting in selective mixing together of species that could be vertically separated under less energetic conditions. In fact, Burd

et al. (1992) found that the above plume zooplankton population was a mixed species assemblage. While the results of these studies may lend some credence to the ideas concerning the role of zooplankton with respect to the plume, the hypothesis stated above is speculative. It may, however, provide a mechanism to explain zooplankton feeding dynamics and avoidance of adverse chemical conditions in the plume, the explanation offered by Thomson et al. (1992a) for the absence of zooplankton in the plume core.

The presence of the zooplankton above the plume, their absence within the plume itself, and an unsolved settling particle flux mystery concerning perplexing minima in biogenic and inorganic detrital particles at plume depths (Roth and Dymond, 1989) prompts one to speculate about what relationship there might be among these observations.

Why do the zooplankton congregate above the plume? How sensitive are the zooplankton, and, given that the neutrally buoyant plume is highly dilute, is the toxin-avoidance hypothesis to explain their absence in the plume realistic? What process(es) would account for the concentration of organic food particles above the spreading plume? Is the source of the particles settling biogenic material from above, or material entrained in the plume? Is some fraction of this material chemosynthetically generated? What effect on settling particle flux would one expect this population to have? Can it explain the dearth of material in the 1900 m sediment traps?

Answering all of these questions is beyond the scope of this manuscript, however I can offer speculation based on results of our work and reports of other investigators. The location of the zooplankton may be explained either by ecological adaptations (e.g. available nutrients or toxin avoidance) or by current transport. Thomson et al. (1992a) found that the deep scattering (i.e. zooplankton-rich) layer persisted 12 km east of the ridge axis where there was no detectable, fine-particle, hydrothermal plume below. This might suggest that the apparent association between the zooplankton and the plume is coincidental, that the zooplankton are ubiquitous at these depths and independent of the presence of the plume. Alternatively, the zooplankton may be sensitive to very low concentrations of dissolved hydrothermal material that are not detectable optically or thermally. The off-axis population might also indicate a non-hydrothermal plume food source for these animals.

The food source for the zooplankton remains elusive. In addition to the presence of the off-axis population, three additional points favor a non-plume food source: 1) Settling particle flux profiles show persistently reduced organic particle fluxes at plume depths relative to depths above and below the plume (Roth and Dymond, 1989), hence, a lack of nutritious material within the plume; 2) Even if the plume carried sufficient food, this would require that heterotrophs make distasteful forays into the toxic waters which they apparently shun; and 3) If the food was most plentiful within the plume, one would expect the zooplankton to reside there too, and they do not. Alternatively, it is plausible that the plume waters do harbor such nutritious morsels as benthic larvae, chemosynthetically derived particles, bacteria or other, laterally advected, allocthanous, organic detritus. Whatever the origin of the food, if attraction to food is the focusing mechanism for the animals, it is necessary either to explain its concentration just above the neutrally buoyant plume, or find evidence of a mechanism by which these swimmers extract their munchies from the contaminated hydrothermal waters. The former is problematic since there is no steep density gradient or other obvious physical condition that would concentrate food particles above the plume. The latter is not currently supported by results of biological investigations.

Regarding a relationship between the zooplankton and the low, plume-depth settling particle fluxes, I propose the following scenario, which might circumvent the issue of a food-concentration mechanism: In the absence of a hydrothermal plume, deep-sea zooplankton distributions would be more spread out vertically. The plume is a chemically undesirable habitat for the animals, and in response to its wafting to and fro with the changing horizontal current velocities, the zooplankton migrate upward in search of non-contaminated sea water. The congregation of zooplankton at other types of marine interfaces, specifically at the boundaries of oxygen minimum zones, has been documented in the literature (Vinogradov and Voronina, 1962; Smith et al., 1991 and references therein). Because high-frequency rotational flow that advects the contaminated water is persistent, the population maintains its above-plume position. The vertical migration causes a higher than average concentration of zooplankton and results in a dense, mixed-species assemblage. The primary food for the animals is sinking organic detritus from above. Much of this material is macro-aggregates which are consumed by some of the larger animals. Due to sloppy feeding and excretion, the

large particles are broken down into finer material which is then available for smaller species. Depending on the number of zooplankton size classes, there may be extensive recycling of organic material within the concentrated, above-plume layer. Some of the material is assimilated, some is solubilized, and what is left may be very finely divided and remain suspended for long periods of time. The net effect of the zooplankton is, therefore, to biologically filter large settling particles. Reduction in settling particle flux beneath this bio-filter, in the plume core, is thereby explained.

This scenario merits further investigation. The efficiency of the zooplankton as particle transformers must be quantified. Relative rates of particle uptake and breakdown versus fecal pellet production must be calculated. Laboratory studies of zooplankton response to hydrothermal solutions, and plankton tows in the neutrally buoyant plume using nets with much smaller mesh sizes (< 1mm) capable of sampling finely divided organic material, might confirm avoidance behaviour and reveal the source of food.

Oceanic implications and relationship to other studies

Quantification of temporal and spatial variability of the Endeavour Ridge hydrothermal plume is a fundamental contribution to the literature concerning oceanic implications of hydrothermal venting. Understanding the oceanic fate of hydrothermal particles requires consideration of advection in addition to chemical, physical and biological particle transformation rates. Ongoing attempts to quantify the residence time and removal pathways of hydrothermal components, measure lateral particle and heat flux, and ascertain the history of hydrothermal activity over geological time scales can benefit from results presented in this manuscript. The basic message from this study is that whether one is designing a field program, interpreting water column data or attempting to model the behaviour of the neutrally buoyant plume, any assumption of temporal or spatial stability of the plume in the vicinity of the vent field must be either supported by local conditions, or rejected and the relevant scales of variability accounted for. The efficacy of future plume sampling programs could be improved by adjusting sampling intervals and spatial grids according to local variability of advective transport. An alternative strategy involving synchronous water column monitoring with both moored and towed sensors is logistically complicated.

Specific examples of studies where consideration of spatial and temporal variability is relevant include: Coale et al. (1991) who demonstrated that high-resolution mapping of the thermochemical characteristics of hydrothermal plumes can help constrain the age and mixing history of the effluent; Trocine and Trefry (1988) who reported on the distribution and chemistry of hydrothermally-derived suspended matter from a vent site on the Mid-Atlantic Ridge; Cowen et al. (1990) who determined scavenging rates of dissolved Mn onto particles in a southern Juan de Fuca Ridge plume; Klinkhammer and Hudson (1986) who inferred from manganese anomalies a large-scale, asymmetrical dispersal pattern of hydrothermal plumes over the East Pacific Rise; and Feely et al. (1992) who tracked hydrothermal plume particles from the Juan de Fuca Ridge several tens of kilometers using suspended matter composition.

Development and refinement of hydrothermal plume models also benefits from a clear understanding of plume dynamics. Lavelle et al. (1992) developed a two-stage scavenging model to describe the transport and deposition of hydrothermal Mn in the vicinity of the ridge crest. The model is quite sensitive to the off-axis flow component. A balance between the rate of macroaggregate scavenging of fine particles and the off-axis velocity is needed to match the model results with the measured sediment distribution of Mn. Our measurements of flow at Endeavour Ridge suggest that the off-axis (across-ridge) velocities are variable, and in some cases, considerably greater than the central model value of 0.2 cm/s used by Lavelle et al. (1992). This may indicate that at Endeavour Ridge, and perhaps elsewhere, macroaggregate scavenging rates may be higher than initially assumed.

The extent to which characteristics of neutrally buoyant hydrothermal plumes from geographically separate vent fields differ is still unknown. One indication of a possibly important difference between the plumes over Endeavour Ridge and over the southern Juan de Fuca Ridge is that the 4-day periodic oscillation so prominent above the southern Juan de Fuca (Cannon et al., 1991) is apparently weak or absent in the vicinity of Endeavour Ridge.

Sedimentological implications of hydrothermal venting have been the focus of some geological studies. For example, Lyle and Olivarez (1992) review evidence from the sediment record for temporal variability of hydrothermal activity on geological time scales. They also discuss the important geochemical role of plume particles in

scavenging dissolved elements of both hydrothermal and sea water origin. Our moored-instrument work measured hydrothermal variability on a much shorter time scale but nevertheless demonstrates that significant variability in settling hydrothermal particle flux occurs over all time scales and has important implications whether it relates to the composition of deep-sea sediments, marine geochemical budgets, or the distribution of deep-sea organisms.

In designing our moored instrument study, one of our goals was to evaluate the relative importance of lateral and settling particle fluxes in and from a hydrothermal plume. The complexity of the currents and lack of transmissometer calibration makes calculation of lateral particle flux difficult. However, the settling particle flux measured in our sediment traps can be compared with Baker and Massoth's (1987) advected mass flux calculations. One approach is to calculate the rain rate of particles over an area of the seafloor beneath the laterally advecting plume. I use the deployment-averaged particle flux at A2 2150 m to represent an area of one square km nearest and including the vent field, and the particle flux at A3 2150 to represent an area of 2 square km south of and adjacent to the A2 area, in the direction of downstream plume transport. The mass flux in the first box is 1.5 g/s (based on the A2 2150 m flux of 4.6 mg/cm^2/y) and in the second box 2.2 g/s (based on the A3 2150 m flux of 3.5 mg/cm^2/y). These values are at least a factor of 100 lower than the values of advective mass flux reported by Baker and Massoth (1987), indicating that the amount of material carried from the vent field in the neutrally-buoyant plume is at least 100 times greater than the amount that settles within several km of the vent field. This result emphasizes, once again, the importance of quantifying neutrally buoyant plume dynamics, toward which goal this paper contributes.

Conclusions

Distribution of hydrothermal heat and particles in the neutrally buoyant plume above Endeavour Ridge is regulated in a complex way by by time-dependent horizontal advection, vent output and biogeochemical particle transformations. Temporal variability over periods of hours to years occurs locally in plume-depth advection, water-column hydrothermal tracer fields and hydrothermal settling particle flux. Periodic variations over time occur within distinct frequency bands, most notably those corresponding to tidal and inertial oscillations. Longer-period fluctuations are evident, for instance 2 to 5-day periodicity and seasonal signals, but are not uniformly pronounced in all records.

Clearly much of the periodicity in temperature and suspended particle concentration is associated with advection; however, horizontal currents cannot fully account for all of the spatial and temporal variability. Evidence that particle transformations play an important role in regulating oceanic and sedimentary distribution of hydrothermal material comes from spatial and temporal patterns of settling hydrothermal particle flux within 15 km of the vent field. Seasonal signals in hydrothermal sedimentation which mirror upper water column productivity cycles are one of the most striking features of our records. Patterns such as variable particle/heat relationships spatially and over time support the hypothesis that hydrothermal effluents with distinctly different particle loads and thermal properties interact dynamically in the water column. Some episodic variability in the hydrothermal plume may be due to horizontal advection or vent pulsation, although during our study at Endeavour Ridge, the effects of such variability are small relative to the advective periodic signals.

Spatial variability associated with the Endeavour Ridge plume extends vertically from just above the plume where zooplankton congregate, to the seafloor where hydrothermal particles eventually come to rest. Horizontally, variability extends away from the vent field to a distance of at least 15 km. Current shears, both vertical and horizontal, are aspects of the flow field that may be important in controlling hydrothermal particle distributions. Patchiness in the suspended particle concentration near the vent field can be accounted for largely by advective processes. These inhomogeneities may be of ecological importance in understanding plume-specific

zooplankton distributions. In turn, understanding the zooplankton behavior may explain previously perplexing patterns in settling particle flux profiles near the ridge crest.

III: A simple model of settling hydrothermal particle flux at Endeavour Ridge based on moored sediment trap and current meter data

Abstract

A simple, steady-state model incorporating first order removal and along-plume advection is developed and used in concert with experimental moored-instrument data to predict patterns of settling hydrothermal particle flux beneath the Endeavour Ridge neutrally buoyant plume. Scaling of sediment-trap measured fluxes within 15 km of an active vent field to reflect beneath-plume fluxes is achieved by using current meter data to determine the fraction of time horizontal currents directed the plume from the vent field toward the moorings, then multiplying the measured fluxes by a factor to account for the time the plume was directed elsewhere. Unscaled fluxes underestimate near-field, beneath-plume hydrothermal particle fluxes by factors of up to 20. From scaled fluxes, the model was used to predict rates of change of settling Cu, Zn, Fe and Mn flux with distance from the vent field, settling fluxes of these elements at the vent field, and the integrated flux of these elements beneath the plume. The rates of change of flux, which vary among elements, as well as spatially and temporally, reflect differences in the kinetics of particle-forming reactions and seasonal upper-ocean inputs of non-hydrothermal particles. Concordance of predicted and measured vent field fluxes attests to the validity of the scaling technique, as well as the model formulation.

Introduction

Along the Earth's submarine spreading ridges, buoyant plumes of particle-rich hydrothermal fluid issue from seafloor vents, dispersing material leached from newly-formed oceanic lithosphere. Upon reaching levels of neutral buoyancy, typically hundreds of meters above the ocean bottom, plumes are steered horizontally by abyssal currents that vary in velocity both temporally and spatially. A fundamental question regarding deep-sea hydrothermal processes concerns the fate of the dissolved and particulate components of the hydrothermal effluent. Ultimately, if the oceanic steady state is to be preserved, all material which enters the sea through hydrothermal venting must be removed via incorporation into seafloor sediments. In the horizontally advecting plume, a combination of physical, chemical and biological processes transform dissolved elements into particles which eventually settle to the seafloor. Among these, sulfide precipitation, oxidation, scavenging of dissolved elements by Fe oxyhydroxides, bacterially mediated scavenging of Mn, aggregation of fine particles enhanced by the rain of organic material settling from the upper water column, and breakdown of large particles or repackaging of fine material into fecal pellets by zooplankton are thought to regulate the settling flux of hydrothermal particles in the vicinity of a hydrothermal vent field. However, the *in situ* rates of many of these biogeochemical processes are not well constrained. Moreover, near Endeavour Ridge, temporally variable current velocity and current shears, which physically control the transport of hydrothermal material, play an important role in determining the spatial distribution of hydrothermal particles.

Results presented in Chapter II show that the rate of change of settling hydrothermal particle flux with distance from the vent field (between moorings) is not described by a single exponential equation. Rather, within several kilometers of the vent field, flux decreases much faster than it does over the next 10 km. This observation prompts a query: Does this pattern reflect horizontal advection of hydrothermal material away from the vent field, or fundamental differences between processes that regulate settling particle flux near the vent field and farther away?

In this paper, I develop a model to calculate changes in the vertical flux of hydrothermal particles with distance along the plume. The relationship between

removal of hydrothermal material from the plume via settling and horizontal flow velocity is evaluated. Model results, which are compared to fluxes measured by sediment traps moored between one and 15 kilometers from an active vent field, spatially constrain particle removal rates that reflect the sum of in-plume particle transformations. Sediment trap-measured fluxes are scaled to reflect true beneath-plume values according to the fraction of time hydrothermal material was directed by currents past the moorings.

Methods

Settling particle flux was measured at depths of the neutrally buoyant hydrothermal plume (≈ 2000m) with sediment traps moored for 259 days from 28 September 1985 to 14 June 1986 at four locations in the vicinity of Endeavour Ridge. The four moorings that together comprise the ER-2 deployment are individually designated A2, R2, A3 and T3 and were positioned 0.5, 1.5, 2.5 and 15 km respectively from the vent field; their locations relative to each other and the vent field are shown schematically in Figure III.1. Sediment trap samples were analyzed for a suite of inorganic and organic components, with temporal resolution of settling particle fluxes of 48 days, the sample cup collection period. Each trap had five sequential sample cups, consecutively numbered 2, 3, 4, 5 and 1. Concurrent hourly measurements of horizontal currents were recorded using current meters moored one meter beneath each sediment trap. Complete descriptions of the mooring array, instruments, sample processing and data are given elsewhere (Chapter II; Dymond and Roth, 1988; Roth and Dymond, 1989; and Thomson et al., 1990).

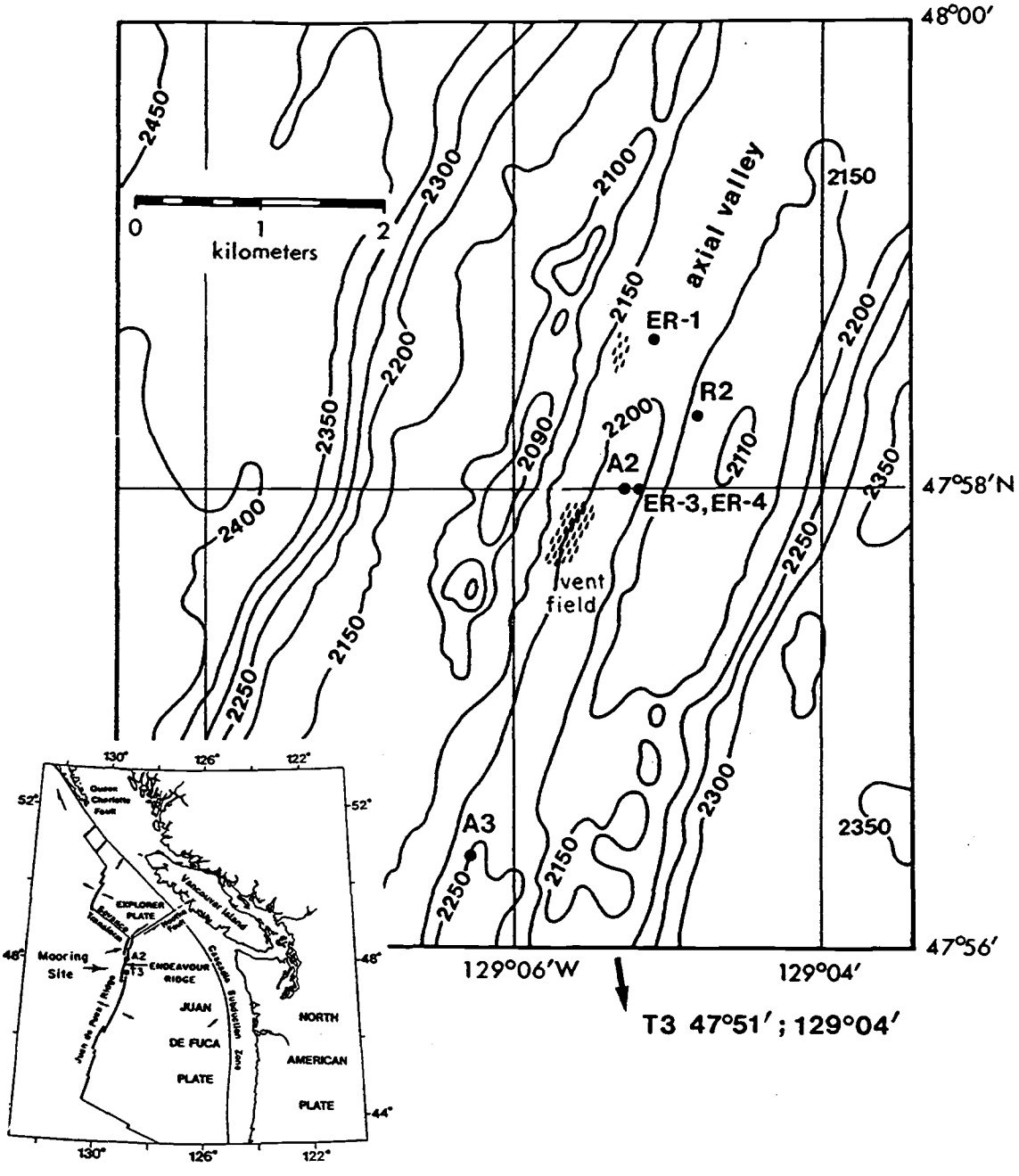

Figure III.1. Location of moorings A2, R2, A3 and T3 which together comprise the ER-2 deployment at Endeavour Ridge, relative to bathymetry and known vent fields. Note that T3 is off the scale of the map. Inset: Location of Endeavour Ridge, a segment of the Juan de Fuca Ridge in the northeast Pacific Ocean.

Model development

The model describing horizontal changes in settling particle flux will be constructed so that horizontal distances are measured in a coordinate system relative to the trajectory of the neutrally buoyant plume. In this quasi-Lagrangian system, x is the along-plume coordinate, y the across-plume coordinate, and x=0 at the vent field. The along-plume velocities are assumed to be constant between points (moorings), and the local change in vertical flux is modelled as a first order loss. Processes which control the removal of a particular hydrothermal element are assumed to be homogeneous between moorings. For reference, symbols used and defined in the text are also listed in Table III.1.

Table III.1. Symbols used in text, alphabetically.

A	width (across-plume dimension) of the plume
D	in-plume dissolved concentration of a particular element
f	scaling factor, dimensionless
F	settling particle flux, μg cm^{-2} y^{-1}
F'	scaled settling particle flux, μg cm^{-2} y^{-1}
F_{1700}	settling particle flux measured above the plume at 1700 m depth, μg cm^{-2} y^{-1}
F_t	settling particle flux integrated over a specified area
F_v	settling flux above the vent field, where x=0, μg cm^{-2} y^{-1}
F_{vm}	measured, vent-field, settling flux, μg cm^{-2} y^{-1}
K_x	along-plume eddy diffusion coefficient, m^2 s^{-1}
K_y	across-plume eddy diffusion coefficient, m^2 s^{-1}
K_z	vertical eddy diffusion coefficient, m^2 s^{-1}
L	decorrelation length scale of the horizontal velocities, m or km
r	local loss rate of settling particle flux, s^{-1} or d^{-1}
t	time, d or y
T	percentage of time plume was directed from vents to a given mooring
u	along-plume horizontal flow velocity, m s^{-1}
U	characteristic value of along-plume velocity, m s^{-1}
U'	turbulent velocity, m s^{-1}
v	across-plume horizontal flow velocity, v≡0, m s^{-1}
w	vertical flow velocity, m s^{-1}
W	characteristic vertical velocity, m s^{-1}
x	along-plume distance, x=0 at vent field, m
x_a	known point, e.g. vent field or mooring position
x_b	known point, e.g. vent field or mooring position
y	across-plume distance, m
z	depth, m
Δ	final - initial

The local rate of change of settling flux of a specified element F ($\mu g\ cm^{-2}\ y^{-1}$), is given by:

$$\frac{\partial F}{\partial t} = -rF - u\frac{\partial F}{\partial x} - v\frac{\partial F}{\partial y} - w\frac{\partial F}{\partial z} + K_x\frac{\partial^2 F}{\partial x^2} + K_y\frac{\partial^2 F}{\partial y^2} + K_z\frac{\partial^2 F}{\partial z^2}, \qquad (1)$$

where r is the loss rate of the settling particle flux (s^{-1} or d^{-1}), u, v and w are horizontal and vertical flow velocities ($m\ s^{-1}$), and K_x, K_y and K_z are the horizontal and vertical eddy diffusion coefficients ($m^2\ s^{-1}$). The second, third and fourth terms on the right side of Eq. 1 are the advection terms; the fifth, sixth and seventh terms are the diffusion terms. In plume coordinates, there is no across-plume velocity, and $v \equiv 0$, thus eliminating the third term of Eq. 1.

In order to simplify, then solve Eq. 1, I compare the relative magnitudes of the terms that control the physical transport of the water parcel from which particles are being removed. The elimination of some terms is thereby justified. Since I believe horizontal advection to be an important process, I compare the size of this term to the others in Eq. 1. The horizontal advection term can be approximated as follows:

$$u\frac{\partial F}{\partial x} \approx U\frac{\Delta F}{\Delta x}, \qquad (2)$$

where Δx is the distance over which F changes, ΔF is the change in F, and U is a characteristic value of along-plume velocity. Likewise for vertical advection:

$$w\frac{\partial F}{\partial z} \approx W\frac{\Delta F}{\Delta z}, \qquad (3)$$

where W is a characteristic vertical velocity. Assuming that $K_x = K_y$ and $\Delta x = \Delta y$, the diffusion terms are approximated as:

$$K_x\frac{\partial^2 F}{\partial x^2} \approx K_x\frac{\Delta F}{\Delta x^2}, \qquad (4)$$

and

$$K_z \frac{\partial^2 F}{\partial z^2} \approx K_z \frac{\Delta F}{\Delta z^2} \quad . \tag{5}$$

In the above approximations, the length scales Δx, Δy, and Δz are chosen so that all ΔF values are equivalent. Each of these terms are divided by the horizontal advection term in order to assess their relative magnitudes. The dimensionless number,

$$\frac{K_x}{U \Delta x} \quad , \tag{6}$$

expresses the magnitude of horizontal diffusion versus advection. The ratio of vertical diffusion to horizontal advection is:

$$\frac{K_z \Delta x}{U \Delta z^2} \quad . \tag{7}$$

The ratio of vertical to horizontal advection is:

$$\frac{W \Delta x}{U \Delta z} \quad . \tag{8}$$

I will assume *a priori* that

$$-rF/\left(U \frac{\Delta F}{\Delta x} \right) \approx 1, \tag{9}$$

and later demonstrate that this is appropriate.

Evaluation of expressions 6, 7, and 8 requires estimation of characteristic values of the included parameters. Table III.2 lists estimates based on data described in the Chapter II, as well as theoretical and experimental work of other investigators. The horizontal eddy diffusion coefficient, K_x (=K_y), is approximated by estimating the turbulent velocity, U', over the characteristic length scale of the experiment, Δx:

$$K_x \approx U'\Delta x\ , \tag{10}$$

where

$$U' = \frac{\Delta U}{L}\Delta x, \tag{11}$$

and ΔU is the change in velocity over the experimental decorrelation length scale, L. The turbulent velocity estimate is derived from data presented in Chapter II. Experimental results show that currents at plume depths are highly correlated within several kilometers of the vent field, but that correlation is low between current meter records obtained at comparable depths 0.5 and 15 km from the vent field. Cross-spectral analysis demonstrates that $3 \times 10^3 < L < 1.5 \times 10^4$ m; I choose a value of 10^4 m. The average difference between flow speed 0.5 and 15 km from the vent field is 0.03 m s^{-1} = ΔU; maximum differences up to 0.1 m s^{-1} occur infrequently. Combining Eqs. 11 and 10, and substituting appropriate values gives:

$$K_x \approx \frac{\Delta U}{L}\Delta x^2 \approx \frac{0.03 \text{ m s}^{-1}}{10^4 \text{ m}}(10^3 \text{ m})^2 = 3 \text{ m}^2 \text{ s}^{-1}\ . \tag{12}$$

This estimate is comparable to the value of 1 m^2 s^{-1} for the horizontal eddy diffusion coefficient determined by Okubo (1971) for length scales of 10^4 m. The vertical eddy diffusion coefficient $K_z << K_x$ and is of the order 10^{-5} - 10^{-4} m^2 s^{-1} (Munk, 1966).

Estimation of the remaining parameters in expressions 6, 7 and 8 is reasonably straightforward. The mean current speed at the plume depth (≈ 2000 m) measured within one kilometer of the vent field (at mooring A2) was 0.052 ± 0.024 m s^{-1}, hence I choose a characteristic value of $U = 0.05$ m s^{-1}. The moorings closest together during the ER-2 deployment, A2 and R2, were separated by approximately one kilometer, and changes in the settling flux of hydrothermal particles were measurable over this distance, thus 10^3 m is a reasonable value for Δx. The vertical distance between sediment traps on the moorings was typically 100 m which is the value chosen for Δz. Finally although we did not measure the vertical velocity, W, in the stably stratified water column in which the neutrally buoyant plume advects laterally, it is reasonable to assume that it is very small relative to the horizontal velocity.

Table III.2. Characteristic scale values

Parameter	Approximate value	Basis for estimate
K_x (= K_y)	3 $m^2 s^{-1}$	Calculated from experimental data as the change in velocity over decorrelation length scales. Described in text.
K_z	10^{-5} - 10^{-4} $m^2 s^{-1}$	Munk(1966)
U	0.05 m s^{-1}	Average experimental plume-core horizontal velocity; see Chapter II.
W	$<<U$	
Δx (= Δy)	10^3 m	Horizontal distance between moorings over which flux changes
Δz	10^2 m	Vertical distance between sediment traps over which flux changes

Using the parameter values in Table III.2, the values of the dimensionless expressions 6, 7, and 8 are respectively 0.06, 2 x 10^{-4}, and 0.01 (assuming, for the latter value, that W is a factor of 1000 less than U). That these values are significantly less than unity indicates that the terms in Eq. 1 for horizontal diffusion, vertical diffusion, and vertical advection are of much smaller magnitude than the term for horizontal advection. Eliminating these terms produces a simplified form of Eq. 1:

$$\frac{\partial F}{\partial t} = -rF - u\frac{\partial F}{\partial x} \quad . \tag{13}$$

If we assume that the system is in a steady state, then

$$0 = -rF - u\frac{\partial F}{\partial x} \text{ or } rF = -u\frac{\partial F}{\partial x} \, . \tag{14}$$

Eq. 14 is easily integrated between points x_a and x_b, where $F(x_a) = F_a$ and $F(x_b) = F_b$ are known quantities. Solving for r, the local rate of change of flux:

$$r = \frac{-u}{x_b - x_a} ln\left(\frac{F_b}{F_a}\right) . \qquad (15)$$

Positive values of r reflect a decrease in hydrothermal settling flux with distance from the vent field, and the magnitude of r reflects the rate of change of settling particle flux over this distance (large r implies large horizontal changes in flux). Using Eq. 15, one can solve for r by specifying the following parameters: along-plume horizontal advection, fluxes of a particular hydrothermal element at two grid points in the along-plume coordinate system, and the distance between the points. Values for these parameters can be estimated from experimental data, as will be discussed in the next section.

Results

Using elemental settling particle fluxes F_a and F_b measured at a given depth on pairs of moorings which are a known distance apart, $(x_b - x_a)$, and estimating the along-plume horizontal advection, u, I have solved Eq. 15 for local rates of change of copper, zinc, iron and manganese fluxes. Results for deployment-averaged fluxes measured at 1950 ± 50 m depths are shown in Table III.3. Each value of u in Table III.3 is the mean of two deployment-averaged velocities calculated from the progressive vector diagrams (PVD) representing horizontal flow at each of the moorings (see Chapter II). Mean velocities at plume depths used in this averaging were 1.7, 3.0 and 0.6 km d^{-1} for moorings A2, A3 and T3, respectively.

Table III.3. Solutions for r, unscaled

Mooring pair	(x_b-x_a) (km)	u (m s^{-1})	$r_{(Cu)}$ (d^{-1})	$r_{(Zn)}$ (d^{-1})	$r_{(Fe)}$ (d^{-1})	$r_{(Mn)}$ (d^{-1})
A2,A3	3	0.027	2.20	1.54	0.91	-0.70
A2,T3	15	0.015	0.37	0.25	0.13	-0.03
A3,T3	13	0.024	0.24	0.14	0.05	0.08

Of the four mooring positions, those of A2, A3 and T3 lie roughly along a line and can be considered to represent three increasing distances from the vent field. The decrease in r for Cu, Zn and Fe between the (A2,A3) and (A3,T3) pairs shown in Table III.3 indicates that the rate of change of settling particle flux of these elements is one to two orders of magnitude greater within the first several kilometers from the vent field than over the next 10+ kilometer interval. In units of s^{-1}, $r_{(A2,A3)}$ for Cu, Zn and Fe are of order 10^{-5}, which when substituted in Eq. 9 shows that the *a priori* assumption was valid, i.e. that the loss term, $-rF$, and the horizontal advection term in Eq. 1 are of similar magnitude. Negative r values in Table III.3 imply that the settling hydrothermal particle flux increased between the two moorings and away from the vent field.

Although some anticipated patterns are observed in Table III.3, there exists a fundamental problem inherent in the solutions for r based on measured fluxes. While the model assumes that fluxes are measured within and along the plume trajectory, due to the temporal and spatial variability of horizontal flow at Endeavour Ridge, the measured fluxes which were obtained at fixed positions do not reflect true under-plume fluxes. The measured fluxes underestimate values of F_a and F_b because the hydrothermal plume was guided in the vent-to-mooring direction only a fraction of the total deployment time.

Pursuant to calculating more accurate r values, I attempt to estimate more accurate under-plume fluxes by scaling the measured fluxes. This is achieved using probability density functions (PDF) for the flow direction measured at each mooring, i.e. the fraction of time the velocity was in a given direction. From the PDF, one can determine the fraction of time horizontal velocity was directed in such a way as to transport hydrothermal material from the vent field to the mooring. The PDFs based on flow velocities measured at 1900-2000 m at each mooring for the total deployment and for the five sediment trap cup periods are plotted in Figure III.2. Recognition that each sediment trap was located directly along the plume path only a fraction of time allows the measured fluxes to be scaled up by a factor, $f \geq 1$, that accounts for the flux that would have been measured, had the instruments been in the plume 100 percent of the time. Thus $f = 1/T$ where T is the fraction of time that the flow was directed from the vent field toward the mooring. Values of T can be calculated directly from the flow direction PDFs by integrating under the curve between a range of directions.

A scaled version of Eq. 15 is given by:

$$r = \frac{-u}{x_b - x_a} ln\left(\frac{F_b'}{F_a'}\right), \qquad (16)$$

where $F_b' = f_b F_b$ and $F_a' = f_a F_a$, f_b and f_a are scaling factors, and all other terms are unchanged. The factors, T, were calculated assuming that only a narrow range of the directions, measured at the mooring, would transport material from the vent field to the mooring. The range is estimated from the distance between the vent field and each mooring assuming a constant horizontal dimension of the plume above the vent field. This range of directions becomes smaller farther from the vent field; this effect is taken

Figure III.2. Probability density functions (PDF) showing occurrence of flow directions at plume depths plotted on a schematic map of the Endeavour Ridge study site. PDFs are for: a) the entire ER-2 deployment period (9/28/85 - 6/14/86); b) 10/6/85 through 11/22/85, the time interval corresponding to sediment trap collection cup 2; c) 11/23/85 through 1/9/86, the time interval corresponding to sediment trap collection cup 3; d) 1/10/86 through 2/26/86, the time interval corresponding to sediment trap collection cup 4; e) 2/27/86 through 4/15/86, the time interval corresponding to sediment trap collection cup 5; and f) 4/16/86 through 6/14/86, the time interval corresponding to sediment trap collection cup 1. Filled triangles represent the approximate locations of the four moorings relative to the primary vent field (shaded square) which is within the one-kilometer-wide axial valley oriented 20°T and bounded by ridge crests (shaded parallel lines). Note that T3 is off the scale of the map. In the panel associated with each mooring, the fraction of the total deployment time horizontal flow measured at nominal depths of 1900-2000 m was toward directions between 0 and 360°T in 10° increments is plotted versus direction. The area under each curve = 1. From these diagrams, the fraction of time flow was oriented over a range of directions (see text) is estimated as the area under the curve between the bounding directions.

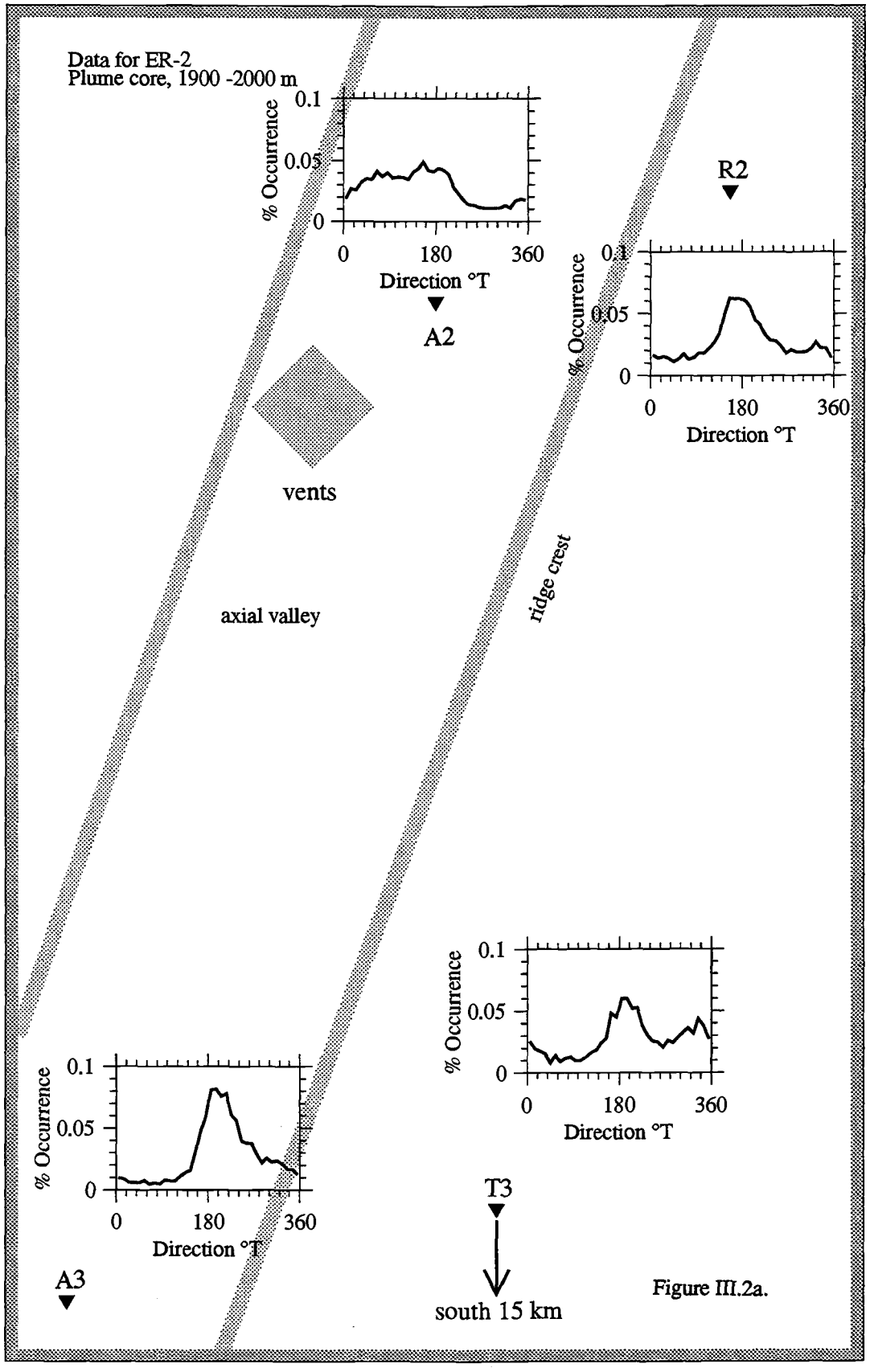

Figure III.2a.

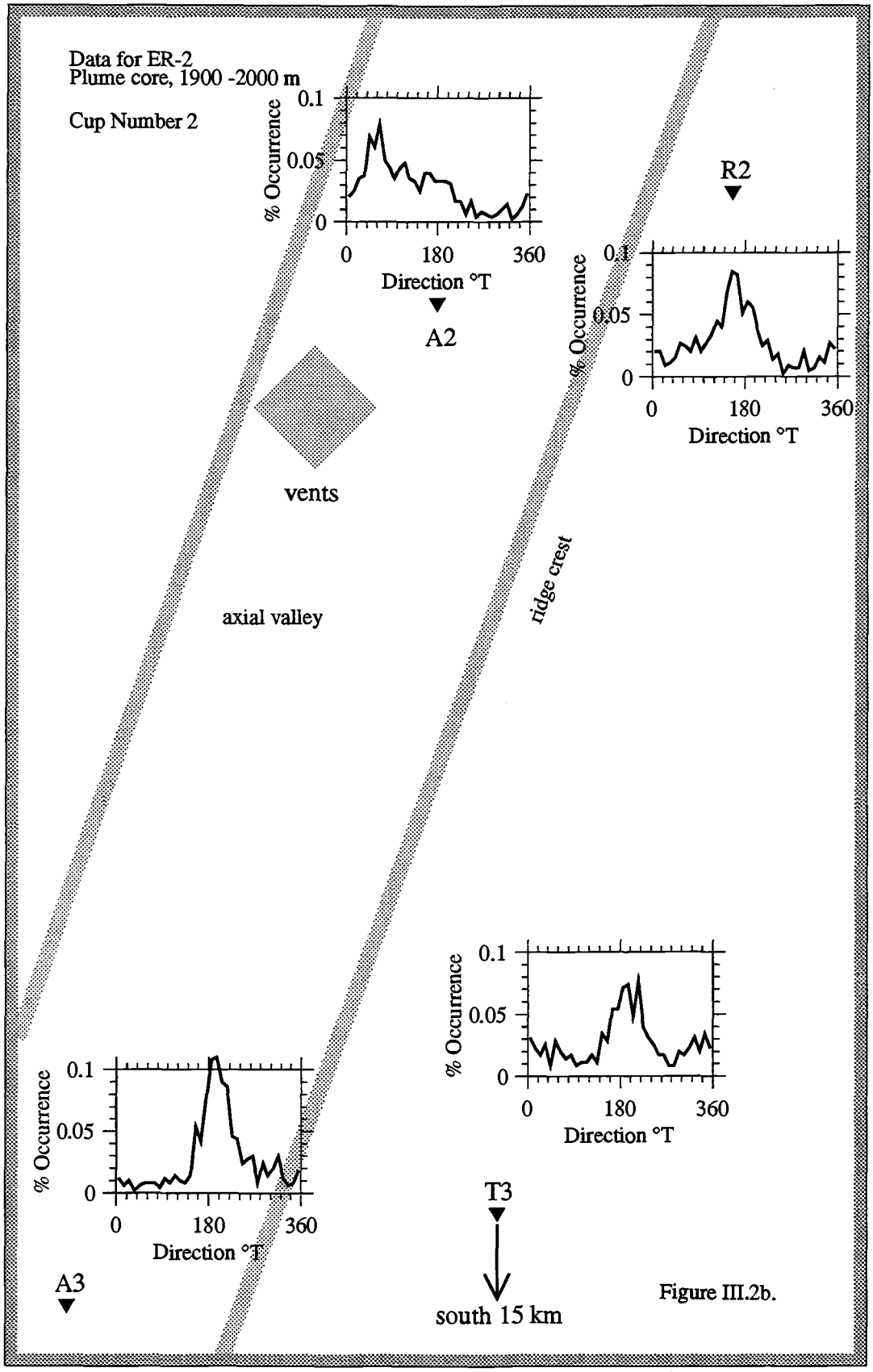

Figure III.2b.

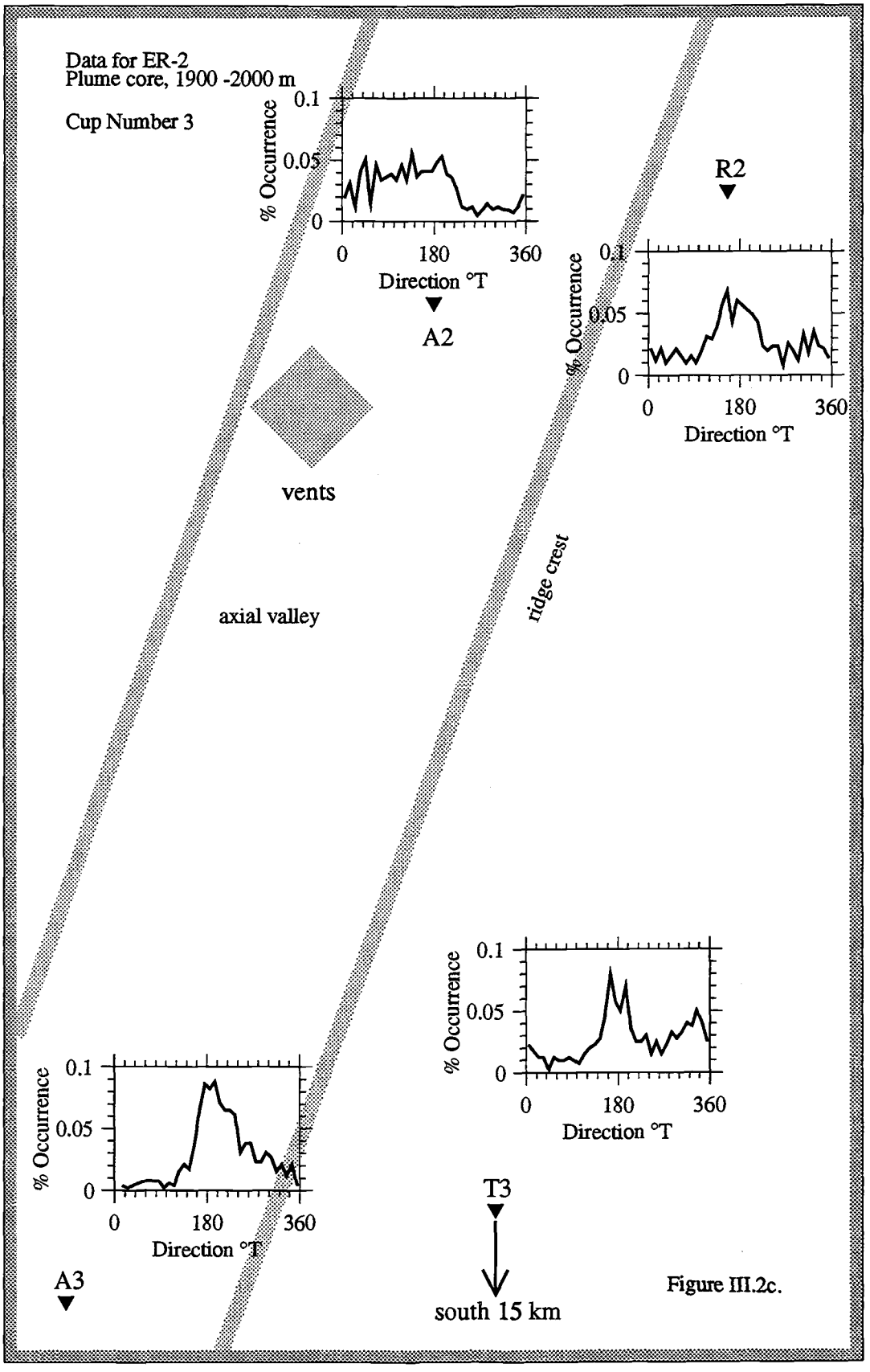

Figure III.2c.

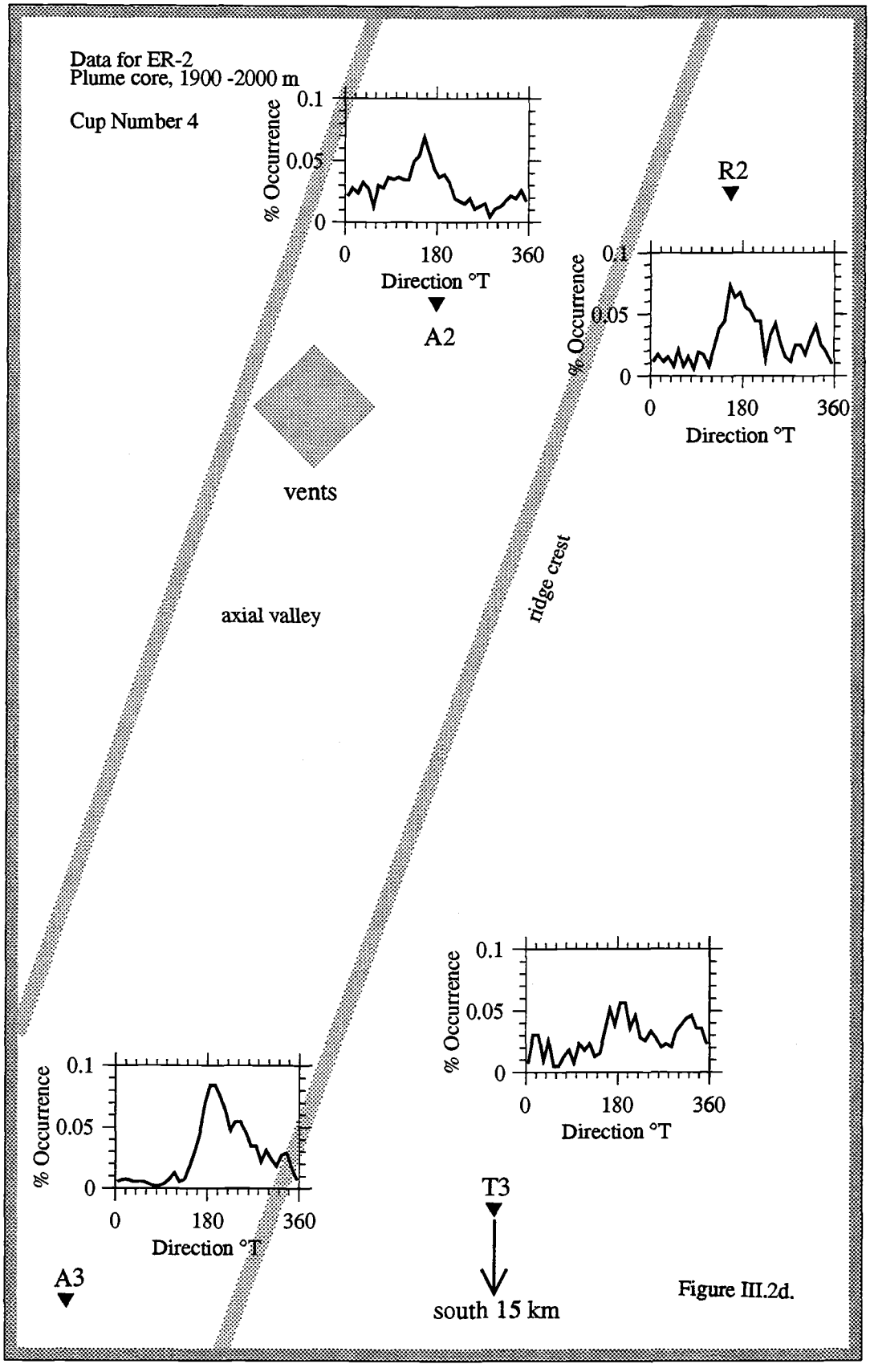

Figure III.2d.

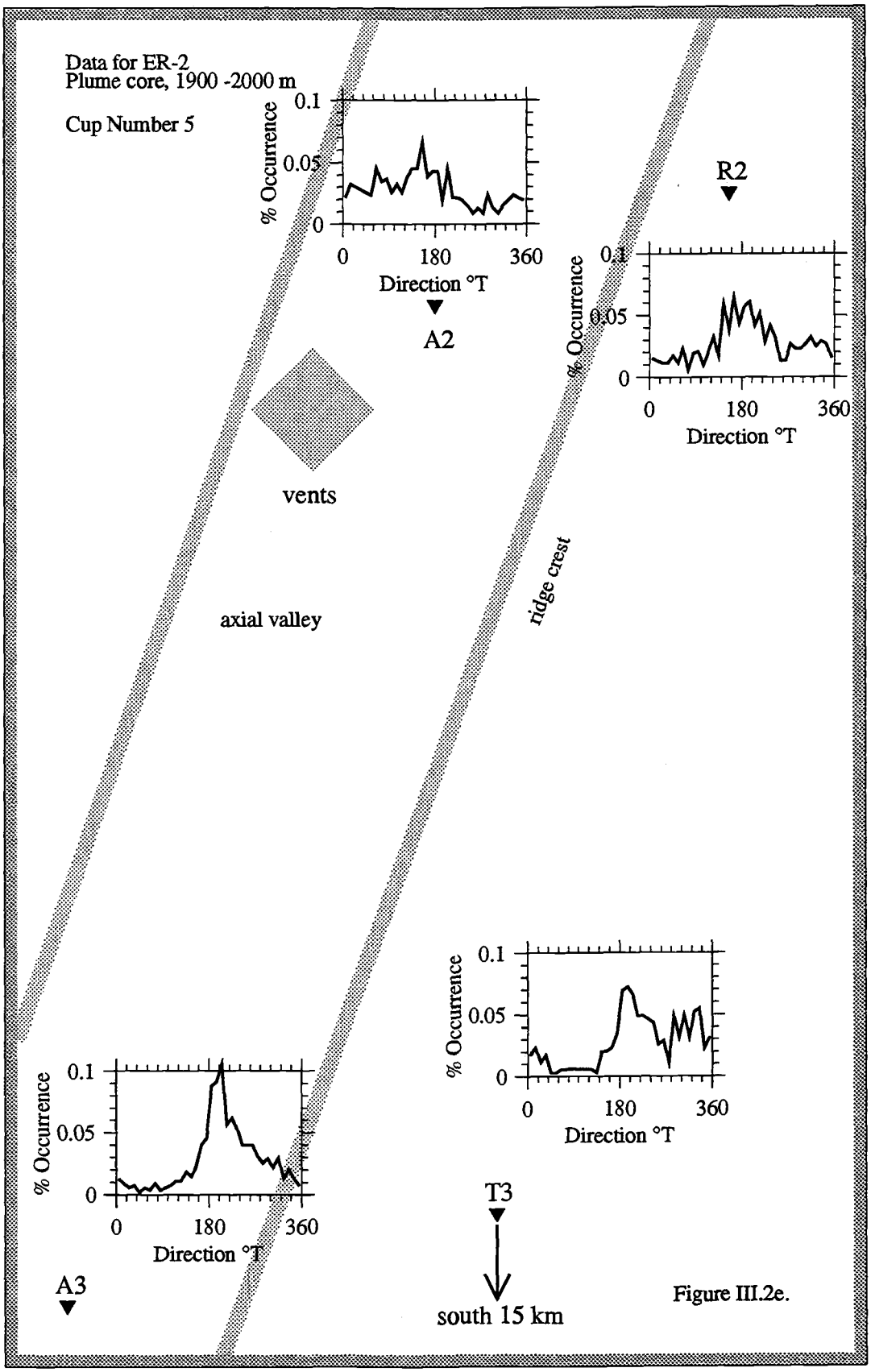

Figure III.2e.

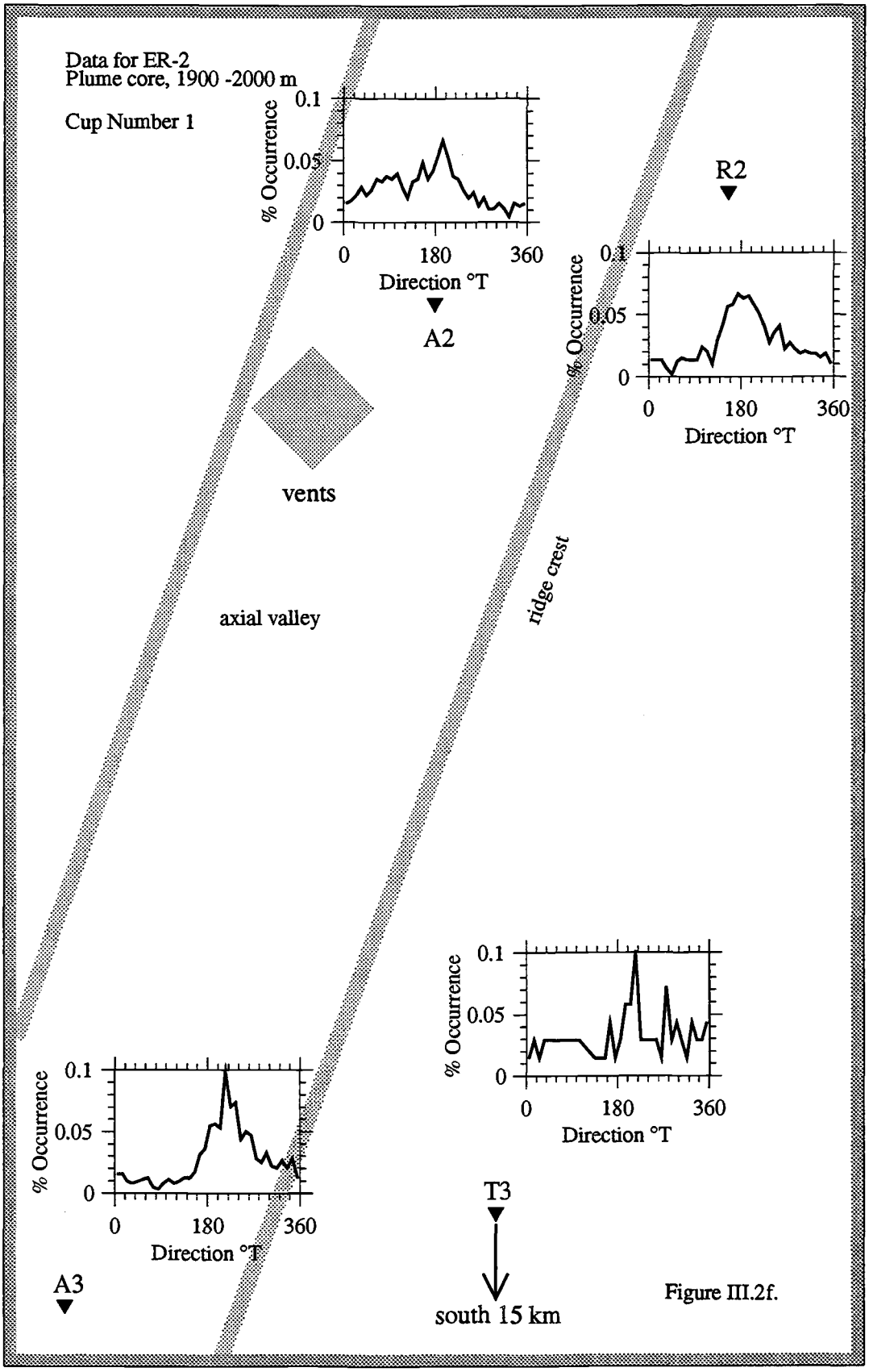

Figure III.2f.

into account by decreasing the directional range of 40° used for mooring A2 and R2 to 30° and 20° for moorings A3 and T3 respectively. Table III.4 summarizes the fraction of time each sediment trap was within plume influence for the entire deployment period and by sediment trap cup interval.

Table III.4. Estimation of T

Mooring	vent-field-to-mooring direction ± range	fraction of time flow occurred (T): cup period					
		2	3	4	5	1	All
A2	50 ± 20 °T	0.300	0.164	0.133	0.165	0.131	0.14
R2	65 ± 20 °T	0.109	0.089	0.070	0.073	0.050	0.08
A3	195 ± 15 °T	0.400	0.320	0.312	0.295	0.218	0.25
T3	170 ± 10 °T	0.142	0.177	0.130	0.089	0.085	0.10

The values in Table III.4 for T are rough estimates with errors of approximately ±10% due primarily to the sensitivity of T to the magnitude of the directional range. Depending on the specific PDF in Figure III.2, a change of ±10° in the directional range can change the relevant area under the curve, hence the estimate of T by 0.01 to 0.04. Nevertheless, scaling the settling hydrothermal particle fluxes by appropriate factors to compensate for directional variability of horizontal flow provides better approximations of the true fluxes along the axis of the neutrally buoyant plume, and consequently more accurate values of r in solutions to Eq. 15. For all cup periods at the three moorings, $2.5 \leq f \leq 12$. Among cup periods at a particular location, f varies by a factor of ≤ 2.3, and at all three moorings, the cup 1 period corresponds to the time of maximum f, i.e., the plume was seldom directed toward the moorings. Measured and scaled hydrothermal settling particle fluxes are given in Table III.5.

Table III.5.

Measured and scaled plume-core hydrothermal settling fluxes (μg cm^{-2} y^{-1})

mooring, cup	*f*	flux (measured) Cu	Zn	Fe	Mn	flux (scaled) Cu	Zn	Fe	Mn
A2,									
2	3.3	13.80	33.90	176.0	2.11	45.4	112.0	582	6.96
3	6.1	4.77	9.09	51.4	0.42	29.1	55.4	314	2.54
4	7.5	1.46	3.28	20.0	0.16	10.9	24.6	150	1.23
5	6.1	3.48	5.79	38.0	0.35	21.3	35.3	232	2.13
1	7.6	21.00	26.80	220.0	1.90	160.0	204.0	1672	14.40
All	7.1	9.74	16.60	109.0	0.87	69.1	118.0	777	6.15
R2,									
2	9.1	0.35	0.76	19.4	0.94	3.19	6.89	177.0	8.57
3	11.2	0.11	0.28	5.9	0.41	1.27	3.09	65.6	4.62
4	14.3	0.12	0.27	6.2	0.44	1.74	3.85	88.0	6.36
1	20.0	0.42	0.72	35.1	0.76	8.48	14.40	703	15.10
All	12.5	0.25	0.48	16.9	0.60	3.09	6.04	211	7.46
A3,									
2	2.5	0.87	1.32	33.7	2.14	2.19	3.30	84.2	5.36
3	3.1	0.38	0.52	15.2	1.22	1.18	1.61	47.0	3.77
4	3.2	0.23	0.44	10.1	0.80	0.73	1.42	32.2	2.57
5	3.4	0.28	0.45	16.8	1.54	0.97	1.52	57.2	5.23
1	4.6	0.36	4.45	41.4	1.86	1.66	20.50	190	8.56
All	4.0	0.58	2.29	34.1	2.12	2.31	9.17	136	8.47
T3,									
2	7.0	0.12	0.20	26.4	1.27	0.81	1.36	185	8.92
3	5.6	0.90	0.13	14.4	0.88	0.50	0.71	80.8	4.96
4	7.7	0.10	0.21	18.0	1.08	0.77	1.63	138	8.29
5	11.2	0.14	0.19	23.5	1.70	1.62	2.15	263	19.00
1	11.8	0.18	3.14	34.6	1.36	2.14	37.10	409	16.10
All	10.0	0.13	0.96	24.2	1.27	1.31	9.56	242	12.70

Table III.6. Values of r based on scaled fluxes, by cup period

Mooring pair, cup	(x_b-x_a) (km)	u (ms^{-1})	$r_{(Cu)}$ (d^{-1})	$r_{(Zn)}$ (d^{-1})	$r_{(Fe)}$ (d^{-1})	$r_{(Mn)}$ (d^{-1})
(A2,A3)						
2	3	0.026	2.27	2.64	1.45	0.20
3	3	0.029	2.68	2.96	1.58	-0.33
4	3	0.031	2.42	2.54	1.37	-0.66
5	3	0.029	2.58	2.63	1.17	-0.75
1	3	0.025	3.29	1.66	1.57	0.38
All	3	0.027	2.64	1.98	1.35	-0.25
(A2,T3)						
2	15	0.015	0.35	0.38	0.10	-0.02
3	15	0.015	0.35	0.38	0.12	-0.06
4	15	0.015	0.23	0.23	0.01	-0.16
5	15	0.016	0.24	0.26	-0.01	-0.20
1	15	0.016	0.40	0.16	0.13	-0.01
All	15	0.015	0.34	0.22	0.10	-0.06
(A3,T3)						
2	13	0.023	0.15	0.14	-0.12	-0.08
3	13	0.025	0.14	0.13	-0.09	-0.05
4	13	0.025	-0.01	-0.02	-0.24	-0.19
5	13	0.028	-0.01	-0.06	-0.28	-0.24
1	13	0.023	-0.04	-0.09	-0.12	-0.10
All	13	0.024	0.09	-0.01	-0.09	-0.06
(A2,R2)						
2	1	0.021	4.82	5.06	2.16	-0.38
3	1	0.020	5.42	4.99	2.70	-1.03
4	1	0.023	3.65	3.69	1.06	-3.27
1	1	0.021	5.32	4.81	1.57	-0.08
All	1	0.022	5.91	5.64	2.48	-0.37

Using the scaled fluxes of Table III.5, new values for the rate of loss of settling particle flux, r, were calculated (Table III.6). These values of r were used to interpolate $F(x)$, the settling flux versus distance from the vent field, for each cup period, and for the whole deployment (Figure III.3). The model solutions in Table III.6 describe changes in hydrothermal settling particle flux with distance from the vent field.

Figure III.3. Settling fluxes of Cu, Zn, Fe and Mn as a function of distance from the vent field. Data are for: a) the entire ER-2 deployment period (9/28/85 - 6/14/86); b) 10/6/85 through 11/22/85, the time interval corresponding to sediment trap collection cup 2; c) 11/23/85 through 1/9/86, the time interval corresponding to sediment trap collection cup 3; d) 1/10/86 through 2/26/86, the time interval corresponding to sediment trap collection cup 4; e) 2/27/86 through 4/15/86, the time interval corresponding to sediment trap collection cup 5; and f) 4/16/86 through 6/14/86, the time interval corresponding to sediment trap collection cup 1.Open circles denote fluxes measured at moorings A2, A3 and T3. Filled circles represent scaled fluxes described in text. Open and filled squares at x=0 are values of F_V, vent-field fluxes determined by backwards extrapolation from A2 (dotted lines). The equations for the solid curves connecting measured and scaled fluxes between moorings are obtained by rearranging Eq. 15 in the text to solve for flux at each distance. For comparison, dashed lines between A2 and T3 fluxes show the rate of change of settling flux that would be erroneously assumed if measurements were made at only these two locations. Because the three mooring sites were not precisely along a straight line, and it was necessary to preserve the actual distances between moorings, the distance between T3 and the vent field is depicted as being slightly greater (by about 1 km) than in reality.

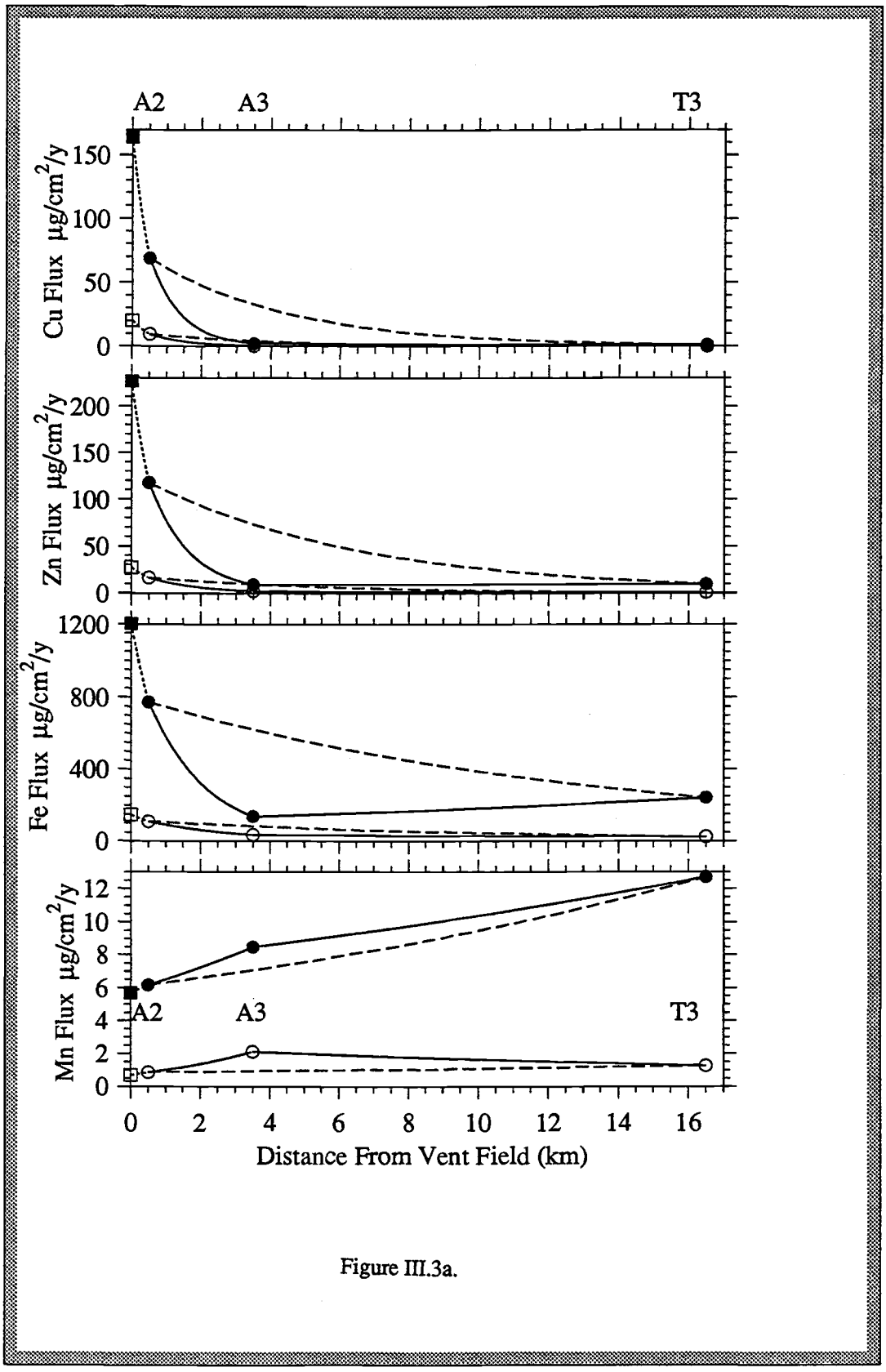

Figure III.3a.

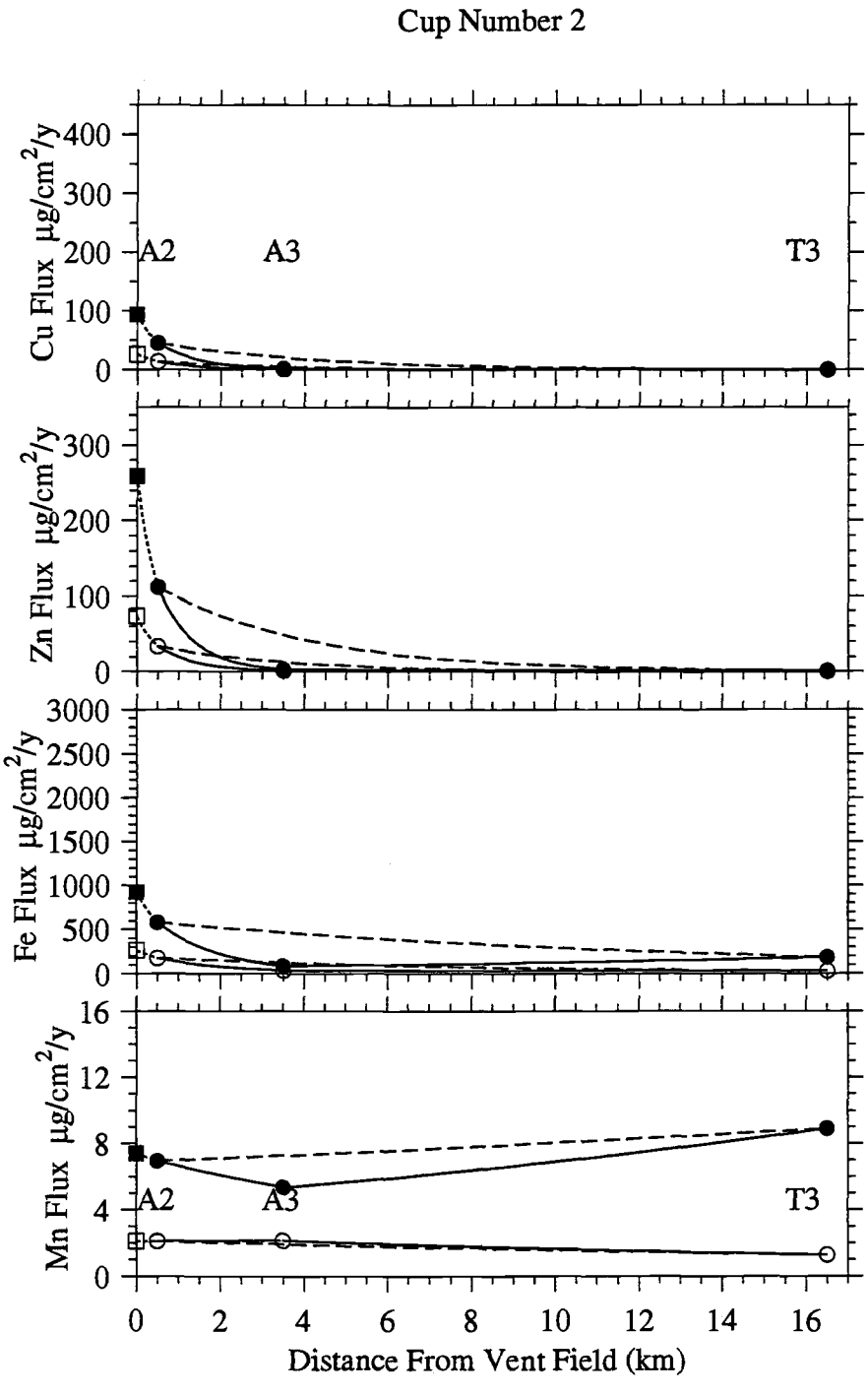

Figure III.3b.

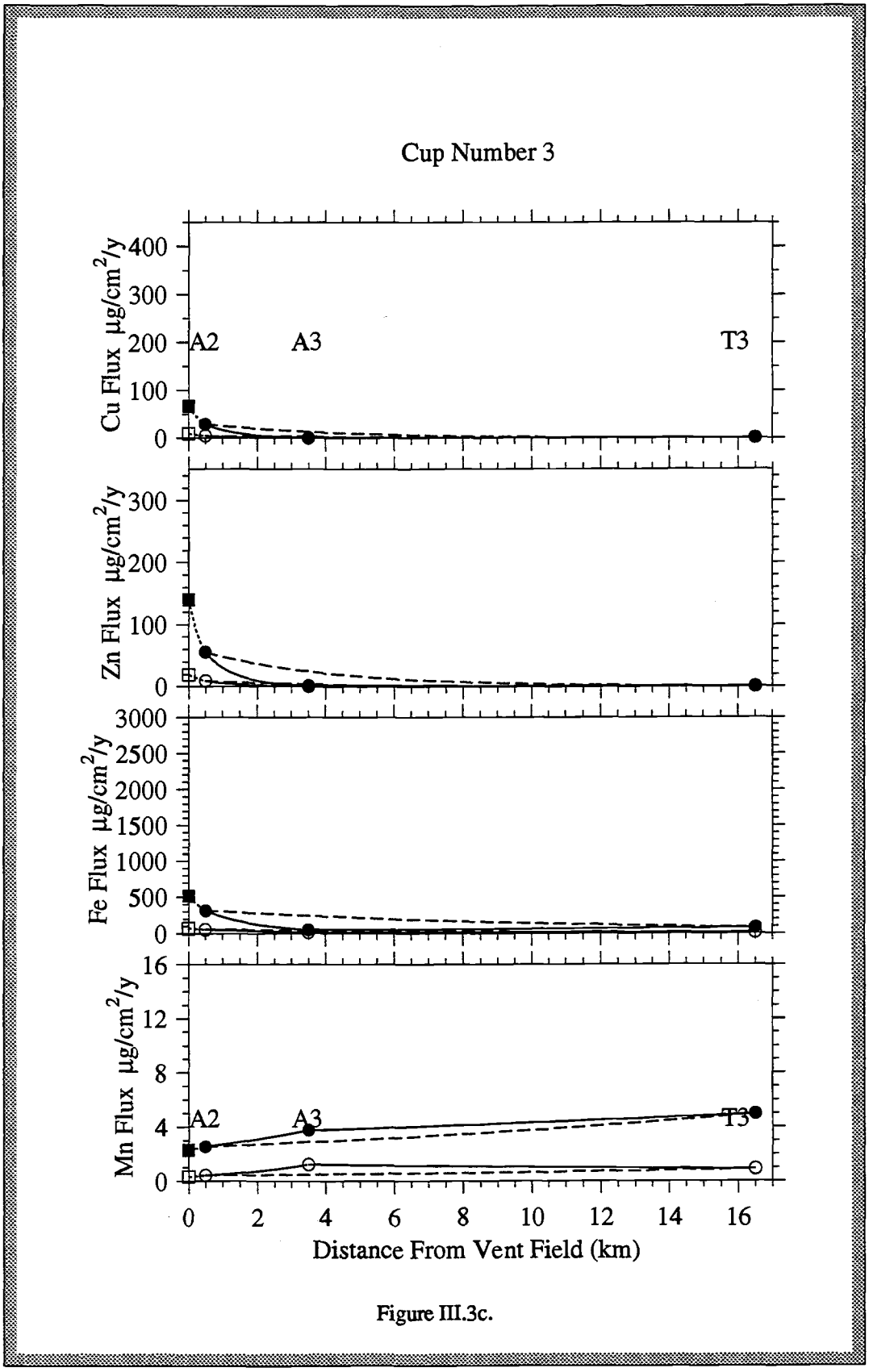

Figure III.3c.

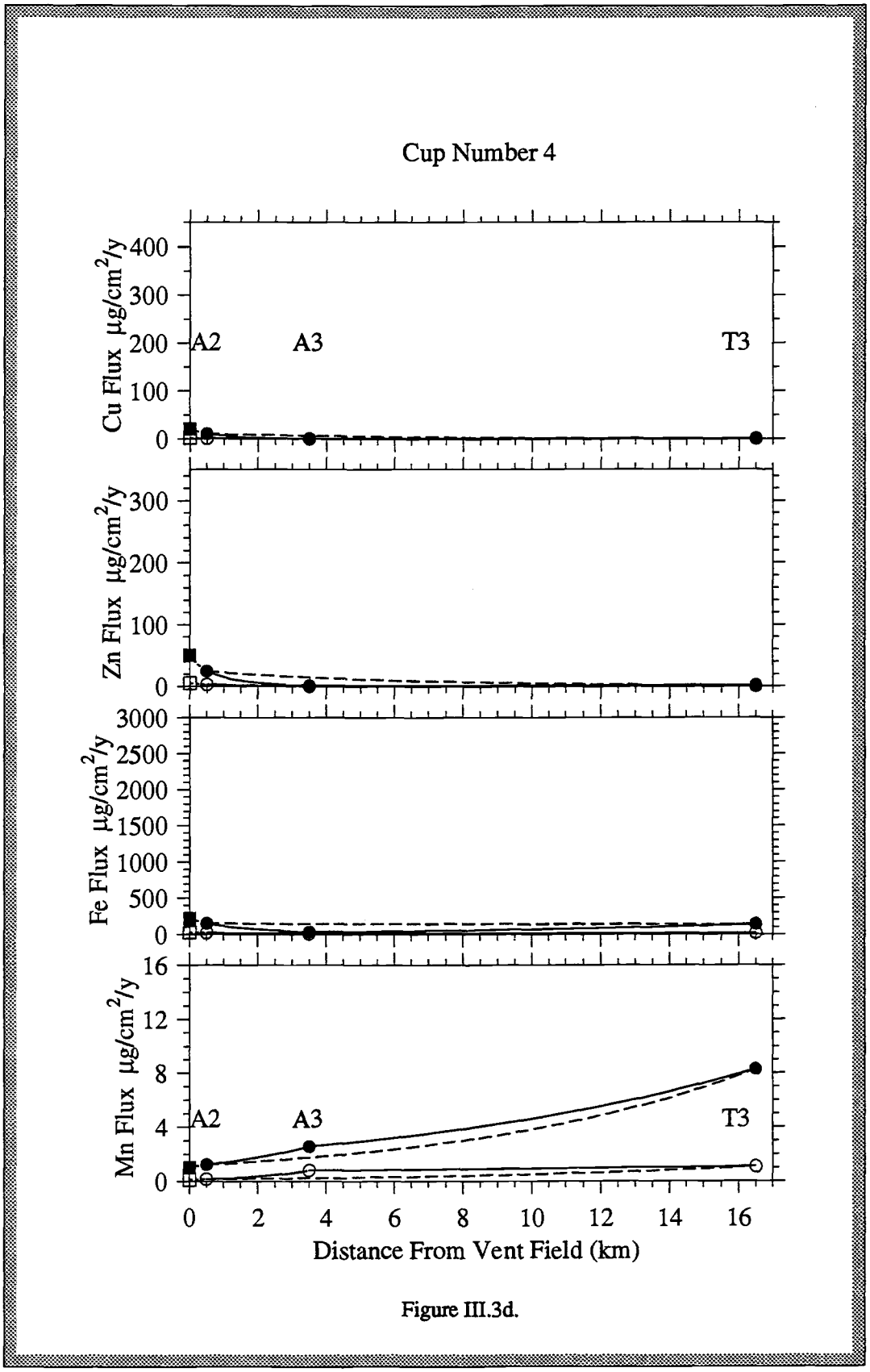

Figure III.3d.

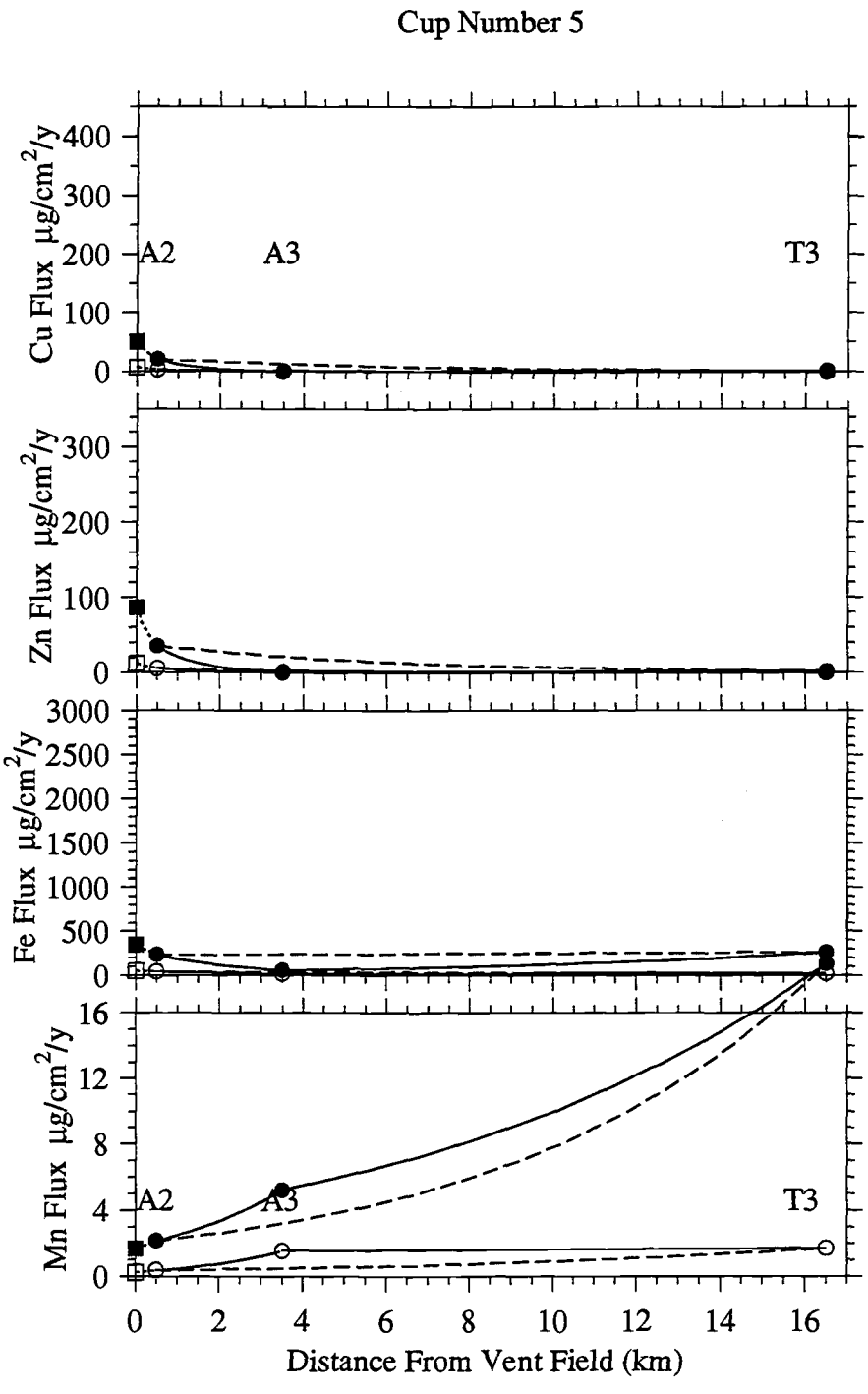

Figure III.3e.

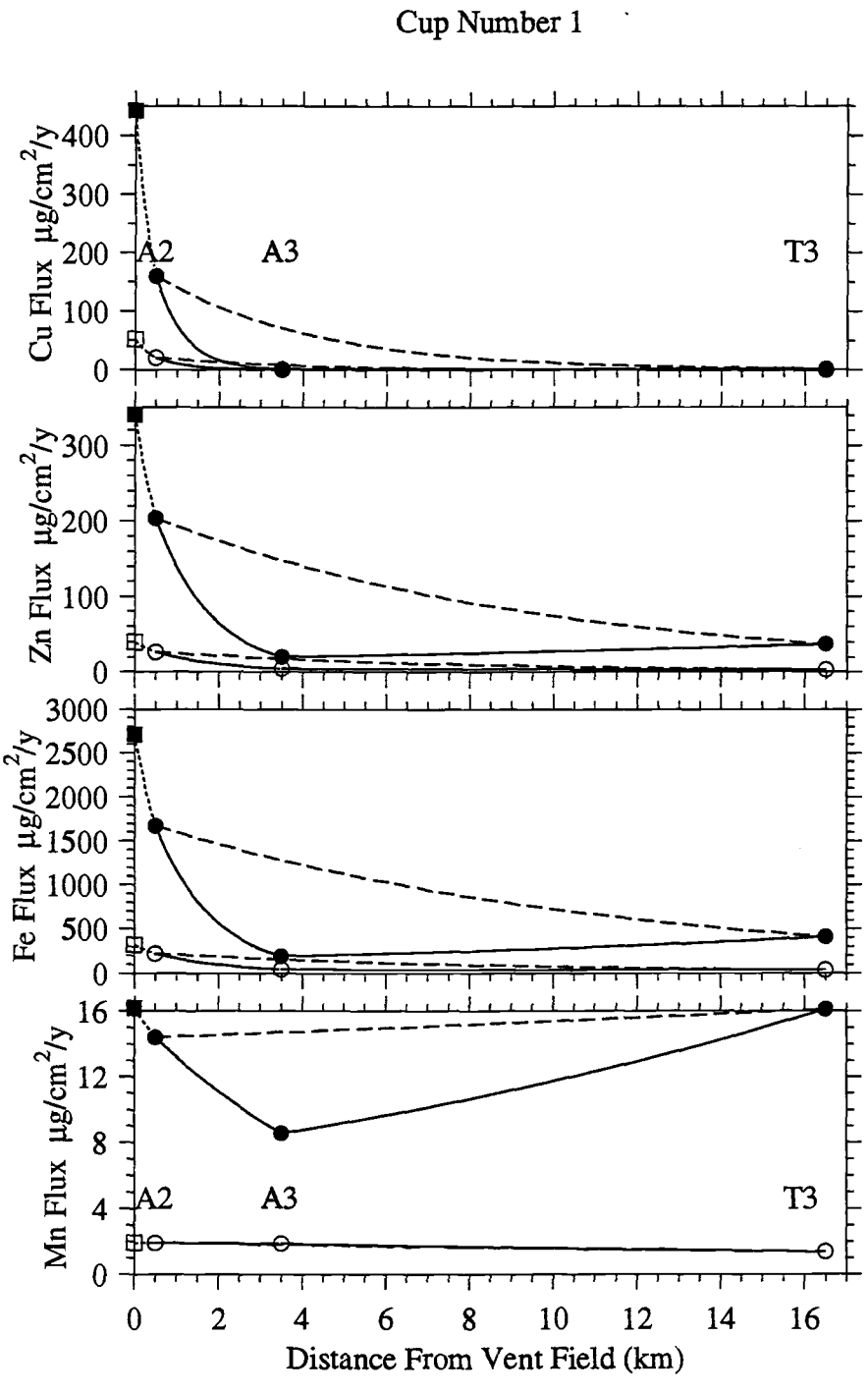

Figure III.3f.

Comparison of $r_{(A2,A3)}$ and $r_{(A3,T3)}$ reveals that the rate of change of Cu, Zn and Fe flux is 1-2 orders of magnitude higher within 3 kilometers of the vent field than over the next 10+ kilometer interval (Figure III.3a). The effect of scaling measured fluxes is to increase Cu, Zn and Fe removal rates by 20, 28 and 48 percent close to the vent field (between moorings A2 and A3), but to decrease, or even change the sign of, already low removal rates for the same elements farther from the vents (between moorings A3 and T3). Results of previous sediment trap experiments at Endeavour Ridge within two kilometers of the vent field confirm the trend of dramatically enhanced hydrothermal particle flux close to the vent field (Dymond and Roth, 1988).

Recognition that there are significant sources of error in calculated r values necessitates sensitivity analysis. As is shown by Eq. 15, r is directly proportional to u and the natural logarithm of the ratio of settling fluxes, but inversely proportional to Δx. Using the distance between moorings as Δx is an underestimate, since the plume meanders, thus, ignoring all other factors, the calculated r values in Table III.6 could be high. The estimate of along-plume velocity, u, also has some associated error, but it may be of either sign. Comparatively, however, the sensitivity of r to variations in the ratios of measured or scaled fluxes is high for values of $F_b/F_a < 1$, since r varies directly as $ln(F_b/F_a)$. In the case of fluxes scaled to compensate for horizontal flow direction, on which values in Table III.6 are based, r varies directly as $ln(F_b'/F_a')$, where, to reiterate, $F_b' = f_bF_b$ and $F_a' = f_aF_a$ and f_b and f_a are scaling factors ≥ 1. Thus relative values of both measured fluxes and scaling factors will influence r. Because the scaling factors are large relative to the measured fluxes, at least for Cu, Zn and Mn, and I consider their associated errors to be substantial ($\pm$ 10% of T), most of the error in r associated with fluxes can be attributed to scaling. The sensitivity of r to changes in the model parameters is shown graphically in Figure III.4, for $F_b/F_a = 0.2$.

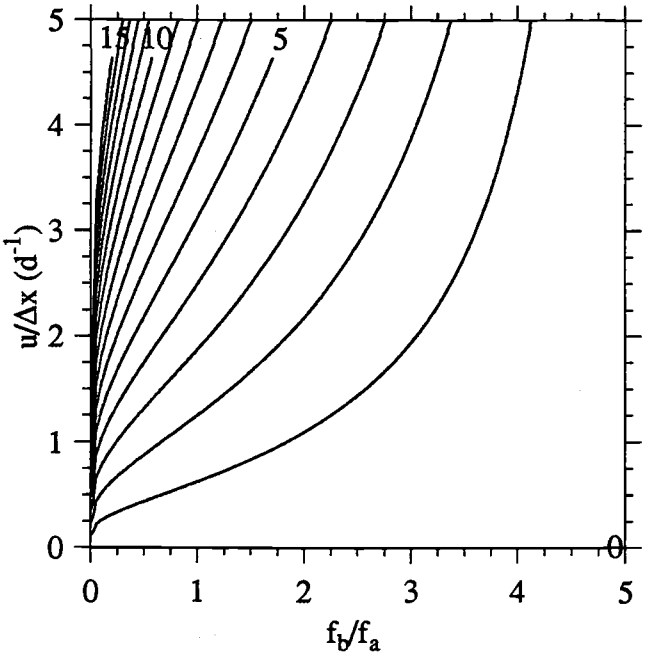

Figure III.4. Sensitivity of r to changes in model parameters. Contour lines are r values where $1 \leq r \leq 15$ and $F_b/F_a = 0.2$. To find the sensitivity for a different value of F_b/F_a, for example $c(F_b/F_a)$, f_b/f_a should be divided by the same factor, c.

Horizontal diffusion, which was shown to be much smaller than horizontal advection in the original model equation and thus ignored, is included in an equation given by Fischer et al. (1979) for the steady-state distribution of a tracer undergoing first order decay in a channel with constant cross section and dispersion coefficient. From this equation, the along-plume horizontal diffusion term not included in the expression for r in Eq. 15 is:

$$\frac{-K_x}{\Delta x^2}\left[ln\frac{F_b}{F_a}\right]^2 \quad . \tag{17}$$

Expression 17 could be added to the right side of Eq. 15, but since $K_x/\Delta x^2$ is believed to be small, the inclusion of this term would produce little change in the calculated r values.

Discussion

In the previous section a model was developed to describe the influence of local loss and advection on settling particle flux. Knowledge of the local physical oceanography was used to rescale measured settling particle fluxes. The model was then used to calculate loss rates of settling particle flux. For copper, zinc and iron, these loss rates are highest near the vent field. In contrast, the model produces negative loss rates for manganese, i.e. increases in settling flux, away from the vent field.

Interpretation of *r* values

The pattern of near-vent field hydrothermal particle flux primarily reflects the rapid kinetics of sulfide precipitation which accelerates Cu, Zn and Fe removal via particle settling. Sulfide precipitation is largely dependent on metal and sulfur concentrations in the fluids, and the precipitation of sulfide minerals such as chalcopyrite, sphalerite, pyrite and marcasite occurs within seconds after hydrothermal fluids leave the vents and mix with seawater (Feely et al., 1992). The sulfur-dominated chemistry of the Endeavour Ridge plume sets up conditions that favor sulfide precipitation. Baker and Massoth (1987) found that the relative concentrations of S and Fe in suspended particles collected in the Endeavour Ridge plume were of the same order of magnitude and that Endeavour Ridge particles were enriched in sulfur relative to particles collected above another vent field along the southern Juan de Fuca Ridge. Particles collected in the Endeavour Ridge plume are also relatively enriched in copper compared to other hydrothermal plumes along the Juan de Fuca Ridge (Feely et al., 1992). In part because the Cu-bearing sulfide particles near the vent field are small (<3 μm), these authors favor a dissolution mechanism to account for their observed rapid decrease in suspended particulate Cu away from the vent field. Model results presented here, however, suggest that near-vent field Cu loss due to settling is also an important removal mechanism.

The $r_{(A2,T3)}$ values which integrate changes in hydrothermal flux over a 15-km distance from the vent field are intermediate between $r_{(A2,A3)}$ and $r_{(A3,T3)}$. It is important to recognize that the $r_{(A2,T3)}$ values considered in isolation would provide a misleading picture of the distribution of hydrothermal particle settling flux around the vent field (Figure III.3). From this, it also follows that with even finer spatial

resolution of settling particle flux within several kilometers of the vent field than was achieved in our moored instrument experiment, it might be possible to further refine the picture of near-vent hydrothermal particle removal.

Temporal variations in the rate of change of flux of hydrothermal elements are shown in Table III.6 and Figures III.3b-f. Over the 259-day deployment period, the rate of change of flux over the first three kilometers varied among cup periods by up to 45% for Cu, 78% for Zn, and 35% for Fe. Along-plume advection over the same time period and distance varied by only 24%. Since $r \propto u$, this suggests that factors in addition to flow velocity may regulate changes in flux over distance. Though the removal mechanisms for hydrothermal Cu and Zn are thought to be similar (sulfide precipitation), the changes in flux of these two elements over time are different. During cup 1, when the flux of Cu decreased most dramatically between A2 and A3 (highest r), Zn flux decreased least (lowest r).

This seemingly puzzling pattern reflects a seasonal augmentation of Zn flux that originates in the upper water column. During the cup 1 period, 16 April - 14 June 1986, measured hydrothermal settling fluxes were high (Table III.4). Seasonal increases in the rain of particles from the upper water column apparently enhance removal of hydrothermal material from the neutrally buoyant plume (see Chapter II). Zinc is both a micronutrient and a substitute for Ca in carbonate tests, thus biogenic particles from the upper ocean constitute an additional source of zinc, over and above the hydrothermal source. In contrast, biogenic sedimentation adds little additional Cu. The settling zinc flux measured above the hydrothermal plume at a depth of 1700 m on mooring A2 was a maximum 0.56 $\mu g\ cm^{-2}\ y^{-1}$ during cup 1 (also the period of highest organic carbon flux) in contrast to 0.19 $\mu g\ cm^{-2}y^{-1}$ in the next highest cup, whereas Cu flux during the cup 1 period at the same depth was 0.13 $\mu g\ cm^{-2}y^{-1}$ and equivalent to the flux measured in the next highest cup period. The biogenic Zn input, which is horizontally uniform, is minor compared to the total Zn flux at plume depths. However, because the total Zn flux is reduced by an order of magnitude over the distance between A2 and A3, the biogenic contribution is relatively much larger at A3. This results in a reduction of r during periods of enhanced non-hydrothermal Zn flux. Thus, the apparent discrepancy in removal rates of Cu and Zn with distance from the vent field is not due to any fundamental difference in the hydrothermal input,

precipitation, or settling of these two elements, rather it reflects seasonal effects that propagate downward from the upper ocean.

Compared to the rate of change of Cu and Zn flux near the vent field, Fe flux decreases less rapidly. The $r_{(A2,A3)}$ values for Fe are up to a factor of two lower than values for Cu and Zn. This may reflect the dual-mechanism removal of Fe, whereby both sulfide precipitation and formation of Fe oxyhydroxides transform Fe from its dissolved form into particles. Sulfides tend to form large (>100 μm), dense, rapidly settling particles, the oxyhydroxide particles tend to be finer (< 2 μm), thus they settle more slowly and are transported farther from the vent field. In contrast to sulfide precipitation which occurs in the buoyant plume, precipitation of iron and manganese oxyhydroxides occurs over longer periods of time in the neutrally buoyant plume because the solubility products of these phases are lower (Feely et al., 1992). Such a two-component (coarse-grained sulfide/fine-grained oxide) particle system was suggested previously by Baker and Massoth (1987) who proposed it to explain the steady decrease in the downplume ratio of light attenuation anomaly to temperature anomaly at Endeavour Ridge. Normative analysis of material collected in sediment traps approximately one kilometer northeast of mooring A2 showed that about 35% of the material collected was composed of sulfides, and <5% of the material was oxides (Dymond and Roth, 1988). If the partitioning of particulate iron into these phases is roughly proportional to their abundance, ≈ {5/(35+5) x 100} = 12% of the plume Fe might be carried as fine-grained oxides, thus accounting for the more gentle decrease in Fe settling flux away from the vent field.

Formation of Mn-rich particles by ordinary kinetic and bacterially mediated oxidation of Mn (II) is slow relative to plume dispersal (Cowen et al., 1990), thus particulate Mn concentration and settling flux increases with distance from the vent field (Feely et al., 1992). Lavelle et al. (1992) develop a two-stage scavenging model to describe the deposition of hydrothermal Mn, and their model results show a Mn flux maximum approximately 25 km away from the ridge-crest source. The settling flux of Mn, on average, more than doubles between the vent field and mooring T3, about 15 km away (Figure III.3a), however there is considerable temporal variability in this pattern (Figures III.3b-f). As for the other hydrothermal elements, Mn removal from the hydrothermal plume is enhanced during the period of high upper ocean productivity (Figure III.3f), and as for Zn, biogenic input may supply additional Mn.

Evaluating the steady-state assumption

In order to solve Eq. 13 for r, an assumption of steady-state was made, meaning that flux of a hydrothermal element at a fixed point does not change over time. Here I justify that assumption. Clearly, measured fluxes integrated over 48-day cup periods are not constant (Table III.5). Some of this variability is due to the time-variable flow regime and to seasonal upper water column processes (Chapter II). High-frequency (tidal/inertial) flow variability is averaged out by integrating fluxes over 48-day periods. Longer-period changes in flow direction are accounted for, albeit roughly, by scaling using PDFs. Still, scaled cup-averaged fluxes at a single mooring are not constant, although temporal variability does decrease with distance from the vent field (Table III.5). The largest inter-cup changes in hydrothermal element flux are associated with seasonal processes (Chapter II) which are homogeneous over our experimental spatial scales. This means that a flux increase at A2 is echoed by proportional flux increases at A3 and T3. Since r depends on the ratio of the fluxes at two points (Eq. 16), its value does not depend on how the magnitude of a single flux varies in time. Values of r are locally relatively constant (Table III.6). So in regard to describing changes in flux with distance from the vent field over time scales used in this model the steady-state assumption is valid.

The steady-state assumption would not hold if large changes in vent output propagated downplume and cause horizontal temporal inhomogeneity in settling particle flux. The steady-state model is also not applicable in the case of episodic event plumes, nor is it appropriate over very short time scales where high-frequency flow variability is an important consideration.

Backwards extrapolation - predicting F_v

From the rate of change of flux between moorings A2 and A3, it is possible to extrapolate backwards toward the vent field, thereby predicting the settling flux of each hydrothermal element directly above the vent field, F_v. Solving Eq. 15 for F_b where b is at the vent field, so F_b becomes F_v, gives:

$$F_v = F_{A2} \; exp\left\{\frac{r\, x_{A2}}{u}\right\}, \qquad (18)$$

where F_{A2} is the settling flux of each element at ≈ 2000 m depth at mooring A2, r is $r_{(A2,A3)}$, x_{A2} is the distance between mooring A2 and the vent field (500 m), and u is the average velocity recorded at 2000 m depth at A2 (0.0177 m s^{-1}). Solutions to Eq. 18 based on both measured and scaled fluxes are given in Table III.7 and shown graphically as dotted lines leading to filled squares in Figure III.3. Also shown in Table III.7 are elemental fluxes measured in an 8-day deployment of a sediment trap using the submersible, ALVIN, 21 m above the Endeavour Ridge vent field (water depth 2178 m) beginning 31 August 1984 (Dymond and Roth, 1988). These values of measured, vent-field flux are designated F_{vm}.

Table III.7. Model predictions

Flux predicted at vent field , F_v ; the range of F_v calculated by cup period for scaled fluxes, F_v *range*; flux measured at vent field (Dymond and Roth, 1988), F_{vm}, all in ($\mu g\ cm^{-2}\ y^{-1}$); and total fluxes integrated to 16.5 km, F_t (tonnes y^{-1}). A metric tonne is 10^6 g.

Element*	F_v	F_v *range*	F_{vm}	F_t
Cu_m	20			0.85
Cu_s	164	20-450	332	5.7
Zn_m	27			2.1
Zn_s	226	50-340	285	13.6
Fe_m	146			25.6
Fe_s	1203	250-2700	4367	161
Mn_m	0.69			1.0
Mn_s	5.7	1-16	7.16	6.5

* Subscripts m and s denote values based on measured and scaled fluxes.

The predicted vent-field fluxes of Cu, Zn and Fe based on scaled fluxes of these elements measured more than one year later, 0.5 km northeast of the vent field and approximately 200 m above bottom agree remarkably well with the measured fluxes. Considering potentially large errors due to scaling and restrictions imposed by model assumptions the agreement is striking. Predicted and measured fluxes, F_v and F_{vm}, are not only the same order of magnitude, but the 8-day measured values, except that for Fe, fall within the range of cup-period variability in F_v. The predicted mean Cu flux is half the measured Cu flux; predicted and measured mean Zn and Mn fluxes are nearly equivalent; and the Fe flux prediction is low by a factor of <4. The observation that $F_{vm} > F_v$ for Cu, Zn and Fe suggests that the rate of change of hydrothermal particle flux over the first 0.5 km away from the vent field is even higher than over the next 2.5 km interval ($r_{(vents,A2)} > r_{(A2,A3)}$).

Integrating hydrothermal element fluxes - estimating F_t

By estimating the horizontal dimensions of the neutrally buoyant plume, total hydrothermal element outputs can be calculated using scaled settling particle fluxes. The general equation for integrated flux, F_t, is:

$$F_t = \int_0^x F(x)A(x)dx = A\int_0^x F(x)dx \qquad (19)$$

where $A(x)$ is the width (across-plume dimension) of the plume and $F(x)$ is the settling flux some distance, x, along the plume axis. From Baker and Massoth's (1987) areal map of light attenuation anomaly above Endeavour Ridge, the plume can be approximated as a 4-km-wide rectangle, thus as a first approximation, A = 4 km. The integral is solved for each of the inter-mooring distances: x=0 to x_{A2}, x_{A2} to x_{A3}, and x_{A3} to x_{T3}.

The total elemental settling particle fluxes integrated over the horizontal dimensions of the ER-2 mooring deployment are given in Table III.7 and plotted as a function of distance from the vent field in Figure III.5. Over the first 15 km away from the vent field, of the four elements considered, the integrated scaled flux of Fe is highest, followed by Zn which is an order of magnitude lower, then Mn and Cu which are about half of Zn. These figures show that beyond about 5 km from the vent field changes in particulate hydrothermal flux of Cu and Zn progress more slowly than for Fe and Mn. The integrated fluxes of Fe and Mn still increase relatively rapidly at a beyond $\approx$ 15 km from the vent field. The integrated scaled settling flux of particulate Mn at approximately 15 km from the vent field is 0.2 g s^{-1}, two orders of magnitude less than the estimated vent flux of Mn given by Rosenberg et al. (1988), 15-40 g s^{-1}, implying that only a small fraction of hydrothermal Mn is removed from the Endeavour Ridge plume via particle settling over distances of at least 15 km. This supports the contention that the behavior of hydrothermal Mn in the neutrally buoyant plume is relatively conservative.

It is important to recognize that the curves in Figure III.5 reflect only the removal of particulate phases from the neutrally buoyant plume; the integrated fluxes are not equivalent to vent-field output of these elements. As the distance from the vent field tends to infinity the integrated fluxes of hydrothermal components tend toward

Figure III.5. Total settling fluxes of Cu, Zn, Fe and Mn (F_t) beneath a 4-km-wide plume as a function of distance from the vent field. Data are for the entire 259-day deployment period. Solid lines and filled circles represent integration based on scaled fluxes; dashed lines and open circles reflect integration of measured fluxes. A metric tonne is 10^6 grams.

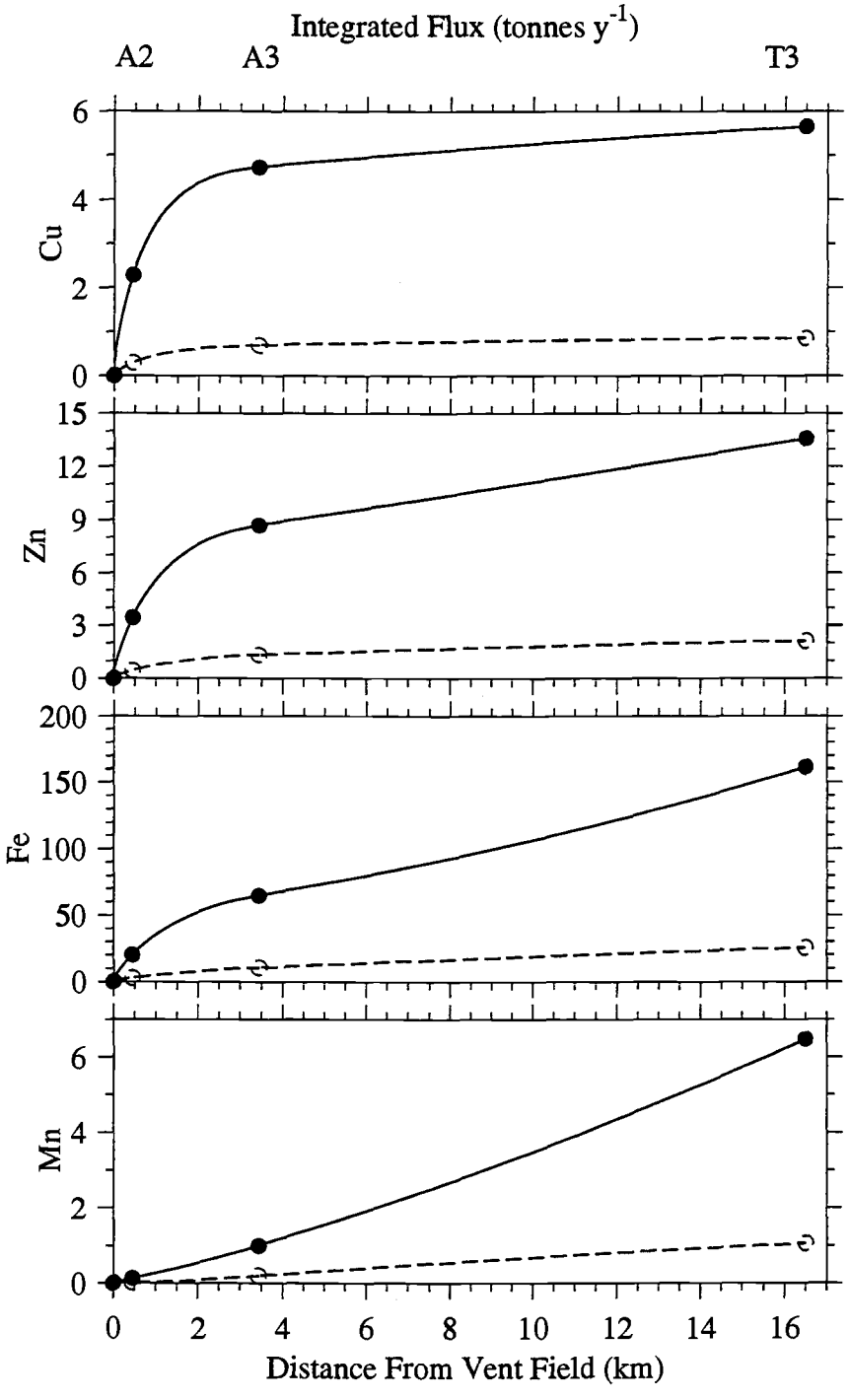
Integrated Flux (tonnes y-1)
A2
A3
T3
Cu
Zn
Fe
Mn
Distance From Vent Field (km)

Figure III.5.

Figure III.6. Integrated settling fluxes of Cu, Zn, Fe and Mn (F_t) beneath a 4-km-wide plume as a function of distance from the vent field. Data are for the cup 1 period (16 April - 13 June 1986. Solid lines and filled circles represent integration based on scaled fluxes; dashed lines and open circles reflect integration of measured fluxes. A metric tonne is 10^6 grams.

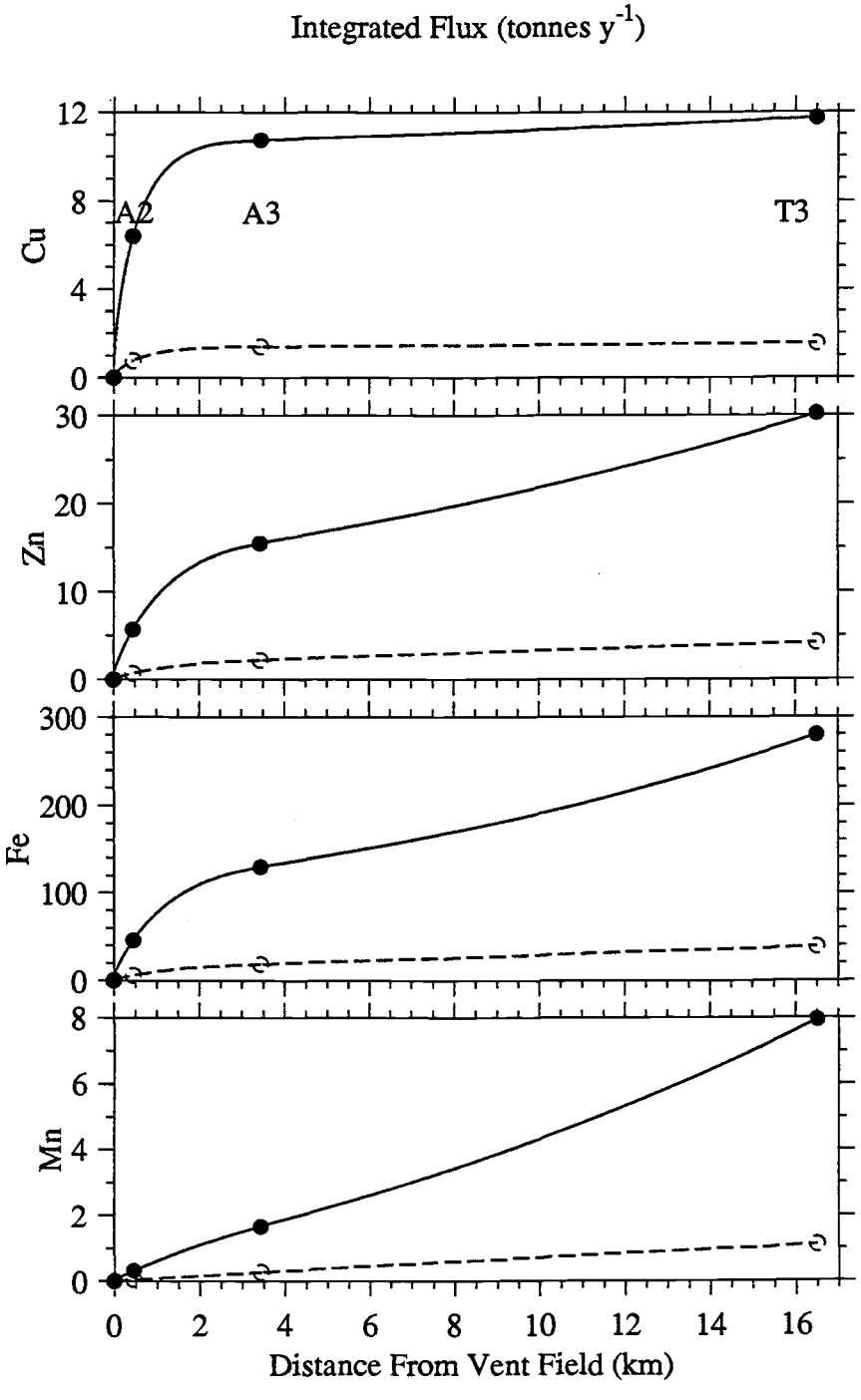
Integrated Flux (tonnes y-1)
Cu
Zn
Fe
Mn
A2
A3
T3
0
4
8
12
10
20
30
100
200
300
2
6
0
2
4
6
8
10
12
14
16
Distance From Vent Field (km)

Figure III.6.

asymptotes which, in theory, could provide estimates of the total output from the vent field. However, the transformation of hydrothermal components from the dissolved phase to sinking particles is incomplete within 15 km of the vent field. Comparison of integrated fluxes for the 2-month, cup 1 period (Figure III.6) with the mean, deployment-averaged data in Figure III.5 illustrates the effects of seasonal variation in particle-removal efficiency. Enhanced flux of above-plume particles during the cup 1, high-productivity, spring period is reflected in plume-depth scaled fluxes that are approximately a factor of two higher than the mean fluxes shown in Figure III.5. The larger integrated fluxes reflect more efficient removal of hydrothermal material rather than increases in vent output. Thus, although determination of vent output from the integrated settling particle fluxes is not possible, in some cases these values reflect lower limits to the total vent output. For example, the Cu flux at T3 shown in Figure III.6, $\approx$ 12 tonnes y^{-1}, is a lower limit estimate of Cu output from the vent field.

Influence of non-hydrothermal fluxes

The scaling of measured fluxes in Eq. 16 assumes that the hydrothermal plume is the source of all Cu, Zn, Fe and Mn. In reality, some fraction of the total flux of these elements measured at plume depths is derived from above the plume, thus should not be multiplied by the scaling factor, f. The non-hydrothermal fluxes were measured in sediment traps positioned above the neutrally buoyant plume at 1700 m depth on mooring A2 (Table III.8).

Table III.8. Above-plume, non-hydrothermal fluxes measued at 1700 m depth at A2

Cup period	----F_{1700} ($\mu g/cm^2/yr$)----- Cu	Zn	Fe	Mn
2	0.08	0.19	12.20	0.30
3	0.07	0.16	4.86	0.15
4	0.04	0.10	3.09	0.09
5	0.13	0.14	5.19	0.23
1	0.13	0.56	20.1	0.48
All	0.09	0.25	9.86	0.27

Above-plume fluxes measured at A2, F_{1700}, are representative of the above-plume fluxes over the horizontal dimensions of our experiment. Thus Eq. 16 can be rewritten as:

$$r = \frac{-u}{x_b - x_a} \ln\left(\frac{f_b(F_b - F_{1700}) + F_{1700}}{f_a(F_a - F_{1700}) + F_{1700}}\right) \qquad (20)$$

where the above-plume flux is included in the calculation, but not scaled. Eq. 20 can be further rewritten as:

$$r = \frac{-u}{x_b - x_a} \ln\left(\frac{f_b F_b + \{F_{1700}(1-f_b)\}}{f_a F_a + \{F_{1700}(1-f_a)\}}\right) \qquad (21)$$

so that the difference between Eqs. 16 and (21) is given by the expressions in curly brackets. For Cu, Zn and Fe, the effect of separating above-plume and hydrothermal contributions to the total flux is negligible. By scaling the non-hydrothermal contribution to the total flux, the values of scaled flux of these elements in Table III.5 overestimate the settling flux by less than ten percent. This difference is so small that it is undetectable in Figure III.3. For Mn, the effect is slightly more noticeable; the scaled values in Table III.5 are up to 30% too high. This difference reflects a proportionally higher non-hydrothermal flux of Mn at plume depths, relative to the non-hydrothermal contributions of Cu, Zn and Fe. For all four elements, the effect of these scaling differences on values of r is minimal, and the shapes of the curves in Figure III.3 are virtually unchanged.

Relationship of changes in F to changes in dissolved hydrothermal element concentrations, D

Inferring or interpreting changes in the concentration of dissolved hydrothermal components in the neutrally buoyant plume from model results requires consideration of the relationship between the dissolved pool and the settling flux. Dissolved components are eventually transformed into particles which settle from the plume, thereby decreasing the total in-plume concentration of hydrothermal elements. The transformation of an element between dissolved phase and incorporation into a settling particle is not necessarily governed by one rate constant, nor is it by definition a unidirectional process. Precipitation, dissolution, aggregation, and disaggregation can occur consecutively or simultaneously, and the rates of these particle-forming and

particle-removal processes may be biologically mediated. Moreover, advection of the hydrothermally enriched, particle-laden seawater influences the spatial distribution of dissolved tracers and particle-deposition patterns. Thus, removal of hydrothermal elements from the plume via settling particles does not necessarily imply that the dissolved concentration of the same elements in the plume decreases proportionally.

Although the present model predicts changes in settling particle flux with distance from the vent field, it is not possible to quantify changes in dissolved hydrothermal element concentrations within the advecting plume from model results alone. The origin of the settling particles is not specified in the model; it is not known if specific particles were formed or entrained in the buoyant plume (i.e., already in the neutrally buoyant plume prior to advection), if they are forming or dissolving as the plume advects, or if additional, non-hydrothermal particles are incorporated into the neutrally buoyant plume. However, with additional information on dissolved element distributions, it is possible to make inferences about the relationship between changes in settling particle fluxes and the in-plume dissolved concentrations of hydrothermal elements, thereby extending the usefulness of the model.

There are four possible scenarios that describe changes in dissolved concentration with respect to changes in settling particle flux of a particular element with distance downplume. For a specified element, if D is dissolved concentration, and F is settling flux, with distance from the vent field:

1. D decreases and F decreases; or
2. D increases and F decreases; or
3. D increases and F increases; or
4. D decreases and F increases.

For hydrothermal elements whose removal is governed by first order precipitation and settling, and the rate of precipitation is fast relative to along-plume advection, and there are no additional inputs besides venting, decreasing flux with distance from the vent field should be accompanied by a decrease in the in-plume dissolved pool (scenario 1). Such is probably the case for Cu, however dissolution of fine, Cu-bearing particles may suppress the rate at which the dissolved concentration decreases. Another way both D and F could decrease would be through local physical

removal of one or both phases from the plume via ingestion and assimilation by living, swimming organisms.

Dissolution of primary hydrothermal particles (those formed or entrained in the buoyant plume) in the advecting plume could result in a decrease of F and a concomitant increase in D (scenario 2). Knowledge of hydrothermal particle dissolution rates or measurements of D would be required to quantify the contribution of this process in producing the observed patterns of decreasing F with distance from the vent field. Another way scenario 2 could occur is if particle formation is limited by the concentration of some other element. If this other element is depleted before all of the element under consideration is removed, F might decrease and D could remain unchanged (but probably not increase). For example, if sulfide formation was the only particle-forming removal mechanism for Fe (it is not), when S was depleted Fe settling flux would decrease, or cease, and dissolved Fe would remain unchanged.

The behavior of an element for which there is a source in addition to hydrothermal fluid may be described by the third scenario. In fact, scenario 3 requires additional input of the element, since without such a source, the balance between the dissolved and particulate pools would force a decrease in either D or F. Zinc, in a rough way, illustrates this pattern. Input of non-hydrothermal Zn associated with biogenic particles could augment F and D (pending particle dissolution in the latter case). Results presented earlier suggest that the rate of decrease in Zn flux is not as high as would be expected were there no additional input. Although the decrease in r_{Zn} is not in fact accompanied by an increase in F with distance from the vent field, locally (at a mooring) F does increase over time. If the magnitude of the non-hydrothermal input of an element is sufficient, the potential for scenario 3 exists.

An element such as Mn, whose transformation from dissolved to particulate phase is unidirectional, but slow relative to horizontal advection might exhibit behavior described by scenario 4. Barring non-hydrothermal inputs, and reaction limitations mentioned previously, F will increase and D will decrease within some limited distance from the vent field. Eventually, very far from the vent field, perhaps hundreds or thousands of kilometers, r values for an element like Mn will become positive and both F and D will decrease.

The examples above illustrate the difficulty in attempting to use the particle flux model developed here to unequivocally predict or interpret changes in the along-plume, dissolved concentrations of hydrothermal elements. However, because the dissolved and particulate hydrothermal phases are related, by applying some knowledge of geochemistry and the rates of relevant particle transformation processes, along-plume changes in settling particle flux predicted by the model can help constrain changes in dissolved hydrothermal element concentrations as well.

Relationship to other investigations

The work presented here addresses changes in settling particle flux over spatial scales intermediate between those considered in earlier attempts to model the deposition of particles in the vicinity of hydrothermal vent fields. Using a simple model of plume development and measured flow rates from seafloor hot springs, Converse et al. (1984) calculated that about 97% of the sulfide particles which form in the buoyantly rising plume are advected away from the vent field in the neutrally buoyant plume. Lyle et al. (1986) used Mn accumulation rates in deep-sea sediment cores to model Mn accumulation as a function of distance over 1000 km from the East Pacific Rise crest. His model assumes Stokes law settling, a specific particle size distribution, and low abyssal current velocity. While his predictions agree well with measured accumulation rates, spatial resolution is poor within 50 km of the ridge axis. Lavelle et al. (1992) develop a two-stage scavenging model for hydrothermal Mn deposition which predicts changes in settling Mn flux up to several hundred kilometers from the spreading ridge axis.

Comparison of Lyle's sedimentary Mn accumulation rates with our sediment trap measured fluxes suggests that the output of hydrothermal Mn from the East Pacific Rise far exceeds output from the Endeavour Ridge vent field. In two transects at 17°S and 19°S, Mn accumulation measured 19 and 5 km from the Rise crest was 86 and 36 $\mu g/cm^2/y$, respectively (Lyle et al., 1986). These values are up to an order of magnitude higher than Mn fluxes within 15 km of the Endeavour Ridge vent field, and the difference reflects the relatively higher intensity of the East Pacific Rise hydrothermal system.

Model results of Lavelle et al. (1992) agree closely with results presented here. An off-axis peak in Mn flux of approximately 10 $\mu g/cm^2/y$ occurs about 25 km from

the ridge axis. This off-axis Mn peak is verified by suspended particle concentration data (Feely et al., 1992) and sediment core accumulation rates (Lavelle et al., 1992). These observations support the model results given here which indicate that Mn flux increases over the first 15 km away from the vent field.

Conclusions

A simple steady-state model of hydrothermal settling flux, including first order removal and along-plume advection, was formulated. Based on measured fluxes of hydrothermal elements from the Endeavour Ridge neutrally buoyant plume, the model was used to predict rates of change of settling flux with distance from the vent field, settling fluxes of Cu, Zn, Fe and Mn at the vent field, and the integrated flux of these elements beneath the plume. In addition, the dependence of settling particle flux on along-plume velocity was made explicit. Scaling of sediment-trap measured particle fluxes to reflect beneath-plume fluxes was accomplished by using current meter data to estimate the fraction of time the neutrally buoyant plume interacted with each mooring. Model predictions of hydrothermal settling particle flux at the vent field based on scaled sediment trap data agree remarkably closely with previously measured fluxes; this attests to the validity of both the model formulation and the scaling technique used here. Poor agreement of measured vent field fluxes and predictions based on unscaled settling fluxes demonstrate the importance of considering the effects of local horizontal flow on the interpretation of Eulerian data. Unscaled sediment trap data underestimate beneath-plume hydrothermal particle fluxes by factors of 2.5 to 20, and underestimate near-field rates of change of flux by up to 50%.

Although settling fluxes of Cu, Zn and Fe decrease exponentially with distance along the plume axis, the rate of change in flux is orders of magnitude higher within the first few kilometers than over distances beyond about five kilometers. Of the four elemental fluxes modelled Cu decreases most rapidly, followed by Zn, then Fe. The differences in removal rates among these elements apparently reflect fundamental differences in the sulfide and oxyhydroxide-forming processes which regulate precipitation and particle size. In contrast to fluxes of the other three elements, Mn flux increases steadily up to at least 15 km along-plume, an observation consistent with the slow oxidation kinetics of this element. In addition to the kinetics of particle-forming reactions, experimental data suggest that seasonal effects are an important determinant of local removal rates of hydrothermal material.

The simple one-dimensional model presented here provides a framework for integrating specific geochemical and physical oceanographic observations, thus

extending the usefulness of spatially limited measurements. Knowledge of horizontal advection at the depth of the neutrally buoyant plume together with measurements of settling hydrothermal particle fluxes at fixed points can be used to predict deposition of hydrothermal elements at other sites, and, in some cases, to estimate the total vent field output of an element.

IV: Transport and settling of organic material in a deep-sea hydrothermal plume: evidence from particle flux measurements

Abstract

Results of time-series experiments using moored sediment traps to quantify the settling hydrothermal particle flux above Endeavour Ridge suggest that the oceanic effects of carbon production associated with mid-ocean ridge hydrothermal systems are not limited to the area immediately surrounding seafloor vents. We hypothesize that particulate organic material is entrained, possibly generated in, and removed from the hydrothermal plume at least two kilometers from a site of active venting. More than 95 percent of the organic carbon collected 21 m directly above a site of hydrothermal fluid discharge has a near-bottom, chemosynthetic source. Up to 62 percent of the total organic carbon flux measured 100-200 m above bottom and ≈ 2 km northeast of the vent field (47°57.05'N, 129°06.30'W, depth≈2200 m) is chemosynthetic. Despite injection of organic carbon at plume depths, perplexing minima in the fluxes of biogenic and inorganic detrital particles are observed at plume-depth 1900-meter traps. Possible explanations for the attenuated particle fluxes include removal of material from the laterally advecting plume by zooplankton feeding, biologically-mediated particle breakdown, and the effect of currents on particle collection. Patterns of particle flux we observed indicate simultaneous addition and removal of organic material at plume depths (i.e. nutrient cycling), and support the hypothesis that laterally-dispersing hydrothermal plumes are three-dimensional, biologically active zones in the deep sea.

Introduction

Organisms that thrive near deep-sea hydrothermal vents use organic carbon produced by chemolithotrophic bacteria; however, dissemination of this primary organic carbon and the oceanic effects of apparently localized food sources have yet to be quantified. Carbon isotopic data (Rau, 1985) and *in situ* carbon fixation rates (Karl et al., 1980) have confirmed the assertion that chemosynthetic bacteria in and near submarine hydrothermal vents form the nutritional base of a benthic food chain. Plumes extend hundreds of kilometers from spreading ridge crests, as buoyant discharge from hydrothermal vents rises and then spreads laterally. It is plausible that these plumes disperse organic carbon and other nutrients along with heat and inorganic particulate material. Bacterial chemosynthesis fueled by anomalously high concentrations of gases [e.g.CH_4 (Lilley et al., 1983; Jannasch and Mottl, 1985)] and reduced metals [e.g.Mn^{+2} (Klinkhammer et al., 1986)] may even continue to generate organic matter in the advecting plume. This nutrient-rich flow may harbor plume-specific zooplankton that consume organic matter enriched in the hydrothermal discharge and, as agents of particle removal and formation, regulate flux of this material to the seafloor. In this paper, the adjective chemosynthetic is used to denote the fraction of organic particle flux measured at depth that does not have an upper water column (photosynthetic) source. The term simply implies growth from chemically-derived energy and may include primary production (lithoautotrophy) as well as secondary (heterotrophic) growth supported by the former. It is beyond the scope of this paper to identify conclusively the source (eg. bacteria, zooplankton) of the chemosynthetic particulate organic material measured in our sediment traps.

Methods

To evaluate the plume as a transporter of vent-associated organic matter, we deployed sediment traps within and near an active hydrothermal vent field characterized by both black smokers (>300°C) and also by more diffuse flow. Two experiments began in September 1984 in the axial valley of Endeavour Ridge, the northern segment of the Juan de Fuca Ridge in the northeast Pacific Ocean. One Soutar-type sediment trap (collecting surface area = 0.1 m^2) was positioned with the submersible *Alvin*, 21 m above a vent opening in the buoyantly-rising, hydrothermal plume for eight days. We deployed a second mooring bearing five larger (0.5 m^2) sediment traps at nominal depths of 700, 1200, 1700, 1950,and 2100 m 2 km northeast of the vent field (47°58'N, 129°55.5'W, depth ≈ 2200 m); it remained in place 340 days. A second vent field was located ≈ 500 m to the south of the mooring site, where two submersible dives revealed a thriving community of vent organisms, diffuse hydrothermal fluid discharge, yet no vigorous black smoker activity. These observations suggest that though closer to the mooring than the major vent field, the smaller, more quiescent field would not be a major contributor to the hydrothermal plume or the particulate material caught by the sediment traps.

We also report here preliminary results of a third, 260-day experiment which began in September 1985. The central mooring in an array occupied the site of the previous 340-day mooring, and so the particle fluxes measured by five traps at nominally 1500, 1700, 1950, 2050, and 2150 m extend the previous record. It is known from numerous CTD tows and hydrocasts at the site that hydrothermal effluent spreads laterally in a layer between ≈ 100 and 300 m above the ≈ 2200 m bottom (Lupton et al., 1985). Thus,traps deeper than ≈ 1900 m collected particles in and beneath the plume layer; traps above sampled the background, non-hydrothermal rain of biogenic particles generated in the upper water column as well as continentally-derived material.

The moorings featured the non-metallic design that prevents contamination of the sediment trap samples (Dymond and Lyle, 1985). We observed unexpectedly intense corrosion of metallic mooring hardware at depths corresponding to the hydrothermal plume (discussed below), hence, use of nonmetallic components also

helped ensure mooring integrity during extended exposure to plume fluids. Both Oregon State University (OSU)-designed (Dymond and Lyle, 1985) and Soutar-designed traps (Soutar et al., 1977) were used on the earlier mooring. Comparisons have demonstrated that agreement in particle-collection efficiency is within 10% for these similarly shaped conical traps (Fischer, 1984). The dual-cone Soutar-traps were fitted with the OSU sample-cup changer system; thus, all traps provided data for the same four sample collection periods (Table IV.1). Only OSU-traps were used on the second mooring. Sodium azide was used to prevent bacterial alteration of material in the sample cups. Sample preparation followed procedures previously discussed (Dymond et al., 1981) which minimize contamination and sample splitting errors. Splits of the sample were analyzed for organic (C_{org}) and carbonate carbon (C_{CaCO3}) using an acid/oxidizing acid (modified LECO) procedure (Weliky et al., 1983) and these results are shown in Table IV.1. An Aanderaa rotor current meter and Seatech light-beam transmissometer were positioned beneath the deepest trap on the first mooring; three such instrument packages were used on the second mooring. These instruments record advection of fine particles in the hydrothermal plume; these data are discussed in Chapter II.

Table IV.1. Measured particle fluxes

Particle fluxes measured in four sediment traps moored for 340 days ≈2 km from the hydrothermal vent field and a single, smaller trap deployed for 8 days within the vent field. Sequential cups are labelled 2, 3, 4, and 5; cups 0 refer to the entire deployment period.

Trap depth (m)	Cup	Start date	Sample period (days)	Bulk flux (mg cm^{-2} y^{-1})	C_{org} Flux (μg cm^{-2} y^{-1})	$CaCO_3$ (μg cm^{-2} y^{-1})	C_{org}/C_{CaCO_3} (μg cm^{-2} y^{-1})
1200	Mean	9/8/84	336	2.90	145.1	1451	0.83
	2	9/8/84	91	1.65	129.2	731	1.47
	3	12/8/84	91	1.93	123.8	826	1.25
	4	3/9/85	91	5.81	225.4	3103	0.61
	5	6/8/85	63	1.92	82.8	1013	0.68
1700	Mean	9/8/84	336	2.70	127.2	1305	0.81
	2	9/8/84	91	1.71	118.1	701	1.40
	3	12/8/84	91	1.57	81.8	695	0.98
	4	3/9/85	91	5.33	213.1	2735	0.65
	5	6/8/85	63	1.97	81.6	992	0.69
1950	Mean	9/8/84	336	1.27	59.2	439	1.12
	2	9/8/84	91	1.71	80.2	477	1.40
	3	12/8/84	91	0.68	32.8	197	1.38
	4	3/9/85	91	1.55	72.6	638	0.95
	5	6/8/85	63	1.08	47.6	447	0.89
2178	Mean	9/8/84	336	2.46	92.1	612	1.25
	2	9/8/84	91	3.02	113.7	647	1.46
	3	12/8/84	91	1.39	53.4	257	1.73
	4	3/9/85	91	2.66	104.7	857	1.02
	5	6/8/85	63	2.89	98.5	720	1.14
2178	N/A	8/31/84	8	27.64	1185.8	553	17.88

Results and Discussion

The flux of biogenic and inorganic detrital components decreases sharply between the 1700 and 1950 m sediment traps (Figures IV.1a and IV.1b). Below 1950 m, the flux of non-hydrothermal particles does increase; however, fluxes measured deeper than 1950 m still may be anomalously low, reflecting losses incurred above. In contrast, dramatic increases in the flux of hydrothermally-derived metals and sulfur in the sediment traps below 1700 m are clear evidence of hydrothermal input (Figure IV.1c). Copper and zinc fluxes measured at 2100 m are two orders of magnitude higher than the above-plume (1700 m) values. Iron, manganese and barium increase over the same depth range by factors of 15, 11, and 4, respectively. Sulfur, which is undetectable in the 1700 m trap, increases by a factor of three between 1950 and 2100 m. Scanning electron microscopy and X-ray diffraction analysis document the presence of sulfides, sulfates, and elemental sulfur in the 1950 and 2100 m trap samples (Dymond and Roth, 1988; Dymond et al., 1987).

The reduced biogenic and inorganic detrital fluxes are perplexing, and, with respect to possible plume transport of chemosynthetic material, the dearth of biogenic indicators (organic carbon, calcium carbonate, opal) at plume depths is troublesome. The pattern implies that reduced gases and metals, which are highly enriched in the plume, do not support continued productivity of entrained auto- and heterotrophic organisms. If chemosynthetic carbon production added significantly to the rain of non-hydrothermal organic carbon from the upper water column, we would expect the flux of organic carbon to increase in the lower two traps, yet it does not (Figure IV.1a). To infer that chemosynthesis is a phenomenon restricted to the region of active venting would be consistent with the 10-fold increase in organic carbon flux measured in the near-vent, eight-day trap, and also with observations that macrofaunal abundance drops markedly at the margins of active vent fields (Hessler et al., 1985). However, close scrutiny of our data, specifically the interrelationship of biogenic components, suggests that this conclusion is too hasty. Rapid cycling of particles in the plume may inhibit settling into our traps. In the remainder of this paper, we will discuss physical, chemical and biological processes that may affect particle collection, and we will present evidence that suggests the biologically-active plume hypothesis merits further investigation.

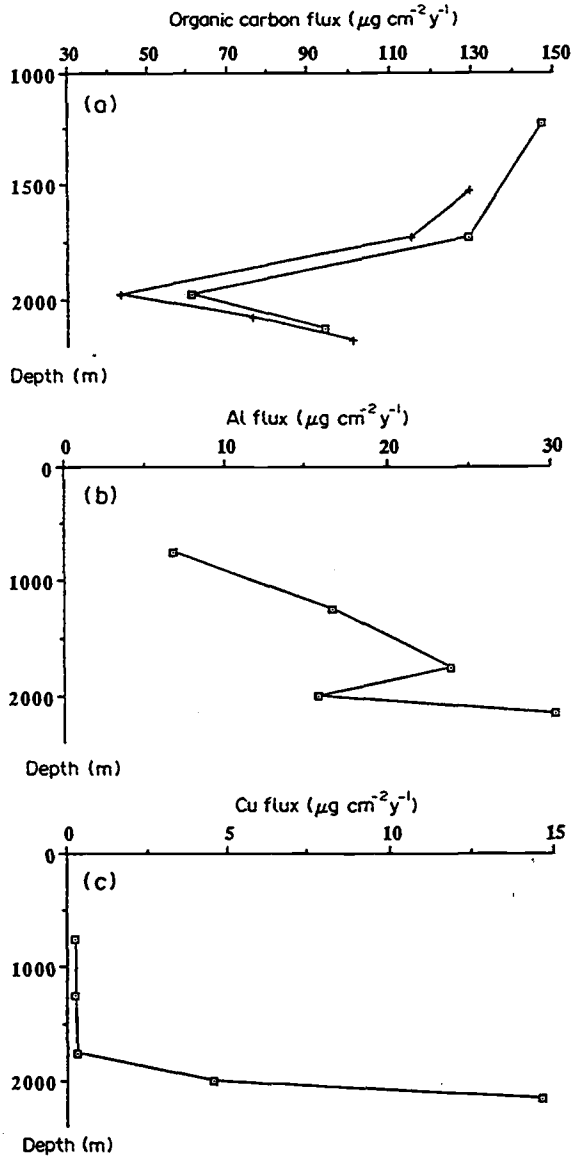

Figure IV.1. Fluxes of organic carbon, aluminum and copper as a function of depth measured ≈ 2 km from a major hydrothermal vent field over 340 days. The plume spreads laterally in a layer ≈200 m thick and 100-300 m above bottom. Organic carbon,*a*, and aluminum,*b*, of primarily terrigenous origin, decrease by nearly a factor of 2 in the plume. The removal of these elements may be related. Cu, *c*, is shown as an example of constituents strongly-enriched in the hydrothermal effluent. Squares denote the 340-day mooring deployment, Endeavour Ridge - 1 (ER-1) ; crosses indicate results from the subsequent 260-day experiment (ER-2).

The ratio approach

Since the composition of sediment trap samples reflects the sum of multiple water column processes, resolving simultaneous addition and removal of a component may be difficult. However, changes in the **ratios** of biogenic components with depth can reveal patterns that suggest concurrent production and consumption of organic matter. This approach is similar to that used by Suess and Muller (1980) who explained the total organic matter at the water-sediment interface as a mixture of detrital, biomass and sorbed organic matter based on characteristic elemental ratios of each component. In the samples from the plume, we find that the biogenic composition of settling particles contrasts with patterns observed in sediment trap experiments conducted in environments where hydrothermal input is not influential. Depth profiles of three biogenic component ratios, C_{org} / C_{CaCO3}, C_{org} /opal, and C_{org} /N, support the hypothesis that chemosynthetic biomass plays a role in the plume as far away as two kilometers from the vent field.

C_{org}/C_{CaCO3}

The flux ratio of organic carbon to carbon in calcium carbonate (Figure IV.2) varies geographically in the upper water column because it reflects the relative abundances of carbonate and non-carbonate producing organisms (Dymond and Lyle, 1985). Regardless of the initial ratio, however, as particles settle, organic carbon is respired more rapidly than calcium carbonate is dissolved (Walsh et al., 1988). Consequently, a decrease in C_{org}/C_{CaCO3} with depth, which has been observed at many sites (Dymond and Lyle, 1985; Dymond and Collier, 1988), is expected. We attribute the sharp **increase** in the ratio for the plume-layer samples at 1950, 2050, and 2100 m to the addition of new, chemosynthetic biomass rich in organic carbon and essentially devoid of $CaCO_3$ to the background, photosynthetic carbon flux. Dissolution of $CaCO_3$ by acidic hydrothermal waters is an alternative explanation. Hydrothermal fluid,which is diluted 10^3 -10^4 times (Lupton et al., 1985) as it rises and advects the 2 km from the vent field to our mooring, is unlikely to cause substantial excess carbonate dissolution as particles settle from the top of the plume at approximately 1900 m to the 1950 m trap. It should also be noted that the high alkalinity of the preservatives used in our sediment trap cups prevents carbonate dissolution of particles within the trap itself. The common occurrence of unetched aragonitic pteropod shells attests to this fact. The C_{org}/C_{CaCO3} ratio of the sample

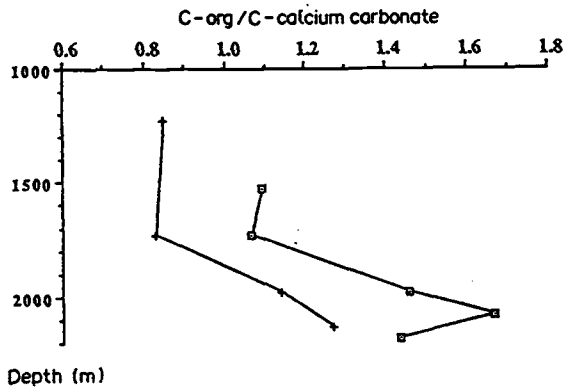

Figure IV.2. Dramatic increases in the ratio of C_{org} to C_{CaCO3} at plume depths suggest an input of chemosynthetically-derived C_{org}. Because organic carbon is more labile, the ratio typically decreases with depth. Squares denote the 340-day mooring deployment, Endeavour Ridge - 1 (ER-1) ; crosses indicate results from the subsequent 260-day experiment (ER-2).

collected in the 8-day, near-field experiment is ≈ 18, in contrast to values near unity in the upper water column traps. It is highly improbable that this large value reflects solely dissolution of $CaCO_3$, since it would require dissolution of ≈ 95 percent of the settling carbonate. Furthermore, the carbonate flux measured in the 8-day trap (21 m above bottom) is similar to that measured in the 1700 m trap. Since particle settling rates are on the order of hundreds of meters per day (Dymond and Roth, 1988), this is not surprising and indicates minimal dissolution of calcium carbonate between 1700 m and the seafloor. In summary, although both $CaCO_3$ and C_{org} fluxes exhibit decreases in the plume-affected trap samples (1900 m and deeper), the increase in C_{org}/C_{CaCO3} suggests that organic carbon addition occurs simultaneously with removal of these components.

C_{org} /opal

A profile of of C_{org} /opal with depth (Figure IV.3a) also suggests a plume-level organic carbon injection. The recycling of organic carbon from settling particles is faster than that of biogenic opal (Walsh et al., 1988) and should result in a decrease of this ratio with depth. In the samples from the plume-level traps, the observed near-bottom increase in the ratio cannot be explained by opal dissolution because hydrothermal fluids are not undersaturated with respect to opal. In fact, observed precipitation of opal from hydrothermal fluids (Feely et al., 1987; Tivey and Delaney, 1986) suggests that the magnitude of the C_{org} /opal increase at plume depths may underestimate the amount of chemosynthetic carbon addition. The marked increase in C_{org}/opal on an annual basis (Figure IV.3a) is also observed in all cup periods except cup 2 (9/8/84-12/7/84) (Figure IV.3b). During this period net transport of hydrothermal material was to the east (across-ridge), in contrast to other sampling periods when flow was predominantly south-southeastward (roughly parallel to the ridge). This anomalous interval may be linked to physical dispersal processes. We lack, however, a satisfactory explanation for this observation since relatively high fluxes of inorganic hydrothermal elements such as Fe, Cu, Zn and S were recorded during the same period (Dymond and Roth, 1988).

C_{org} /N

The third observation, a decrease in C_{org} /N in plume-depth samples, is consistent with input of biomass at the plume level (Figure IV.4). Nitrogen is remineralized from settling organic material more rapidly than carbon following the

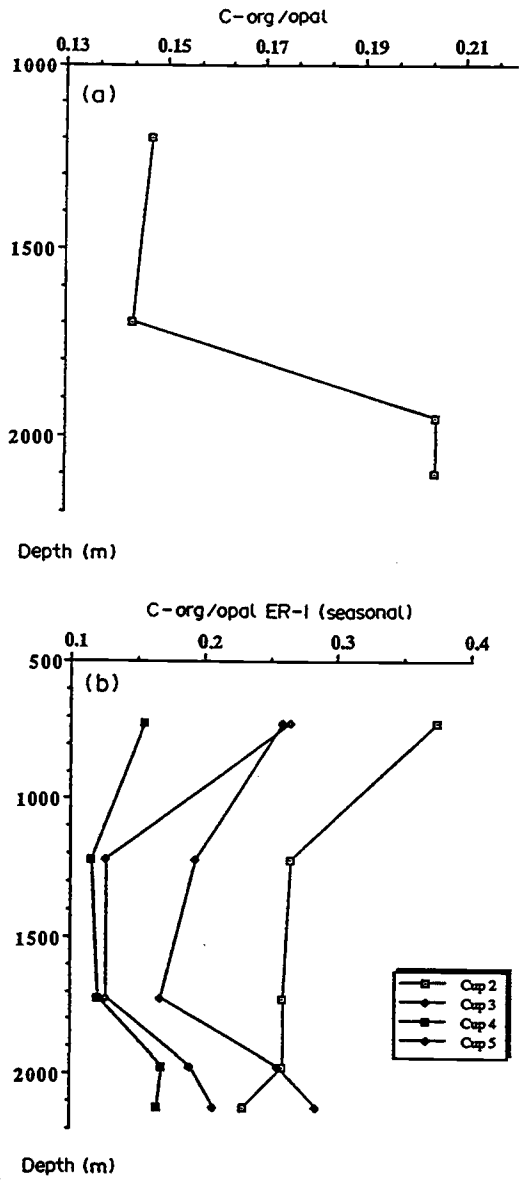

Figure IV.3. Marked increases in the ratio of C_{org} to opal at plume depths suggest an input of chemosynthetically-derived C_{org}. Typically, this ratio decreases with depth because particulate organic carbon is recycled more rapidly than biogenic opal. Data from the 340-day deployment are shown on an annual basis in *a* , and on a seasonal basis (sample cups 2-4) in *b*.

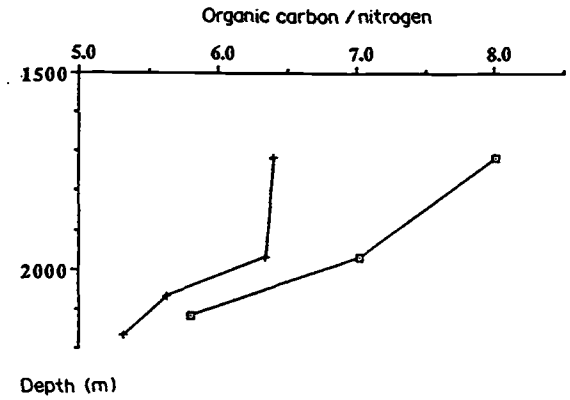

Figure IV.4. A decrease in the ratio of C_{org} to N at plume depths suggests addition of chemosynthetic organic material with a C/N ratio less than that of more degraded organic particles from the upper water column. Since nitrogen is recycled more rapidly than carbon from settling organic particles, the ratio typically increases with depth. Squares denote the 340-day mooring deployment (ER-1) ; crosses indicate results from the subsequent 260-day experiment (ER-2).

Redfield ratio prediction (Redfield et al.,1963), therefore, as photosynthetic organic material ages, the C/N ratio in the particulate flux typically increases (Knauer et al., 1979; Suess and Muller, 1980). We note a distinct decrease in this ratio at depths ≥ 1950 m which may reflect an input of fresh organic matter with a C/N ratio smaller than that of the background organic material at these depths. This is consistent with the findings of Comita et al. (1984) who reported a decrease in the C/N ratio of particulate organic material (POM) in East Pacific Rise (EPR) 21° N vent fluids with water temperature. Their filtered samples were enriched in organic carbon and more labile than POM in non-vent water, and biochemical analysis indicated that zooplankton and larger benthic organisms were the dominant source of this material. Relative contributions to POM in our trap samples from primary chemosynthetic material (entrained by the plume from the vent field) and products of secondary biological activity (e.g. plume-dwelling heterotrophs which feed on organic carbon-rich particles) cannot be quantitatively determined from this data. We will show in a later section, however, that the low C/N ratio of the organic material added at plume depths suggests a bacterial source.

In summary, the **quality** of the biogenic fraction of sediment trap material suggests that organic matter, is introduced at depths influenced by the hydrothermal plume. The net fluxes, i.e. **quantity,** of all biogenic components (including carbon), decrease at plume depths; however, the decrease in organic carbon is proportionately less than other biogenic constituents. We attribute this observation to an input of fresh biomass, transported, and possibly generated, in the plume. Assertion of concurrent particle removal and organic matter addition raises questions which we will address in the remainder of the paper: What causes the decrease in biogenic and detrital particle flux at some depth > 1700 m? What is the source of the new organic material at depth? Are the processes that cause particulate flux reduction and biomass production related? Following that discussion, we will attempt to quantify relative addition and removal of organic material.

Decrease in Settling Particle Flux

Minima in bulk and Al, Ti, C_{org}, $CaCO_3$ and opal fluxes at 1950 m show that in-plume particle removal affects inorganic detritus as well as organic material. Comparable minima are not observed in the profiles of metals and sulfur which are enriched in hydrothermal fluid; this is probably because the plume, the dominant source

of these elements, is so influential below ≈1900 m. We have calculated the "missing" amount of representative components at 1950 m; these are the differences between the flux expected at 1950 m (determined by extrapolating the measured 1200 m - to - 1700 m trend to 1950 m) and the measured 1950 m flux. During year 1, 43% of the aluminum, 50% of the organic carbon, 64% of the carbonate carbon, and 66% of the opal could be missing at 1950 m. We will show later that if the chemosynthetic carbon flux is included, the loss of organic carbon is significantly greater than 50 percent. Because the minima at 1950 m are documented for the individual sample cups and confirmed by two consecutive annual mooring deployments, instrumental failure cannot account for this finding. Dissolution of organic matter within trap sample cups does result in loss of some labile particulate material and will be discussed in a later section. However, the 1950 m minima in the flux profiles of Al, Ti, C_{org}, $CaCO_3$ and opal cannot be accounted for by dissolution of organic matter. In this section, we consider the strengths and shortcomings of physical and biological explanations for the observed reduction in particle flux.

Physical Oceanographic Effects

Do the dynamics of deep-sea currents cause the low fluxes observed? It is conceivable that strong cross-currents could reduce the collection efficiency of our sediment traps. Flow measured 80 m above bottom was highly variable in velocity, and speeds in excess of 10 cm s^{-1} were frequently recorded (Roth and Dymond, 1986). Previous studies have shown that sediment trap collecting efficiency diminishes when current speeds exceed 15 cm s^{-1} (Baker et al., 1985; Gardner, 1980). The intermittent effect of swift flow, however, would not result in overall reduction of settling flux. There is little evidence at present to support a claim that current velocity in the 200-300 m thick plume layer was greater than at levels above or below where relatively higher fluxes were recorded. Gordon et al. (1987) report a 6 cm s^{-1} current shear within the upper 15 m of the Endeavour Ridge plume which was detected in a vertical lowering of an acoustic doppler current profiler (Thomson and Gordon, 1987) between 1870 and 1910 m (a depth comparable to our 1950 m trap). Though this is an instantaneous measurement, it is an indication that variations in the lateral transport of particles with depth may occur, and this effect may have bearing on the collection of particles in our sediment traps. The reduction in flux which might be caused by strong currents would effect biogenic, detrital and hydrothermal particles alike; however removal of hydrothermal components may be more difficult to detect since the input of these

elements (e.g.. Fe, Zn, Cu, S) increases so dramatically at depth . In summary, the data neither support nor invalidate the hypothesis that lateral particle transport attenuates particle flux at plume depths.

Biological Effects

We offer several explanations of the distinctive particle flux profiles based on the general hypothesis that organisms inhabit the laterally-spreading hydrothermal plume and consume particles which would, in their absence, settle into the sediment traps. Such a scenario requires that material be effectively **removed** from the water column above the traps because transformation into fecal material could have an inverse effect, i.e. accelerated settling. We suggest three possible mechanisms for removal. Microbial decomposition of large particles into finer-grained material or dissolved compounds could cause a reduction in settling particle flux by enhancing horizontal transport of particulate material. Micro-zooplankton,which are neutrally buoyant while living, could ingest bacteria and fine-grained organic material, thus also keeping it in suspension until lateral flow sweeps these small animals beyond the mooring site. Finally, macro-zooplankton might graze close to the plume source where particle concentrations are higher so that the residual plume passing our mooring would be depleted of particles. In contrast to smaller micro-organisms, macro-zooplankton are capable of swimming at speeds an order of magnitude greater than the prevailing flow, and thus could maintain an advantageous position with respect to food supply. Sloppy feeding by zooplankton might also transform large particles into smaller particles or dissolved organic carbon which does not settle into our traps (Copping and Lorenzen, 1980).

Bacteria

Results of recent investigations suggest that the plume harbors microbial populations. Microbial biomass enrichments in buoyant hydrothermal discharge have been documented (Lilley et al., 1983; Jannasch, 1983; Baross and Deming, 1985; Winn et al.,1986) as well as in the laterally spreading plume at distances greater than 4 km from the vents (Cowen et al.,1986). Bacteria may be expelled from the vents, entrained from the vent-field environs, or actively growing in the plume. Jannasch and Mottl (1985) point out that bacterial productivity should be highest where hydrothermal effluent mixes slowly with oxygenated seawater; it is conceivable that conditions in the dispersing plume favor aerobic chemosynthesis.

Bacterial effects may be two-fold with respect to particle removal and organic carbon addition. Breakdown of particles by dissolution or disaggregation may be microbially mediated and thus accelerated in the plume. Small particles remain in suspension and could be carried away from the mooring site by lateral currents before settling into the sediment traps. Our observation of extreme corrosion of metallic mooring components **only** at plume depths is evidence of anomalous conditions. There, type 316 stainless steel shackles, which normally exhibit no corrosion, were 1/4 to 1/3 dissolved, and a dark organic (bacterial?) slime coated our instruments. The process which causes unusual corrosion of mooring hardware also may promote particle degradation, and we speculate that this chemical process is mediated by biological activity occurring at solid surfaces since there is no evidence to suggest a source or mechanism of maintaining a pool of corrosive seawater in this region of highly variable current speeds and flow directions (Roth and Dymond, 1986). On the other hand, chemoautotrophic bacteria may enhance particle formation in which production of organic material in the plume is fueled by reduced metals and sulfur. Subsequent consumption by bacteriovores and larger predators could produce more particles. Another mechanism by which microbial activity may augment particle flux is through the formation of rapidly settling marine snow. It has been suggested that bacteria play a role in the aggregation of small particles and the conversion of dissolved to particulate organic carbon (Alldredge, 1984). Bacterial particle breakdown, causing a reduction in settling flux therefore may occur simultaneously with enhanced particulate organic carbon flux since, as primary producers, bacteria may constitute the base of a food chain.

Zooplankton

In addition to particle-breakdown caused by microorganisms, ingestion of particles by zooplankton between 1700 and 1950 m also could produce the 1950 m flux minima by removing organic matter from the plume before the water passes the trap, or by actively transporting material by the traps. Why would zooplankton populate a water mass as apparently transitory as the hydrothermal plume? From what is known about the distribution of zooplankton in the oceans, it is reasonable to hypothesize that the plume provides a suitable niche for an animal population. The laterally spreading plume may be a relatively rare, nutrient-rich lens in the deep sea, which is inhabited by specifically adapted organisms (Berg and Van Dover, 1987). Organic material in the

plume may be allochthonous; for example, bits of the fauna that thrive near the seafloor vent openings may be entrained in the buoyant plume and carried far from the vent field. As discussed above, biomass also may be generated in the plume. Thus, a strong gradient is present between ambient bottom water that is relatively food-depleted and hydrothermal fluid which is infused with both the raw materials (reduced chemicals, i.e. energy sources) for chemoautotrophic primary production, as well as entrained organic particles from the vent field. The relatively enriched plume, with boundaries established by physical parameters (buoyancy, density stratification, regional flow), presents a confined volume that zooplankton can readily locate. This situation is comparable to the congregation of zooplankton in particle-rich benthic boundary (nepheloid) layers (Wishner, 1980). Amphipods and copepods were plentiful on *in situ* pump filters (Comita et al., 1984), and macrozooplankton abundance and biomass one to four orders of magnitude greater than in other deep-sea areas were reported directly above a hydrothermal vent field on the East Pacific Rise (Smith, 1985). More recently, Berg and Van Dover (1987) reported enriched benthopelagic macrozooplankton biomass and abundance at hydrothermal vents on the East Pacific Rise and in the Guaymas Basin; however, the presence of populations in distal plumes has not yet been documented by plankton tows.

Buoyant hydrothermal plumes may drive abyssal circulation (Stommel, 1982) which is favorable to survival of plankton. An analogy also can be drawn to the hypothesis that planktonic species need semi-closed gyre circulation patterns if they are to persist (McGowan, 1971). In the case of plume-specific zooplankton, the pertinent circulation geometry may be highly-localized, vertically-oriented cells forced by venting of hydrothermal fluids, rather than large-scale, horizontal gyres. The upward limb of such cells is the buoyant plume that induces substantial entrainment (Lupton et al., 1985). To replace the entrained water, flow towards the vent field must occur. Mass balance dictates that downwelling must accompany upwelling, however this may be relatively diffuse. Particle settling, enhanced through biological repackaging, i.e. fecal pellet production, may be a process which effectively closes these vertical circulation cells.

Eat-and-Run Scenarios

1. An hypothesis that zooplankton reduce the settling particle flux begs reconciliation with the generally accepted idea that repackaging of fine-grained material

into more rapidly settling fecal pellets enhances the downward transport of particles in the ocean. The flux enhancement scenario assumes that consumption and excretion occur in approximately the same location. If, however, heterotrophs feed at the mooring location and defecate at another site, they remove some fraction of the settling particulate material. This situation may be analogous to anomalous particle fluxes reported in upper water column collections. In many cases, particulate fluxes of organic carbon and other biogenic components increase between 500 m and 1500 m (Knauer and Martin, 1981; Fischer, 1984; Dymond, 1984; Knauer et al., 1984; Dymond and Collier, 1988). Since these components are recycled as they settle, a decrease in flux is expected. The increase in flux has been attributed to such processes as lateral transport (Honjo et al., 1982), chemosynthetic carbon production (Karl et al., 1984), and zooplankton feeding dynamics (Urrere and Martin, 1981). Most descriptions of this pattern have referred to it as a mid-depth flux maximum, however, it could alternatively be described as an upper water column flux deficiency. Systematic flux decreases below 1500 m (Fischer, 1984; Dymond and Collier, 1988) support this interpretation. Thus vertically migratory zooplankton, which consume above the 1950 m trap and excrete below the trap depth, are a plausible explanation for our experimental results. Over this depth range, perhaps just tens of meters thick, we may be observing the effect of just one in a series of overlapping vertical migrations which may regulate POM transport throughout the water column (Urrere and Martin, 1981, and references therein).

2. Horizontal migration of particle-consumers is an alternative explanation for plume-depth flux decreases. In this case, zooplankton are transported laterally by dynamic deep-sea currents, which move the particle-rich plume to-and-fro like a whiplash in slow motion. Swarms of feeding zooplankton pass the mooring string, and, if their uptake exceeds excretion as they pass, the net result will be a dearth of material in the sediment traps below. It could be argued that continuous occupation of the plume by zooplankton would, over time, result in a balance being struck between the amount of material removed from and added to the settling particle flux via their feeding. However, since some portion of food consumed is used for growth, expended metabolically and possibly released as dissolved substances, particle uptake may exceed fecal pellet production. Predators drawn to the swarm of zooplankton may feast upon them, then swim quickly away, further reducing particulate organic material. The variability of deep-sea current velocity is another factor that could perturb steady-state

conditions. Zooplankton feeding may be synchronized with tidal motions, which are important regulators of lateral particle flux (Roth and Dymond, 1986). Removal of the inorganic detritus may be explained by indiscriminate particle feeding. Fecal pellets containing both coccolithophorids and sulfide particles observed in traps deployed within the plume suggest that such mixed particle ingestion occurs (Dymond and Roth, 1988).

Addition of Organic Material

Quantifying the addition of organic carbon to the settling particle flux when it is simultaneously being removed by a different process could be accomplished with distinct tracers of a chemosynthetic source. Stable isotopes have been used to suggest a chemosynthetic source of carbon (Rau and Hedges, 1979); however, more recent studies have demonstrated that carbon isotopic ratios in chemosynthetic organisms exhibit a broad range of values (Rau, 1985). The range of values reflects biogeochemical pathways with distinct isotopic fractionations and possible temperature effects which can complicate attempts to use the isotopic data to quantify the contributions from chemosynthetic sources. The carbon isotopic composition of vent bacteria grown *in situ* has not yet been measured (David Karl, personal communication). Preliminary carbon isotope data on our samples from the 8-day and year 1 traps (John Hayes, personal communication) support the complexity of the isotopic systematics. Samples with the greatest chemosynthetic contribution (see below) and greatest fraction of hydrothermally-derived particles (e.g. Cu, Zn, Fe and S) tend to have heavier carbon isotopic compositions. There are some exceptions to this observation however, and relatively large variations in the carbon isotopic composition of suspended particles indicate that a single chemosynthetic end-member cannot explain the carbon isotopic data. A complete discussion of these data will be presented in Hayes et al., (in prep). Consequently, we have chosen to use the changes in the C_{org}/ C_{CaCO3} and $C_{org}/$ opal ratios to estimate the chemosynthetic carbon contribution.

If we assume that the C_{org}/ C_{CaCO3} ratios measured in the 1700-m traps (above the plume) are the maxima which would be observed at greater depths were it not for the addition of chemosynthetic carbon, we can calculate the **fraction of chemosynthetically-derived organic carbon** in our samples as follows:

Assume: Total C = C_{org} + C_{CaCO3}

C_{org} = $C_{photosynthetic}$ + $C_{chemosynthetic}$

$C_{chemosynthetic\ (1700\ m)}$ = 0, but $C_{chemosynthetic\ (\geq 1950\ m)} > 0$

$C_{chemosynthetic}$ contains no $CaCO_3$, so $CaCO_{3\ (1700\ m)}$ = $CaCO_{3\ (\geq 1950\ m)}$.

It follows that if there is no $C_{chemosynthetic}$ contribution, then

$$\frac{C_{org}}{C_{CaCO_{3\ (1700\ m)}}} = \frac{C_{org}}{C_{CaCO_{3\ (1950\ m)}}}$$

and the ratio of these fractions = 1. Conversely, addition of $C_{chemosynthetic}$ would increase C_{org} at 1950 m and the ratio would be < 1.

Then we can calculate the fraction, $\frac{C_{chemo}}{C_{org}}$, in samples ≥ 1950 m:

$$\frac{C_{chemo}}{C_{org}} \times \frac{C_{org}}{C_{CaCO_{3\ (\geq 1950\ m)}}} = \frac{C_{org}}{C_{CaCO_{3\ (\geq 1950\ m)}}} - \frac{C_{org}}{C_{CaCO_{3\ (1700\ m)}}}$$

Hence, the **fraction of chemosynthetically-derived organic carbon** in our samples is:

$$Corg_{\ chemo} = 1 - \left[\frac{\left\{ C_{org} / C_{CaCO_3} \right\}_{1700m}}{\left\{ C_{org} / C_{CaCO_3} \right\}_{depth \geq 1950m}} \right]$$

On an individual sample cup basis, chemosynthetic carbon accounts for up to 62 percent of the total measured organic carbon flux (year 2, 2050 m, cup 5). Values of this input for the year 1 experiment based on a similar calculation using opal rather than calcium carbonate as a reference flux agree well and are given in brackets, { }, in

Table IV.2 Organic carbon particle fluxes

Trap depth (m)	Year	Measured ($C_m + P_m$)	Missing ($C_r + P_r$)	C_m	C_r	C_t	P_m	P_r	P_t	Total ($C_t + P_t$)	% Chemo.
1950	1	58.6	117.8	16.4	33.0	49.4	42.2	84.8	127	176.4	28{30}
1950	2	41.5	132.4	11.2	35.7	46.9	30.3	96.7	127	173.9	27
2050	2	75.6	122.8	27.2	44.2	71.4	48.4	78.6	127	198.4	36
2100	1	92.6	102.8	32.4	36.0	68.4	60.2	66.8	127	195.4	35{30}
2150	2	99.2	72.4	25.8	18.8	44.6	73.4	53.6	127	171.6	26

C, chemosynthetic; P, photosynthetic; subscripts m, r, and t refer to measured, missing (removed), and total.

Known:

($C_m + P_m$), the trap-measured C_{org} flux.

$C_{org\ chemo}$, the fraction of chemosynthetic carbon, calculated by the method discussed in the text. Using this fraction we can separate C_m and P_m.

P_t is the background flux. We use the C_{org} flux at 1700 m, because this above-plume trap is not influenced by hydrothermal (chemosynthetic) input, and according to the model of PACE *et al.* (1987), very little C_{org} is lost due to normal degradation upon further descent. 127 is the year 1 flux.

Calculations:

1. $P_r = P_t - P_m$.
2. Assuming that the photo- and chemosynthetic carbon are removed at the same rate, we can use the relative proportions of photo- and chemosynthetic carbon in the measured flux to partition the "missing" flux into contributions from these two sources. That is:

$C_m/(C_m + P_m) = C_r/(C_r + P_r)$ and solving for C_r: $C_r = C_m P_r/P_m$.

3. Finally, $C_t = C_m + C_r$.

Table IV.2. The maximum chemosynthetic carbon contribution on a sample cup basis derived by this method is 41 percent (year 1, 2100 m, cup 3). Estimates of annual chemosynthetic contribution to organic carbon flux are presented in Table IV.2 along with values for normal, photosynthetic input. Because copper content, an indicator of hydrothermal input, correlates with the percent chemosynthetic carbon (Figure IV.5), we believe our estimate of chemosynthetic contribution is proper. Table IV.2 also lists values for "missing" organic carbon at depths ≥ 1950 m which are the differences between the flux estimates based on our calculation and the measured values. The contributions of measured and missing chemosynthetic and photosynthetic organic carbon within and beneath the plume layer are shown in Figure IV.6. As might be expected, the chemosynthetic carbon component of the eight-day vent-field trap is much larger than the far-field traps. The total organic carbon flux for this trap is ≈ 10 times that of the average 1700 m traps. Furthermore, the C_{org}/ C_{CaCO3} ratio is 18 which,when used in the above calculation, suggests that 95 percent of the carbon collected in the trap is chemosynthetic.

By a method analogous to that explained above, we have calculated the fraction of chemosynthetically-derived nitrogen in our samples and determined the C/N ratio of chemosynthetic POM flux. The range of values for both years, 2.4 - 5.2 is considerably lower than that of marine phytoplankton which have characteristic C/N values of ≈ 7. Our values are much lower than those reported by Comita et al. (1984), 10-15, for filtered material from warm vent waters. In our samples C/N_{chemo} decreases between 1950 and 2150 m. Although the C/N ratio of hydrothermal vent organisms is unknown, the anomalously low values suggest that this material is predominantly bacterial. According to Wheeler and Kirchman (1986), bacteria have a characteristic C/N ratio of 3-4 ; Goldman et al. (1987) report values of 4-6.

Removal of Organic Material

The mean annual "missing" carbon, $(C_r + P_r)$, $= 110 \pm 11$ μg/cm^2 (109 ± 32 μg/cm^2 in year 2) over the depth range 1950 - 2150 m of the hydrothermal plume; also, "missing" carbon generally decreases with depth. Variations with depth in the four organic carbon components, measured and missing chemosynthetic and photosynthetic fluxes, are shown in Figure IV.6. Observations that the missing carbon exceeds the measured flux at each depth except the deepest trap (2150 m), and that the maximum chemosynthetic flux at 2050 m corresponds to the "core" of the plume layer illustrate

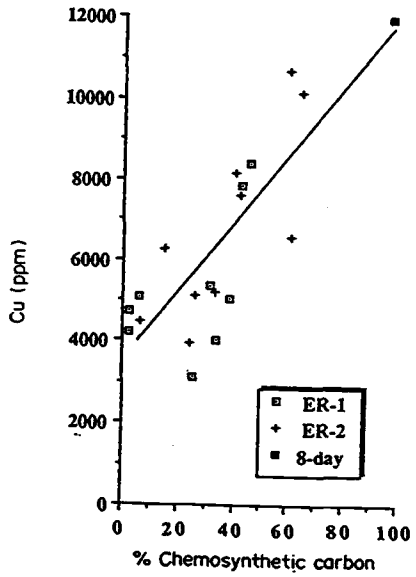

Figure IV.5. The linear relationship ($r^2 = 0.67$) between copper content and percentage chemosynthetic carbon in samples from the 8-day, vent-field trap (box), ER-1 (squares) and ER-2 (crosses) collected at depths ≥ 1950 m. Both Cu and C_{chemo} are expected to increase in samples most effected by hydrothermal input. Correlation between these independent indicators of hydrothermal influence supports the validity of our approach to calculating the chemosynthetic carbon contribution (see text).

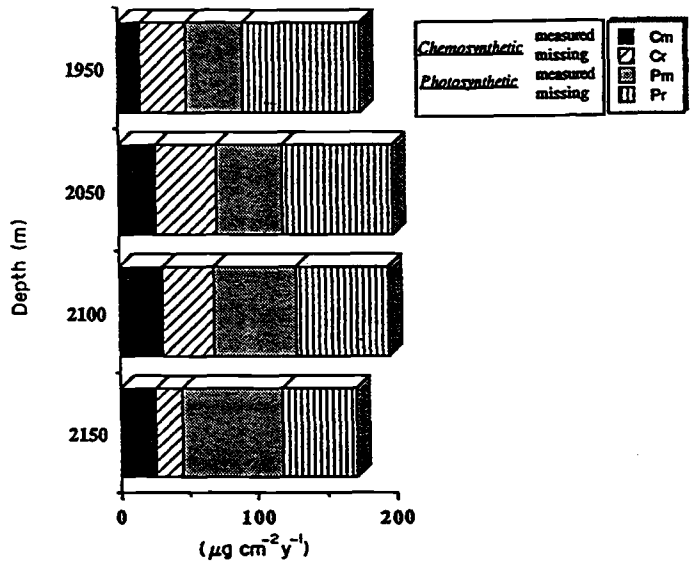

Figure IV.6. The total organic carbon flux at four depths is represented by the length of bar. Data for 1950, and 2100 m are from the 340-day experiment; the 2050 and 2150 m value is from the year 2 trap deployment. Contributions from measured (subscript m) and "missing" (subscript r) particulate organic carbon are shown (see text and Table 2). These two components are further partitioned into contributions from photosynthetic (P_m and P_r), and chemosynthetic (C_m and C_r) sources. Amounts of "missing" chemosynthetic carbon are minima because we assume that the relative proportions of photo- and chemosynthetic carbon in the measured and "missing" fractions are equivalent. Since chemosynthetic carbon may be more nutritious (less degraded, lower C/N ratio) than the photosynthetic fraction, it may constitute a larger proportion of the carbon removed by biologic processes at plume-influenced depths.

simultaneous removal and addition of organic carbon. Our estimates of the fraction of the missing chemosynthetic carbon, C_r, are conservative. Chemosynthetic organic material may be relatively more nutritious than pelagic (photosynthetic) material which has been degraded by extensive biologic recycling during descent. Thus, preferential uptake of chemosynthetic carbon is expected, and C_r:P_r would be greater than C_m:P_m.

Dissolution of organic carbon within sample cups is most pronounced in the shallower traps and decreases with depth. At 700 m as much as 60 percent of the particulate organic carbon becomes soluble after entering the trap; at 1200 m less than 30 percent is soluble. This pattern presumably reflects the loss of more labile carbon as particles sink. Since solubility of organic carbon occurs predominantly at shallower depths, the 1200-to-1700 m extrapolation calculation of missing carbon is relatively insensitive to solubility effects. Correction for soluble carbon would boost our estimates of missing organic carbon. Also, the fresher, chemosynthetic carbon entering the 1950 m trap may be more soluble than the aged, photosynthetic carbon at 1700 m, and this would result in an underestimate of C_r.

To evaluate the significance of the observed particulate carbon loss, we compare our flux data with predictions of the empirical carbon degradation model of Pace et al. (1987). This model {$POC/PP = 3.523\ z^{-0.734}$, where POC is particulate organic carbon, PP is primary production, and z is water depth} predicts that approximately one percent of the organic carbon which leaves the euphotic zone reaches the deep sea and that only 0.14 percent of primary production (photosynthetic) is lost between 1700 and 1950 m due to normal degradation processes. Assuming that the POC flux in the 1700 m , above-plume trap reflects only normal degenerative loss, we can use it to calculate primary production, and subsequently the POC flux expected at 1950 m. This calculation reveals that 48 percent of the POC flux is lost between 1700 and 1950 m. Furthermore, if the "missing" carbon flux (Table IV.2) is included, the computed POC loss increases to 70 percent. From this we can see that although the absolute magnitude of POC loss is small relative to primary production, it is substantial relative to the POC pool in the deep sea. This observation may have important implications with respect to ecological processes within abyssal and benthic communities as well as bearing on sediment geochemistry in areas influenced by hydrothermal plumes.

The preceding discussion demonstrates the importance of a multidisciplinary approach to understanding the biogeochemistry and dynamics of deep-sea hydrothermal plumes. Interpretation of our particle flux data suggests that an intriguing interplay of rock, seawater and life occurs in the deep ocean. The hypotheses that plume chemistry both regulates and is modified by biological activity and that the oceanic effects of hydrothermal activity extend far beyond vent-field boundaries await further testing.

Bibliography

Alldredge, A., Macroscopic Organic Aggregates (Marine Snow) In: Global Ocean Flux Studies, Proceedings of a Workshop, Woods Hole, National Academic Press, 166-179, 1984.

Asper, V.L., W.G. Deuser, G.A. Knauer and S.E. Lohrenz, Rapid coupling of sinking particle fluxes between surface and deep ocean waters, Nature, 357, 670-672, 1992.

Bacon, M.P., C.-A. Huh, A.P. Fleer and W.D. Deuser, Seasonality in the flux of natural radionuclides and plutonium in the deep Sargasso Sea, Deep-Sea Research, 32(3), 273-286, 1985.

Baker, E.T. and S.R. Hammond, Hydrothermal venting and the apparent magmatic budget of the Juan de Fuca Ridge, J. Geophys. Res., 97(B3), 3443-3456, 1992.

Baker E.T., and J.W. Lavelle, The effect of particle size on the light attenuation coefficient of natural suspensions, J. Geophys. Res., 89(C5) 8197-8203, 1984.

Baker, E.T., J.W. Lavelle, R.A. Feely, G.J. Massoth and S.L. Walker, Episodic venting of hydrothermal fluids from the Juan de Fuca Ridge, J. Geophys. Res., 94(B7) 9237-9250, 1989.

Baker, E.T., J.W. Lavelle, and G.J. Massoth, Hydrothermal particle plumes over the southern Juan de Fuca Ridge, Nature, 316, 342-344, 1985.

Baker, E.T. and G.J. Massoth, Hydrothermal plume measurements: A regional perspective, Science, 234, 980-982, 1986.

Baker, E. T. and G. J. Massoth, Characteristics of hydrothermal plumes from two vent fields on the Juan de Fuca Ridge, northeast Pacific Ocean, Earth and Planetary Science Letters, 85, 59-73, 1987.

Baker, E.T., G.J. Massoth, and R.A. Feely, Cataclysmic hydrothermal venting on the Juan de Fuca Ridge, Nature, 329, 149-151, 1987.

Baker, E.T., H.B. Milburn and D.A. Tennant, Field assessment of sediment trap efficiency in a high energy environment, EOS, 66, 1307, 1985.

Baross, J.A. and J.W. Deming, The role of bacteria in the ecology of black smoker environments, Bulletin of the Biological Society of Washington, 6, 355-371, 1985.

Bartz, R., J.R. V. Zaneveld and H. Pak, A transmissometer for profiling and moored observations in water, SPIE Ocean Opt. V,160, 102-108, 1978.

Berg, C.J. and C.L. Van Dover, Benthopelagic macrozooplankton communities at and near deep-sea hydrothermal vents in the eastern Pacific Ocean and the Gulf of California, Deep-Sea Research, 34, 379-401, 1987.

Bishop, J.K.B., The correction and suspended particulate matter calibration of Sea Tech transmissometer data, Deep-Sea Res., 33(1), 121-134, 1986.

Burd, B.J., R.E. Thomson and G.S. Jamieson, Composition of a deep scattering layer overlying a mid-ocean ridge hydrothermal plume, Marine Biology, 113, 517-526, 1992.

Butterfield, D.A., G.J. Massoth, R.E. McDuff, J.E. Lupton and M.D. Lilley, Geochemistry of hydrothermal fluids from Axial Seamount Hydrothermal Emissions Study Field, Juan de Fuca Ridge: Subfloor boiling and subsequent fluid-rock interactions, J. Geophys. Res., 95(B8), 12,895-12,922, 1990.

Butterfield, D.A., R.E. McDuff, M.D. Lilley and G.J. Massoth, Chemical heterogeneity in vent fluids from the Endeavour Ridge (abstract), Eos Trans., 70(43), 1163, 1989.

Cannon, G.A., D.J. Pashinski and M. Lemon, Mid depth flow near hydrothermal venting sites on the southern Juan de Fuca Ridge, J. Geophys. Res., 96, 12,815-12,831, 1991.

Chadwick, Jr., W.W., R.W. Embley and C.G. Fox, Evidence for volcanic eruption on the southern Juan de Fuca Ridge between 1981 and 1987, Nature, 352, 325-328, 1991.

Coale, K.H., C.S. Chin, G.J. Massoth, K.S. Johnson and E.T. Baker, In situ chemical mapping of dissolved iron and manganese in hydrothermal plumes, Nature, 352, 325-328, 1991.

Comita, P.B., R.B. Gagosian and P.M. Williams, Suspended particulate organic material from hydrothermal vent waters at 21° N, Nature, 307, 450-453, 1984.

Converse, D.R., H.D. Holland and J.M. Edmond, Flow rates in the axial hot springs of the East Pacific Rise (21°N): implications for the heat budget and the formation of massive sulfide deposits, Earth and Planetary Science Letters, 69, 159-175, 1984.

Copping, A.E. and C.J. Lorenzen, Carbon budget of a marine phytoplankton-herbivore system with carbon-14 as a tracer, Limnology and Oceanography, 25, 873-882, 1980.

Cowen, J.P., G.A. Massoth and E.T. Baker, Bacterial scavenging of Mn and Fe in a mid- to far-field hydrothermal particle plume, Nature, 322, 169-171, 1986.

Cowen, J. P., G. J. Massoth and R. A. Feely, Scavenging rates of dissolved manganese in a hydrothermal vent plume, Deep Sea Research, Part A, 37(10A), 1619-1637, 1990.

Delaney, J.R., R.E. McDuff, M.K. Tivey and J.E. Lupton, Measurements of 400°C hydrothermal fluids and temporal variability in the Endeavour vent field (abstract), Eos Trans., 70(43) 1163, 1989.

Delaney, J.R., V. Robigou, R.E. McDuff and M.K. Tivey, Geology of a vigorous hydrothermal system on the Endeavour Segment, Juan de Fuca Ridge, J. Geophys. Res., Paper 92JB00174, in press, 1992.

Deuser, W.G., Seasonal and interannual variations in deep-water particle fluxes in the Sargasso Sea and their relation to surface hydrography, Deep-Sea Research, 33(2), 225-246, 1986.

Dymond, J., E. Baker and J. Lupton, Plumes: the oceanic limb of seafloor hydrothermal systems, Position paper prepared for Mid-ocean Ridge workshop at Salishan Lodge in Oregon, April 1987.

Dymond, J. and R. Collier, Biogenic particle fluxes in the equatorial Pacific: Evidence for both high and low productivity during the 1982-1983 El Nino, Biogeochemical Cycles, 2, 129-137, 1988.

Dymond, J., K. Fischer, M. Clauson, R. Cobler, W. Gardner, M.J. Richardson, W. Berger, A. Soutar and R. Dunbar, A sediment trap intercomparison study in the Santa Barbara Basin. Earth and Planetary Science Letters, 53, 409-418, 1981.

Dymond, J. and M. Lyle, Flux comparisons between sediments and sediment traps in the eastern tropical Pacific: Implications for atmospheric CO_2 variations during the Pleistocene, Limnology and Oceanography, 30, 699-712, 1985.

Dymond, J. and S. Roth, Plumefall: a record of settling particle flux on the Endeavour Ridge using moored sensors, EOS , 67, 1027-1028, 1986.

Dymond, J. and S. E. Roth, Plume-dispersed hydrothermal particles: A time-series record of settling flux from the Endeavour Ridge using moored sensors, Geochimica et Cosmochimica Acta, 52, 2525-2536, 1988.

Feely, R.A., T.L. Geiselman, E.T. Baker, G.J. Massoth and S.R. Hammond, Distribution and composition of buoyant and nonbuoyant hydrothermal plume particles from the ASHES vent at Axial Volcano, Juan de Fuca Ridge, J. Geophys. Res., 95(B8), 12,855-12,874, 1990a.

Feely, R.A., M.A. Lewison, G.J. Massoth, G. Robert-Baldo, J.W. Lavelle, R.H. Byrne, K.L. Von Damm and H.C. Curl, Jr., Composition and dissolution of black smoker particulates from active vents on the Juan de Fuca Ridge, J. Geophys. Res., 92(11), 11,347-11,363, 1987.

Feely, R.A., G.J. Massoth, E.T. Baker, J.P. Cowen, M.F. Lamb and K.A. Krogsland, The effect of hydrothermal processes on mid-water phosphorous distributions in the northeast Pacific, Earth Planet. Sci. Lett., 96, 305-318, 1990b.

Feely, R.A., G.J. Massoth, E.T. Baker, G.T. Lebon and T.L. Geiselman, Tracking the dispersal of hydrothermal plumes from the Juan de Fuca using suspended matter compositions, J. Geophys. Res., 97(B3), 3457-3468, 1992.

Feely, R.A., J.H. Trefry, G.J. Massoth and S. Metz, A comparison of the scavenging of phosphorus and arsenic from sea water by hydrothermal iron oxyhydroxide in the Atlantic and Pacific Oceans, Deep-Sea Res., 38(6), 617-623, 1991.

Fischer, H. B., E. J. List, R. C. Y. Koh, J. Imberger and N. H. Brooks, Mixing in inland and coastal waters, Academic Press, New York, 483 p., 1979.

Fischer, K., Particle fluxes to the eastern tropical Pacific Ocean - sources and process. Ph.D. thesis, Oregon State University, Corvallis, 241 pp., 1984.

Fischer, K., J.Dymond, M. Lyle, A. Soutar and S.Rau, The benthic cycle of copper: Evidence from sediment trap experiments in the eastern tropical North Pacific Ocean, Geochim. Cosmochim. Acta, 50, 1535-1543, 1986.

Gardner, W.D., Sediment trap dynamics and calibration: a laboratory evaluation, Journal of Marine Research, 38, 17-39, 1980.

Goldman, J.C., D.A. Caron and M.R. Dennett, Regulation of gross growth efficiency and ammonium regeneration in bacteria by substrate C:N ratio, Limnology and Oceanography, 32, 1239-1252, 1987.

Gordon, R.L., R. Thomson and J. Dymond, Acoustic Doppler Measurements in a Hydrothermal Plume, Fall AGU Meeting Late Abstract, Poster O41D-08, 1987.

Hammond, S.R., J.S. Lee, A. Malahoff, R. Feely, R.W. Embley and J. Franklin, Discovery of high-temperature venting on the Endeavour Segment of the Juan de Fuca Ridge (abstract), Eos Trans. AGU, 65, 1111, 1984.

Haury, L.R., H. Yamazaki and E.C. Itsweire, Effects of turbulent shear flow on zooplankton distribution, Deep-Sea Research, 37(3), 447-461, 1990.

Hessler, R.R., W.M. Smithey Jr.and C.H. Keller, Spatial and temporal variation of giant clams, tube worms and mussels at deep-sea hydrothermal vents, Bulletin of the Biological Society of Washington, 6, 411-428, 1985.

Honjo, S., S.J. Manganini and J.J. Cole, Sedimentation of biogenic matter in the deep-sea, Deep-Sea Research, 29, 609-625, 1982.

Jannasch, H.W., Microbial processes at deep sea hydrothermal vents, In: Hydrothermal Processes at Seafloor Spreading Centers , P. A. Rona, K. Bostrom, L. Laubier and K.L. Smith Jr.,editors, Plenum Press, New York, 677-709, 1983.

Jannasch, H. W. and M.J. Mottl, Geomicrobiology of deep-sea hydrothermal vents, Science, 229, 717-725, 1985.

Johnson, H.P. and V. Tunnicliffe, Time-series measurements of hydrothermal activity on the northern Juan de Fuca Ridge, Geophys. Res. Lett., 12, 685-688, 1985.

Juniper, S.K., J.A.J. Thompson and S.E. Calvert, Accumulation of minerals and trace elements in biogenic mucus at hydrothermal vents, Deep-Sea Research, 33(3), 339-347, 1986.

Kadko, D.C., N.D. Rosenberg, J.E. Lupton, R.W. Collier and M.D. Lilley, Chemical reaction rates and entrainment within the Endeavour Ridge hydrothermal plume, Earth and Planet. Sci. Letters, 99, 315-335, 1990.

Karl, D.M., C.O. Wirsen and H.W. Jannasch, Deep-sea primary productivity at the Galapagos hydrothermal vents, Science , 207, 1345-1347, 1980.

Karl, D.M., G.A. Knauer, J.H. Martin and B.B. Ward, Bacterial chemolithotrophy in the ocean is associated with sinking particles, Nature, 309, 54-56, 1984.

Klinkhammer, G.H., H. Elderfield, M. Greaves, P. Rona and T. Nelsen, Manganese geochemistry near high-temperature vents in the Mid-Atlantic rift valley, Earth and Planetary Science Letters, 80, 230-240, 1986.

Knauer, G.A., J.H. Martin, and K.W. Bruland, Fluxes of particulate carbon, nitrogen and phosphorous in the uppermost water column of the northeast Pacific, Deep-Sea Research, 26A, 97-108, 1979.

Knauer, G.A. and J.H. Martin, Primary production and carbon-nitrogen fluxes in the upper 1500 meters of the northeast Pacific, Limnology and Oceanography, 26, 181-186, 1981.

Knauer, G.A., J.H. Martin and D.M. Karl, The flux of particulate organic matter out of the euphotic zone, In: Global Ocean Flux Studies. Proceedings of a Workshop, Woods Hole, National Academic Press, pp. 136-150, 1984.

Lavelle, J.W., J.P. Cowen and G.J. Massoth, A model for the deposition of hydrothermal manganese near ridge crests, J. Geophys. Res., 97, 7413-7428, 1992.

Lilley, M.D., J.A. Baross, D.A. Butterfield, E.J. Olson, R.E. McDuff, S.A. Macko, J.A. Whelhan and C.N. Dahm, Volatiles in Endeavour vent fluids, Eos Trans. 70(43) 1163, 1989.

Lilley, M.D., J.A. Baross and L.I. Gordon, Reduced gases and bacteria in hydrothermal fluids: The Galapagos Spreading Center and 21° N East Pacific Rise, In: Hydrothermal Processes at Seafloor Spreading Centers, P. A. Rona, K. Bostrom, L. Laubier and K.L. Smith Jr.,editors, Plenum Press, New York, pp 411-449, 1983.

Little, S.A., K.D. Stolzenbach and R.P. Von Herzen, Measurements of plume flow from a hydrothermal vent, J. Geophys. Res., 92, 2587-2596, 1987.

Little, S.A., K.D. Stolzenbach and F.J. Grassle, Tidal current effects on temperature in diffuse hydrothermal flow: Guaymas Basin, Geophysical Research Letters, 15(13), 1491-1494, 1988.

Lupton, J.E., Water column hydrothermal plumes on the Juan de Fuca Ridge, J. Geophys. Res.,95(B8), 12,829-12,842, 1989.

Lupton, J.E., J.R. Delaney, H.P. Johnson and M.K. Tivey, Entrainment and vertical transport of deep-ocean water by buoyant hydrothermal plumes, Nature 316,621-623, 1985.

Lyle, M., M. Leinen, R.M. Owen and D.K. Rea, Late Tertiary history of hydrothermal deposition at the East Pacific Rise, 19° S: Correlation to volcano-tectonic events, Geophys. Res. Lett., 14, 595-598, 1987.

Lyle, M. and A. Olivarez, Hydrothermal sediments and the record of hydrothermal activity at mid-ocean ridges, RIDGE Events, 3(1), p 39, 1992.

Lyle, M., R.M. Owen and M. Leinen, History of hydrothermal sedimentation at the East Pacific Rise, 19°S, Init. Repts. DSDP Leg 92, 585-596, U.S. Government Printing Office, Washington D.C., 1986.

Massoth, G.J., D.A. Butterfield, J.E. Lupton, R.E. McDuff, M.D. Lilley and I.R. Jonasson, Submarine venting of phase-separated hydrothermal fluids at Axial Volcano, Juan de Fuca Ridge, Nature, 340, 702-705, 1989.

McCave, I.N., Particulate size spectra, behavior, and origin of nepheloid layers over the Nova Scotia continental rise, J. Geophys. Res., 88, 7647-7666, 1983.

McDuff, R.E., V.A. Atnipp and J.T. Wells, Time-series studies of fluid output from the Endeavour vent field,Eos Trans., 71, 1619, 1990.

McDuff, R.E. and J.R. Delaney, A time-series of fluid output from black smoker hydrothermal vents, Endeavour Segment, Juan de Fuca Ridge (abstract), Eos Trans., 70(43), 1161, 1989.

McGowan, J.A.The Micropaleontology of Oceans, (eds Funnell, B. & Riedel, W.) 3-74 , 1971.

MERGE Group, Regional setting and local character of a hydrothermal field/sulfide deposit on the Endeavour Segment of the Juan de Fuca Ridge (abstract), Eos Trans. AGU, 65, 1111, 1984.

Metz,S. and J.H. Trefry, Field and laboratory studies of metal uptake and release by hydrothermal precipitates, submitted,

Metz, S., J.H. Trefrey and T.A. Nelsen, History and geochemistry of a metalliferous sediment core from the Mid-Atlantic Ridge at 26°N, Geochim. Cosmochim. Acta, 52, 2369-2378, 1988.

Middleton, J.H. and R.E. Thomson, Modeling of hydrothermal plumes, Can. Tech. Rep. Hydrogr. Ocean Sci., 69, 18 pp., Fish. and Oceans, Ottawa, 1986.

Mullineaux, L.S., P.H. Wiebe and E.T. Baker, Hydrothermal vent plumes: Larval highways in the deep sea?, Oceanus, 34 (3), 64-68, 1991

Munk, W., Abyssal recipes, Deep-Sea Research, 23, 613-628, 1966.

Okubo, A., Oceanic diffusion diagrams, Deep-Sea Research, 18, 789-802, 1971.

Pace, M.L., G.A. Knauer, D.M. Karl and J.H. Martin, Primary production, new production and vertical flux in the eastern Pacific Ocean, Nature , 325, 803-804, 1987.

Pak, H., Fluctuations of beam-attenuation coefficient in the lowest 2 m on the continental rise off Nova Scotia, Marine Geology, 51, 77-97, 1983.

Pond, S. and G.L. Pickard, Introductory Dynamical Oceanography, 2nd edition, Pergamon Press, 1983.

Rau, G.H. and J.I. Hedges, Carbon-13 depletion in a hydrothermal vent mussel: Suggestion of a chemosynthetic food source, Science, 203, 648-649, 1979.

Rau, G.H., $^{13}C/^{12}C$ and $^{15}N/^{14}N$ in hydrothermal vent organisms: ecological and biogeochemical implications, Bulletin of the Biological Society of Washington, 6, 243-247, 1985.

Redfield, A.C., B.H. Ketchum and F.A. Richards, The influence of organisms on the composition of seawater, In: The Sea ,Volume 2, M.N. HILL, editor, Wiley & Sons, New York, pp 26-77, 1963.

Riddihough, R.P., Recent movements of the Juan de Fuca plate, J. Geophys. Res., 89, 6980-6994, 1984.

Robigou, V., J.R. Delaney, R.E. McDuff and M.K. Tivey, Geology of the Endeavour Segment of the Juan de Fuca Ridge and its associated hydrothermal fields (abstract), Eos Trans., 70(43), 1161, 1989.

Rosenburg, N.D., J.E. Lupton, D. Kadko. R. Collier, M.D. Lilley and H. Pak, Estimation of heat and chemical fluxes from a seafloor hydrothermal vent field using radon measurements, Nature, 334, 604-607, 1988.

Roth, S. and J. Dymond, Where wafts the hydrothermal plume? A moored-sensor record of lateral particle flux above Endeavour Ridge, EOS , 67, 1027, 1986.

Roth, S.E. and J. Dymond, Transport and settling of organic material in a deep-sea hydrothermal plume: evidence from particle flux measurements, Deep-Sea Res., 36(8) 1237-1254, 1989.

Schultz, A., J.R. Delaney and R.E. McDuff, On the partitioning of heat flux between diffuse and point source sea-floor venting, J. Geophys. Res.,97(B9), 12,299-12,314, 1992.

Smith, K.L., Jr., Macrozooplankton of a deep sea hydrothermal vent: In situ rates of oxygen consumption, Limnol. Oceanogr., 30(1), 102-110, 1985.

Smith, M.O. and J. R. Delaney, Variability of emitted radiation from two hydrothermal vents (abstract), Eos Trans, 70(43), 1161, 1989.

Smith, S.L., K. Banse, J.K. Cochran, L.A. Codispoti, H.W. Ducklow, M.E. Luther, D.B. Olson, W.T. Peterson, W.L. Prell, N. Surgi, J.C. Swallow and K. Wishner, U.S. JGOFS: Arabian Sea Process Study, U.S. JGOFS Planning Report No. 13, Woods Hole Oceanographic Institution, Woods Hole Massachusetts, 164 pp., 1991

Soutar, A., S.A Kling, P.A. Crill, E. Duffrin and K.W. Bruland, Monitoring the marine environment through sedimentation, Nature, 226, 136-139, 1977

Spinrad, R.W., Testing of optical properties and development of application procedure for OMP-8 antifoulant on submersible optical surfaces, Sea Tech, Inc. Reference Technical Report 8701, 44 p.,1987

Spinrad, R.W. and J.R.V. Zaneveld, An analysis of the optical features of the near-bottom and bottom nepheloid layers in the area of the Scotian Rise, J. Geophys. Res., 87(C12), 9553-9561, 1982.

Spinrad, R.W., J.R.V. Zaneveld and J.C. Kitchen, A study of the optical characteristics of the suspended particles in the benthic nepheloid layer of the Scotian Rise, J. Geophys. Res., 88(C12), 7641-7646, 1983.

Stakes, D and W.S. Moore, Evolution of hydrothermal activity on the Juan de Fuca Ridge: Observations, mineral ages, and Ra isotope ratios, J. Geophys. Res., 96 (B13), 21739-21752,1991.

Stommel, H., Is the South Pacific helium-3 plume dynamically active? Earth and Planetary Science Letters, 61,63-67, 1982.

Suess, E. and P.J. Muller, Productivity, sedimentation rate and sedimentary organic matter in the oceans II. -Elemental fractionation. Biogeochimie de la matiere organique a l'interface eau-sediment marin, Marseille 25-27 Avril 1979, Colloques Internationaux du C.N.R.S. No 293,17-26, 1980.

Taylor, S.R., Abundance of chemical elements in the continental crust: a new table, Geochimica et Cosmochimica Acta, 28,1273-1285, 1964.

Thomson, R.E., B.J. Burd, A.G. Dolling, R.L. Gordon and G.S. Jamieson, The deep scattering layer associated with the Endeavour Ridge hydrothermal plume, Deep-Sea Research, 39(1), 55-73, 1992a.

Thomson, R.E. and K.Y. Chow, Butterworth and Lanczos-window cosine digital filters: with application to data processing on the Univac 1106 computer, Pacific Marine Science Report 80-9, Institute of Ocean Sciences, Sidney, B.C., 54 pages, 1980.

Thomson, R.E., J.R. Delaney, R.E. McDuff, D.R. Janecky and J.S. McClain, Physical characteristics of the Endeavour Ridge hydrothermal plume during July 1988, Earth and Planetary Science Letters, 111, 141-154, 1992b.

Thomson, R.E. and R.L. Gordon, Deep current profiles with an ADCP, EOS , 68, 1688, 1987 .

Thomson, R.E., R. L. Gordon and A. G. Dolling, An intense acoustic scattering layer at the top of a mid-ocean ridge hydrothermal plume, J. Geophys. Res., 96(C3), 4839-4844, 1991.

Thomson, R.E., R.L. Gordon and J. Dymond, Acoustic Doppler current profiler observations of a mid-ocean ridge hydrothermal plume, J. Geophys. Res., 94, 4709-4720, 1989.

Thomson, R.E., S.E. Roth and J. Dymond, Near-inertial motions over a mid-ocean ridge: Effects of topography and hydrothermal plumes, J. Geophys. Res., 95(C5), 7261-7278, 1990.

Tivey, M.K. and J.R. Delaney, Growth of large sulfide structures on the Endeavour segment of the Juan de Fuca Ridge. Earth and Planetary Science Letters. 77(3/4), 303-319, 1986.

Tivey, M.K., L.O. Olson, V.W. Miller and R.D. Light, Temperature measurements during initiation and growth of a black smoker chimney, Nature, 346, 51-54, 1990.

Trefry, J.H., R.P. Trocine, G.P. Klinkhammer and P.A. Rona, Iron and copper enrichment of suspended particles in dispersed hydrothermal plumes along the Mid-Atlantic Ridge, Geophys. Res. Lett., 12(8), 506-509, 1985.

Trocine, R.P. and J.H. Trefry, Distribution and chemistry of suspended particles from an active vent site on the Mid-Atlantic Ridge at 26°N, EPSL,88, 1-15, 1988.

Tyler, P.A., Seasonality in the deep sea, Oceanog. Mar. Biol. Annu. Rev., 26, 227-258, 1988.

Urrere, M.A. and G.A. Knauer ,Zooplankton fecal pellet fluxes and vertical transport of particulate organic material in the pelagic environment, Journal of Plankton Research, 3, 369-387, 1981.

Vinogradov, M.E. and N.M. Voronina, Influence of the oxygen deficit on the distribution of plankton in the Arabian Sea, Deep Sea Research, 9, 523-530, 1962.

Walker, S.L. and E.T. Baker, Particle-size distributions within hydrothermal plumes over the Juan de Fuca Ridge, Mar. Geol.,78, 217-226, 1988.

Walsh, I., J. Dymond and R. Collier, Rates of recycling of biogenic components of settling particles in the ocean derived from sediment trap experiments, Deep-Sea Research, 35, 48-53, 1988.

Weliky, K., E. Suess, C.A. Ungerer, P.J. Muller and K. Fischer, Problems with accurate carbon measurements in marine sediments: A new approach, Limnology and Oceanography, 28, 1252-1259, 1983.

Wheeler, P.A. and D.L. Kirchman, Utilization of inorganic and organic nitrogen by bacteria in marine systems, Limnology and Oceanography, 31, 998-1009, 1986.

Winn, C.D., D.M. Karl and G.J. Massoth, Microorganisms in deep-sea hydrothermal plumes, Nature, 320, 744-746, 1986.

Wishner, K.F., The biomass of the deep-sea benthopelagic plankton, Deep-Sea Research, 27, 203-216, 1980.